
**Search for Heavy Neutral Higgs Bosons
in the $\tau^+\tau^-$ Final State in LHC
Proton-Proton Collisions at $\sqrt{s} = 13$ TeV
with the ATLAS Detector**

Dissertation

zur Erlangung des akademischen Grades
Doctor rerum naturalium
(Dr. rer. nat.)

vorgelegt der
Fakultät Mathematik und Naturwissenschaften der
Technischen Universität Dresden

von
Lorenz Hauswald
geboren am 26.02.1989 in Meißen

2017



1. Gutachter: Prof. Dr. Arno Straessner
2. Gutachter: Prof. Dr. Jochen Dingfelder

eingereicht am 06.02.2017
verteidigt am 12.05.2017

Kurzfassung

Es gibt experimentelle und theoretische Hinweise, dass das Standardmodell der Teilchenphysik trotz seines enormen Erfolgs selbst bei Energien deutlich unterhalb der Planckskala keine hinreichende Beschreibung des Universums ist. Das minimale supersymmetrische Standardmodell, eine der vielversprechendsten neuen Theorien, die bedeutende offene Fragen klären soll, sagt neben anderen neuen Teilchen zusätzliche neutrale und geladene Higgsbosonen voraus. Bei der Suche nach den neuen schweren neutralen Bosonen sind Zerfälle in zwei hadronisch zerfallende Tauleptonen besonders interessant, da sie in großen Teilen des Parameterraums das zweitgrößte Verzweigungsverhältnis haben und eine deutlich bessere Untergrundunterdrückung erlauben als für den führenden Zerfall in b -Quark-Paare. Diese Suche, basierend auf Proton-Proton-Kollisionen die 2015 und 2016 bei einer Schwerpunktsenergie von 13 TeV vom ATLAS-Detektor am Large Hadron Collider am CERN aufgezeichnet wurden, wird in dieser Dissertation vorgestellt. Es wurden keine signifikanten Abweichungen von der Standardmodellvorhersage festgestellt und daher CL_s -Ausschlussgrenzen berechnet, sowohl modellunabhängig als auch in verschiedenen MSSM-Benchmark-Szenarien. Aufgrund von Verbesserungen der Ereignisselektion und der Methoden der Untergrundabschätzung, sowie der höheren Kollisionsenergie, sind die MSSM-Ausschlussgrenzen deutlich stärker als in vorherigen Suchen. Die obere Grenze auf $\tan \beta$ im $m_h^{\text{mod}+}$ MSSM-Benchmark-Szenario reicht von 10 bei $m_A = 300$ GeV bis zu 48 bei $m_A = 1.2$ TeV bei einem Konfidenzniveau von 95 %.

Abstract

There are experimental and theoretical indications that the Standard Model of particle physics, although tremendously successful, is not sufficient to describe the universe, even at energies well below the Planck scale. One of the most promising new theories to resolve major open questions, the Minimal Supersymmetric Standard Model, predicts additional neutral and charged Higgs bosons, among other new particles. For the search of the new heavy neutral bosons, the decay into two hadronically decaying tau leptons is especially interesting, as in large parts of the search parameter space it has the second largest branching ratio while allowing for a considerably better background rejection than the leading decay into b -quark pairs. This search, based on proton-proton collisions recorded at $\sqrt{s} = 13$ TeV in 2015 and early 2016 by the ATLAS experiment at the Large Hadron Collider at CERN, is presented in this thesis. No significant deviation from the Standard Model expectation is observed and CL_s exclusion limits are determined, both model-independent and in various MSSM benchmark scenarios. The MSSM exclusion limits are significantly stronger compared to previous searches, due to the increased collision energy and improvements of the event selection and background estimation techniques. The upper limit on $\tan \beta$ at 95 % confidence level in the $m_h^{\text{mod}+}$ MSSM benchmark scenario ranges from 10 at $m_A = 300$ GeV to 48 at $m_A = 1.2$ TeV.

Contents

1	Introduction	1
2	Theoretical Foundations	3
2.1	The Standard Model of Particle Physics	3
2.1.1	The Higgs Mechanism	6
2.1.2	Success and Shortcomings of the Standard Model	8
2.2	Monte Carlo Simulation	10
2.3	The Minimal Supersymmetric Extension of the Standard Model . . .	12
2.3.1	Phenomenology of the MSSM Higgs Sector	15
2.3.2	Signal Monte Carlo Event Samples	17
2.3.3	MSSM Benchmark Scenarios	20
2.3.4	Experimental Constraints	22
3	The ATLAS Experiment	27
3.1	The Large Hadron Collider	27
3.2	The ATLAS Experiment	29
3.2.1	The Inner Detector	31
3.2.2	The Calorimeters	33
3.2.3	The Muon Spectrometer	35
3.2.4	Trigger Systems	36
3.3	Data Recorded at the Beginning of LHC Run 2	37
4	Physics Object Reconstruction	39
4.1	Low-Level Objects	39
4.2	Jet Reconstruction	40
4.3	Muons	44
4.4	Electrons	46
4.5	Hadronic Tau Decays	48
4.6	Removal of Object Ambiguities	51
4.7	Missing Transverse Momentum	51
5	Event Selection	53
5.1	Event Cleaning	53
5.2	Event Pre-Selection	54

5.3	Main Event Selection	54
6	Background Estimation	61
6.1	Background Monte Carlo Event Samples	61
6.2	QCD Multijet Background	63
6.2.1	Fake Factor Measurement	63
6.2.2	Background Validation	71
6.3	W+jets Background	73
6.4	Modelling of $\tau_{\text{had-vis}}$ Misidentification Rates in Monte Carlo Back- grounds	74
7	Systematic Uncertainties	83
7.1	Luminosity Uncertainty	83
7.2	Background Monte Carlo Modeling	83
7.3	Signal Acceptance	85
7.4	Modeling of Background with Misidentified $\tau_{\text{had-vis}}$	88
7.5	Detector-Related Uncertainties	89
8	Results	93
8.1	Methodology of the Statistical Analysis	93
8.2	Results of the Statistical Analysis	97
8.3	Limits	101
9	Summary and Outlook	105
A	Additional Signal Region Variable Distributions	109
B	Nuisance Parameter Rankings	115
C	Limit Tables	119
D	Implementation Details	121
	List of Figures	131
	List of Tables	135
	List of Abbreviations	137
	Bibliography	139
	Acknowledgments	163

Chapter 1

Introduction

The field of particle physics may be on the brink of discoveries with the potential to significantly change our understanding of the universe. By international collaboration involving the most complex experiments, the quest to learn about the cosmos, both at the smallest and the largest scales, has advanced far. The Standard Model (SM) [1–13], which describes the elementary particles and their interactions, is one of the most precisely tested models in science. It not only describes most of the experimental observations, but also, based on basic theoretical principles, predicted several new discoveries in the last decades. Its last elementary building block, the Higgs boson, has been discovered only recently at CERN, after a half-century long search [14, 15].

Despite its huge success, the Standard Model is unable to answer some of the key questions of contemporary physics, for instance about the nature of dark matter. This unknown source of gravity has a contribution to the total energy content of the universe over five times higher than that of baryonic matter [16]. The hierarchy problem [17], resulting in an unnaturally large fine-tuning of the bare Higgs mass, and the conjecture of a grand unified theory are also motivating the search for new physics. Among the existing theories which extend the Standard Model to include new phenomena aiming to answer these questions, perhaps the most promising is Supersymmetry (SUSY). It predicts many more elementary particles by introducing an additional symmetry between bosonic and fermionic states. The concept of symmetry is very important for particle physics, as it is deeply connected to conservation laws, as stated by Noether’s theorem. Symmetries guided the development of the best models currently available. One very popular model implementing SUSY is the Minimal Supersymmetric Standard Model (MSSM), which is the most economic way to introduce SUSY in terms of particle content. Besides the superpartners for each known elementary particle, it predicts additional neutral (A , H) and charged (H^\pm) Higgs bosons, which are a promising gateway to new physics beyond the SM.

These new Higgs bosons are expected to be accessible by the currently largest particle collider, the Large Hadron Collider (LHC) [18] at CERN, which recently

increased its proton-proton collision energy to an unprecedented 13 TeV. To observe the increasingly complex interactions occurring in the collision of the LHC proton beams, very sophisticated detectors, as well as large computational resources are necessary. The ATLAS detector [19], one of the main experiments at the LHC, is capable of reliably detecting these events.

Among the numerous decay channels of the hypothetical A/H Higgs particles, the decay to two tau leptons is particularly interesting, as it is favored in large parts of the search parameter space. Despite its higher branching ratio, the decay to a pair of bottom quarks is much less sensitive due to its more difficult background rejection and higher trigger thresholds. The tau is the only lepton able to decay to hadronic final states and it does so in the majority of the cases. These hadronic decays have similarities to the hadronic jets formed in the detector by highly energetic quarks or gluons, which are many orders of magnitude more common in the proton-proton collisions, making the background estimation very challenging. It is the goal of this thesis to search for additional heavy neutral Higgs bosons decaying to two hadronically decaying tau leptons in proton-proton collisions recorded by the ATLAS detector during the first year of LHC operation at a center-of-mass energy of 13 TeV. Similar searches, based on LHC data recorded at collision energies of 7 TeV and 8 TeV as well as at other collider experiments, did not find any evidence of new physics in this search channel [20–27]. Although the integrated luminosity of the data used for this new search is only about half as large as in the previous search at the LHC, a sensitivity gain is expected, as the increase in cross section is up to about one order of magnitude, especially at high mass (~ 1 TeV), depending on the production process and additional model parameters. Furthermore, significant improvements to the analysis methods are presented in this thesis, resulting in an additional sensitivity advantage.

The document is structured as follows. After an overview of the theoretical foundations and the motivation of this work in Chapter 2, the Large Hadron Collider and ATLAS experiment are described (Chapter 3). In Chapter 4, the reconstruction of the physics objects that are used in this search is discussed. The event selection, aiming to increase the discovery significance, is the topic of Chapter 5. A key aspect of this data analysis is the estimation of the background, which is detailed in Chapter 6. Chapter 7 provides details on the effect of systematic uncertainties on the analysis. The statistical method and its results are presented in Chapter 8. Finally, a summary of the findings and comparison to other recent results is given in Chapter 9.

In this thesis, natural units are used for mass, energy, momentum and spin, i.e. $\hbar = c = 1$. Details specific to ATLAS internal software are listed in Appendix D.

Chapter 2

Theoretical Foundations

During the last decades, an enormous amount of experimental data have been collected in the field of particle physics. These observations have been made possible by substantial technological progress and the dedication of thousands of physicists around the world. It is at least as important to *interpret* this data and a significant effort involving some of the most famous physicists of the 20th and 21st century has brought the field a huge step towards the ultimate goal, a model consistent with all observations – a theory of everything. The building of this model is an iterative process. New observations prompt the invention of new or the extension of existing models. Good models make predictions, which the experiments are striving to confirm or reject. It is the goal of this thesis to test such a prediction experimentally. This chapter gives a summary of the current state of the models which motivated this work.

2.1 The Standard Model of Particle Physics

The Standard Model (SM)¹ is a gauge quantum field theory with the gauge symmetry $SU(3)_C \times SU(2)_L \times U(1)_Y$, describing the electroweak and strong interactions. It is a combination of quantum chromodynamics (QCD) [1–5], described by $SU(3)_C$ with color charge C , and electroweak theory [6–8], a unification of weak and electromagnetic interactions, described by the $SU(2)_L \times U(1)_Y$ symmetry with the weak isospin \vec{T} (only present for left-handed fermions and right-handed antifermions) and hypercharge Y .

Elementary particles arise as excitations of quantum fields. The SM has 12 fermions, particles with half-integer spin that follow Fermi-Dirac statistics, which constitute the known matter particles. They are further divided into leptons, which do not participate in the strong interaction, and quarks, which have color charge and therefore undergo strong interaction. One further distinguishes charged leptons and neutrinos. Each

¹This section gives a brief overview of the SM, more detailed descriptions can be found e.g. in Refs. [28–30].

fermion has an antiparticle, which besides opposite charges has the same properties.²

The bosonic fields of the SM, adhering to Bose-Einstein statistics, give rise to gauge bosons of spin 1 and the Higgs boson of spin 0. Gauge bosons act as mediators of interactions. The massless photon enables electromagnetic interactions (QED $U(1)_Q$). The massive W^+ , W^- and Z bosons are responsible for weak interactions. W^\pm bosons only couple to left-handed fermions and right-handed antifermions (parity violation). Finally, the strong interaction is mediated by eight massless gluons, which carry different sets of color and anticolor charges. A distinctive feature of QCD is that the coupling strength becomes smaller with decreasing distance (or increasing momentum scale), the *asymptotic freedom*. On the other hand, at low energy all quarks have to form a color singlet, a phenomenon called *color confinement*. The force between quarks within a color singlet grows as their distance increases, preventing free colored states. When the gluon field between the separating quarks reaches a high enough energy, a new quark-antiquark pair is created, resulting in two color singlets. In contrast to W^\pm , Z and gluons, photons do not self-interact at tree level (leading order of perturbation theory), as they are uncharged. Fermions of the standard model appear in 3 generations, which have similar properties, besides the mass. Most of the luminous matter in the universe consists of the charged first generation particles: up and down quarks and electrons, as the more massive second and third generation particles tend to decay to lighter ones. An overview of the properties of all SM elementary particles is given in Table 2.1.

The SM Lagrangian can be divided into four terms, which are summarized in the following:

$$\mathcal{L}_{\text{SM}} = \mathcal{L}_{\text{gauge}} + \mathcal{L}_{f,\text{kin}} + \mathcal{L}_{\text{Higgs}} + \mathcal{L}_{f,\text{mass}}. \quad (2.1)$$

Kinetic gauge boson term $\mathcal{L}_{\text{gauge}}$ Below, there is an overview of the SM symmetry groups, their generators and the associated gauge fields with their field strength and couplings.

- $U(1)_Y$: generated by hypercharge Y , coupling g' , gauge field B_μ with field strength $B_{\mu\nu} = \partial_\mu B_\nu - \partial_\nu B_\mu$
- $SU(2)_L$: generated by three 2×2 matrices $T^a = \sigma_a/2$ (σ_a : Pauli matrices), coupling g , gauge fields W_μ^a with field tensor $F_{\mu\nu}^i = \partial_\mu W_\nu^i - \partial_\nu W_\mu^i - g\epsilon^{ijk}W_\mu^jW_\nu^k$ (ϵ^{ijk} : Levi-Civita pseudotensor)
- $SU(3)_C$: generated by eight 3×3 matrices t^C , coupling g_s , gluon fields \mathcal{A}_μ^C with field strength $G_{\mu\nu}^A = \partial_\mu \mathcal{A}_\nu^A - \partial_\nu \mathcal{A}_\mu^A - g_s f_{ABC} \mathcal{A}_\mu^B \mathcal{A}_\nu^C$ (f_{ABC} : structure constants of $SU(3)$)

²It is not yet clear whether neutrinos have antiparticles. Maybe they are their own antiparticles (Majorana neutrinos) [31, 32].

name		mass	electric charge Q	weak isospin T_3^W	color charge C
Fermions					
Quarks					
u	up	2.2 MeV	$\frac{2}{3}$	$+\frac{1}{2}$	r,g,b
c	charm	1.27 GeV			
t	top	173.21 GeV			
d	down	4.7 MeV	$-\frac{1}{3}$	$-\frac{1}{2}$	r,g,b
s	strange	96 MeV			
b	bottom	4.18 GeV			
Leptons					
ν_e	electron neutrino	unknown	0	$+\frac{1}{2}$	—
ν_μ	muon neutrino	unknown			
ν_τ	tau neutrino	unknown			
e	electron	511 keV *	-1	$-\frac{1}{2}$	—
μ	muon	105.7 MeV *			
τ	tau	1.777 GeV *			
Bosons					
γ	photon	0	0	0	—
W^\pm	W bosons	80.385 GeV	± 1	± 1	—
Z^0	Z boson	91.19 GeV *	0	0	—
g	gluons	0	0	0	8 color combinations
H	Higgs boson	125.1 GeV	0	—	—

Table 2.1: Elementary particles of the Standard Model [28]. Masses marked with * have been measured to higher precision and are rounded here for brevity.

With these, the kinetic gauge term can be written as:

$$\mathcal{L}_{\text{gauge}} = -\frac{1}{4}B_{\mu\nu}B^{\mu\nu} - \frac{1}{4}F_{\mu\nu}^a F^{a\mu\nu} - \frac{1}{4}G_{\mu\nu}^A G^{A\mu\nu}.$$

Kinetic fermion term $\mathcal{L}_{f,\text{kin}}$ The term describing the interaction of fermions with the gauge fields and free fermion fields is:

$$\mathcal{L}_{f,\text{kin}} = \sum_f i\bar{\psi}_f \gamma^\mu D_\mu \psi_f.$$

In the sum over the fermion Dirac fields, the parity violation is considered by omitting right-handed neutrinos and expressing the right-handed charged fermions as singlets: e_R , u_R , d_R . Furthermore, there are left-handed doublets for quarks, $q_L = (u_L, d_L)^T$, and leptons, $\ell_L = (\nu_L, e_L)^T$. Terms for the second and third generations are analogous. There are significant flavor changing charged currents (interactions across generations) in the quark sector, enabled by a mixing of the mass eigenstates of the down-type quarks (by convention) to form the corresponding eigenstates of the weak interaction. This mixing is implemented by the Cabibbo–Kobayashi–Maskawa matrix [9, 10], which is unitary and has four degrees of freedom (three mixing angles and a complex phase leading to CP violation). A similar mixing occurs in the lepton sector

with the Pontecorvo–Maki–Nakagawa–Sakata matrix [33, 34] which leads to neutrino oscillation. This is a consequence of neutrinos having nonzero (but very small, still unmeasured) mass.

Some of the terms of the gauge covariant derivative D_μ appear only for some of the fields:

$$D_\mu = \partial_\mu + ig'YB_\mu + \underbrace{igT^aW_\mu^a}_{\text{for left-handed doublets}} + \underbrace{ig_s t^A A_\mu^A}_{\text{for quarks}}. \quad (2.2)$$

Evaluating $\mathcal{L}_{f,\text{kin}}$ for the left-handed lepton doublet ℓ_L yields:

$$-\frac{g}{2}(\bar{\nu}_L, \bar{e}_L)\gamma^\mu \left[-\frac{g'}{g}B_\mu + \begin{pmatrix} W_\mu^3 & W_\mu^1 - iW_\mu^2 \\ W_\mu^1 + iW_\mu^2 & -W_\mu^3 \end{pmatrix} \right] \begin{pmatrix} \nu_L \\ e_L \end{pmatrix}.$$

One can see that the off-diagonal terms of the matrix yield flavor-changing interactions. These can be related to the physically observed W^\pm bosons: $W^\pm = 1/\sqrt{2}(W_\mu^1 \mp iW_\mu^2)$. Similarly, the B_μ and W_μ^3 fields (resulting in flavor conserving interactions) mix to yield the photon A_μ and Z boson by rotation in the space of the left-handed doublet:

$$\begin{pmatrix} A_\mu \\ Z_\mu \end{pmatrix} = \begin{pmatrix} \cos \theta_W & \sin \theta_W \\ -\sin \theta_W & \cos \theta_W \end{pmatrix} \begin{pmatrix} B_\mu \\ W_\mu^3 \end{pmatrix}.$$

By requiring that the photon does not couple to neutrinos, one can show how the weak mixing angle depends on the electroweak couplings:

$$\tan \theta_W = \frac{g'}{g}.$$

The relationship of the electric charge to hypercharge and isospin is given by the Gell-Mann–Nishijima equation [35, 36]:

$$Q = T_3 + \frac{Y}{2}.$$

The local $\text{SU}(2)_L \times \text{U}(1)_Y$ gauge invariance postulation is not compatible with massive gauge bosons. In case of A_μ , this is consistent with the observation, however the nonzero masses of the W^\pm and Z bosons break the symmetry. Any mass terms inserted ad hoc into the Lagrangian violate renormalizability. Also mass terms for fermions break the symmetry due to the asymmetry between left-handed and right-handed states.

2.1.1 The Higgs Mechanism

In 1964 a solution to the mass problem was developed by Guralnik, Hagen and Kibble [11], Brout and Englert [12], as well as Higgs [13]. By the process of spontaneous symmetry breaking, the Lagrangian stays invariant under the gauge symmetries, while

the vacuum state does not and thus the masses for the gauge bosons are generated while keeping the theory renormalizable. This method was implemented by Salam [8] and Weinberg [7] into the electroweak theory proposed by Glashow [6], which is often considered as the birth of the Standard Model. The Higgs mechanism introduces a scalar Higgs field ϕ , which is an $SU(2)_L$ doublet and has no color charge. It can be parametrized as:

$$\phi = \begin{pmatrix} \phi^+ \\ \phi^0 \end{pmatrix},$$

with complex fields ϕ^+ and ϕ^0 . The Higgs potential is

$$V(\phi) = \mu^2 \phi^\dagger \phi + \lambda (\phi^\dagger \phi)^2,$$

where for spontaneous symmetry breaking to occur, μ^2 must be negative and $\lambda \geq 0$. This has nonzero minima at the vacuum expectation value (VEV) v :

$$v = \sqrt{\frac{-\mu^2}{\lambda}}.$$

The potential is shown in Fig. 2.1.

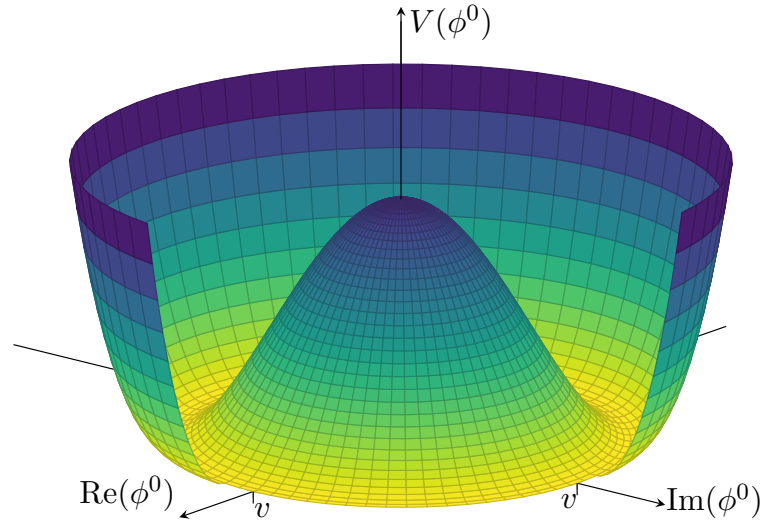


Figure 2.1: Visualization of the Higgs potential.

In the unitary gauge the doublet can be written in its common parametrization:

$$\phi = \frac{1}{\sqrt{2}} \begin{pmatrix} 0 \\ v + h \end{pmatrix},$$

where three degrees of freedom are absorbed as longitudinal components of W^\pm and Z ,

effectively giving them their masses. The remaining degree of freedom h is interpreted as the Higgs boson, an excitation of the Higgs field. After spontaneous symmetry breaking a $U(1)_Q$ symmetry of the ground state remains, so the photon stays massless, as observed. The kinetic and potential Higgs field terms of the Standard Model Lagrangian (Eq. 2.1) are:

$$\mathcal{L}_{\text{Higgs}} = (D^\mu \phi)^\dagger (D_\mu \phi) - V(\phi),$$

where the covariant derivative D_μ includes the coupling terms g and g' (see Eq. 2.2). Terms proportional to v^2 in the kinetic part reveal the masses of the gauge bosons (at tree level):

$$m_W = \frac{gv}{2}, \quad m_Z = \frac{gv}{2 \cos \theta_W}, \quad m_\gamma = 0.$$

Hence, the vacuum expectation value can be measured without knowing the Higgs mass: $v = 246 \text{ GeV}$. The Higgs mass (from the bilinear h term) is

$$m_h = \sqrt{2\lambda}v.$$

The fermions gain mass by interaction with the Higgs field, called Yukawa interaction:

$$\mathcal{L}_{f,\text{mass}} = -y_e \bar{\ell}_L^i \phi_i e_R - y_d \bar{q}_L^i \phi_i d_R - y_u \epsilon_{ij} \bar{q}_L^i \phi^{*j} u_R + \text{h.c.}$$

Terms proportional to v are interpreted as mass terms, e.g.

$$\mathcal{L}_{e,\text{mass}} = \frac{y_e v (\bar{e}_L e_R + \bar{e}_R e_L)}{\sqrt{2}} = \frac{y_e v \bar{e} e}{\sqrt{2}}$$

and thus the electron mass in dependence of the Yukawa coupling y_e is

$$m_e = \frac{y_e v}{\sqrt{2}}$$

(and similar for the down-quark mass). For the up-quark additionally the asymmetric tensor ϵ_{ij} is introduced to generate the mass. It is not clear yet how the neutrino masses are generated. A mass term via Yukawa interaction similar to up-quarks is possible when introducing sterile neutrinos [37]. Alternatively they could have Majorana mass, if they are their own antiparticles. Models where neutrino masses are generated by both Dirac and Majorana mechanisms exist (Seesaw).

2.1.2 Success and Shortcomings of the Standard Model

The SM has 19 free parameters³, which have all been measured. The parameters are the masses of the charged fermions, the gauge couplings, the CKM mixing angles and

³Parameters related to the neutrino masses and mixing are neglected here, as the corresponding mechanism is still unclear.

CP-violating phase, QCD vacuum angle⁴ and the Higgs vacuum expectation value and Higgs boson mass. Some of these parameters belong to the most precisely measured observables in science. Not only is the SM a good description of particles and their interaction, but also it has considerable predictive power. For instance it predicted the existence of W and Z bosons. Even their masses could be predicted based on previous measurements of the weak mixing angle. The discovery of these bosons in 1983 at CERN [39–42] was a huge success of the model. Also the gluon was predicted before its 1979 discovery at DESY [43–46]. Other successful predictions include the existence of the charm and top quarks. The most recent confirmation of a half-century old SM prediction is the Higgs observation at ATLAS and CMS in 2012 [14, 15]. Furthermore, the SM is tested by high precision measurements, which can also be sensitive to physics beyond the SM. One of these very accurately tested predictions is the anomalous magnetic moment of the electron. Its current measurement has a relative uncertainty of the order of 10^{-10} and agrees well with the calculation [47].

This huge success of the SM is also a motivation to study and eliminate its shortcomings. An obvious problem is the omission of gravity. The apparent incompatibility of QFT and general relativity means a combined theory probably has to be based on a new theoretical framework. String theory [48], currently the best contender of a theory of everything, still lacks falsifiability. However, at energies that are small compared to the Planck scale gravity is negligible, making the SM a viable effective theory in that regime.

The SM also does not describe dark matter, a form of non-baryonic matter which does not interact significantly with electromagnetic radiation and comprises 27 % of the total energy content of the universe, over five times more than ordinary matter [28]. Dark matter has been indirectly observed, for instance by measuring the rotational velocity of objects orbiting galactic centers, which is expected to be indirectly proportional to \sqrt{r} (radius of orbit around galactic center, r). Instead, the velocity is observed to be approximately constant at large radii, which implies the existence of an invisible source of gravity forming a halo around the galactic center [49, 50]. Other dark matter measurements are based on gravitational lensing and cosmic microwave background anisotropies [16]. While the hypothesis that dark matter consists of as yet undiscovered particles is currently most actively searched for, alternative theories exist (e.g. [51, 52]).

Another important phenomenon that the SM fails to describe in a sensible way is dark energy, which makes up most of the energy content of the universe. Estimates of the vacuum energy density from QFT, which is expected to contribute to the cosmological constant, are at least 40 orders of magnitude too large compared to the observed bounds [53].

Even more open questions exist, for instance: Why are there three fermion genera-

⁴The QCD vacuum angle is a parameter that allows for violation of CP-symmetry in QCD. QCD CP-violation has not been observed and limits on the electric dipole moment of the neutron constrain this parameter to very small values [38].

tions? Why is there such a large asymmetry between baryonic and antibaryonic matter in the universe? Why are the values of the SM parameters as they are?

Indications for discrepancies between SM prediction and measurements exist as well. One of them is the anomalous magnetic dipole moment of the muon, currently showing a 3.6σ tension between theory and experiment [28, 54].

Finally, there is the hierarchy problem [17], which is concerned with the large differences between the energy scales, e.g. between electroweak scale and the Planck scale. This leads to very large quantum corrections to the Higgs mass and this results in an amount of fine-tuning of the bare Higgs mass that is considered unnatural.

These problems necessitate new physics beyond the SM and there are good reasons why such a new theory should be accessible at TeV scales and thus might be observable at the LHC.

2.2 Monte Carlo Simulation

Calculations of kinematic observables based on the Lagrange density of the SM are in most cases too complex to perform analytically, particularly for the QCD processes of the proton-proton collision. The many possibilities of parton interactions and a high collision energy lead to a large phase space of initial and final states. Instead, events are modeled using Monte Carlo simulation, carried out in several steps. The structure of the event generation is visualized in Fig. 2.2.

At first, the scattering amplitudes (related to the cross section), appearing as elements of the S-matrix, are calculated perturbatively for the hard scattering, based on the Feynman rules of the model. The matrix element $\mathcal{M}_{ab \rightarrow X}$ of partons a and b resulting in state X , calculated up to a fixed order of α_s , is connected to the hadronic cross section σ using the factorization theorem [56]:

$$\sigma(pp \rightarrow X) = \sum_{a,b} \int_0^1 dx_a dx_b \int d\Phi_n f_a^{h_1}(x_a, \mu_F) f_b^{h_2}(x_b, \mu_F) \frac{|\mathcal{M}_{ab \rightarrow X}|^2(\Phi_n; \mu_F \mu_R)}{2x_a x_b s}. \quad (2.3)$$

This is a convolution of the squared matrix element, $|\mathcal{M}|^2$, with the parton distribution functions (PDFs), f , of partons a and b in their respective hadrons h_1 and h_2 . The differential phase space element $d\Phi_n$ enforces momentum conservation and includes the possible final state configurations. The PDFs have been measured at certain momentum scales. Their value at different scales is obtained using the DGLAP evolution equation [57–59]. The factorization scale μ_F and renormalization scale μ_R are arbitrary and usually chosen as a characteristic scale of the process, e.g. the transverse momentum of a final state particle or a resonance mass. A residual dependency on μ_F and μ_R emerges, as the perturbative series is truncated at a certain order of α_s , resulting in a systematic uncertainty of the cross section.

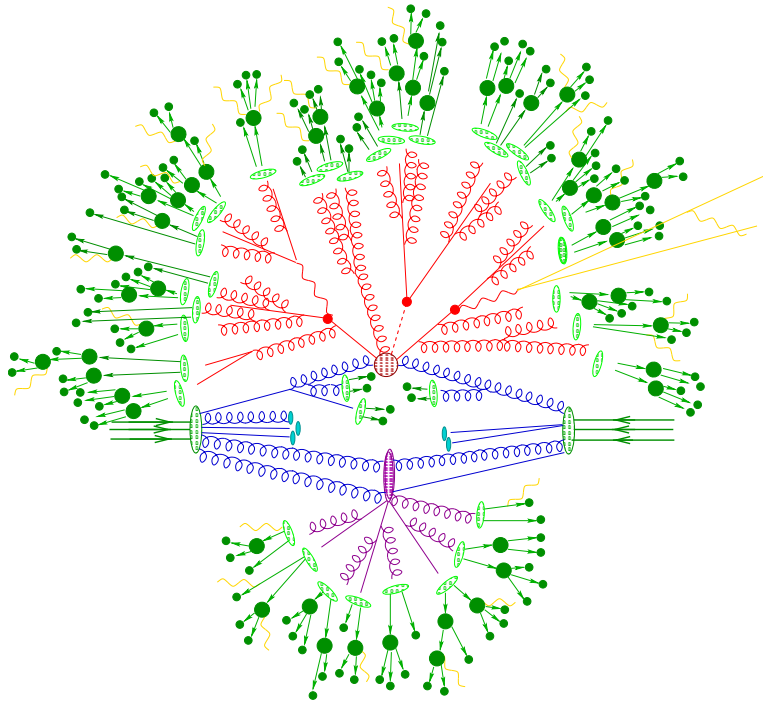


Figure 2.2: Visualization of the stages of event generation (dark red: hard scattering, light red: parton shower, light green: hadronization, dark green: decay, yellow: QED bremsstrahlung, purple: underlying event) [55].

Both initial and final state partons develop parton showers by successive gluon emissions, gluon splittings and quark pair production (called initial state radiation – ISR and final state radiation – FSR). This is modeled iteratively, where the probability and shape of each branching is determined by the Sudakov form factor and the splitting kernels [38]. Eventually, this process is aborted when the interaction scale evolution, determined by the DGLAP equations, has dropped below the hadronization scale, usually chosen at the order of 1 GeV. Initial state radiations are usually modeled using the corresponding reverse evolution instead. Electromagnetic corrections, i.e. QED bremsstrahlung, are usually simulated separately.

To avoid double counting of jets that might be modeled both by matrix element and parton shower, these regimes need to be merged using dedicated algorithms, for instance CKKW (Catani-Krauss-Kuhn-Webber [60, 61]) or MLM [62].

The partons resulting from the parton shower have to be combined to form colorless hadronic states. As the hadronization is a non-perturbative process, it is simulated with empirical models, which free parameters are obtained from measurements. Finally, the decays of unstable hadrons and leptons are simulated. These are mostly well known from calculations and measurements.

Additional hard parton-parton interactions occur due to the compositeness of the primary protons. These *multiple parton interactions* (MPI) are described with dedicated

semi-empirical models.

While particle-level studies can give insight in kinematic distributions and effects of systematic uncertainties arising from generator parameters, a simulation of the generator response has to be performed to compare the Monte Carlo generated events to recorded events. At ATLAS this simulation is performed using the ATHENA software framework [63]. Particle propagation and interaction with the detector material is performed by GEANT4 [64]. An alternative fast simulation algorithm exists, which is less precise but more economical with computing resources [65]. Pile-up events, i.e. proton-proton interactions happening simultaneously to the main hard scattering, are simulated separately as minimum-bias events and their energy depositions are superimposed to the main event. The multiplicity distribution of pile-up events is chosen to match the expected distribution in data. Afterwards, the expected detector response to the energy depositions is simulated. The following event reconstruction is the same as for recorded events and is described in Chapter 4.

2.3 The Minimal Supersymmetric Extension of the Standard Model

Symmetries are very important in particle physics and closely accompany the development of the SM. Exploring additional symmetries consistent with current results often leads to important insights or discoveries. Supersymmetry (SUSY) is a spacetime symmetry relating fermionic and bosonic states.⁵ Such transformations can only be implemented by spinorial operators Q_a (with spin index a):

$$Q_a |J\rangle = |J \pm 1/2\rangle ,$$

which therefore carries a spin of $1/2$ itself. Based on the Haag-Lopuszanski-Sohnius extension of the Coleman-Mandula theorem [67, 68], one can construct the algebra of these operators. The irreducible representations of the SUSY algebra are called supermultiplets, containing the bosonic and fermionic states, which are their respective superpartners. The SUSY generators commute with the four-momentum generator of spacetime displacements P^μ ,

$$[Q_a, P^\mu] = [Q_a^\dagger, P^\mu] = 0 ,$$

and therefore the masses of the superpartners have to be the same, if SUSY is unbroken. Additionally the SUSY generators commute with the SM generators of the gauge transformations, which means the superpartners have the same charges of $SU(3)_C \times$

⁵The summary given in this section follows the description in Refs. [17, 66].

$SU(2)_L \times U(1)_Y$. Furthermore, there are the following anti-commutation relations:

$$\begin{aligned}\{Q_a, Q_b\} &= \{Q_a^\dagger, Q_b^\dagger\} = 0, \\ \{Q_a, Q_b^\dagger\} &= \sigma_{ab}^\mu P_\mu,\end{aligned}$$

where σ^μ are the Pauli matrices.

There are two possible supermultiplets for SM extensions. Chiral supermultiplets contain a two-component Weyl fermion (massless) of spin $1/2$ and a complex scalar (spin 0). On the other hand, gauge supermultiplets have a Weyl fermion and a vector boson (spin 1). Only fermions from chiral supermultiplets can have different gauge transformations for left-handed and right-handed states and therefore all SM fermions have to be in chiral supermultiplets. Their spin-0 superpartners are called squarks, sleptons and sneutrinos. There are left-handed and right-handed sleptons and squarks, where the handedness refers to their superpartners. They exhibit the same gauge interaction properties as their SM counterparts, i.e. right-handed sfermions do not couple to W bosons.

Due to its spin, the Higgs boson has to be part of a chiral supermultiplet as well. However, more than one Higgs supermultiplet is necessary to avoid gauge anomalies. Another reason is that in SUSY only Higgs with hypercharge $Y = +1/2$ can couple to up-type quarks, while $Y = -1/2$ only couple to down-type quarks and charged leptons. Therefore in the MSSM an additional complex Higgs doublet is introduced. The Higgs superpartners are called higgsinos.

The SM gauge bosons are part of gauge supermultiplets and their fermionic superpartners are called gauginos, specifically gluino, bino and winos. Analogous to the W^3 and B mixing, a wino and the bino mix to form a zino and photino.

Remarkably, if SUSY is unbroken, the hierarchy problem is solved, as the superpartner loop contributions to the Higgs mass cancel each other out. However, none of the predicted superpartners has been discovered so far, which means they can not have the same mass as their SM counterparts and thus SUSY has to be spontaneously broken. This means there is a vacuum state that is not invariant under SUSY transformations, leading to higher masses of the predicted superpartners. The mechanism of SUSY breaking is not clear, so for the time being it is implemented by explicitly symmetry breaking terms in the Lagrangians and separating its origin from its effects. The MSSM includes *soft* symmetry breaking, with a SUSY breaking scale not much larger than 1 TeV. This is the preferred method, as the residual fine-tuning of the Higgs mass grows with the SUSY breaking scale and in this case would still be small enough for the hierarchy problem to be commonly considered as solved. Therefore the lightest superpartners are expected not above the TeV scale, which is a big motivation to search for SUSY at the LHC.

Another intriguing property of the MSSM is the possibility of the unification of

gauge couplings at some energy scale. The running of the gauge couplings, i.e. the change of these couplings with the energy scale, is determined by the renormalization group equations. As this evolution depends on the particles that contribute to higher order corrections, in SUSY the running of gauge couplings changes above the SUSY breaking scale, where superpartners contribute. In the MSSM the couplings meet almost exactly around a scale of 10^{16} GeV, as shown in Fig. 2.3 with a comparison to the SM evolution. This unification would strongly indicate the existence of a grand unified theory, i.e. a bigger symmetry group describing a unified force with one common coupling. This is another strong argument for SUSY and for the MSSM in particular, as the gauge unification depends on the particle content and requires a SUSY breaking scale below a few TeV.

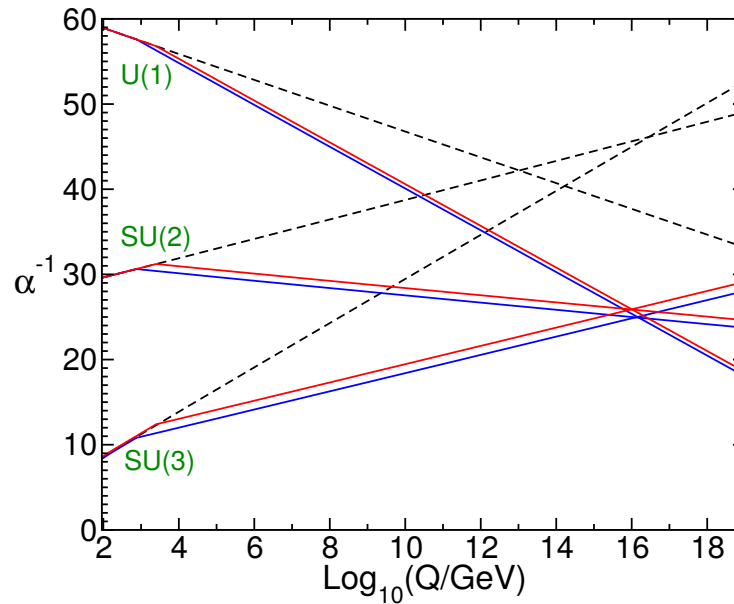


Figure 2.3: Evolution of inverse gauge couplings in the MSSM (blue and red lines, for different particle masses) and SM (dashed lines) [17]. Note that if there is really a unification and a GUT exists, at energies above the unification there is only one running coupling.

In the MSSM an additional symmetry is introduced, which adds the multiplicatively conserved quantum number R-parity:

$$R = (-1)^{3(B-L)+2s}.$$

It depends on the baryon number B , the lepton number L and the spin s . It is added to prohibit interactions that are strongly limited by experimental evidence. In particular it forbids the decay of the proton, which mean lifetime is currently measured to be at least 10^{29} years [28]. All discovered particles have $R = +1$, while their superpartners,

the sparticles, have $R = -1$. This means only even numbers of sparticles can be involved in an interaction. From R-parity conservation it also follows that the lightest sparticle (LSP) must be stable and all sparticle decays have to have an odd number of sparticle decay products (eventually LSPs). LSPs with electric charge are experimentally disfavored [69]. For instance, charged LSPs would be likely incorporated in ocean water and searches for heavy hydrogen-like atoms set stringent limits. Strongly interacting LSPs are also disfavored. So there is good reason to expect the LSP to be an only weakly interacting massive particle (WIMP) and therefore an excellent candidate for dark matter. In the MSSM the best LSP candidate is a neutralino, which is a mixing among bino, neutral wino and higgsinos.

2.3.1 Phenomenology of the MSSM Higgs Sector

The two Higgs doublets H_u (weak hypercharge $Y = +1/2$) and H_d ($Y = -1/2$) can be written as:

$$H_u = \begin{pmatrix} H_u^+ \\ H_u^0 \end{pmatrix}, H_d = \begin{pmatrix} H_d^0 \\ H_d^- \end{pmatrix}.$$

Then the tree-level scalar potential is [17, 66]

$$\begin{aligned} V = & \left(|\mu|^2 + m_{H_u}^2 \right) \left(|H_u^+|^2 + |H_u^0|^2 \right) \left(|\mu|^2 + m_{H_d}^2 \right) \left(|H_d^0|^2 + |H_d^-|^2 \right) \\ & + \left[b \left(H_u^+ H_d^- - H_u^0 H_d^0 \right) + \text{h.c.} \right] \\ & + \frac{1}{8} \left(g^2 + g'^2 \right) \left(|H_u^+|^2 + |H_u^0|^2 - |H_d^0|^2 - |H_d^-|^2 \right)^2 + \frac{1}{2} g^2 |H_u^+ H_d^{0*} + H_u^0 H_d^{-*}|^2. \end{aligned}$$

Here, μ is the higgsino mass parameter and the terms proportional to m_{H_u} , m_{H_d} and b are soft SUSY breaking contributions. The charged components H_u^+ and H_d^- can not get VEVs. This can be seen after an $SU(2)_L$ gauge transformation such that $H_u^+ = 0$ at the minimum of the potential ($\partial V / \partial H_u^+ = 0$), which implies that also $H_d^- = 0$ and thus $U(1)_Q$ remains unbroken. In order for spontaneous symmetry breaking of $SU(2)_L \times U(1)_Y$ to occur, V must have a lower bound and H_u^0 and H_d^0 should have nonzero VEVs. This is fulfilled when

$$\begin{aligned} 2b & < 2|\mu|^2 + m_{H_u}^2 + m_{H_d}^2 \text{ and} \\ b^2 & > \left(|\mu|^2 + m_{H_u}^2 \right) \left(|\mu|^2 + m_{H_d}^2 \right), \end{aligned}$$

which also means that $m_{H_u}^2 \neq m_{H_d}^2$. Often $m_{H_u}^2 = m_{H_d}^2$ is assumed at large scales (e.g. in minimal supergravity mSUGRA [70]), but the renormalization group evolution of m_{H_u} can make it negative around the electroweak scale.

The VEVs are then determined by $\partial V / \partial H_u^0 = \partial V / \partial H_d^0 = 0$. The resulting VEVs $v_u = \langle H_u^0 \rangle$ and $v_d = \langle H_d^0 \rangle$ are restricted by experiment as they generate the W and Z

masses:

$$v_u^2 + v_d^2 = \frac{v^2}{2} = \frac{2m_W^2}{g^2} \approx (174 \text{ GeV})^2.$$

The ratio of the VEVs is usually defined as

$$\tan \beta \equiv \frac{v_u}{v_d}.$$

The two complex Higgs doublets have eight degrees of freedom. Like in the SM, three of them are the longitudinal degrees of freedom of the W and Z bosons (with corresponding would-be Goldstone bosons G^\pm and G^0). Thus, there are 5 remaining scalar Higgs mass eigenstates, the CP-even h and H , two charged H^\pm and a CP-odd A . At tree level these are related to the gauge eigenstates as:

$$\begin{aligned} \begin{pmatrix} H_u^+ \\ H_u^0 \end{pmatrix} &= \begin{pmatrix} \sin \beta G^+ + \cos \beta H^+ \\ v_u + 1/\sqrt{2} (\cos \alpha h + \sin \alpha H + i \sin \beta G^0 + i \cos \beta A) \end{pmatrix}, \\ \begin{pmatrix} H_d^0 \\ H_d^- \end{pmatrix} &= \begin{pmatrix} v_d + 1/\sqrt{2} (-\sin \alpha h + \cos \alpha H - i \cos \beta G^0 + i \sin \beta A) \\ -\cos \beta G^- + \sin \beta H^- \end{pmatrix}. \end{aligned}$$

The mixing angle α that diagonalizes the mass matrix of h and H is determined by:

$$\frac{\sin 2\alpha}{\sin 2\beta} = \frac{m_H^2 + m_h^2}{m_h^2 - m_H^2} \quad \text{and} \quad \frac{\tan 2\alpha}{\tan 2\beta} = \frac{m_A^2 + m_Z^2}{m_A^2 - m_Z^2}, \quad (2.4)$$

and α is usually chosen to be $-\pi/2 < \alpha < 0$.

Then the masses of the Higgs bosons can be written as:

$$\begin{aligned} m_{h,H}^2 &= \frac{1}{2} \left(m_A^2 + m_Z^2 \mp \sqrt{(m_A^2 - m_Z^2)^2 + 4m_Z^2 m_A^2 \sin^2(2\beta)} \right), \\ m_{H^\pm}^2 &= m_A^2 + m_W^2. \end{aligned} \quad (2.5)$$

Therefore at tree level the MSSM Higgs mass spectrum depends on two unknown parameters, usually chosen as $\tan \beta$ and m_{H^\pm} or m_A . By convention $m_h < m_H$ and while m_A, m_H, m_{H^\pm} can get arbitrarily large, there is an upper bound for m_h (following from Eq. 2.5):

$$m_h < m_Z |\cos(2\beta)|.$$

Large quantum corrections increase that bound up to about 135 GeV, making it compatible with the 125 GeV Higgs discovery. These corrections are mainly driven by top and stop loops. The largest radiative correction depends on the mixing angle α , the stop masses and the stop mixing angle. Therefore the 125 GeV Higgs discovery indirectly restricts these parameters, requiring a large stop mixing and/or large stop masses.

The couplings of the Higgs also depend on α and β . The running masses of the SM

fermions are

$$m_{u,c,t} = \frac{1}{\sqrt{2}} y_{u,c,t} v \sin \beta, \quad m_{d,s,b} = \frac{1}{\sqrt{2}} y_{d,s,b} v \cos \beta \quad \text{and} \quad m_{e,\mu,\tau} = \frac{1}{\sqrt{2}} y_{e,\mu,\tau} v \cos \beta.$$

Based on these and the requirement that the Yukawa couplings should not become non-perturbatively large, one can set rough limits on $\tan \beta$:

$$1.2 \lesssim \tan \beta \lesssim 65.$$

An interesting special case is the decoupling limit, where $m_A \gg m_Z$. Then $\alpha \approx \beta - \frac{\pi}{2}$ and the heavy Higgs bosons become almost degenerate: $m_A \approx m_H \approx m_{H^\pm}$. It also enhances the compatibility of the 125 GeV Higgs discovery with the MSSM h . The α and β dependencies of the heavy neutral Higgs couplings to SM fermions are:

$$\begin{aligned} Hb\bar{b}, H\tau^+\tau^- &\propto \frac{\cos \alpha}{\cos \beta} \xrightarrow{m_A \gg m_Z} \tan \beta, \\ Ht\bar{t} &\propto \frac{\sin \alpha}{\sin \beta} \xrightarrow{m_A \gg m_Z} -\cot \beta, \\ Ab\bar{b}, A\tau^+\tau^- &\propto \tan \beta, \\ At\bar{t} &\propto \cot \beta. \end{aligned}$$

The heavy CP-even Higgs decouples from the SM vector bosons for heavy A :

$$HW^+W^-, HZZ \propto \cos(\beta - \alpha) \xrightarrow{m_A \gg m_Z} 0.$$

In the decoupling limit the h couples to SM particles like the SM Higgs. However, compared to the SM Higgs, the h has additional couplings involving the additional Higgs bosons and sparticles and therefore the production cross sections and decay width can differ.

2.3.2 Signal Monte Carlo Event Samples

The $\tau^+\tau^-$ decay of the heavy neutral Higgs is enhanced with $\tan \beta$. In that parameter range the coupling of H to W and Z is suppressed, unless m_A is rather small. The A can not couple to W and Z at tree level due to CP invariance. Therefore the Higgs production via the vector boson fusion and Higgsstrahlung processes, which have some significance for SM Higgs measurements, is negligible in this case. Gluon-gluon fusion, the main SM Higgs production process at the LHC, is important in the MSSM as well. However, at high $\tan \beta$ the top Yukawa coupling is suppressed, so the $\tan \beta$ -enhanced b -quark contributions to the quark loop are more important. For the same reason, top-associated Higgs production ($t\bar{t}H$) plays a minor role and instead b -associated production becomes the dominant Higgs production process at high $\tan \beta$. Additionally,

in the gluon-gluon fusion production of the CP-even Higgs bosons, sparticles (mainly stop and sbottom) contribute to the loop, which lowers the cross section in the parameter space of interest (high m_A , high $\tan \beta$) [71]. The study presented in this thesis considers the two main production mechanisms – b -associated production and gluon-gluon fusion, which Monte Carlo generation is described below. The Feynman graphs of important production processes are shown in Fig. 2.4.

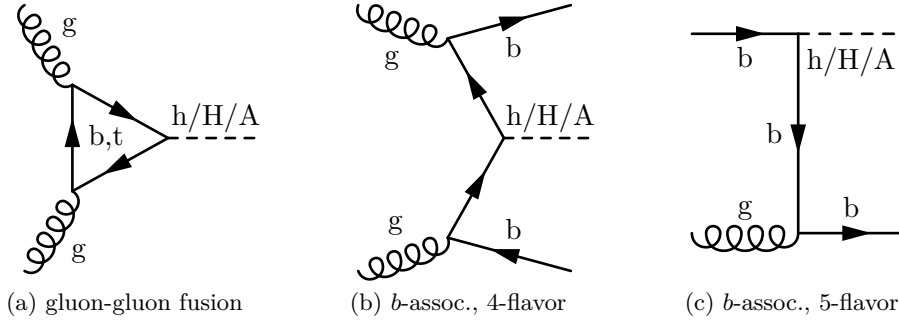


Figure 2.4: Examples of important MSSM Higgs production tree level Feynman diagrams.

b -associated Higgs production There are two common ways to calculate high-energy processes involving b -quarks: four-flavor and five-flavor scheme [72, 73]. In the five-flavor scheme, the bottom quark mass is neglected and it is treated similarly to the light partons and thus appears as initial state with its parton density function in the factorization theorem (Eq. 2.2). In the four-flavor scheme, the b -quark mass is not neglected, but it does not appear as initial state parton. Both methods have computational advantages and disadvantages, depending for instance on the typical scale of the process [73]. The two approaches yield equivalent results at high order, but can differ significantly at (low) fixed order.

For this study, the process is generated using a process module with calculations described in [73], embedded in the MADGRAPH5_aMC@NLO generator software package (version 2.1.2) [74]. This generator calculates the hard process including next-to-leading order (NLO) QCD corrections and employs the four-flavor scheme, which was found to be superior in this case, as the matching to the parton shower yields better results. The narrow-width approximation is employed, which neglects the Higgs decay width. This is valid for the study presented here, as the reconstructed mass resolution is generally significantly larger than the decay widths predicted by the MSSM with the parameter sets considered in this search. The parton shower is simulated with PYTHIA 8.210 [75] and the matching of matrix element and parton shower is performed using the MC@NLO method [76].

Due to the occurrence of top-quark loops at NLO, interference terms appear in the

four-flavor scheme cross section [73]:

$$\sigma_{bbH}^{4\text{FS}} = \underbrace{\alpha_S^2 y_b^2 \Delta_{y_b^2}^{(0)}}_{\sigma_{y_b^2}} + \alpha_S^3 \left(y_b^2 \Delta_{y_b^2}^{(1)} + \underbrace{y_b y_t \Delta_{y_b y_t}^{(1)}}_{\sigma_{y_b y_t} \alpha_S^{-3}} \right) + \mathcal{O}(\alpha_S^4).$$

The relative importance of $\sigma_{y_b^2}$ and $\sigma_{y_b y_t}$ depends on the model hypothesis, in particular on m_A and $\tan \beta$. At high $\tan \beta$ the $y_b y_t$ contribution is small and therefore neglected for this search. This affects only potential kinematic differences between the $\sigma_{y_b^2}$ and $\sigma_{y_b y_t}$ generation, as the total cross section is scaled to the prediction to be tested (see Sect. 2.3.3). The analytic results of the four-flavor scheme and five-flavor scheme are combined using Santander matching [77].

The four-flavor scheme PDF `CT10nlo_nf4` [78] is utilized for the hard process calculation. For the parton shower the `NNPDF23_1o` PDF [79] is used.

Due to the matching of the matrix element and parton shower, to avoid double counting of emissions, the event samples contain negatively weighted events. The fraction of these events in the generated samples is around 40 %, which reduces the effective number of events by factor ~ 5 and thus increases the relative statistical uncertainty ~ 25 -fold. Therefore a large number of generated events of the order of one million per mass hypothesis is required, which entails a large computational cost, especially for the simulation of the ATLAS detector response. To alleviate the computational effort, the fast ATLAS simulation `At1Fast-II` [65] is utilized. One sample ($m_{A/H} = 400$ GeV) was produced additionally with full simulation and the comparison showed no statistically significant differences in the reconstructed Higgs mass spectrum.

Gluon-gluon fusion The gluon-gluon fusion event samples are generated at NLO using the POWHEG-BOX generator framework [71], which applies the POWHEG method (acronym: positive weight hardest emission generator), and PYTHIA 8.186 for the parton shower generation. The PDF for the matrix element generation is `CT10` [78], while for the parton shower `CTEQ6L1` [80] is applied. The simulated Higgs decay width ranges from 1 % at 300 GeV to 3 % at 1.2 TeV. These values were chosen to be close to the widths predicted by the $m_h^{\text{mod}+}$ scenario (described in the next section) in the $\tan \beta$ range of the expected sensitivity limit of the search. Their calculation was performed with `FeynHiggs` [81–86].

Samples were generated separately for the $\tau_{\text{lep}} \tau_{\text{had}}$ ⁶ and $\tau_{\text{had}} \tau_{\text{had}}$ Higgs decays. The mass hypotheses and the respective event sample sizes are listed in Table 2.2. Due to the higher signal selection efficiencies, it is possible to reduce the sample size for Higgs masses above 0.5 TeV without significant increase in statistical uncertainty.

⁶The leptonic tau decay, $\tau \rightarrow e \bar{\nu}_e \nu_\tau$ or $\tau \rightarrow \mu \bar{\nu}_\mu \nu_\tau$ is denoted as τ_{lep} and τ_{had} is the notation for all decays with mesons in the final state.

mass hypotheses in GeV	number of events per sample [$\times 10^3$]	
	gluon-gluon fusion	b -associated production
300, 350, 500	50	900
400	50	1250
600, 700, 800, 1000, 1200	40	750

Table 2.2: The Higgs mass hypotheses for which signal Monte Carlo samples were generated and their respective sample size.

2.3.3 MSSM Benchmark Scenarios

While at leading order the MSSM Higgs sector is determined by only m_A and $\tan\beta$, higher order corrections depend on a larger parameter set. A scan of the whole parameter space is unfeasible, therefore only the m_A and $\tan\beta$ parameters are varied within a few well-motivated parameter sets, the so-called benchmark scenarios.

In this Higgs search CP-odd A and CP-even H are not distinguished. The signal components (i = gluon-gluon fusion, b -associated production) are scaled to the combined cross section multiplied by the $\tau\tau$ branching ratios:

$$\sigma_i(pp \rightarrow A) \times \text{BR}(A \rightarrow \tau\tau) + \sigma_i(pp \rightarrow H) \times \text{BR}(H \rightarrow \tau\tau).$$

The benchmark scenarios explored in this search are described in the following. Calculations of the cross sections and branching ratios for a range of $m_A - \tan\beta$ points are supplied by the LHC Higgs Cross Section Working Group [87]. Besides for the hMSSM scenario [88, 89], the Higgs masses, α mixing and branching ratios are calculated with **FeynHiggs** 2.10.2 [81–86]. Based on these, the **SusHi** [90] software is applied to calculate the inclusive cross sections of the gluon-gluon fusion process. This includes supersymmetric QCD corrections up to next-to-leading order [91, 92], NNLO QCD top quark corrections in the heavy-top limit [93, 94], as well as electroweak contributions of light quarks [95, 96]. The cross section of the b -associated production is calculated in the five-flavor scheme with **SusHi** at NNLO QCD based on [97] and in the four-flavor scheme at NLO QCD as described in [98, 99]. Details of the technical setup and the values of the input parameters of these tools (in particular the SM masses and decay widths) are given in Ref. [87].

The m_h^{max} scenario This scenario is one of the oldest commonly used parameter sets. It is designed to maximize the mass of the light CP-even Higgs in the decoupling limit [100] and was already used in the MSSM Higgs searches at LEP [20]. As it was already known by the LEP2 limits that the lightest Higgs would be relatively heavy for the MSSM and the 125 GeV Higgs had not been discovered yet, the m_h^{max} scenario was also one of the main benchmarks in LHC Run 1.⁷ However, portions of the $m_A - \tan\beta$

⁷LHC Run 1 is the first period of data taking, between 2009 and 2013.

parameter space are disfavored by the 125 GeV discovery and only the relatively large theoretical uncertainty of about 3 GeV of the MSSM m_h prediction ensures that a significant portion of the parameter space is still unexplored. The benchmark is included here in a slightly updated version [101] for comparison with earlier results.

The m_h^{mod} scenario This benchmark takes into account the 125 GeV discovery and the parameters are chosen so that a large portion of the $m_A - \tan \beta$ space ($\tan \beta \gtrsim 6$) is compatible with the measured $m_h \pm 3$ GeV [101]. There are two variants, $m_h^{\text{mod}+}$ and $m_h^{\text{mod}-}$, where the $+$ and $-$ correspond to the sign of the stop mixing parameter X_t . It is one of the most commonly used benchmarks in early LHC Run 2.⁸ Heavy neutral Higgs production cross sections and $\tau\tau$ branching ratios for the $m_h^{\text{mod}+}$ are shown in Fig. 2.5.

The light stop scenario While the m_h^{mod} scenario achieves the radiative corrections to m_h by a relatively high stop mass ($M_{\text{SUSY}} = 1$ TeV) and a moderate stop mixing parameter, it is possible to accommodate significantly lighter stop masses $M_{\text{SUSY}} = 500$ GeV by increasing the stop mixing. The experimental limits on the stop masses depend on the mass of the lightest neutralino $\tilde{\chi}_1^0$, but even for $m_{\tilde{\chi}_1^0}$ that maximize these limits, the current ATLAS results [102–105] still allow for stop masses below 1 TeV. Due to the larger stop mixing, the stop contributions to the loop in the gluon-gluon fusion process become more important, reducing the gluon-gluon fusion cross section compared to for instance m_h^{mod} . The benchmark is in agreement with $m_h = (125 \pm 3)$ GeV for $\tan \beta \gtrsim 10$, but in contrast to m_h^{mod} , a moderate reduction in theoretical uncertainty would raise that limit significantly [101].

The light stau scenario The presence of relatively light staus increases the diphoton decay width of the lightest CP-even Higgs. This benchmark [101] was partially motivated by a slightly higher $h \rightarrow \gamma\gamma$ signal strength in early Higgs results compared to the SM prediction [14, 15]. Recent results do not show such excess [106, 107], but also do not exclude an enhanced diphoton rate. The light stau benchmark is compatible with the Higgs mass measurement for $\tan \beta \gtrsim 5$.

The tau-phobic scenario This benchmark [101] considers the effects of the mixing between the CP-even MSSM Higgs bosons. The chosen parameter set results in relatively light staus and significantly different couplings to down-type fermions compared to the other benchmarks. As the name suggests, the branching ratios to tau leptons are reduced in most of the parameter space. The parameter space at $\tan \beta \gtrsim 48$ is disfavored by the 125 GeV Higgs observation.

⁸LHC Run 2 data taking started in 2015 and is planned to stop in 2018.

The hMSSM scenario The hMSSM benchmark [88, 89] takes into account the recent experimental results, especially the Higgs mass and the indication that squark and gluino masses are probably not significantly below 1 TeV. It was shown that under certain well-motivated assumptions [87] ignoring the radiative corrections to the Higgs masses is a good approximation given the experimental and theoretical uncertainties. As the hMSSM benchmark is compatible to the Higgs observation by design, also low values of $\tan\beta$, which are disfavored by most common benchmarks, can be explored (down to $\tan\beta \approx 1$). At low m_A there is an area of the $m_A - \tan\beta$ plane where the hMSSM is ill defined. However, this region is anyway already excluded by LHC searches and also indirect limits from the couplings of the observed Higgs exclude low masses of the heavy MSSM Higgs bosons. The masses and α mixing angle in the hMSSM are simply given by Eqs. 2.5 and 2.4. The branching ratios are calculated with HDECAY [108]. Effective cross sections for the gluon-gluon fusion and b -associated Higgs production processes in the hMSSM scenario are shown in Fig. 2.6.

Fig. 2.7 shows the ratio of the effective cross sections of gluon-gluon fusion over the sum of b -associated production and gluon-gluon fusion in the hMSSM scenario. It demonstrates the large importance of b -associated production at high $\tan\beta$. The other scenarios show very similar signal compositions.

2.3.4 Experimental Constraints on the MSSM Higgs Sector

The first important experimental constraints on the MSSM Higgs sector come from searches conducted at the LEP experiments [20]. These searches are sensitive to the main Higgs production mechanisms at the LEP electron-positron collider: Higgsstrahlung ($e^+e^- \rightarrow HZ$ or hZ) and pair production ($e^+e^- \rightarrow AH$ or Ah). These processes are suppressed for high $\tan\beta$ at heavy Higgs masses above m_Z , therefore the LEP result is sensitive to low $\tan\beta$, which limits have still not been fully surpassed by the LHC experiments. The Tevatron searches for b -associated MSSM Higgs production [21–23] were the first to explore the high $\tan\beta$ region at masses above 93 GeV. These early limits from LEP and Tevatron are shown in Fig. 2.8.⁹

Already with an integrated luminosity of 36 pb^{-1} recorded at $\sqrt{s} = 7 \text{ TeV}$ by each ATLAS and CMS in 2010, the collaborations were able to surpass the Tevatron limits in searches for $\tau^+\tau^-$ resonances [24, 25], see Fig. 2.9.

A combination of the results of most search channels based on the complete LHC Run 1 data set for each ATLAS and CMS [26, 27], displayed in Fig. 2.10, shows significant progress in covering the $m_A - \tan\beta$ plane, with di-tau decay channels covering the high- $\tan\beta$ region up to 1 TeV and low- m_A /low- $\tan\beta$ limits by searches for di-boson Higgs decays.

⁹ For the m_h^{max} variant of the Tevatron limit in Fig. 2.8 the higgsino mass parameter μ is negative, while the LEP limit plot, as well as the search presented in this thesis, use a positive μ value in m_h^{max} . The difference between the limits of these m_h^{max} variants is generally very small.

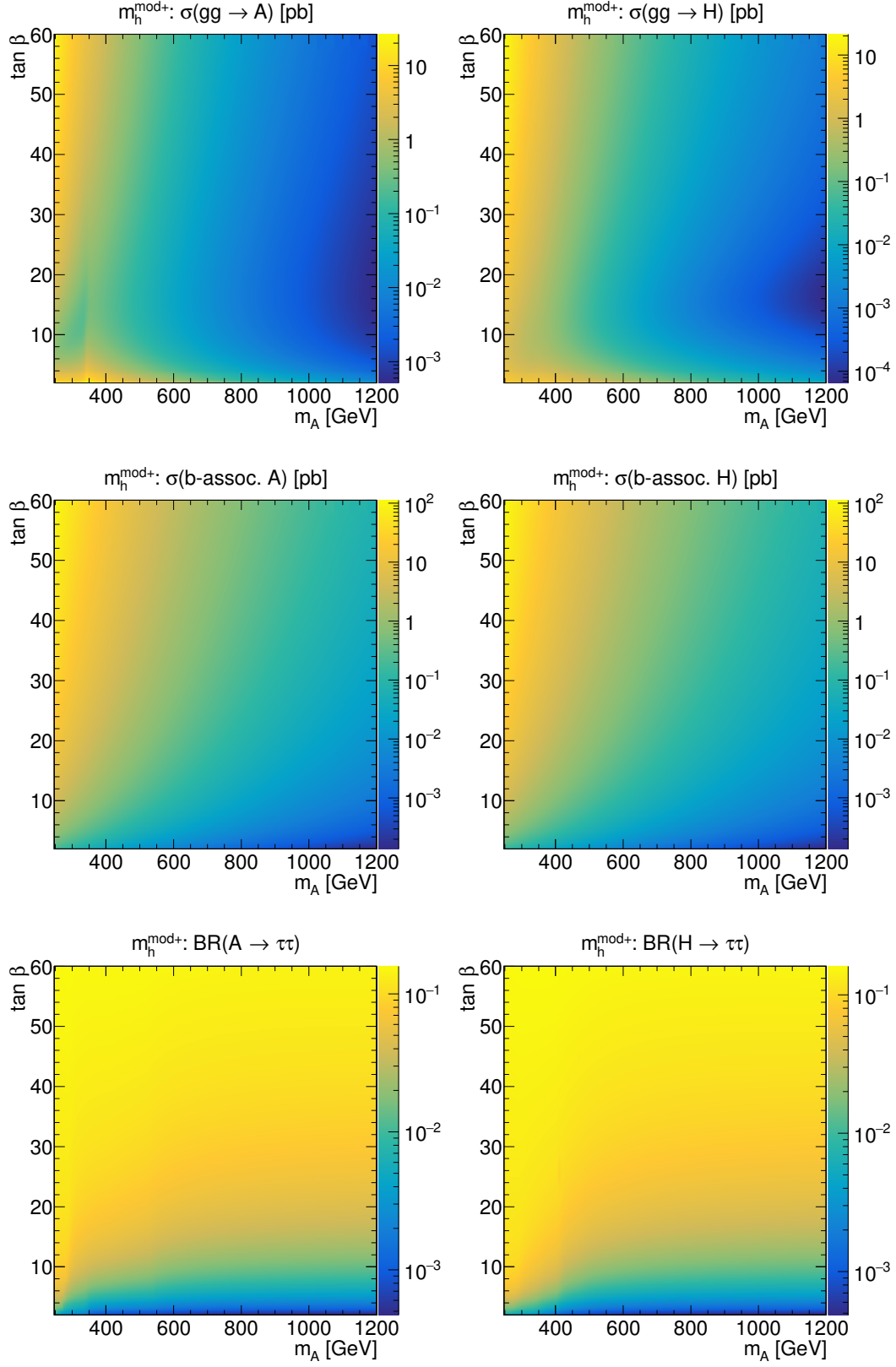


Figure 2.5: Heavy neutral Higgs production cross sections and $\tau\tau$ branching ratios for the $m_h^{\text{mod}+}$ MSSM benchmark scenario. The numbers are provided by [87].

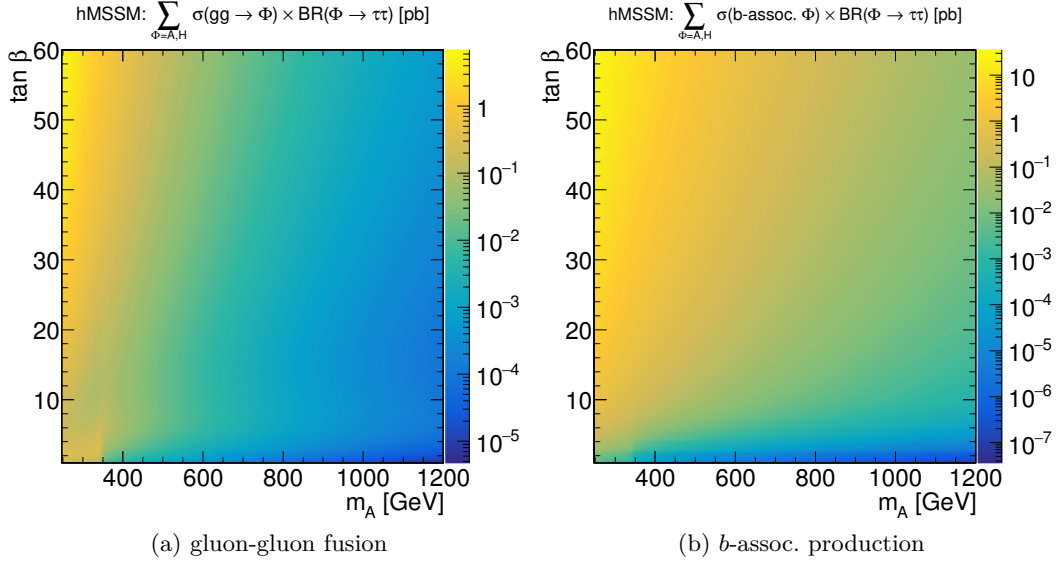


Figure 2.6: Sum of heavy neutral Higgs production cross sections multiplied by $\tau\tau$ branching ratios for the hMSSM benchmark scenario. The numbers are provided by [87].

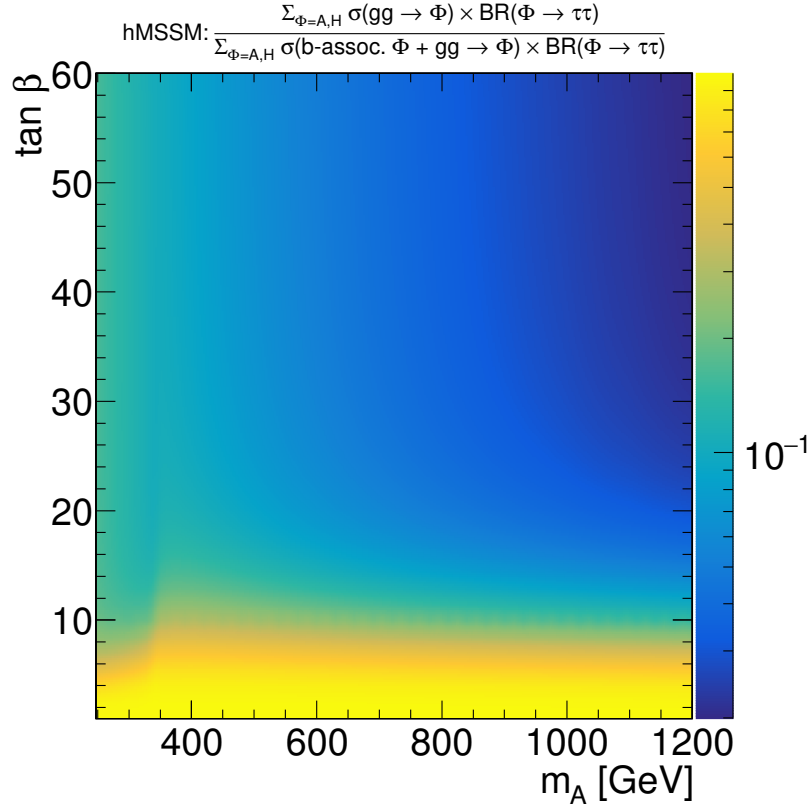


Figure 2.7: Ratio of the sums of heavy neutral Higgs production cross sections multiplied by $\tau\tau$ branching ratios for gluon-gluon fusion and b -associated production in the hMSSM benchmark scenario. The calculations are based on numbers provided by [87].

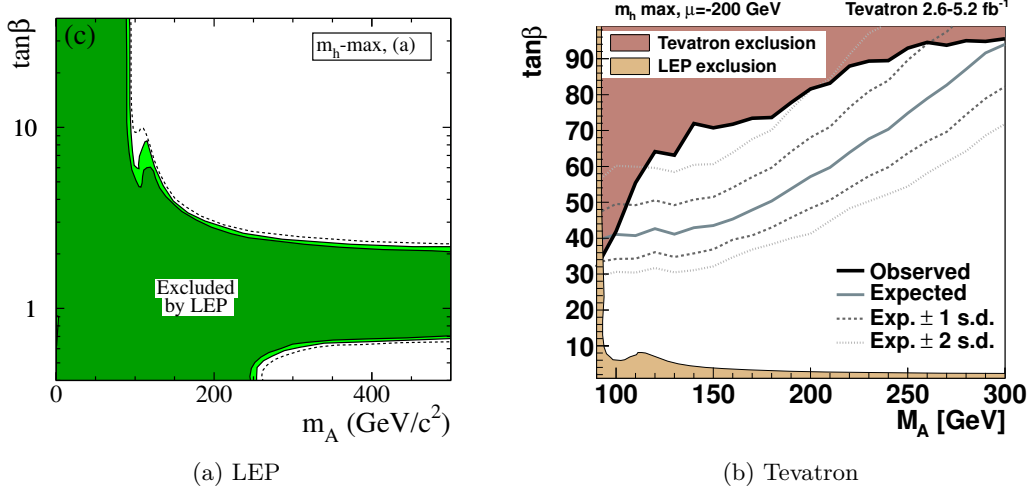


Figure 2.8: Exclusion limits from MSSM Higgs searches at LEP [20] and Tevatron [23] in the m_h^{\max} benchmark scenario. The light green area of the LEP limit corresponds to 95 % CL, while the dark green area has a CL of 99.7%. The dashed line in Subfig. (a) is the expected upper limit at 95 % CL.

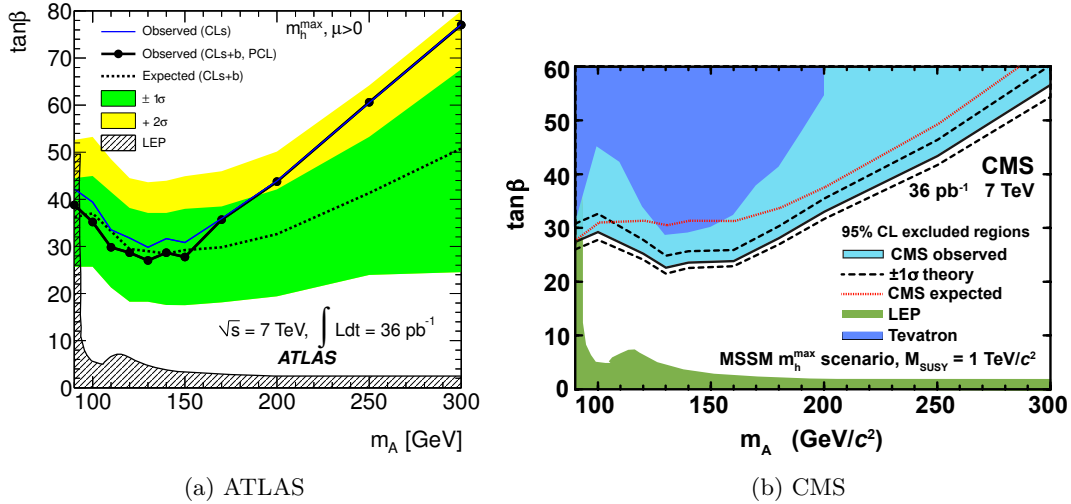


Figure 2.9: Exclusion limits from MSSM Higgs searches at ATLAS [24] and CMS [25] in the m_h^{\max} benchmark scenario, based on data recorded in 2010 at a center-of-mass energy of 7 TeV.

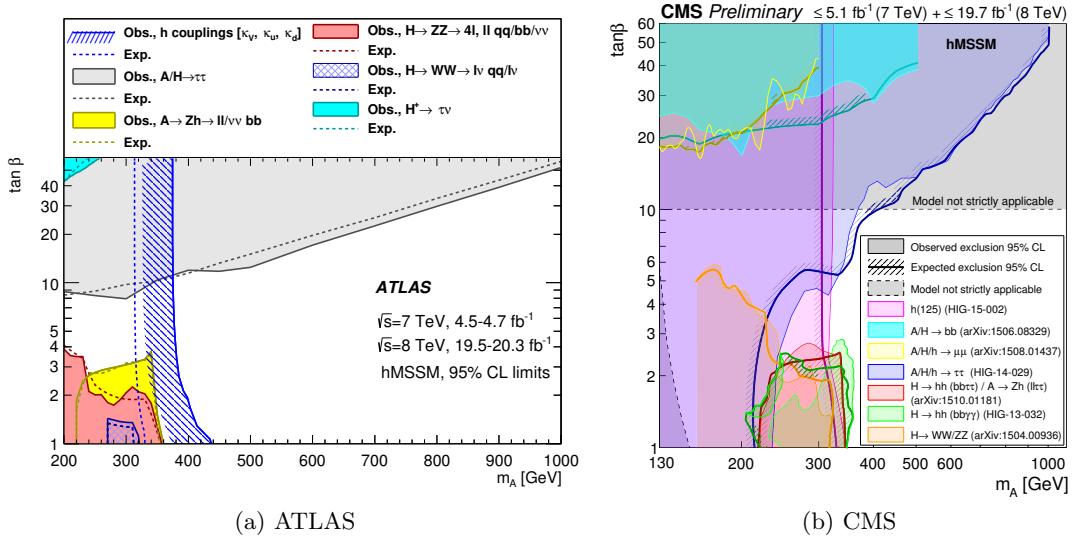


Figure 2.10: Exclusion limits from MSSM Higgs searches at ATLAS [26] and CMS [27] in the hMSSM benchmark scenario, based on data recorded in LHC Run 1.

Indirect constraints on the MSSM Higgs sector come from the measurement of the 125 GeV Higgs mass and its couplings, from search limits on sparticle masses, as well as electroweak precision measurements and astrophysical experiments. There are efforts to study how a combination of many of these experimental results influences the status of the MSSM, e.g. Ref. [109].

Chapter 3

The ATLAS Experiment

The CERN particle physics laboratory near Geneva (Switzerland) is by far the biggest of its kind and hosts experiments responsible for important discoveries, like the W , Z (1983, UA1/2 collaborations [39–42]) and Higgs boson (2012, ATLAS and CMS collaborations [14, 15]). These major scientific advancements have been enabled by technological breakthroughs, many of which have also happened at CERN (e.g. stochastic cooling, van der Meer [110]). Currently the focus of CERN is on the proton collider physics program at the Large Hadron Collider. The LHC and its pre-accelerators, as well as its performance at the beginning of LHC Run 2 is described in Sects. 3.1 and 3.3. ATLAS belongs to the most sophisticated particle physics detectors to date. An overview of its properties is given in Sect. 3.2.

3.1 The Large Hadron Collider

The LHC [18, 111] is a synchrotron accelerator that collides protons at four interaction points. It is located up to 175 m below the surface and crosses the Franco-Swiss border. With a circumference of 27 km it is currently the largest particle collider. It is designed to achieve a center-of-mass energy \sqrt{s} of 14 TeV. After the operation of the Large Electron Positron collider (LEP) ended in 2000, the LHC installation started, reutilizing the LEP tunnel.

The 1232 superconducting dipole magnets, cooled by liquid helium to 1.9 K, bend the counter-rotating proton beams with magnetic fields up to 8.3 T. Quadrupole magnets in alternating focusing and defocusing configuration (FODO cells) keep the transverse size of the beam small. Further corrections of the beams are performed by sextupole, octupole and decapole magnets.

Besides the center-of-mass energy, the luminosity is a key performance parameter of any accelerator. At colliders it can be calculated as

$$L = \frac{n_b N_b^2 f \gamma F}{4\pi \epsilon \beta^*}, \quad (3.1)$$

depending on the number of bunches per beam n_b , the number of protons per bunch N_b , the revolution frequency f , the relativistic factor of the protons γ , the beta function at the crossing point β^* , the transverse normalized emittance ϵ and a geometric reduction factor F arising due to the crossing angle. The event rate of a given process is given by its cross section multiplied by the luminosity. Multiplying with the integrated luminosity $L_{\text{int}} = \int_T L dt$ gives the total number of expected events occurring in a given time T .

During Run 1 (2009-2013) the collider delivered an integrated luminosity of about 6 fb^{-1} at a center-of-mass energy of 7 TeV and 23 fb^{-1} at 8 TeV [112] to the main experiments ATLAS [19] and CMS [113]. Furthermore, lead-lead ion and lead-proton collisions are part of the LHC physics program. After the *Long Shutdown 1*, a 2 years long maintenance period (2013-2014), the collider started to operate at a center-of-mass energy of 13 TeV, a new accelerator record. Magnet quenches (the sudden loss of superconductivity of a magnet, induced by a deposition of a relatively small amount of energy $\sim \text{mJ}$) result in loss of beam and potential damage [114]. When increasing the current (and therefore the magnetic field and beam energy) after the magnets have been warm for some time (like during the Long Shutdown 1), quenches occur more often due to mechanical disturbances. After the magnets underwent a certain number of quenches (training), the quench rate drops and the magnet is ready for nominal use. As the training would take longer and reduce the integrated luminosity in the first years of Run 2 (2015-2018), it was decided to postpone the 14 TeV operation until later in Run 2 or Run 3 [115].

The LHC design luminosity is $10^{34} \text{ cm}^{-2} \text{ s}^{-1}$, which was surpassed in July 2016. While the highest number of proton bunches per beam at that time was 2064 and therefore smaller than the design value of 2808, the beta function β^* at the ATLAS interaction point was 0.4 m, significantly smaller than the anticipated value of 0.55 m of the design report [116]. The transverse normalized emittance ϵ reached values as low as $3.40 \mu\text{m rad}$ at the start of the fill (design value $3.75 \mu\text{m rad}$). The number of protons per bunch was within about 10 % of the planned value of 1.15×10^{11} . In 2015 the bunch spacing was reduced from 50 ns to 25 ns, which is the best possible configuration.

As the LHC, like all synchrotrons, has a limited energy range, determined primarily by the capabilities of its magnets, protons have to be injected into the ring with a significant kinetic energy and are then further accelerated to the collision energy. The pre-accelerator complex [117], consisting of updated older CERN accelerators, is depicted in Fig. 3.1. As a first step, protons (extracted from H_2 gas) are accelerated to 50 MeV in the linear accelerator LINAC2 [118], which has been operated since 1978 and was upgraded in 1993 to increase the intensity. It is planned to be replaced by LINAC4 [119] in 2020, which started operation in 2013 and will enable a significant increase of LHC luminosity after 2025 (HL-LHC [120]). The protons are then injected into the Proton Synchrotron Booster (PSB) [121], a circular accelerator with a diameter of 50 m, which has four beam pipes on top of each other and is in operation since 1972.

Originally it had a final energy of 800 MeV and was upgraded to 1.4 GeV [122] to meet the requirements of the LHC. The proton energy is further increased to 25 GeV by the Proton Synchrotron (PS), which is 200 m in diameter. It is the oldest of CERN's main accelerators, with first beam in 1959, but has been improved several times since then and supplied beams of a wide range of different particles to many of the most important accelerators and experiments at CERN [123]. Finally, the last pre-accelerator, the Super Proton Synchrotron (SPS) brings the protons to 450 GeV and two separate transfer lines and injectors get them into the LHC. The SPS is the second largest accelerator at CERN with a circumference of 7 km. Its use as a collider resulted in the discovery of W and Z bosons in 1983. Contrary to the LHC, all pre-accelerators rely on conventional electromagnets (operated at room temperature). Significant upgrades to all pre-accelerators are being implemented to prepare for the high luminosity operation of the LHC [124].

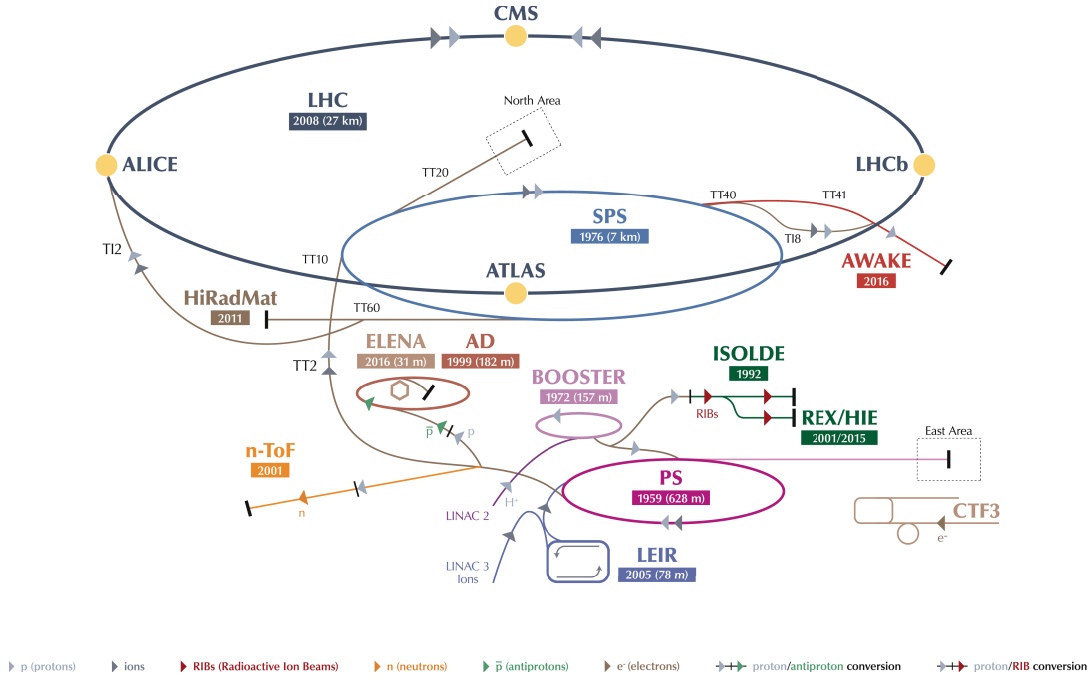


Figure 3.1: Schematic overview of the current CERN accelerator complex, with year of first operation and circumference in parentheses ([125], cropped)

3.2 The ATLAS Experiment

The ATLAS collaboration, today consisting of about 5300 members of 94 different nationalities [126], was founded by the merge of the ASCOT and EAGLE proto-collaborations. After the formal proposal (“Letter of Intent” 1992 [127]) and a technical proposal in 1994 [128], it was officially approved by CERN and construction started in 1997. The detector is situated in a cavern at “Point 1”, the LHC interaction point

closest to the main campus. Its cylindrical form around the interaction point results in a large angular acceptance. With a height of 25 m and length of 44 m, it is the largest detector at the LHC [19]. An overview of the detector is shown in Fig. 3.2. The main detector systems are reviewed in the following sections.

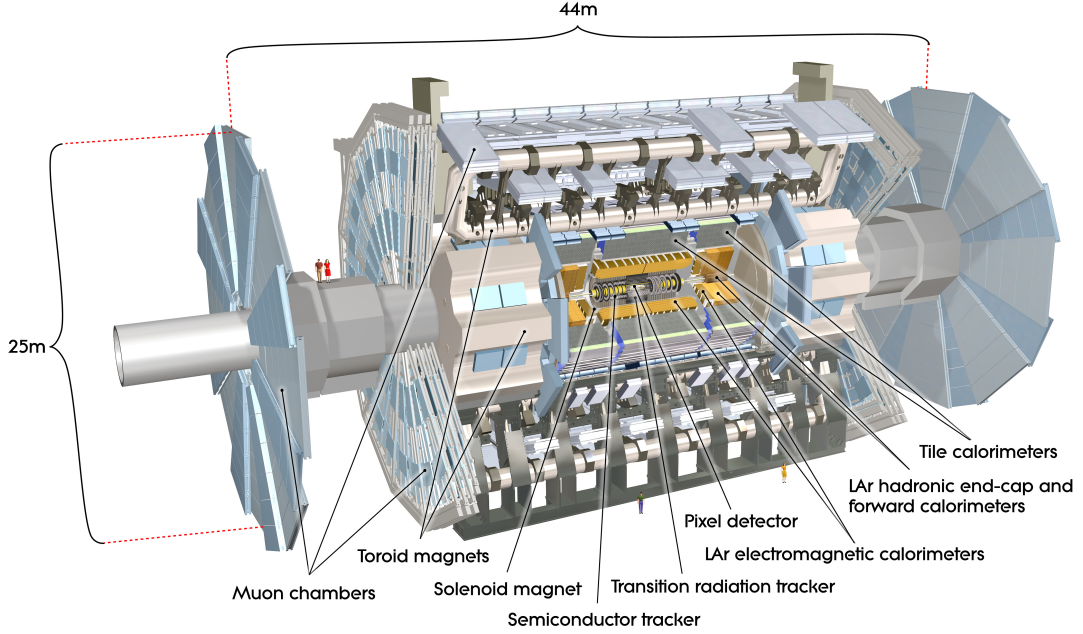


Figure 3.2: A schematic view of the ATLAS detector and its subsystems [129].

ATLAS is commonly described in a coordinate system with the origin at the nominal interaction point. In Cartesian coordinates the beam pipe is located around the z -axis and the x -axis is parallel to ground level, pointing towards the center of the LHC ring. Usually the detector and reconstructed particles are given in polar coordinates (see Fig. 3.3), with the azimuthal angle ϕ (measured from the x -axis in the transverse plane). Instead of the polar angle θ (measured between the z -axis and the radius vector), most of the time the pseudorapidity η , defined as

$$\eta = -\ln \tan \left(\frac{\theta}{2} \right)$$

is used, as differences in η are invariant under longitudinal boosts for particles with large Lorentz factors.

In Fig. 3.4 it is visualized how the pseudorapidity depends on the polar angle. The angular separation of physics objects is usually expressed as the distance in the η - ϕ -plane:

$$\Delta R = \sqrt{(\Delta\phi)^2 + (\Delta\eta)^2}.$$

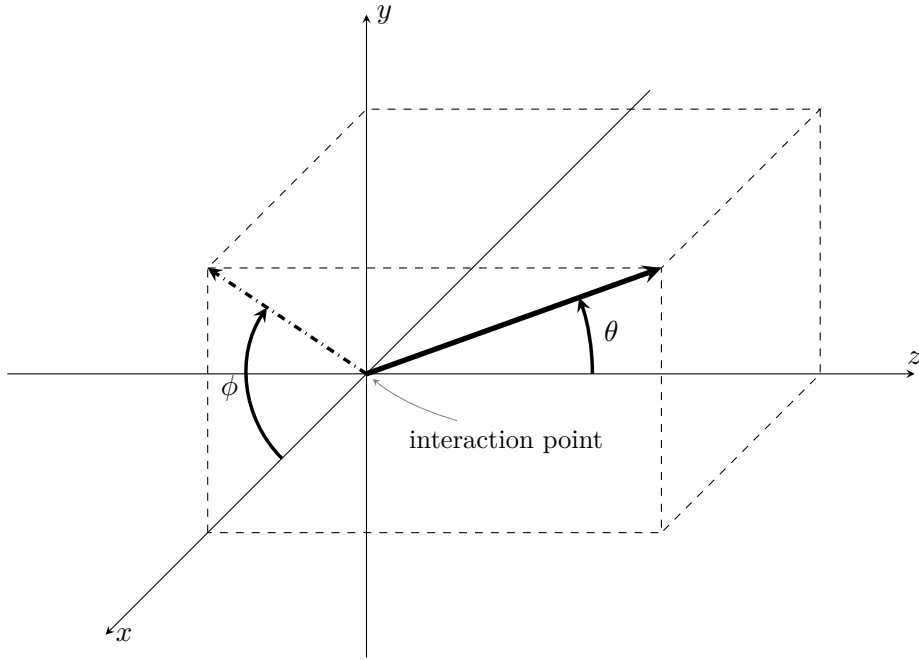
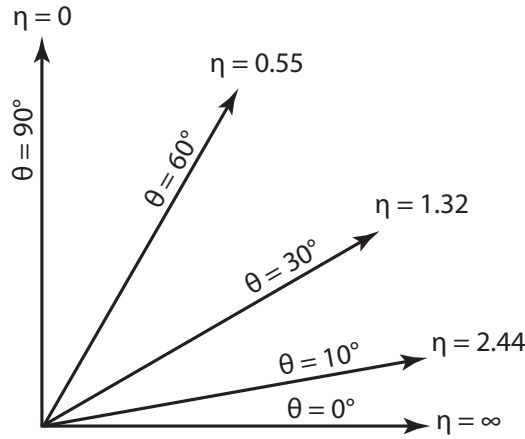


Figure 3.3: The ATLAS coordinate system.

Figure 3.4: Visualization of pseudorapidity η and polar angle θ [130].

3.2.1 The Inner Detector

The Inner Detector is dedicated to the measurement of charged particle trajectories and vertices. It is installed closest to the beam pipe up to a radius of 1.15 m. A strong magnetic field of 2 T, generated by the central solenoid, permeates the Inner Detector, which allows for the reconstruction of charged particle momentum and charge using the track curvature induced by the Lorentz force. The large number of particles per event, resulting in a considerable amount of radiation, as well as the high track density (particularly within high energy jets), place severe requirements on the design of the Inner Detector. The three subdetectors, shown in a schematic cutaway view in Fig. 3.5

are described in the following.

Pixel detector The innermost detector, the Pixel, has four cylindrical layers of silicon pixel arrays (up to a radius of 12 cm) and three disks of pixel modules on each side (15 cm outer radius). Ionizing particles are detected as they create electron-hole pairs in the semiconductor pixels. The very fine granularity of the over 92 million readout channels results in a very small impact parameter and vertex resolution as low as a few μm (cf. Sect. 4.1). The innermost pixel layer is called the Insertable B-Layer (IBL) [131] and was added as part of the detector upgrade program in Long Shutdown 1. To get the IBL as close as only 3.3 cm to the beam, also the beam pipe had to be replaced. This additional sensory information in proximity of the beam yields a significant improvement in secondary vertex reconstruction efficiency and resolution and therefore positively affects b -tagging and τ_{had} identification performance (cf. Chapter 4). The IBL will also reduce the loss of efficiency that is expected due to radiation damage, especially affecting the layer that was closest to the beam before the upgrade. As the current Inner Detector is not going to be able to withstand the radiation damage and was not designed to reconstruct the large number of tracks expected at the HL-LHC, it is planned to be completely replaced with a new system in 2024 [132].

Semiconductor Tracker (SCT) The SCT consists of four cylindrical layers between 30 cm and 51 cm from the beam, as well as nine disks ($28\text{ cm} < \text{radius} < 56\text{ cm}$) on each end-cap. The detection principle is similar to the Pixel, but the cathodes have the form of strips, which reduces the number of readout channels, of which the SCT has 6.3 million. Charged particle trajectories usually cross eight SCT strips, corresponding to four space points, as each strip misses position information in one dimension, which is recovered by small-angle stereo strips (strips rotated by 40 mrad relative to the others). The Pixel and the SCT are often called the Silicon Detectors and each have a pseudorapidity acceptance of $|\eta| < 2.5$.

Transition Radiation Tracker (TRT) The TRT is the outermost tracking detector and covers pseudorapidities of $|\eta| < 2.0$. It consists of long drift tubes of 4 mm diameter and provides a track measurement in the $R - \phi$ plane. They are filled with a gas mixture of 70 % xenon, 27 % carbon dioxide and 3 % oxygen. To reduce the cost of gas leaks, in some regions xenon is replaced by argon [133]. The gas is ionized by charged particles passing through the tube and the resulting free electrons drift in the electric potential between the straw walls and the gold-plated tungsten anode wire (32 μm in diameter) in the middle of the straw. Highly relativistic particles emit transition radiation when crossing media with different dielectric constants. In the TRT this is achieved by thin polypropylene fibers and foils between the tubes. These highly collinear photons are absorbed by the xenon gas, facilitated by its high atomic number, and the increased measured current enables the discrimination of electrons and particles with

lower Lorentz constant γ , in particular charged pions. This information is also utilized in the distinction of hadronically decaying tau leptons against jets initiated by hard quarks or gluons.

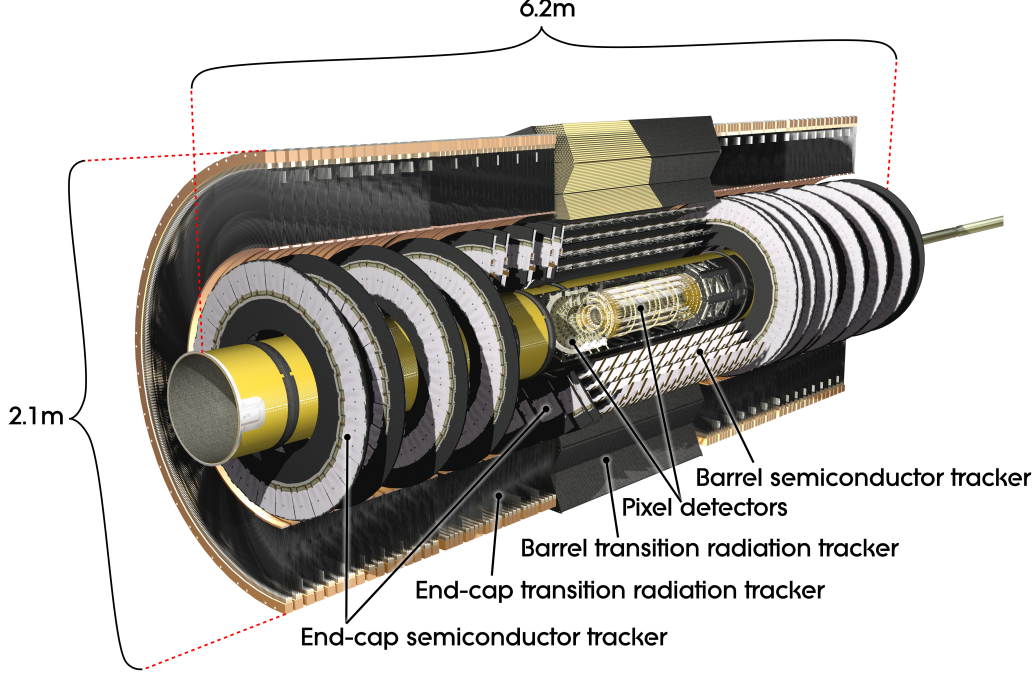


Figure 3.5: Schematic view of the Inner Detector [134].

3.2.2 The Calorimeters

As shown in Fig. 3.6, ATLAS has several calorimetry systems installed around the Inner Detector. The goal is to absorb all particles besides muons and neutrinos within the calorimeters and measure their energy. A large pseudorapidity acceptance up to $|\eta| = 4.9$ enables a precise measurement of the missing transverse momentum. The energy is measured using *sampling calorimeters*, which have alternating layers of absorber material and active medium. This design has a worse energy resolution due to the passive layers, but is more cost-effective than homogeneous calorimeters.

Electromagnetic Calorimeter (ECAL) The ECAL, dedicated primarily to induce and measure electromagnetic showers, is installed around the Inner Detector. It consists of a barrel part (EMB) at $|\eta| < 1.5$ and an end-cap part (EMEC) at each side, covering pseudorapidities up to $|\eta| = 3.2$. Its outer radius is 2 m. Liquid argon (LAr) is utilized as active material with lead absorbers in an accordion geometry. There are three layers, each segmented into cells in $\eta - \phi$. Most of the energy is deposited in the second layer, which has by far the biggest radial or longitudinal size. The granularity decreases with the distance to the interaction point. In the high pseudorapidity regions ($2.5 < |\eta| < 3.2$)

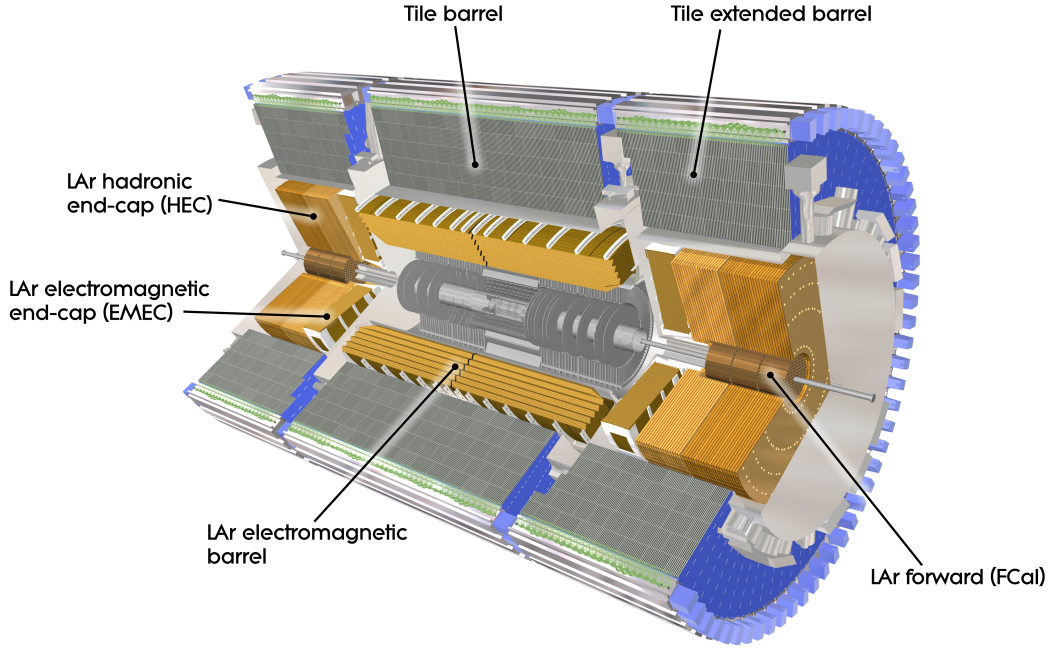


Figure 3.6: Schematic view of the ATLAS calorimeters [135].

there are only two layers, with coarser granularity. The energy is determined by the ionization current measured by the copper and kapton electrodes in the middle of the 4 mm wide LAr gaps. Energy that was absorbed by material upstream of the ECAL can be estimated by the presampler, an additional thin layer of LAr in front of the EMB and EMEC at $|\eta| < 1.8$.

Hadronic Calorimeter (HCAL) For measurement of hadronic particle showers, there are three systems: the Tile calorimeter, the hadronic end-cap calorimeter (HEC) and the forward calorimeter (FCal). The Tile calorimeter is installed outside the ECAL and has an outer radius of 4.25 m and is located at pseudorapidities up to $|\eta| = 1.7$. It uses steel as absorber material and plastic scintillator tiles as active medium. The scintillator tiles are read out by photomultipliers at the end of wavelength shifting fibers. There are three layers of Tile cells, which $\eta - \phi$ granularity decreases towards the outside. Additional thin modules are placed in the gap between barrel and extended barrel part to reduce the energy loss due to this transition. The Tile calorimeter has three in-situ calibration systems: a laser, a charge injector and a radioactive Caesium source.

The HEC covers $1.5 < |\eta| < 3.2$ and has four layers on each side. Its absorber copper plates (25-50 mm) are separated by 8.5 mm LAr gaps. Each LAr gap has three separate electrodes, allowing the measurement in four separate LAr drift zones.

The FCal is located around the beam pipe on both sides in the very forward region

of the detector ($3.1 < |\eta| < 4.9$). It has three layers with copper as absorber in the first one and tungsten being used in the outer two layers. The active material is LAr, which is filled in thin tubes with coaxial electrode copper rods.

Before the start of HL-LHC it is planned to replace the LAr and Tile calorimeter electronics, to enable the operation at high luminosities (radiation tolerance, trigger rates) [136].

3.2.3 The Muon Spectrometer

Besides neutrinos, which very rarely interact within the detector, muons are the only particles that are usually not absorbed in the calorimeters and are supposed to be detected by the outermost part of the detector – the muon spectrometer (see Fig. 3.7). It measures their momentum in $|\eta| < 2.7$ using the curvature of the trajectories induced by the toroidal magnetic fields with a bending power up to 7.5 Tm. Muons with $p_T < 3$ GeV are likely to be absorbed before reaching the muon spectrometer. There

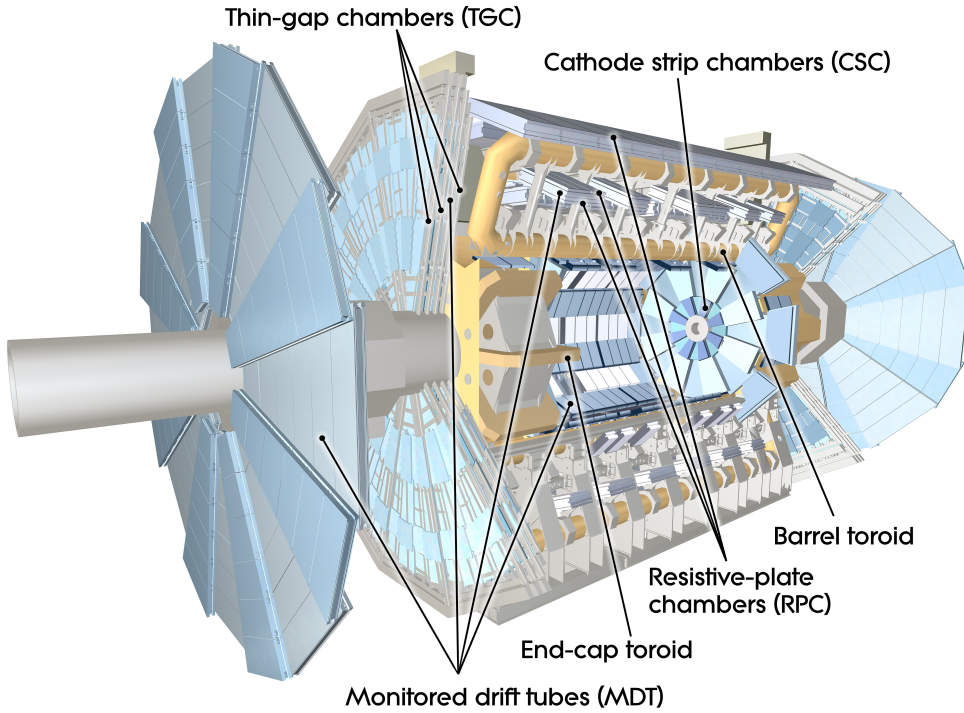


Figure 3.7: Schematic view of the ATLAS muon systems [137].

are three layers of Monitored Drift Tube chambers (MDTs) in the barrel and end-caps which provide the precision measurement of the momentum in $|\eta| < 2.7$. The MDTs consist of an arrangement of cylindrical drift chambers of 3 cm diameter, filled with a gas mixture of argon and carbon dioxide (97/3 %) at 3 bar. The free electrons arising due to ionization are collected by an axial tungsten-rhenium anode. In the inner layer of the end-cap ($2.0 < |\eta| < 2.7$) Cathode-Strip Chambers (CSCs) are installed instead of

MDTs, due to their superior time resolution and capability to handle a higher particle flux. The CSCs are multiwire proportional chambers with an Ar/CO₂ mixture of 4:1 and a square grid of cathode strips and anode wires. Additionally, there are detector systems dedicated to muon triggers, the Resistive Plate Chambers (RPC) in the barrel and Thin Gap Chambers (TGC) in the end-caps. Their fast signal time makes them well suited as a trigger system. They are also used to complement the MDT and CSC measurements by an additional coordinate. The RPC has three layers that are in front, in between and behind the MDT layers. It operates by measuring the avalanches that occur due to the high voltage between two resistive plates separated by 2 mm spacers. The four layers of TGCs are multiwire proportional chambers filled with a highly quenching gas mixture.

3.2.4 Trigger Systems

With a collision rate of up to 40 MHz and due to limitations in data storage and detector readout bandwidth, it is impossible to write out every event. Furthermore, the huge majority of events is of minor interest, as they originate from processes that are either well known or have such a huge cross section that a small subsample is sufficient to study them. On the other hand, the events of major interest are usually very rare and it is important to record as many of them as possible. Therefore it is essential to have a trigger system with a fast and efficient event selection. The ATLAS trigger system has been significantly upgraded in Long Shutdown 1 to cope with the more demanding conditions in LHC Run 2 [138, 139] (higher beam energy and luminosity). In a first stage, the Level 1 trigger has about 2.5 μ s to send the trigger decision to the detector buffers and has to reduce the rate by usually over two orders of magnitude to 100 kHz (significant improvement compared to 70 kHz before the upgrade). There are three Level 1 subsystems. One is *L1Calo*, which uses calorimeter information of reduced granularity to trigger electrons, photons, hadronic tau decays, jets and (missing) transverse energy. The other system with a direct detector interface is *L1Muon*, which primarily uses TGC and RPC information to make fast decisions on muon trigger items. In the central L1 trigger system, the information of *L1Calo* and *L1Muon* is received and the final decision is made. For this it can also use the recently added *L1Topo* that combines information from multiple *L1Calo* and *L1Muon* objects as well as their kinematics (e.g. angular separation, invariant mass).

Events accepted by any Level 1 trigger, are further processed by the *High Level Trigger* (HLT), which operates on the full event information (or in some cases on regions of interest pre-selected by the Level 1 trigger). While the Level 1 trigger uses custom-made electronics based on FPGAs, the HLT runs on a conventional computer cluster and has about 0.2 s on average to decide. The target average HLT rate is 1 kHz, a significant improvement compared to 0.6 kHz in LHC Run 1.

The set of active triggers usually changes during the data taking, as the intensity of

the beam changes. Trigger items may be prescaled, i.e. a specified fraction of positive trigger decisions is randomly ignored, which makes it possible to use triggers which unprescaled rates are too high to record their events.

A fast tracker trigger system (FTK) [140] that provides tracking information to the HLT is being prepared for operation later in Run 2. Among others, this will benefit tau and b -jet triggers. Another important pending upgrade will improve the granularity of calorimeter information available to L1Calo [141] and therefore also benefit tau triggers. It will be installed during Long Shutdown 2 (2018-2019).

3.3 Data Recorded at the Beginning of LHC Run 2

The data utilized for this thesis was recorded between the 16th of August 2015 and the 10th of July 2016. ATLAS records data in *runs*, periods of recording where usually most of the detector configuration is unchanged (besides trigger thresholds, which have to be adjusted to the change of luminosity during the LHC fill). In nominal operation there is one run per LHC fill. ATLAS runs are divided into *luminosity blocks*, which are approximately two minutes long. As described in Chapter 5, some luminosity blocks are excluded from the analysis for various reasons. The total integrated luminosity is determined by summing the values of the considered luminosity blocks. The luminosity measurement is mainly based on the LUCID-2 detector, which was installed in 2013 [142]. It measures Cherenkov radiation in quartz close to the beam pipe using photomultipliers. Other means of luminosity determination exist. Currently also the Beam Conditions Monitor (BCM) [143] and the inner detector (e.g. via counting of tracks) are able to measure the luminosity bunch by bunch. Furthermore, the calorimeters provide luminosity information integrated over many bunches. The ALFA detector [144] will also provide absolute luminosity measurements.

Data recorded earlier in 2015 with 50 ns bunch spacing are not considered for this analysis, as they correspond to a small integrated luminosity and would have to be analyzed separately due to differences in calibration. A small fraction of the integrated luminosity delivered by LHC ($\sim 5\text{-}10\%$) was not recorded by ATLAS, due to temporary problems with detector components or dead time. During 2015, for technical reasons the IBL had to be disabled during two runs. The corresponding data (0.2 fb^{-1}) is not considered for this search. Also, data recorded while the toroid magnet was disabled is discarded for this analysis. Fig. 3.8a shows the evolution of the integrated luminosity of the dataset (after filtering of “bad” luminosity blocks, see Sect. 5.1). The peak luminosity per day, see Fig. 3.8b, increased over the period of data taking, as the LHC operation was iteratively optimized, for instance by gradually increasing the number of bunches per beam. With increasing luminosity also the number of interactions occurring per bunch crossing (*in-time pile-up*) goes up. The distribution of the average number of interactions per bunch crossing $\langle\mu\rangle$ for this data set is shown in Fig. 3.9. Monte Carlo

simulated events are weighted such that their $\langle\mu\rangle$ distribution matches that of data.

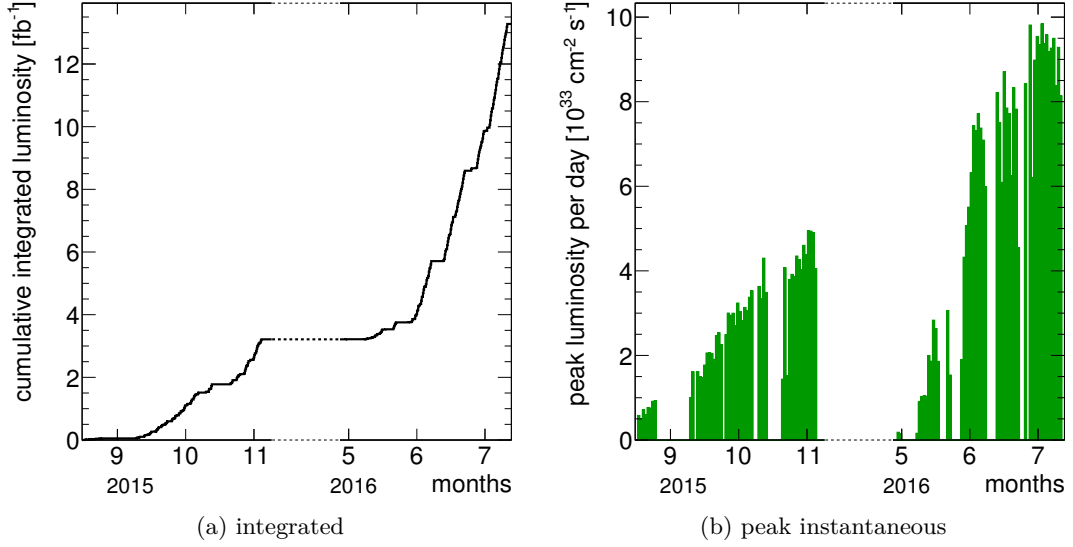


Figure 3.8: Growth of the recorded integrated luminosity (a) and the peak luminosity per day (b) during the data taking from 16th of August 2015 to 10th of July 2016. Only the data analysed for this search is considered.

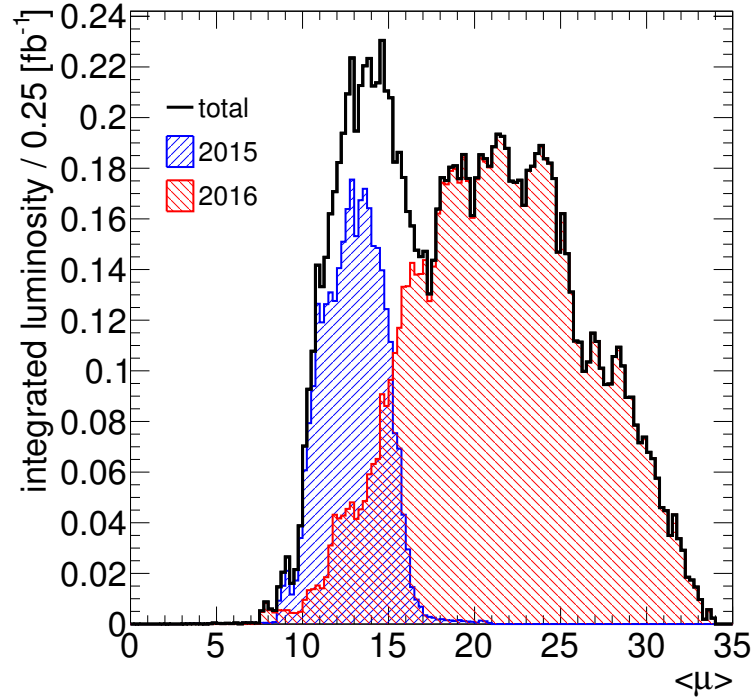


Figure 3.9: Average number of interactions per bunch crossing in the data set analysed in this search.

Chapter 4

Physics Object Reconstruction

The unprocessed output of the ATLAS detector or its simulation is not suitable for most physics analyses. Instead, reconstruction and identification algorithms are applied to combine information from multiple detector components and distinguish objects from each other. This chapter describes these algorithms for the physics objects relevant for the analysis presented in this thesis.

4.1 Low-Level Objects

Most high-level object reconstructions are based on tracks, primary and decay vertices, and calorimeter clusters. To reconstruct the trajectories of charged particles, the Inner Detector hits, caused by energy losses along the flight path of particles, are associated to form tracks. In ATLAS, the tracks of primary charged particles are built using *inside-out* track finding [145, 146]. This algorithm is seeded using information of the innermost layers of the Pixel detector and then follows the general direction to the outer layers of the Inner Detector to build track candidates. Afterwards, a Kalman filter is applied iteratively to all hits associated to the track candidate and outlier hits are rejected. The amount of misidentified trajectories and tracks with shared hits is reduced using dedicated ambiguity solving algorithms. In a last step the track is extended to the TRT and fitted together with the track from the silicon detectors. The resulting track has five parameters, which consist of the location on a plane, as well as two angles and the curvature of the trajectory. Additionally, *outside-in* track finding is performed, which is seeded in the TRT and directed towards the silicon detectors. In particular, this recovers tracks from decays of long-lived particles that decay beyond the silicon detectors. Based on track quality criteria like the number of silicon hits, tracks are usually filtered further for the reconstruction of higher level physics objects. The commonly used “loose” track quality selection results in reconstruction efficiencies over 90 %, with dependencies on the pseudorapidity and track transverse momentum, p_T [147]. Important track properties are the transverse and longitudinal impact parameters

d_0 and z_0 , the projections of the distance between the track and a reference point at the closest point of approach. Their resolution is typically well below 0.01 mm.

Tracks passing certain quality criteria are considered for the reconstruction of vertices, which are points of particle interaction. In an iterative process tracks are associated to vertex candidates and fits are performed to determine the position [148]. The positions of the proton-proton interactions are called primary vertices. The resolution of the Cartesian coordinates of reconstructed vertices is less than 0.35 mm for the z -direction and less than 0.16 mm in x and y directions [149]. With increasing number of associated tracks, the resolution improves by up to about one order of magnitude. The reconstruction efficiency rises from 83 % for vertices with two tracks to almost 100 % for vertices with at least five tracks. The hard scattering vertex is chosen as the primary vertex with the highest $\sum p_T^2$.

To reduce the impact of electric noise and pile-up, and to facilitate further calorimeter-based object reconstructions, the signals of adjacent calorimeter cells are condensed to form *topological clusters* [150]. Starting from a cell with an energy deposition at least four times higher than its expected noise level, topologically connected cells are added to the cluster using a growing-volume algorithm. The cluster energy is calibrated to compensate for losses due to the clustering, inactive detector material and non-compensating calorimeter response. Clusters can be calibrated at the electromagnetic scale, which is tuned to clusters in showers created by electrons (EM topo-clusters). Another common approach, the *local hadronic cell weighting*, corrects for differences between pion and electron showers by estimating the likelihood that a cluster is in an electromagnetic or hadronic shower and weighting the contributions accordingly (LCW topo-clusters).

4.2 Jet Reconstruction

High-energy quarks or gluons form jets consisting of typically low-energy hadrons emitted within a narrow cone. The fragmentation of hard partons occurs due to confinement, which leads to the creation of quark-antiquark pairs when the gluon field energy between quarks in a color-neutral configuration surpasses the mass energy of the new quark pair. Additionally, the transverse size and number of constituents of the jet is increased by emission of gluons from quarks or gluons and the subsequent decays to quark pairs. Eventually, the energy of the partons is too low to form additional particles and only colorless hadrons remain. These hadrons deposit energy in the calorimeters and the charged ones leave tracks in the Inner Detector.

On these objects jet algorithms are applied to identify which of the clusters and/or tracks belong to the same jet. For the analysis presented in this thesis, jets are reconstructed by applying the **FastJet** [151] implementation of the anti- k_t clustering algorithm [152] with a distance parameter $R = 0.4$ to EM topo-clusters. The algorithm

adds a cluster to a pseudojet as long as their distance $d_{ij} = \min(k_{ti}^{-2}, k_{tj}^{-2})\Delta_{ij}^2/R^2$ (with transverse momentum k_t and angular distance $\Delta_{ij} = \sqrt{(\Delta y)^2 + (\Delta\phi)^2}$) is smaller than k_{ti}^{-2} , otherwise the cluster will form a new pseudojet. This process is repeated until all clusters are associated with a jet.

Multiple corrections are applied to the jets. First, their direction is adjusted to point to the hard scatter vertex instead of the center of the detector, improving the η resolution [153–155]. Furthermore, a pile-up subtraction based on a jet area in the $\eta - \phi$ plane and the median pile-up transverse momentum density is performed [156]. Residual pile-up effects on the jet p_T are corrected based on the number of primary vertices and the average number of interactions per bunch crossing [157]. Then the jets are calibrated based on Monte Carlo simulation, where reconstructed jets are matched geometrically to jets constructed from final state particles on Monte Carlo level. The jet energy additionally depends on properties of the jet, like the fraction of energy in certain calorimeter layers or the number of associated tracks. These dependencies are resolved sequentially. Finally, an in-situ calibration is applied, which accounts for differences between simulation and data. It is measured by comparing the ratios of the p_T of a jet and a reference object. A summary of the systematic uncertainty on the jet energy calibration in dependence of p_T and η is shown in Fig. 4.1.

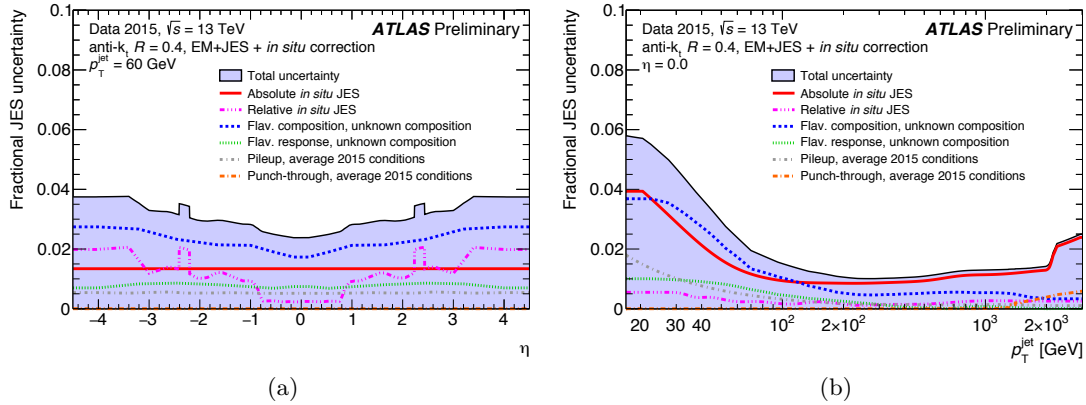


Figure 4.1: Total uncertainty of the jet energy scale in dependence of pseudorapidity (a) and p_T (b) [158].

The jet energy resolution was measured in 8 TeV data [159] and is below 15 %; the lowest value is 3 % for high jet p_T and the central pseudorapidity region ($|\eta| < 0.8$). The uncertainty of the energy resolution is increased to cover changes of the conditions between Run 1 and Run 2, the total uncertainty is shown in Fig. 4.2.

Even after the application of the pile-up subtraction techniques described above, some pile-up jets remain. Most of these with a p_T between 20 GeV and 60 GeV are rejected using a likelihood discriminant called jet vertex tagger (JVT), based on the tracks matched to each jet [156, 160]. One JVT input variable is the jet vertex fraction, which is related to the likelihood of a jet originating from the hard scatter vertex,

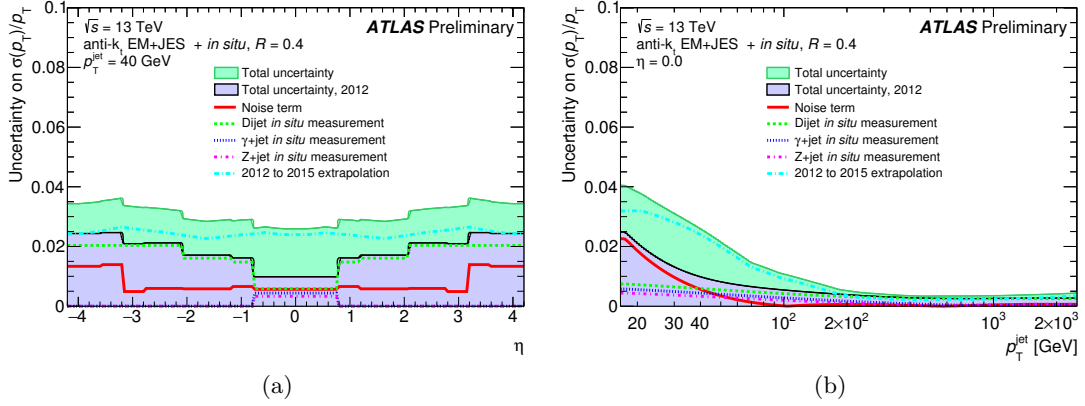


Figure 4.2: Total uncertainty of the jet energy resolution in dependence of pseudorapidity (a) and p_T (b) [153].

corrected for the number of primary vertices. The other variable used for calculating the JVT discriminant is the ratio of the sum of p_T of tracks associated to the jet (and the hard scatter vertex) and the calibrated jet p_T . For the analysis presented here, a JVT cut is applied corresponding to an average signal jet efficiency of 92 %, resulting in a pile-up jet efficiency of the order of only 1 % to 2 %. This dramatically decreases the dependence of the number of hard jets on $\langle\mu\rangle$, as demonstrated in Fig. 4.3a. The JVT signal jet efficiency was calibrated using a tag-and-probe analysis in a $Z(\rightarrow \mu\mu)$ +jets control region in data. A scale factor is derived to correct for small differences in JVT

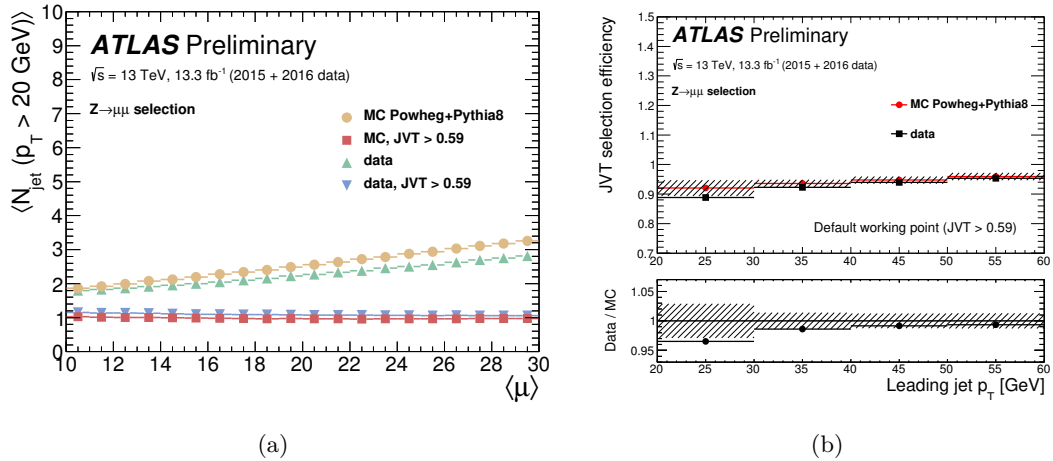


Figure 4.3: Average number of jets with $p_T > 20$ GeV before and after the application of a fixed cut on JVT (a) and selection efficiency of hard-scatter jets in a $Z(\rightarrow \mu\mu)$ +jets region for data and Monte Carlo simulation (b) [161].

performance between data and simulation, as shown in Fig. 4.3b. It is between 97 % and 99 % and for $p_T > 30$ GeV it is compatible with unity within its uncertainties, which arise from the statistical uncertainty, the difference assessed by using different Monte Carlo generators and an uncertainty from the estimation of the residual pile-up

jet contamination in the control region.

After the jet reconstruction, some jets that did not originate from pp interactions remain. Sources for these background jets are beam-induced background (proton losses, e.g. due to beam-gas scattering or proton halo interacting with collimators [162]), particles from cosmic ray showers or electric noise in parts of the calorimeter [163]. A selection based on LAr signal pulse shapes, energy ratio variables and track-based variables, described in [163], is applied to discriminate these backgrounds. Only jets passing the *Loose* selection are kept for this analysis, with a selection efficiency of over 99.5 % for the relevant pseudorapidity range.

Jets containing b -hadrons have properties that make it possible to distinguish them from other types of jets (b -tagging). Most importantly, the lifetime of hadrons with b -flavor is long enough for them to travel a measurable distance before they decay. Most b -hadrons have a mean decay length of about $0.5 \text{ mm} \times \gamma$ [38] (depending on the Lorentz factor γ), so high- p_T b -hadrons usually travel several millimeters. In ATLAS, a multivariate discriminant algorithm combines the output of other algorithms based on the impact parameter, the inclusive secondary vertex reconstruction as well as a multi-vertex algorithm that aims to reconstruct the decay chain up to a third vertex (the decay of a c -hadron from the b -hadron decay) [164]. A boosted decision tree algorithm (BDT) called MV2c10 is trained on $t\bar{t}$ events with a background sample consisting of 10 % c -jets and 90 % light jets. The output of that algorithm for different types of jets in a $t\bar{t}$ sample is shown in Fig. 4.4. For the analysis presented here, jets are classified

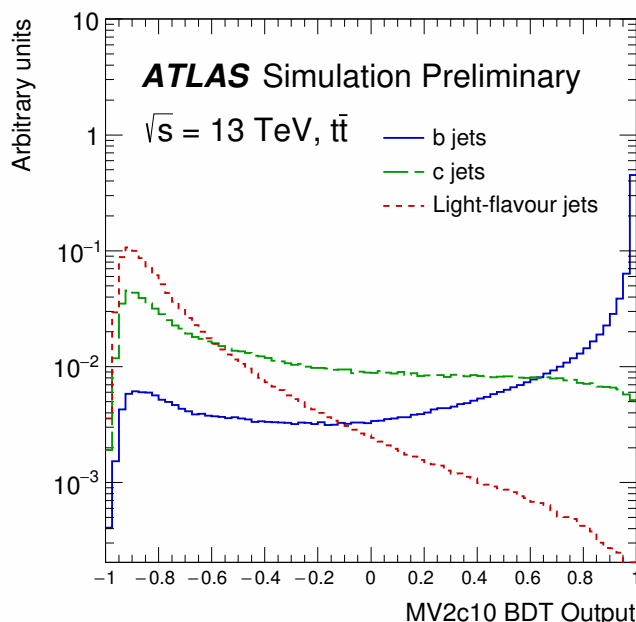


Figure 4.4: MV2c10 b -tagging algorithm output score for b -jets, c -jets and light jets, determined in a $t\bar{t}$ simulation sample [165]. The 70 % working point chosen for the analysis corresponds to a cut at 0.82.

as b -jet if they pass a BDT cut such that the b -jet efficiency is 70 %, corresponding to a misidentification rate of 8.2 % for c -jets, 1.8 % for τ -jets and 0.3 % for light jets, as measured in $t\bar{t}$ simulation [165]. The b -tagging performance improved significantly compared to Run 1, mainly due to the IBL. Scale factors depending on jet p_T to compensate for differences in b -tagging efficiency between data and simulation are determined by a likelihood-based analysis of events in a di-leptonic $t\bar{t}$ -enriched control region [166]. The scale factors are based on data recorded in 2015. Their systematic uncertainty is dominated by the modeling uncertainties of the $t\bar{t}$ Monte Carlo event samples. Jets that are not classified as b -jets in Monte Carlo simulation also receive a scale factor [167].

4.3 Muons

Muons, unlike other particles detected at ATLAS, are usually not stopped in the calorimeters and travel out of the detector, passing the muon spectrometer. Information from all main detector systems is combined to reconstruct muons [168]. Tracks in the muon chamber are reconstructed by applying a Hough transform to the MDT and nearby trigger chamber hits to get an approximate trajectory. Afterwards, track segments are reconstructed in each MDT layer separately, complemented by information from the other muon subdetectors. Finally, a χ^2 fit is performed using all hits per track candidate. The fit is repeated after outlier hits have been removed and again in case additional hits that could belong to the track have been added. The final reconstructed muon uses the track from the muon spectrometer and Inner Detector (combined muon), an Inner Detector track and one track segment in the muon system (segment-tagged muon), the muon spectrometer track compatible to coming from the interaction point (extrapolated muon) or an Inner Detector track and calorimeter deposits consistent with a muon (calorimeter-tagged muon). An overlap removal between these different muon types avoids double counting.

To distinguish prompt muons from background like light meson decays, a muon identification is performed. For this, several quality requirements are applied, related to the compatibility of the measurement in the Inner Detector and muon spectrometer, the goodness of the combined track fit and the quality of the individual tracks. For the analysis presented here, two quality classifications are relevant: *loose* and *medium*. While the *medium* quality muons are required to be of combined or extrapolated type, the *loose* criterion also allows segment-tagged and calorimeter-tagged muons. Quality criteria are applied depending on the type and $|\eta|$ of the muon candidate.

The muon reconstruction efficiency was measured in a $Z \rightarrow \mu\mu$ tag-and-probe analysis. It is shown in Fig. 4.5 for *medium* muons as well as for *loose* muons in $|\eta| < 0.1$. *Loose* muons for larger pseudorapidities have a similar reconstruction efficiency as *medium* muons. The reconstruction efficiency is compared between data and simulation

to determine scale factors in dependence of η and ϕ . In most of the η - ϕ plane the scale factor is within 1 % of unity.

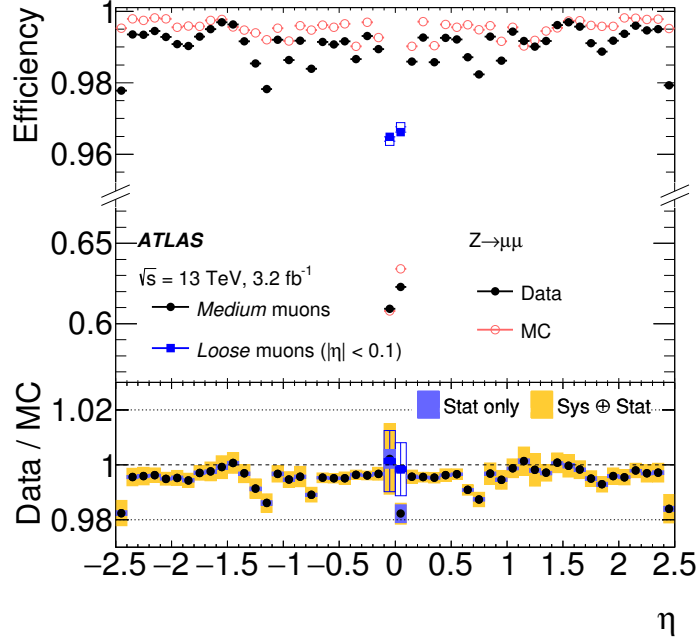


Figure 4.5: Muon reconstruction efficiency as a function of muon pseudorapidity, measured in a $Z \rightarrow \mu\mu$ tag-and-probe analysis for *medium* and *loose* $|\eta| < 0.1$ [168].

For the *medium* muons in the analysis described in this thesis, an additional isolation criterion is applied to select geometrically isolated muons and reject muons that are part of a jet. For this, both the calorimeter-based isolation variable $E_T^{\text{varcone20}}$ (sum of transverse energy within a $\Delta R = 0.2$ cone around the muon, pile-up corrected, without the muon energy) and the track-based isolation variable $p_T^{\text{varcone30}}$ (scalar sum of track p_T with $p_T > 1$ GeV in a cone with p_T dependent size $\Delta R < 0.3$, excluding the muon track) are used. These variables are combined in the *gradient* isolation working point, which is 93 % (99 %) efficient for muons with $p_T = 25$ GeV (60 GeV), as shown in Fig. 4.6.

Despite the sophisticated simulation of the detector response, small differences in muon p_T between data and simulation remain. Therefore, the transverse momentum of muons in simulation is scaled in dependence of η and ϕ and a p_T smearing is applied to match the resolution in data. The correction factors are measured for $J/\psi \rightarrow \mu\mu$ and $Z \rightarrow \mu\mu$ candidate events. For most of the pseudorapidity range the p_T resolution is below 5 %. The uncertainty on the p_T scale is below 0.3 %, as measured in a $Z \rightarrow \mu\mu$ analysis.

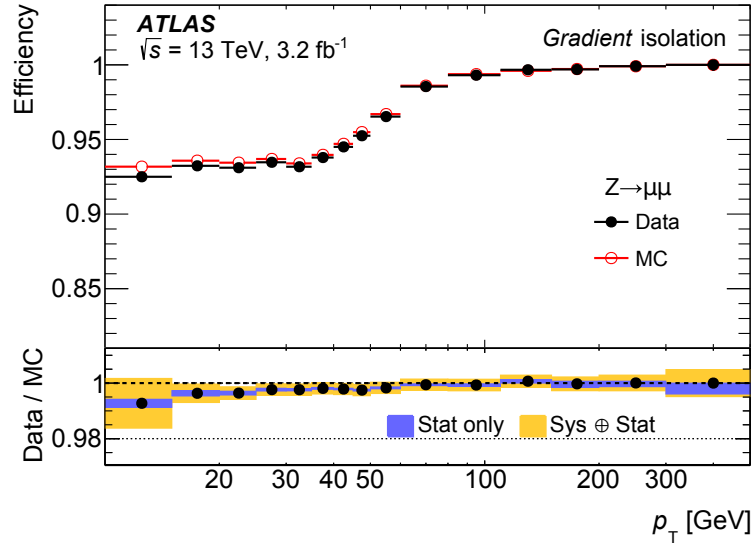


Figure 4.6: Muon isolation efficiency as a function of muon p_T , measured in a $Z \rightarrow \mu\mu$ tag-and-probe analysis [168, 169].

4.4 Electrons

The electron reconstruction in ATLAS depends on an Inner Detector track and a corresponding energy deposition in the calorimeter [170]. A sliding window algorithm is used to reconstruct a seed cluster in the calorimeter. To account for larger QED bremsstrahlung for electrons, the standard track reconstruction is modified. Tracks that fulfil certain quality criteria and that are matched to electron clusters are refit using an electron-specific algorithm. This is repeated with tighter criteria and per electron a primary track is chosen. The calibrated cluster energy is taken as the energy of the reconstructed electron, while the track information is used to determine η and ϕ .

Additionally, the energy is corrected for non-uniformity of the detector response and by using a multivariate regression algorithm trained on Monte Carlo simulation to correct for loss of energy outside the calorimeter or the clusters [171]. To account for small differences of the calibration between simulation and data, both the energy scale (in data) and resolution (in Monte Carlo simulation) are adjusted based on corrections measured in $Z \rightarrow ee$ events. The scaling changes the energy by less than 2 %, except at the edges of the Inner Detector acceptances (where it is about 8 %). The resolution is depending on the pseudorapidity and energy of the electron. In the central $\eta < 0.5$ region it ranges from 2.5 % for 25 GeV to 0.5 % for 1 TeV, for larger η it rises up to 10 % for low energy electrons [172].¹ For most of the pseudorapidity range the reconstruction efficiency is above 97 % and increases with the energy of the reconstructed electron, see Fig. 4.7. The reconstruction efficiency drops in the so-called

¹These values have been determined for Run 1 data, but are still approximately valid, as discussed in Ref. [171]. Only small modifications have been made to correct for changes in conditions between Run 1 and Run 2.

crack region ($1.37 < |\eta| < 1.52$), where barrel and end-cap calorimeters meet.

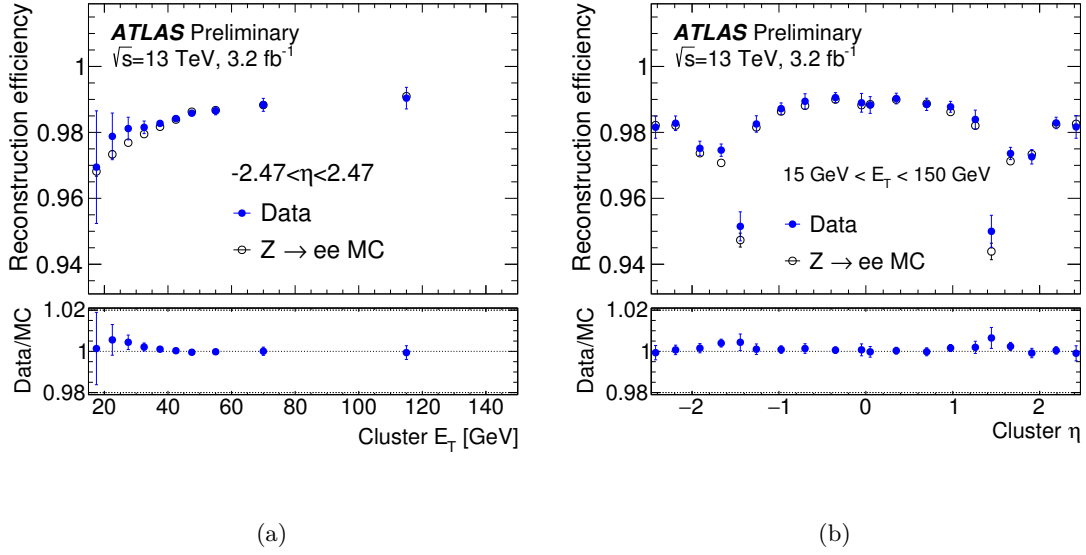


Figure 4.7: Electron reconstruction efficiency measured in $Z \rightarrow ee$ events of 2015 data, in dependence of the transverse energy of the electron clusters (a) and the corresponding pseudorapidity (b) [170].

To reject misidentified electrons, mainly from hadronic jets or converted photons, a likelihood-based identification algorithm is applied. A wide variety of input variables describes properties of the reconstructed electron, like the shape of the electromagnetic shower and information from separate layers of the calorimeters or tracking subsystems. The algorithm has been trained using $Z \rightarrow ee$ and di-jet Monte Carlo simulation. A slight mismodeling of the detector simulation of the shower shapes and a change in conditions in the TRT in 2016, which is not yet reflected in the Monte Carlo simulation used for the training, lead to a difference in identification efficiency between simulation and data, seen in Fig. 4.8. The signal efficiency for the *loose* working point, which is used in the analysis presented in this thesis, is above 90 % for most of the pseudorapidity range, whereas the fraction of misidentified electrons from di-jet simulation is below 1 %.

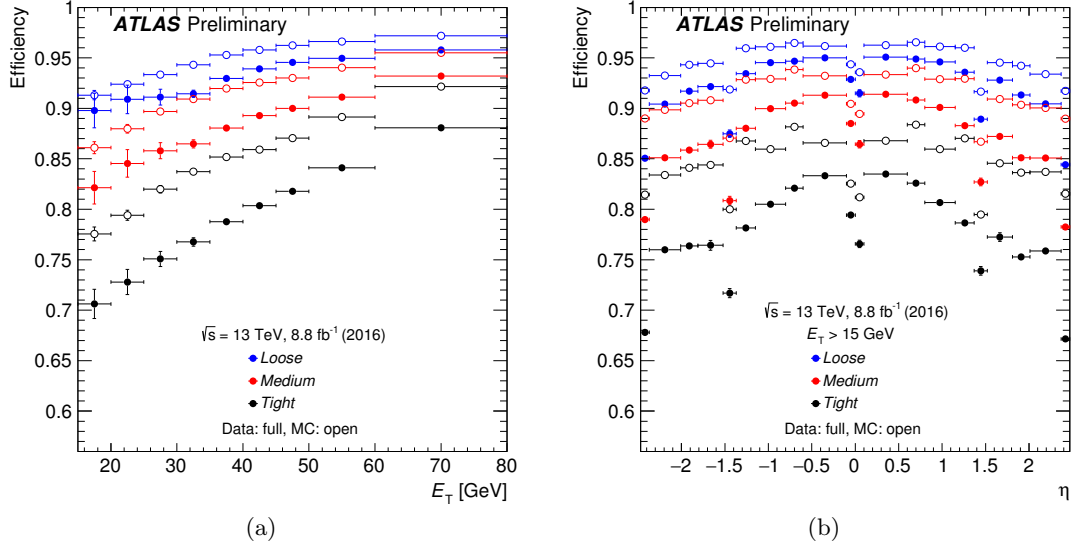


Figure 4.8: Electron identification efficiency measured in $Z \rightarrow ee$ events of 8.8 fb^{-1} 2016 data, in dependence of the transverse energy (a) and pseudorapidity (b) [173].

4.5 Hadronic Tau Decays

Tau leptons decay to two neutrinos and an electron or muon in 35% of the cases [38] (referred to as τ_{lep} in this document). However, these decays are usually not distinguishable from prompt muons or electrons. Due to its high mass of 1.777 GeV , the tau is the only lepton that can also decay to final states with hadrons, which it does in 65% of the cases. These hadronic decays, from hereon called τ_{had} , have one tau neutrino and one or more light mesons in the final state. The reconstruction is concerned with the part visible in the detector (without the neutrino, which usually leaves the detector without detectable interaction) and is denoted as $\tau_{\text{had-vis}}$ hereafter. In the majority of the cases the hadronic decay contains one charged meson (*1-prong*) or three charged mesons (*3-prong*). Additionally, often also neutral mesons and/or photons are created. The mesons are pions most of the time, among the small fraction of other mesons kaons are the most common.

The reconstruction of $\tau_{\text{had-vis}}$ starts with anti- k_t jets with $R = 0.4$, built from LCW topo-clusters and with $p_T > 10 \text{ GeV}$ and $|\eta| < 2.5$ [174, 175]. The $\tau_{\text{had-vis}}$ candidate is associated to the primary vertex which is matched to the highest fraction of the sum of p_T of the tracks within $\Delta R < 0.2$ of the jet axis. This vertex choice is significantly more efficient than using the hard scatter vertex, especially for low p_T and high pile-up conditions. The direction of the $\tau_{\text{had-vis}}$ is recalculated using this vertex. Tracks within $\Delta R < 0.2$ around this new axis (core region), with $p_T > 1 \text{ GeV}$ and satisfying additional track quality criteria (number of associated hits in the tracking subdetectors, impact parameters) are selected as tau tracks. From these tracks also a secondary vertex may be

reconstructed. The reconstruction efficiency of a $\tau_{\text{had-vis}}$ candidate is shown in Fig. 4.9 for 1-prong and 3-prong $\tau_{\text{had-vis}}$, depending on the true (simulated) p_T . Its relative systematic uncertainty is between 2 % and 4.5 %, depending on p_T and the number of tracks N_{track} .

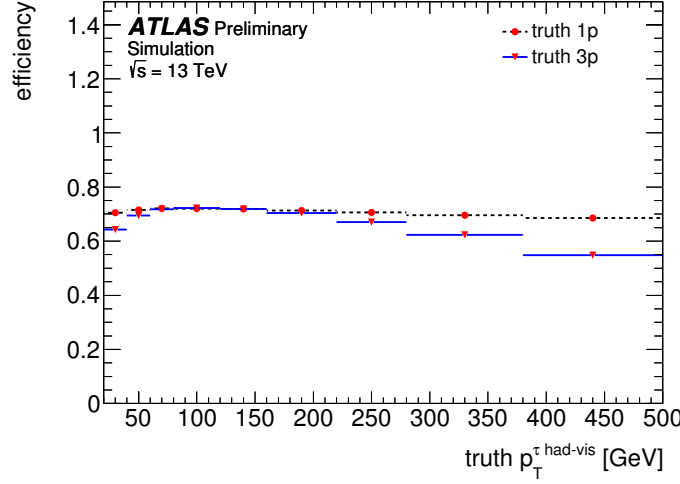


Figure 4.9: Reconstruction efficiency of $\tau_{\text{had-vis}}$ candidates for 1-prong and 3-prong $\tau_{\text{had-vis}}$ in dependence of the true p_T [174].

Reconstructed $\tau_{\text{had-vis}}$ candidates contain a large fraction of jets initiated by quarks or gluons. To distinguish them from genuine $\tau_{\text{had-vis}}$, a multivariate tau identification algorithm based on boosted decision trees is trained and applied separately for 1-prong and 3-prong $\tau_{\text{had-vis}}$. Their input variables use information of the tau tracks, the tau vertex and calorimeter cells and clusters calibrated at EM and LCW scale. A pile-up correction is applied to all input variables, depending on the average number of interactions per bunch crossing. Among others, the identification exploits that true $\tau_{\text{had-vis}}$ decay showers are more collimated, i.e. the fraction of energy deposited in the core region compared to the whole candidate is higher than for jets initiated by quarks or gluons. Also, tau leptons have a mean life time of 2.9×10^{-13} s [28], which in many cases is long enough to measure a secondary vertex (for 3-prong $\tau_{\text{had-vis}}$) or a significant impact parameter of the leading track. The training of the BDTs is performed on Monte Carlo simulation for $Z/\gamma^* \rightarrow \tau\tau$ and di-jet events. Three working points are defined and the respective BDT cuts are dependent on the $\tau_{\text{had-vis}}$ p_T to reduce the p_T dependence of the combined reconstruction and identification efficiency. The working points used in this thesis are *loose* and *medium*, corresponding to a signal efficiency of 60 % and 55 % for 1-prong and 50 % / 40 % for 3-prong $\tau_{\text{had-vis}}$. The identification efficiencies as well as combined identification and reconstruction efficiencies in dependence of the true $\tau_{\text{had-vis}}$ p_T are shown in Fig. 4.10. The relative systematic uncertainty of the identification efficiency is depending on η , p_T and the working point. It is between 5 % and 10 % for most of the parameter space, with peaks up to 20 %.

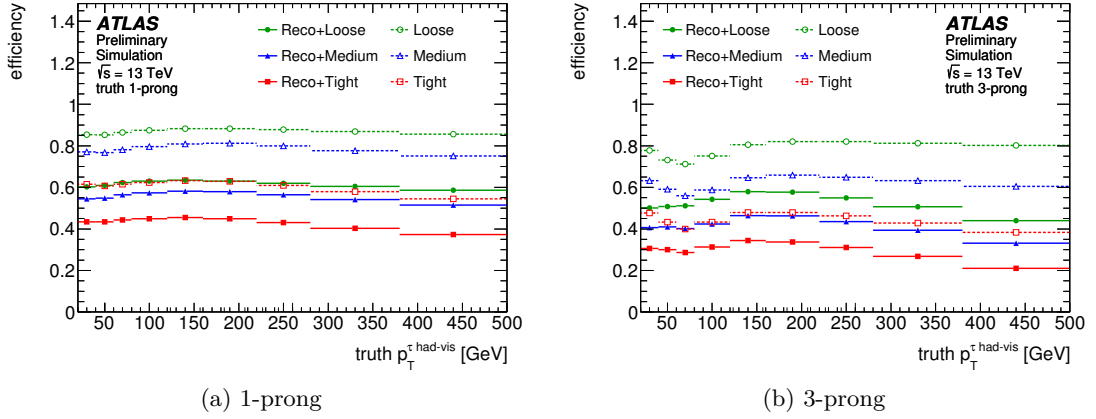


Figure 4.10: $\tau_{\text{had-vis}}$ identification efficiencies as well as combined identification and reconstruction efficiencies in dependence of the true $\tau_{\text{had-vis}}$ p_T [174].

The energy of the $\tau_{\text{had-vis}}$ is based on the energy of the LCW topo-clusters within $\Delta R < 0.2$. A correction (tau energy scale, TES) is applied to estimate the true $\tau_{\text{had-vis}}$ energy: a pile-up subtraction and a response correction to compensate for energy deposition outside the reconstructed clusters, the calorimeter or the core region. The energy resolution increases with $|\eta|$ and decreases with p_T , as shown in Fig. 4.11. The relative systematic uncertainty of the tau energy scale depends on p_T and $|\eta|$ and ranges between 3 % and 6 %.

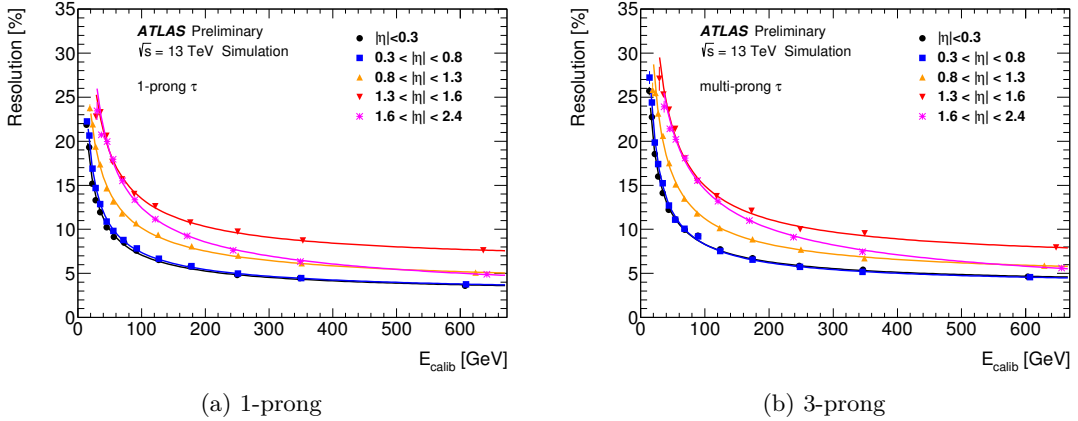


Figure 4.11: $\tau_{\text{had-vis}}$ energy resolution in dependence of calibrated energy and $|\eta|$ [174].

At the level 1 trigger step [176], regions of interest are selected. These regions, which are divided in low granularity calorimeter sections (trigger towers), have to have more than a certain energy in the core region and the surrounding towers must not surpass a certain energy depending on the core energy (isolation criterion). The high-level trigger performs a more precise energy reconstruction based on topo-clusters and rejects low-energy candidate objects. Afterwards, a fast track reconstruction is applied and

between one and three core tracks as well as the absence of isolation tracks are required. For the remaining objects, a more precise track reconstruction is performed and a BDT is applied. The tau trigger BDT is very similar to the offline identification, which is a significant improvement with respect to Run 1. The commonly used tau trigger identification working point `medium1_tracktwo` besides the BDT applies a cut on the number of tau tracks and has a slightly higher signal efficiency than the *medium* working point for reconstructed $\tau_{\text{had-vis}}$. In the analysis presented here, tau triggers selecting single $\tau_{\text{had-vis}}$ are used. The lowest p_T threshold of this trigger during the 2015 and 2016 data taking is 80 GeV and has been raised to 125 GeV and 160 GeV for periods of high luminosity, to keep the trigger rate within technical capabilities. These p_T thresholds of the high level trigger are of the order of 10 GeV below the range of maximum trigger efficiency. These high-level triggers are seeded by a level 1 tau trigger with a 60 GeV p_T threshold.

Tau trigger scale factors are measured for the data recorded in 2015 in a region enriched in $Z \rightarrow \tau_{\text{had}}\tau_{\mu}$ events in dependence of p_T and the number of tau tracks. Their uncertainties have been slightly increased to account for changes in the Monte Carlo simulation since then. For data recorded in 2016 no trigger scale factors have been measured in time for this analysis. Therefore, scale factors of 1.0 with increased uncertainties are utilized in this search.

4.6 Removal of Object Ambiguities

The reconstructions of the physics objects are independent from each other, so geometric overlaps are common, i.e. the detector signals caused by one particle are reconstructed as more than one object. This ambiguity is resolved by removing overlapping objects in an order reflecting the differences in reconstruction and identification efficiencies. Two objects are considered as overlapping if their angular separation ΔR is below a certain value, as listed in Table 4.1.

Removed Object A	Kept Objects B	Angular Separation ΔR
electron	muon	0.2
jet	electron, muon	0.4
$\tau_{\text{had-vis}}$	electron, muon	0.2
jet	2 leading $\tau_{\text{had-vis}}$	0.2

Table 4.1: To resolve physics object ambiguities, all objects A within a cone of ΔR around particles B are removed.

4.7 Missing Transverse Momentum

Based on momentum conservation and the negligible momentum in the transverse plane, the total transverse momentum of undetected particles can be reconstructed using

the measured transverse momentum of all detectable particles. Undetected particles primarily include neutrinos, which are of particular importance to reconstruct properties of tau leptons or the resonance of their origin. Also particles that can in principle be detected by ATLAS can contribute, in case they fail to pass the reconstruction or travel outside the detector acceptance. The missing transverse momentum $\mathbf{E}_T^{\text{miss}}$ is defined as the negative sum of the transverse momenta of all selected physics objects (*hard terms*: electrons, photons, $\tau_{\text{had-vis}}$, muons, jets) and the tracks that are not associated with these objects (the *soft term*) [177]. The $\mathbf{E}_T^{\text{miss}}$ is often expressed by its magnitude E_T^{miss} and azimuthal angle ϕ^{miss} . Another related observable is the total transverse energy $\sum E_T$, which is the scalar sum of the same terms. For the $\mathbf{E}_T^{\text{miss}}$ reconstruction a dedicated object ambiguity removal is performed, which is slightly different than what is used for the main object selection (see Sect. 4.6). For the analysis presented here, only the two $\tau_{\text{had-vis}}$ with the highest p_T are used for the reconstruction of $\mathbf{E}_T^{\text{miss}}$ and no photons are reconstructed. Photons and additional $\tau_{\text{had-vis}}$ enter the calculation as jets.

Acceptance limitations, e.g. uncovered pseudorapidities at $|\eta| > 4.9$ and energy absorbed in inactive material, result in a considerable E_T^{miss} resolution. It can be measured in events with negligible genuine E_T^{miss} , e.g. $Z \rightarrow \ell\ell$. Examples of resolution measurements are shown in Fig. 4.12.

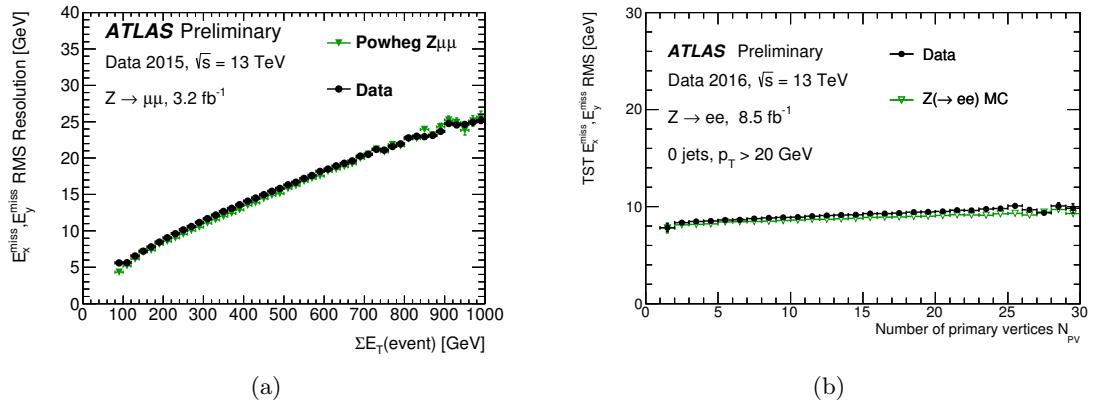


Figure 4.12: Resolution of E_T^{miss} as measured in $Z \rightarrow \ell\ell$ events in dependence of the scalar sum of transverse energy (a, 2015 data) and the number of primary vertices (b, 2016 data) [178, 179].

The systematic uncertainties of the hard term objects trivially propagate through the E_T^{miss} calculation. Additional uncertainties on the scale and resolution of E_T^{miss} arise from the soft term.

Chapter 5

Event Selection

A selection in the form of a series of cuts on event observables is applied to all recorded and simulated events, to improve the discovery significance while keeping the estimation of the background manageable. The development of the event selection and background estimation has been performed *blindly*, i.e. data was not utilized for anything in any event subsample with a significant amount of expected signal. In a second step, a small part of the total data corresponding to 3.2 fb^{-1} was used in the signal region to rule out any obvious background mismodeling. The corresponding signal sensitivity is below the previous exclusion limit. After the total amount of data has been looked at in the signal region, no changes were made to the event selection or background estimation, to avoid observer-expectancy bias.

5.1 Event Cleaning

In this first selection step all events that are not considered to be of sufficient quality are discarded. Most importantly, in data only luminosity blocks with good data quality conditions are selected. These conditions include quality criteria from each detector subsystem as well as data quality checks involving the distribution of basic event observables. For instance, luminosity blocks may be discarded when a significant fraction of a subdetector is not recording data due to technical issues. While still suitable for some analyses, for this search luminosity blocks with inactive toroidal magnet or IBL are not kept. Additionally, in rare cases individual events are discarded due to data corruption, noise bursts in the LAr calorimeter or partially missing detector information. At least one reconstructed primary vertex is required. In a step called jet cleaning, events which contain jets not passing the *Loose* quality selection (cf. Sect. 4.2) after overlap removal (cf. Sect. 4.6) are discarded to avoid negative effects on the $E_{\text{T}}^{\text{miss}}$ calculation. Pile-up jets (as selected by the JVT) below 60 GeV and for $|\eta| < 2.4$ are not considered for the jet cleaning.

5.2 Event Pre-Selection

Trigger Events are required to be accepted by the single-tau high-level trigger (cf. Sect. 4.5) with a 80 GeV p_T threshold. When the instantaneous luminosity is too high, approximately above $5 \times 10^{33} \text{ cm}^{-2} \text{ s}^{-1}$, the rate of this trigger becomes too large and it is prescaled or deactivated. Instead, the 125 GeV single-tau trigger is used for the affected luminosity blocks. The intensity was gradually increased as data taking progressed (cf. Fig. 3.8b), so while most of the data recorded in 2015 can be triggered by this 80 GeV trigger, the majority of the data taken in 2016 has to be triggered with the 125 GeV trigger. As the instantaneous luminosity drops during an LHC fill, the trigger with the lower threshold is usually utilized again towards the end of a fill. The 80 GeV threshold was used to trigger 40.2% of the total integrated luminosity for this analysis. An integrated luminosity of 97 pb^{-1} (corresponding to only 0.7% of the total available integrated luminosity) could not be utilized, as the instantaneous luminosity surpassed $1.0 \times 10^{34} \text{ cm}^{-2} \text{ s}^{-1}$, at which point the 125 GeV single-tau trigger rate becomes too high. As the corresponding measurement is still very statistically limited, no measurement of the 160 GeV single-tau trigger scale factor was available at the time of the finalization of the analysis, hence that trigger could not be utilized. The leading $\tau_{\text{had-vis}}$ candidate has to match to the trigger object within $\Delta R < 0.2$. In Monte Carlo simulated events always the 80 GeV trigger emulation is applied. This is a valid approach, as both triggers use the exact same algorithm (besides the p_T threshold) and the p_T cuts applied to the triggered $\tau_{\text{had-vis}}$ are high enough to be on the trigger efficiency plateau. An average of the scale factors for the two triggers, weighted by the integrated luminosity of their utilization in 2015 and 2016, is applied as event weight in simulated events (see Eq. 5.1).

Lepton Veto To suppress backgrounds with leptonic final states and to ensure orthogonality with the analysis of the $\tau_{\text{lep}} \tau_{\text{had}}$ final state, events with muons or electrons are vetoed. This means all events which contain electrons with $p_T > 15 \text{ GeV}$, $|\eta| < 2.47$ (excluding the transition region between barrel and end-cap calorimeters $1.37 < |\eta| < 1.52$) and passing the *loose* likelihood-based identification or muons with $p_T > 7 \text{ GeV}$, $|\eta| < 2.5$ and passing the *loose* quality criteria are discarded.

$\tau_{\text{had-vis}}$ Pre-selection Only $\tau_{\text{had-vis}}$ with $|\eta| < 2.47$ (excluding the “crack region” with $1.37 < |\eta| < 1.52$) and exactly one or three tracks are considered for the analysis. At pre-selection only events with at least two $\tau_{\text{had-vis}}$ with $p_T > 50 \text{ GeV}$ are kept.

5.3 Main Event Selection

$\tau_{\text{had-vis}}$ Transverse Momenta If the 80 GeV tau trigger was used, the leading $\tau_{\text{had-vis}}$ (τ_0) is required to have $p_T > 110 \text{ GeV}$. This ensures that the trigger efficiency is

approximately independent on $\tau_{\text{had-vis}} p_T$ for all selected $\tau_{\text{had-vis}}$. For events triggered by the 125 GeV tau trigger, this requirement is raised to $p_T(\tau_0) > 140$ GeV. In both cases the leading $\tau_{\text{had-vis}}$ is required to pass the *medium* identification criterion. The subleading $\tau_{\text{had-vis}}$ (τ_1) has to have a p_T of at least 55 GeV and satisfy the *loose* tau identification. As in Monte Carlo simulated events always the lower leading $\tau_{\text{had-vis}} p_T$ threshold is used, the fraction of integrated luminosity triggered by the 80 GeV trigger is used as additional event weight for events with $p_T(\tau_0) < 140$ GeV. Together with the trigger scale factors this leads to an event weight calculated as:

$$w_{\text{trig}} = \begin{cases} f_{80,2015} \times s_{80,2015} + f_{80,2016} \times s_{80,2016} & \text{if } p_T(\tau_0) < 140 \text{ GeV} \\ \sum_{i=80,125} \sum_{j=2015,2016} f_{i,j} \times s_{i,j} & \text{otherwise} \end{cases}, \quad (5.1)$$

where s denotes the trigger scale factor for a given trigger and year of data taking and $f_{i,j}$ is the fraction of integrated luminosity recorded with trigger i in year j relative to the total luminosity in both years. These fractions are:

$$\begin{aligned} f_{80,2015} &= 0.235, \\ f_{125,2015} &= 0.009, \\ f_{80,2016} &= 0.167, \\ f_{125,2016} &= 0.589. \end{aligned}$$

Event Topology The two leading $\tau_{\text{had-vis}}$ have to have opposite electric charge and must have approximately opposite direction in the transverse plane: $\Delta\phi > 2.7$. This increases the signal significance, especially for high mass hypotheses, as the mean $\Delta\phi$ increases with Higgs mass, as shown in Fig. 5.1.¹

Categorization The existence of b -jets in many b -associated Higgs production signal events, and the lack of those in most gluon-gluon fusion signal events, makes it beneficial to categorize in dependence of the number of b -tagged jets in the event. This increases the signal significance, especially for the b -associated production signal.

The b -tag category, required to have at least one b -tagged jet with $p_T > 20$ GeV, is specialized to the search of MSSM Higgs produced in association with b -quarks. The subleading $\tau_{\text{had-vis}} p_T$ cut is raised to 65 GeV, as the estimation of the QCD multijet background was found to be unreliable at low p_T (cf. Sect. 6.2). The main backgrounds in this category are the QCD multijet and $t\bar{t}$ processes.

The b -veto category requires that no b -tagged jets with $p_T > 20$ GeV are present in the event. It provides a good sensitivity to both gluon-gluon fusion and b -associated Higgs signals. The main backgrounds come from QCD multijet and $Z/\gamma^* \rightarrow \tau\tau$ events.

¹The discrepancy between background estimation and data for low $\Delta\phi$ is expected, as the QCD multijet background prediction is only derived for back-to-back topologies of the leading $\tau_{\text{had-vis}}$.

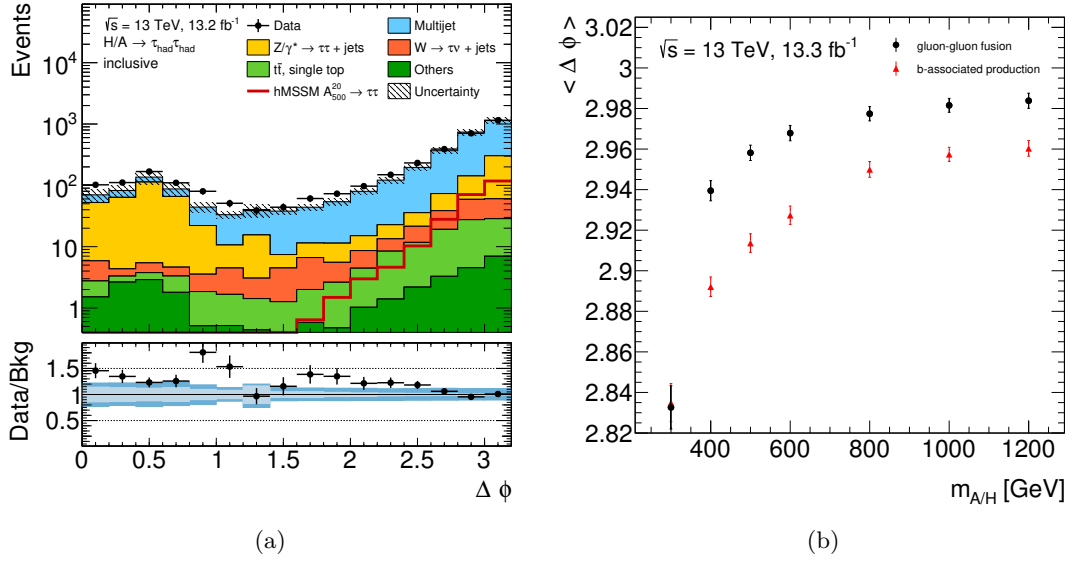


Figure 5.1: Distribution of $\Delta\phi$ before the cut on that observable (a) and mean $\Delta\phi$ for signal in dependence of the mass hypothesis (b).

Distributions of important kinematic observables in these categories are shown in Figs. 5.2 and 5.3. Additional figures can be found in App. A. Observed and predicted background event yields at different stages of the event selection are listed in Table 5.2 with their statistical uncertainties. Table 5.3 shows these numbers for a selection of signal event samples. Signal selection efficiencies for some mass hypotheses are listed in Table 5.1. Due to the $\tau_{\text{had-vis}}$ transverse momentum thresholds, the 200 GeV signal mass event samples have selection efficiencies below 1‰ and therefore this search has very low sensitivity in this low mass range. Furthermore, these event samples are severely statistically limited after the selection and are consequently not considered in this analysis.

Mass Hypothesis [GeV]	200	300	600	1000	1200
<i>b</i> -tag category					
gluon-gluon fusion	0.00	0.04	0.24	0.39	0.35
<i>b</i> -associated prod.	0.03	0.92	5.68	7.00	6.67
<i>b</i> -veto category					
gluon-gluon fusion	0.08	3.17	16.08	17.31	16.12
<i>b</i> -associated prod.	0.06	2.53	10.12	10.03	9.39

Table 5.1: Signal selection efficiencies in percent for a selection of signal event samples.

Data	QCD Multijet	$Z/\gamma^* \rightarrow \tau\tau$	$W(\rightarrow \tau\nu)+\text{jets}$	$t\bar{t}$, single top	Others
Common Selection					
Pre-selection	—	7590 \pm 100	29 160 \pm 420	14 889 \pm 44	10 300 \pm 310
Leading $\tau_{\text{had-vis}} p_T$	—	4199 \pm 83	15 990 \pm 270	8309 \pm 37	5400 \pm 200
Subleading $\tau_{\text{had-vis}} p_T > 55 \text{ GeV}$	—	3845 \pm 79	13 940 \pm 260	7149 \pm 34	4570 \pm 180
Leading $\tau_{\text{had-vis}}$ identification	—	1434 \pm 43	1899 \pm 40	879 \pm 11	237.9 \pm 7.3
Subleading $\tau_{\text{had-vis}}$ identification	—	728 \pm 26	150.7 \pm 5.2	101.3 \pm 3.2	34.4 \pm 1.8
$\Delta\phi > 2.7$	—	355.1 \pm 6.0	88.0 \pm 3.7	57.0 \pm 2.7	15.4 \pm 1.2
Opposite Sign					
Opposite Sign	—	339.1 \pm 5.9	72.9 \pm 3.5	51.9 \pm 2.7	12.9 \pm 1.2
$\Rightarrow b$ -veto category	2006 1493 \pm 12	334.8 \pm 5.8	71.3 \pm 3.5	14.7 \pm 1.4	12.4 \pm 1.1
\Rightarrow Subleading $\tau_{\text{had-vis}} p_T > 65 \text{ GeV}$	1761	307.1 \pm 5.5	59.1 \pm 3.2	42.0 \pm 2.4	11.4 \pm 1.1
b -tag category	63 44.5 \pm 2.1	4.11 \pm 0.86	1.28 \pm 0.17	29.1 \pm 2.0	0.65 \pm 0.49
Same Sign					
Same Sign	1416	16.1 \pm 1.4	15.1 \pm 1.2	5.07 \pm 0.32	2.48 \pm 0.42
$\Rightarrow b$ -veto category	1361 1262 \pm 10	15.9 \pm 1.3	14.7 \pm 1.2	1.85 \pm 0.23	2.41 \pm 0.42
\Rightarrow Subleading $\tau_{\text{had-vis}} p_T > 65 \text{ GeV}$	1231	14.0 \pm 1.2	12.0 \pm 1.1	3.96 \pm 0.29	2.19 \pm 0.41
b -tag category	41 37.9 \pm 1.8	0.136 \pm 0.051	0.306 \pm 0.051	2.46 \pm 0.19	0.052 \pm 0.016

Table 5.2: Expected event yields for SM backgrounds and observed events at different stages of the event selection. The yields of the same-sign region, which is utilized to validate the QCD multijet background estimation (see Sect. 6.2.2), are also listed. All numbers correspond to an integrated luminosity of 13.2 fb^{-1} .

$m_{A/H}$ [GeV]	gluon-gluon fusion						b -associated production		
	300	600	1000	300	600	1000			
Common Selection									
Pre-selection	546.4	± 8.8	1665	± 20	1787	± 21	608	± 10	1656 ± 22 1753 ± 20
Leading $\mathcal{T}_{\text{had-vis}}$ p_T	430.6	± 8.3	1635	± 20	1777	± 21	475.8	± 9.3	1627 ± 22 1745 ± 20
Subleading $\mathcal{T}_{\text{had-vis}}$ $p_T > 55$ GeV	405.8	± 8.0	1592	± 20	1753	± 21	446.8	± 9.0	1591 ± 21 1718 ± 20
Leading $\mathcal{T}_{\text{had-vis}}$ identification	294.9	± 6.8	1224	± 17	1305	± 18	324.2	± 7.8	1242 ± 19 1315 ± 18
Subleading $\mathcal{T}_{\text{had-vis}}$ identification	224.9	± 5.9	1011	± 16	1084	± 16	255.9	± 6.8	1026 ± 17 1078 ± 16
$\Delta\phi > 2.7$	175.8	± 5.1	925	± 15	1001	± 16	197.2	± 6.1	904 ± 16 975 ± 15
Opposite Sign									
Opposite Sign	174.4	± 5.1	912	± 15	982	± 16	195.5	± 6.0	891 ± 16 950 ± 15
$\Rightarrow b$ -veto category	172.1	± 5.1	896	± 15	960	± 16	138.0	± 5.1	564 ± 13 556 ± 12
\Rightarrow Subleading $\mathcal{T}_{\text{had-vis}}$ $p_T > 65$ GeV	154.1	± 4.9	869	± 15	959	± 16	171.7	± 5.6	856 ± 16 932 ± 15
b -tag category	2.12	± 0.63	13.9	± 1.9	21.7	± 2.5	50.3	± 3.0	315.9 ± 9.4 389.8 ± 9.3
Same Sign									
Same Sign	1.42	± 0.32	13.5	± 1.7	19.6	± 2.1	1.63	± 0.69	12.8 ± 2.2 24.4 ± 2.4
$\Rightarrow b$ -veto category	1.33	± 0.31	13.1	± 1.7	18.8	± 2.1	0.74	± 0.57	6.8 ± 1.7 15.2 ± 1.9
\Rightarrow Subleading $\mathcal{T}_{\text{had-vis}}$ $p_T > 65$ GeV	1.24	± 0.30	12.8	± 1.7	19.5	± 2.1	1.31	± 0.63	11.5 ± 2.1 24.0 ± 2.4
b -tag category	0.091	± 0.072	0.43	± 0.24	0.78	± 0.54	0.80	± 0.36	5.3 ± 1.3 9.0 ± 1.5

Table 5.3: Expected event yields for selected signal hypotheses with decays to $\mathcal{T}_{\text{had}}\mathcal{T}_{\text{had}}$ at different stages of the event selection. The yields of the same-sign region, which is utilized to validate the QCD multijet background estimation (see Sect. 6.2.2), are also listed. All numbers correspond to an integrated luminosity of 13.2 fb^{-1} and a signal cross section of 1 pb .

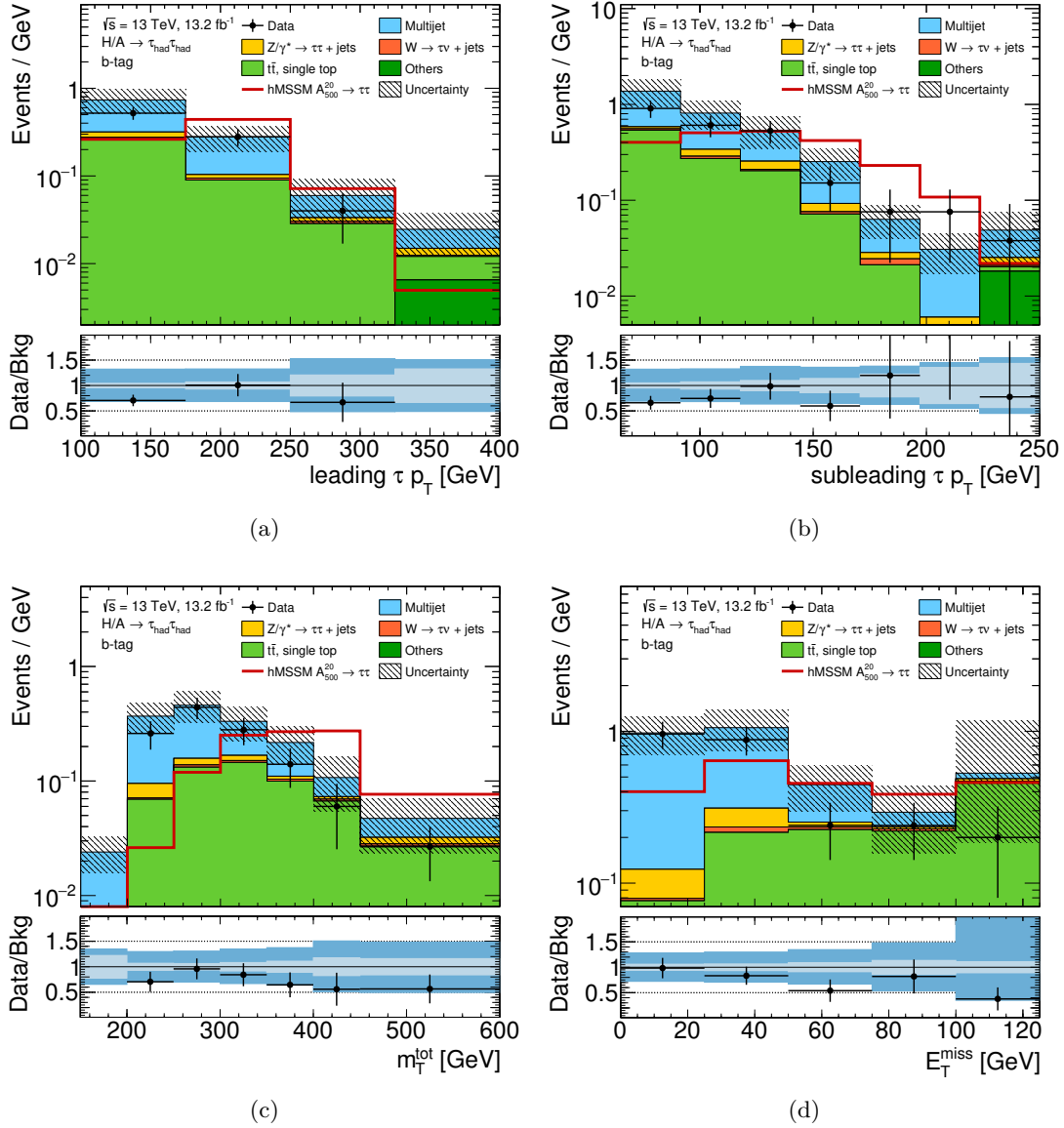


Figure 5.2: Variable distributions in the b -tag category signal region: (a) Leading $\tau_{\text{had-vis}} p_T$, (b) Subleading $\tau_{\text{had-vis}} p_T$, (c) m_T^{tot} , (d) E_T^{miss} . The light blue band in the ratio plot at the bottom visualizes the statistical uncertainty of the combined background estimation, while the darker blue band also includes the systematic uncertainties described in Chapter 7.

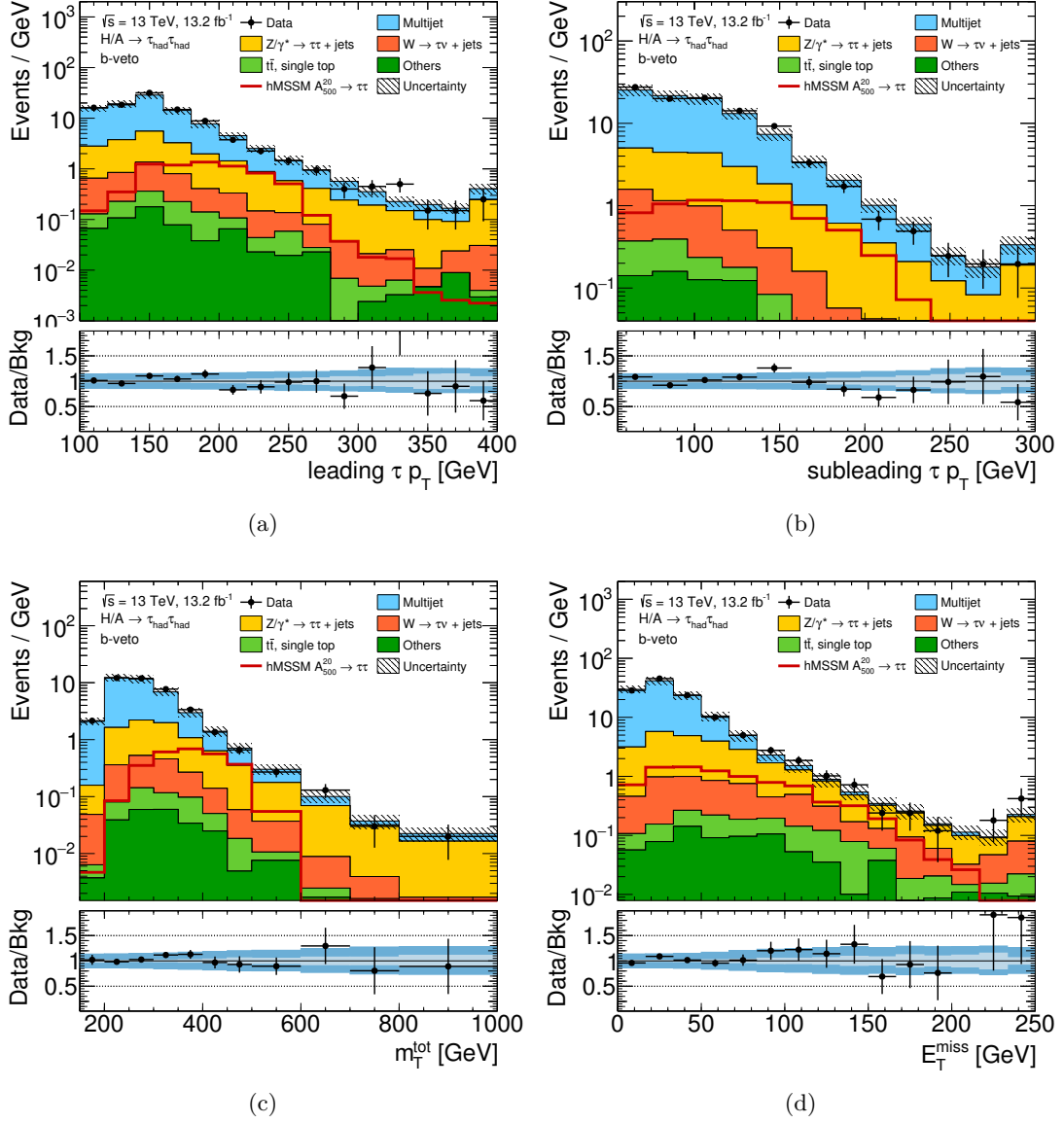


Figure 5.3: Variable distributions in the b -veto category signal region: (a) Leading $\tau_{\text{had-vis}} p_T$, (b) Subleading $\tau_{\text{had-vis}} p_T$, (c) m_T^{tot} , (d) E_T^{miss} . The light blue band in the ratio plot at the bottom visualizes the statistical uncertainty of the combined background estimation, while the darker blue band also includes the systematic uncertainties described in Chapter 7.

Chapter 6

Background Estimation

Backgrounds for this analysis are all processes predicted by the Standard Model that significantly contribute to the signal region. The only significant background with two genuine τ_{had} in the final state is $Z/\gamma^* \rightarrow \tau\tau$. It is the second most important background in the b -veto category. Most of the backgrounds arise from jets misidentified as $\tau_{\text{had-vis}}$. The QCD multijet process is of dominant importance in both categories and its estimation is primarily based on data from regions with very little expected signal, described in detail in Sect. 6.2. All other backgrounds are estimated based on Monte Carlo simulation, but with a correction of the misidentification rate that is derived from a data control region (described in Sect. 6.4). A process where in most cases one $\tau_{\text{had-vis}}$ is genuine and the other one is misidentified is $W(\rightarrow \tau\nu)+\text{jets}$ (cf. Sect. 6.3). Due to the dominant decay of top quarks to $W + b$, in the b -tag category $t\bar{t}$ and single-top processes play a big role. While also genuine $\tau_{\text{had-vis}}$ appear in these decays, the leading contribution comes from events with at least one misidentified τ_{had} . Other backgrounds considered for this analysis are of very minor importance. They include $Z(\rightarrow \ell\ell)+\text{jets}$ and $W(\rightarrow \ell\nu)+\text{jets}$ events, which are heavily reduced by the veto of electrons and muons. The remaining background components come from electroweak production of two vector bosons (WW , WZ , ZZ), which has a very limited impact on the analysis due to its small cross section.

6.1 Background Monte Carlo Event Samples

The $Z/\gamma^*+\text{jets}$ event samples [180] are generated using POWHEG-BOX version 2 [181–183]. The parton shower is simulated with PYTHIA 8.165 [184], using the AZNLO tune [185] and PDF CTEQ6L1 [80]. The PHOTOS++ 3.52 software [186] is applied to model QED emissions from charged leptons and electroweak vertices. The generation is sliced into subsamples of different resonance mass ranges to improve statistical uncertainties in the high-mass tail.

The $W+\text{jets}$ event samples [180] are simulated with the SHERPA 2.2.0 generator

[55]. The matrix element calculation based on COMIX [187] and OPENLOOPS [188] is performed at NLO for up to 2 partons and LO for up to 4 partons. The ME+PS@NLO technique [189] is applied to merge the matrix element calculation with the SHERPA parton shower [190]. A dedicated generator tuning by the SHERPA authors is used with the NNPDF30nnlo PDF [191]. To improve the speed of the event generation, a simplified scale setting prescription in the multi-parton matrix elements was applied and therefore a theory-based re-weighting procedure was performed in dependence of the jet multiplicity at generator level. The W +jets samples are generated in slices of $p_T(W)$ to enhance the statistical uncertainties in the tail of high reconstructed Higgs mass of the analysis.

The W/Z +jets samples are normalized to a cross section calculated analytically at NNLO, which has a relative systematic uncertainty of 5 %.

Event samples of di-boson processes [192] with four charged leptons, three charged leptons and a neutrino or two charged leptons and two neutrinos, as well as processes where one of the bosons decays hadronically and the other leptonically, are simulated with SHERPA 2.1.1. The matrix elements are calculated with COMIX and OPENLOOPS for up to 3 partons at LO and up to 1 parton at NLO, except for the case with three leptons and one neutrino and processes where one boson decays hadronically and a W is involved, in which case there are no partons generated at NLO. The four lepton final state matrix elements contain all diagrams with four electroweak vertices. The Sherpa parton shower is merged to the matrix element with the ME+PS@NLO method. The CT10nlo PDF [78] is utilized. The NLO generator cross sections are scaled down by 9 % to account for the use of a different α_{QED} than currently recommended by the Particle Data Group. The di-boson cross sections have a systematic uncertainty of 6 %.

Samples of $t\bar{t}$, Wt and s-channel single-top background events [193] are generated with POWHEG-BOX version 2 [194–196] and PDF CT10 [78]. The s-channel single-top process is generated in the four-flavor scheme using POWHEG-BOX version 1 [197] and PDF CT10f4 [78]. In this case, MADSPIN [198] is applied for the top quark decay, including spin correlation. A top quark mass of 172.5 GeV is chosen for the generation. The parton shower simulation of all top event samples is performed with PYTHIA 6.428 [199] using PDF CTEQ6L1 [80] and generator tune PERUGIA 2012 [200].

The $t\bar{t}$ cross section [193, 201] is calculated with the program TOP++ 2.0 [202] to NNLO in perturbative QCD and next-to-leading-log order soft-gluon resummation. Cross sections for t-channel and s-channel single-top samples are calculated at NLO QCD using the HATHOR 2.1 software [203–205]. The cross section for the Wt process is calculated at NNLO [205, 206]. For all top samples the cross section uncertainty is 6 %.

In all cases where PYTHIA is employed for parton shower simulation, also the EVTGEN 1.2.0 [207] program is applied to improve the modeling of heavy flavor particle decays.

6.2 QCD Multijet Background

The cross section of the QCD multijet background is several orders of magnitude higher than the signal cross section in the phase space of interest. Despite the heavy suppression by the event selection, it constitutes the leading background contribution in the signal region. The important leading order processes are $gg \rightarrow q\bar{q}$, $gg \rightarrow gg$ and $q\bar{q} \rightarrow gg$. QCD multijet events contribute to the signal region by jets misidentified as $\tau_{\text{had-vis}}$. At the moment it is not feasible to model this background using Monte Carlo simulation, as the fraction of quark- and gluon-initiated jets is currently not modeled well in the considered generators, as shown for other processes in Sect. 6.4. Furthermore, the large cross section of QCD multijet processes at the LHC makes it difficult to cover the relevant phase space sufficiently. Instead, the background estimation is taken from the region where the subleading $\tau_{\text{had-vis}}$ fails the *loose* identification (fail-ID region). Events from that region are weighted by a *fake factor*, which corresponds to the expected ratio of events passing the identification criterion relative to those failing it for each event. This fake factor is measured in a region enriched in QCD multijet events with negligible signal expectation and depends on properties of the subleading $\tau_{\text{had-vis}}$ and event topology. Details of the fake factor measurement are discussed in Sect. 6.2.1. The fail-ID region also contains a small amount of processes other than QCD multijet, e.g. $t\bar{t}$ or $W(\rightarrow \tau\nu)+\text{jets}$. This contamination is corrected by subtracting the Monte Carlo estimated backgrounds weighted by the fake factors. A dedicated sideband region is used to validate the QCD multijet background estimation, as documented in Sect. 6.2.2.

6.2.1 Fake Factor Measurement

Fake factors are measured in a di-jet control region using a tag-and-probe method and are defined as

$$f_{\text{fake}} = \frac{N_{\text{pass } \tau \text{ ID}}}{N_{\text{fail } \tau \text{ ID}}} \Big|_{\text{di-jet}}.$$

Events in the di-jet control region are triggered by any of the following single-jet triggers HLT_j \varnothing with the trigger jet p_{T} thresholds \varnothing of 15, 25, 35, 55, 60, 85, 110, 150, 175, 200, 260, 300, 320, 360 and 380 GeV. Depending on the ATLAS run configuration, many of these triggers have been significantly prescaled or deactivated during data taking. The lowest unprescaled single-jet trigger during the 2015 data taking was HLT_j360, in 2016 it was HLT_j380. The triggers with a threshold of 260 GeV and below were effectively active for an integrated luminosity of less than 250 pb^{-1} .

Each event is required to have at least two $\tau_{\text{had-vis}}$ candidates with $p_{\text{T}} > 55 \text{ GeV}$, $|\eta| < 2.47$ (excluding the transition region between barrel and end-cap calorimeters $1.37 < |\eta| < 1.52$) and one or three tracks. The leading $\tau_{\text{had-vis}}$ candidate is defined as the *tag* τ and should not satisfy the *medium* τ_{had} identification criterion, to prevent

overlap with the signal region selection. Its p_T threshold is raised to 100 GeV. The subleading $\tau_{\text{had-vis}}$ candidate is called the *probe* τ and it has to point in the opposite direction in the transverse plane: $\Delta\phi(\text{tag}, \text{probe}) > 2.7$.

The transverse momentum of the *probe* τ has to be at least 30 % of the *tag* τ p_T , as a dependence of the fake factor for low values of the p_T -balance $p_T(\text{probe})/p_T(\text{tag})$ is observed and in the signal region the vast majority of events is above this value, see Fig. 6.1. The fake factor is increasing for high values of the p_T -balance, most likely due to a change in the jet flavor composition. Due to the limited number of events in the di-jet control region, it is not possible to sensibly parameterize the fake factor in that observable after considering the more important parameterizations discussed below. However, most of this dependency is covered by the p_T -parameterization, as it is strongly correlated to the p_T -balance (correlation factor measured in the inclusive signal region in data: 0.77). This is demonstrated by the small dependence of the data over background ratio on the p_T -balance, as shown in Fig. 6.1b. Furthermore, the impact of any residual dependency is reduced by the relatively small correlation between p_T -balance and m_T^{tot} , with a correlation factor of 0.23.

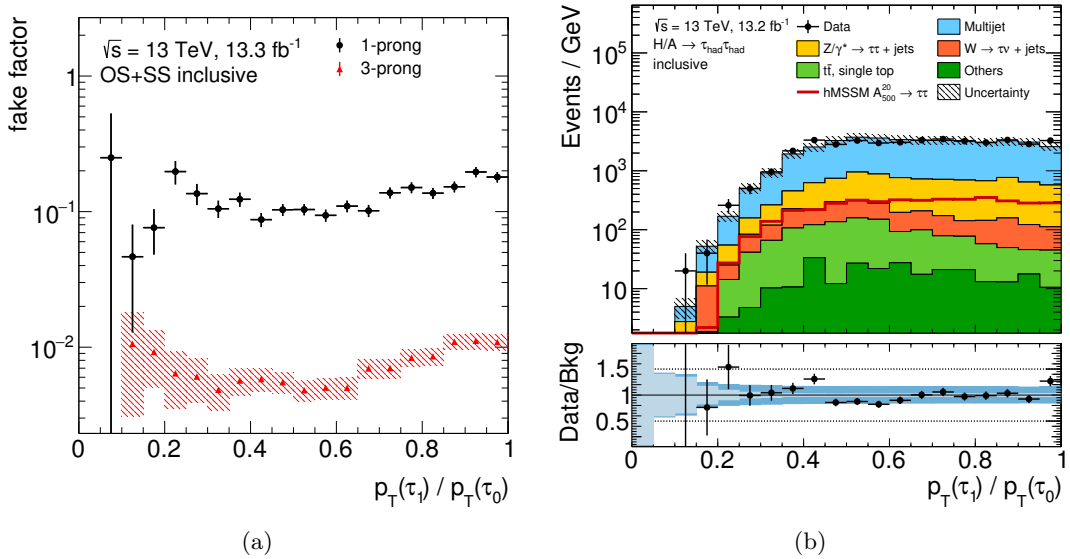


Figure 6.1: Fake factor measured in the di-jet control region depending on the ratio of *probe* to *tag* p_T for 1-prong and 3-prong *probe* tau candidates (a) and distribution of the p_T -balance in the inclusive signal region (b).

The fake factors are checked for significant dependencies to determine their parameterization and to find suitable relaxations of the control region selection to reduce statistical uncertainties. As shown in Fig. 6.3, it is obvious that the fake factor has to be parameterized in the number of tracks and p_T of the *probe* tau. It is also found that fake factors show a dependence on whether a *b*-tagged jet exists in the event, cf. Fig. 6.4. The statistical uncertainty for fake factors in the *b*-tag category is quite high

and makes it difficult to precisely measure the p_T dependence. The fake factor shows no statistically significant dependence of the $tag \tau p_T$ cut. A significant dependence of the fake factor on $\Delta\phi$ is observed (see Fig. 6.5) and therefore this cut can not be relaxed. Furthermore, an additional parameterization of the fake factor depending on the charge product of the two $\tau_{had-vis}$ candidates has to be introduced, as seen in Fig. 6.6. It is found that in the b -tag category the dependence of the fake factor on the number of tracks of the $tag \tau$ is small up to about seven tracks (cf. Fig. 6.2) and the cut is relaxed accordingly for the measurement of the b -tag category fake factors.

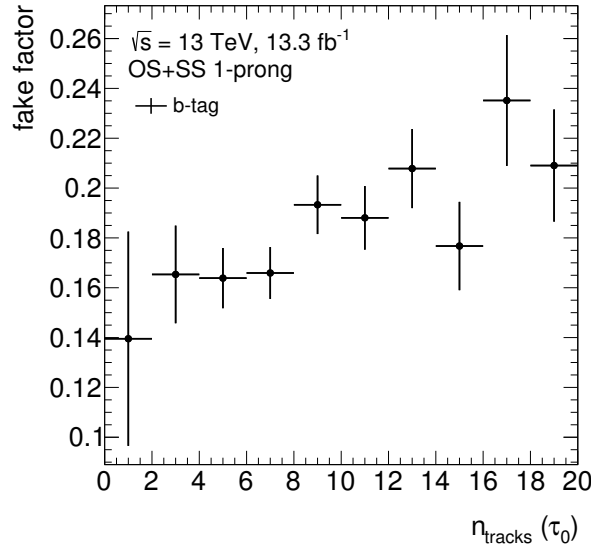


Figure 6.2: Fake factor dependence on the number of tracks of the $tag \tau$ in the b -tag category.

The resulting fake factors are shown in Figs. 6.7 and 6.8. In the b -veto category one can afford to use more bins and the resulting p_T dependence is rather smooth. Therefore the fake factors are interpolated to improve the modeling of their shape and reduce the impact of the choice of binning.

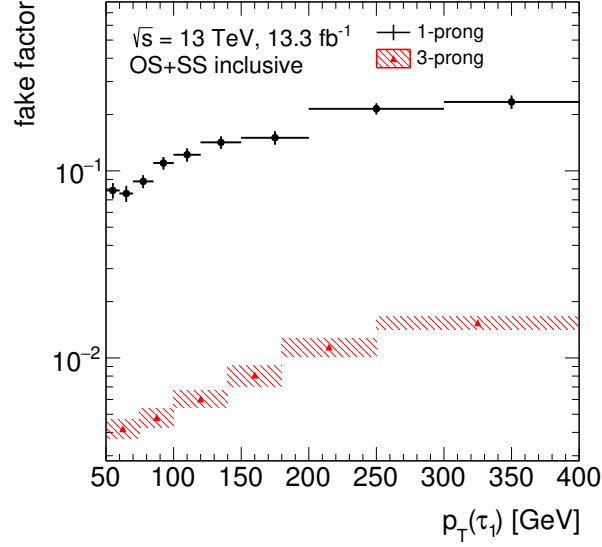


Figure 6.3: Fake factor measured in the di-jet control region depending on the *probe* τ p_T for 1-prong and 3-prong *probe* τ . The selection is inclusive with respect to the charge product of *tag* and *probe* taus and the number of *b*-jets in the event.

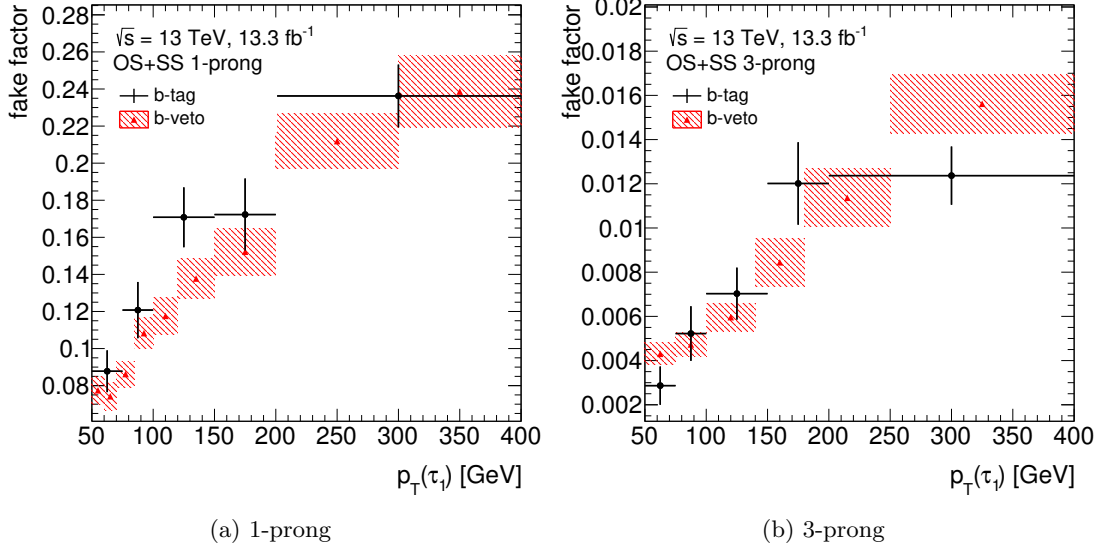


Figure 6.4: Fake factor measured in the di-jet control region depending on the *probe* τ p_T for 1-prong and 3-prong *probe* τ and for *b*-tag and *b*-veto categories. The selection is inclusive with respect to the charge product of *tag* and *probe* taus.

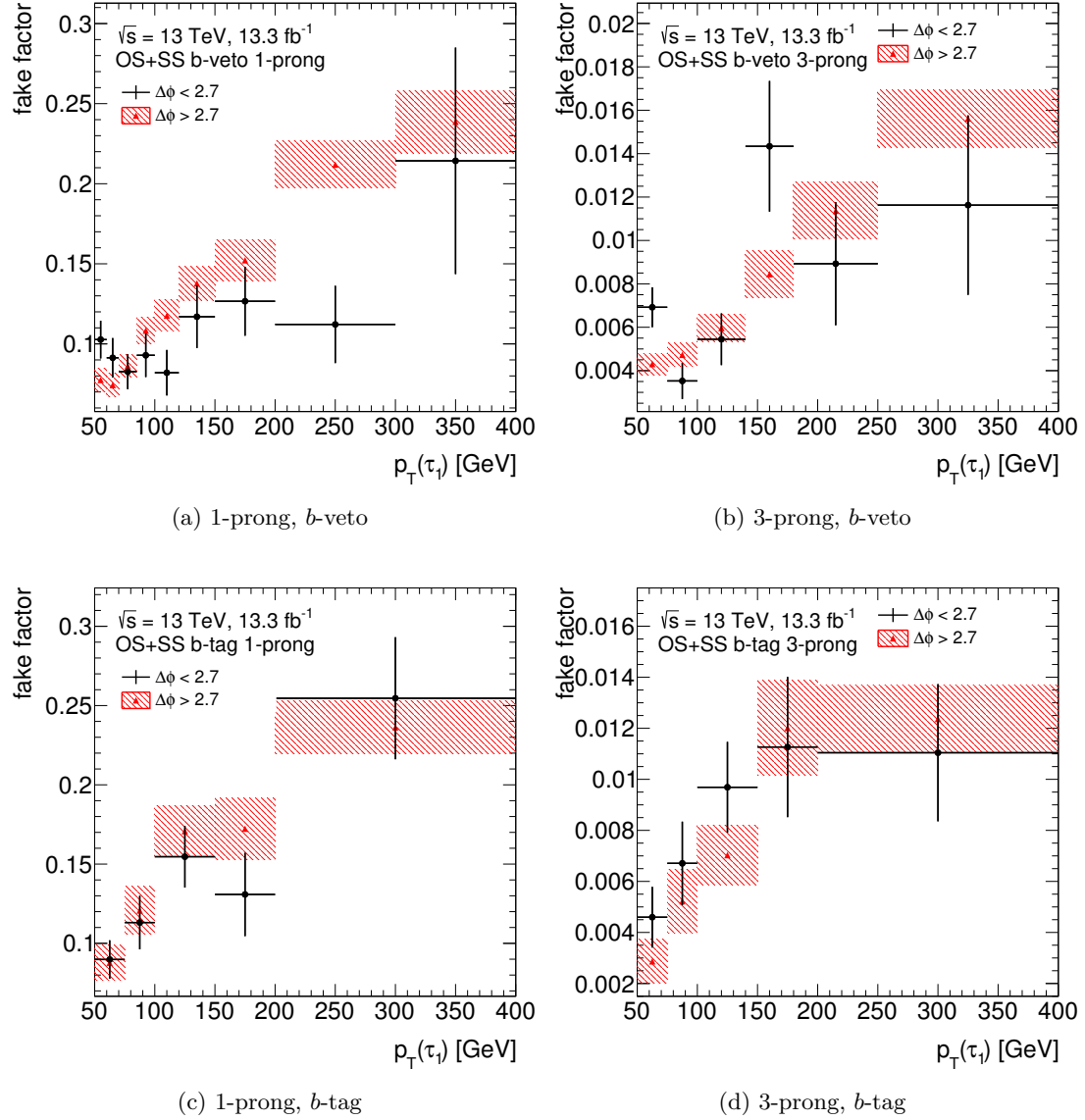


Figure 6.5: Fake factor measured in the di-jet control region depending on $\Delta\phi$ of tag and $probe$ taus, as well as p_T and N_{track} of the $probe$ τ and for b -tag and b -veto categories. The selection is inclusive with respect to the charge product of tag and $probe$ taus.

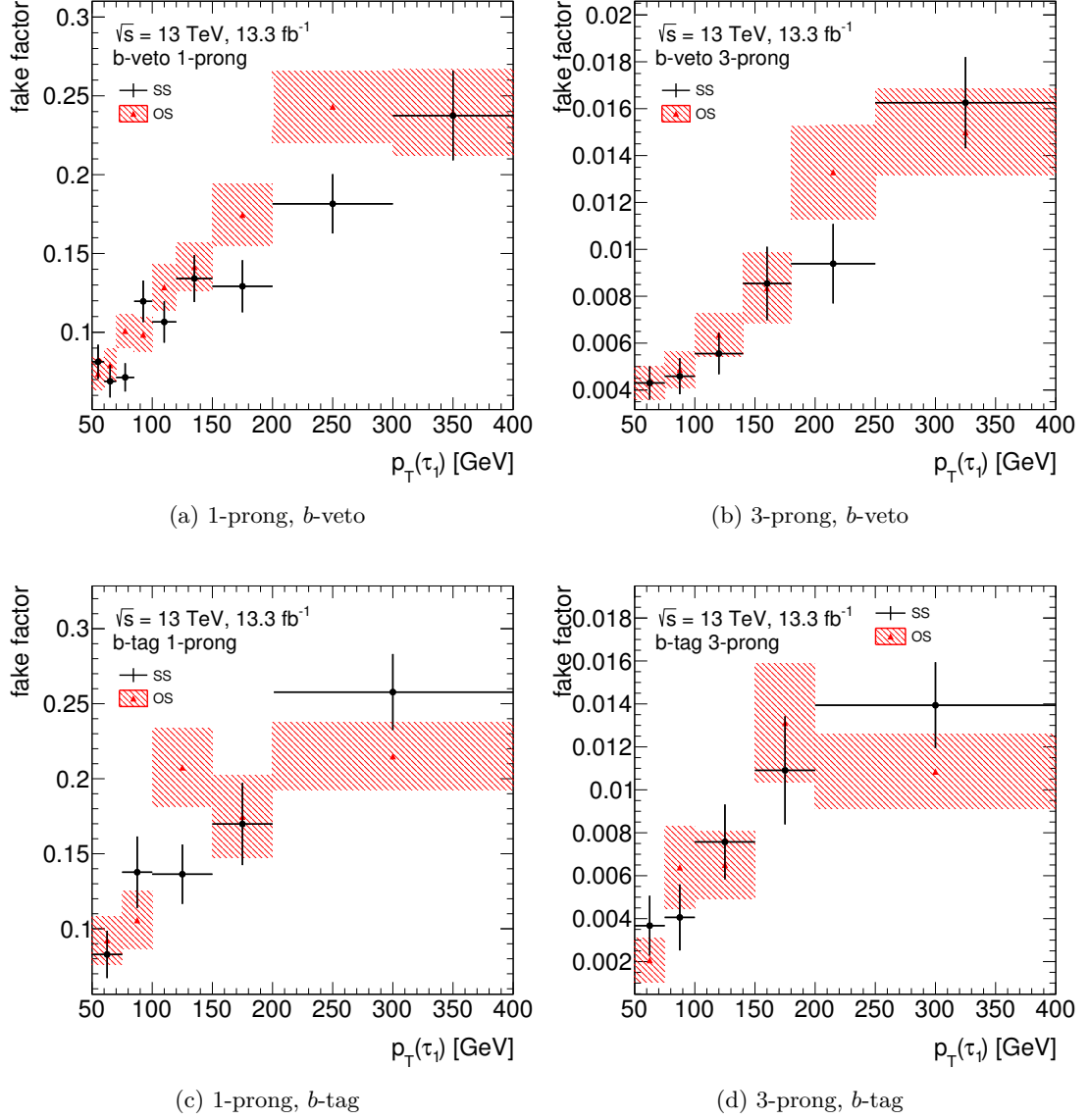


Figure 6.6: Fake factor measured in the di-jet control region depending on the charge product of *tag* and *probe* taus, as well as p_T and N_{track} of the *probe* τ and for b -tag and b -veto categories.

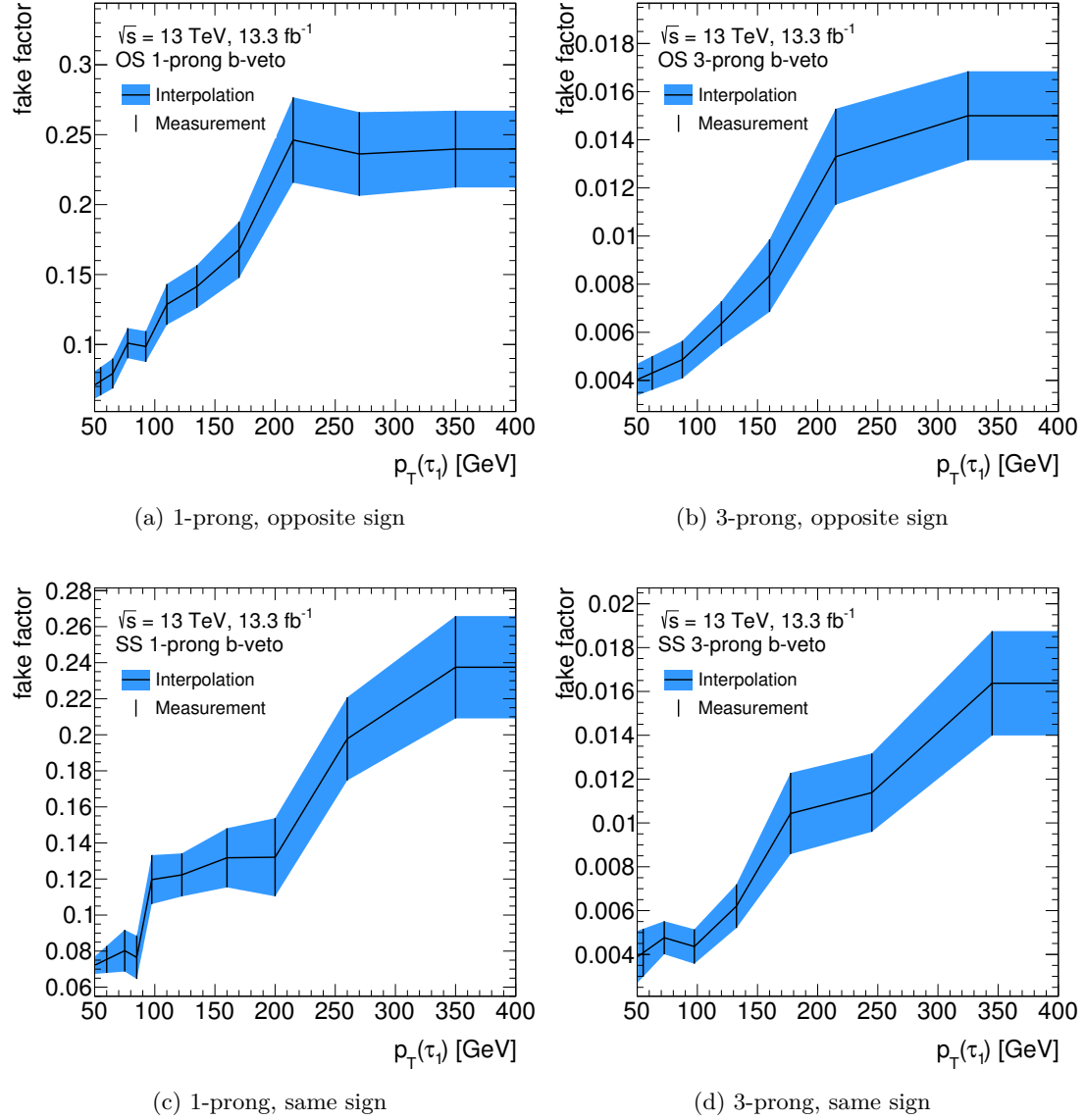


Figure 6.7: Fake factors for the b -veto category measured in the di-jet control region depending on the charge product of tag and $probe$ taus, as well as p_T and N_{track} of the $probe$ τ .

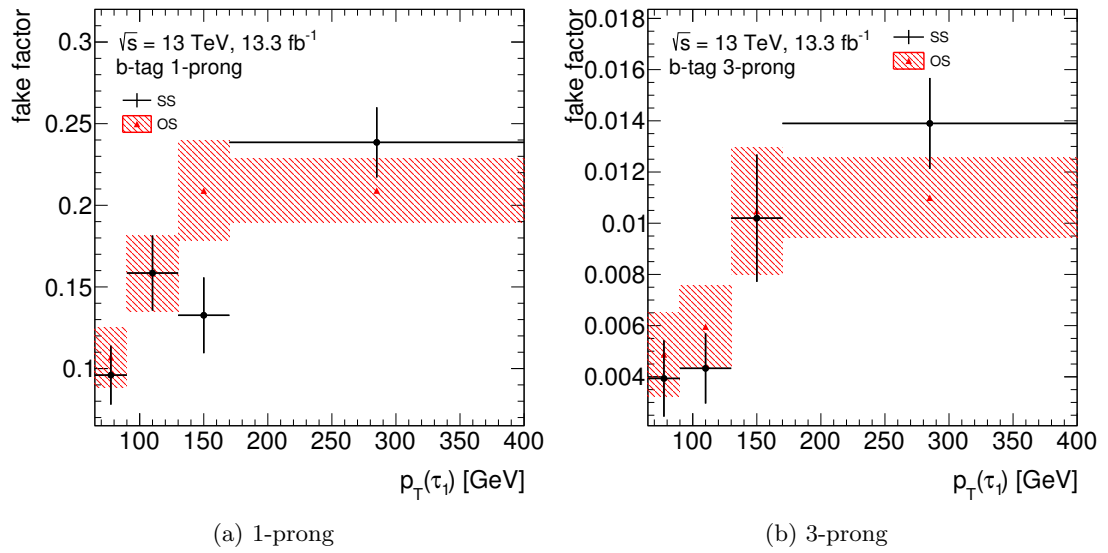


Figure 6.8: Fake factors for the b -tag category measured in the di-jet control region depending on the charge product of tag and $probe$ taus, as well as p_T and N_{track} of the $probe$ τ .

6.2.2 Background Validation

The inversion of the charge product cut results in a region which is dominated by QCD multijet background and which is therefore ideal to validate the fake factor method. As shown in Fig. 6.10, the b -veto fake factors model the background well. In the b -tag validation region a slight mismodeling is observed. Possible explanations include the existence of kinematic differences between di-jet control region and signal region, which can affect the misidentification behavior, e.g. by changing the jet flavor composition. Such a difference would have to be identified and either the selection of the di-jet control region has to be adjusted or the fake factors should get additional parameters. However, due to the low statistics in the b -tag regions, this is not possible for the available integrated luminosity. Instead, a correction to the fake factor is derived for 1-prong $\tau_{\text{had-vis}}$ in the b -tag validation region. The difference between data and uncorrected estimated background is found to have no significant dependence on the subleading 1-prong $\tau_{\text{had-vis}}$ p_T , see Fig. 6.9. A global correction factor has been determined as

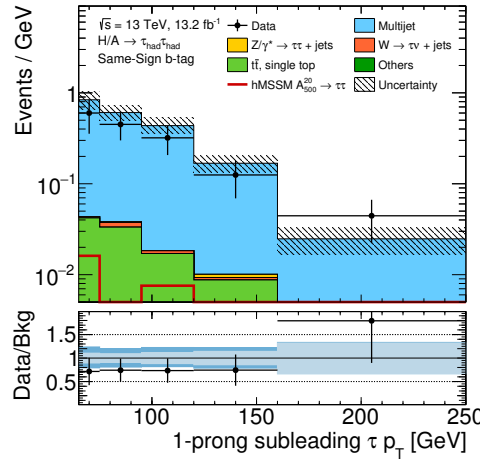


Figure 6.9: Distribution of subleading 1-prong $\tau_{\text{had-vis}}$ p_T in the b -tag validation region before application of the 1-prong fake factor correction derived in that region. The light blue band in the ratio plot at the bottom visualizes the statistical uncertainty of the combined background estimation, while the darker blue band also includes the systematic uncertainties (see Chap. 7).

$f_{\text{corr}} = (\text{data} - \text{other backgrounds}) / \text{uncorr. QCD multijet} = 0.79 \pm 0.16$, considering also the small contribution from backgrounds other than QCD multijet. The uncertainty is statistical only, the impact of systematic uncertainties of the small Monte Carlo estimated backgrounds was found to be negligible. For 3-prong subleading $\tau_{\text{had-vis}}$ the background estimation and data are compatible within the large statistical uncertainty, therefore no correction is applied. The b -tag validation region distributions after the correction are shown in Fig. 6.11.

Furthermore, for $p_T(\tau_1) < 65 \text{ GeV}$ in the b -tag validation region, a mismodeling was observed, caused by the steep gradient of the fake factor at low p_T , which due to

the low sample size can not be modeled sufficiently. Hence, the subleading $\tau_{\text{had-vis}}$ p_T threshold is raised to 65 GeV in the b -tag category.

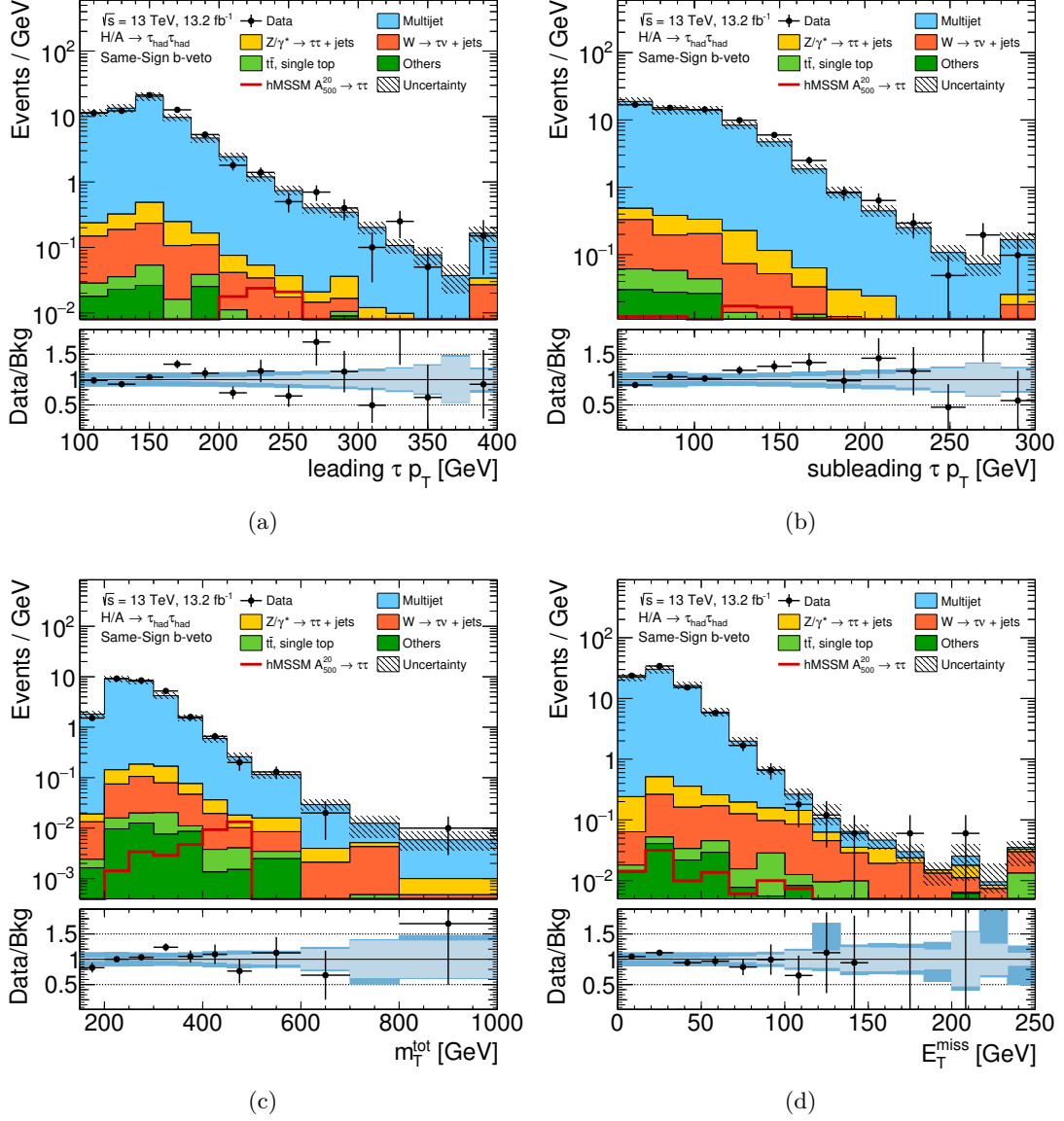


Figure 6.10: Variable distributions in the b -veto same-sign validation region: (a) Leading $\tau_{\text{had-vis}} p_T$, (b) Subleading $\tau_{\text{had-vis}} p_T$, (c) m_T^{tot} , (d) E_T^{miss} . The light blue band in the ratio plot at the bottom visualizes the statistical uncertainty of the combined background estimation, while the darker blue band also includes the systematic uncertainties (see Chap. 7).

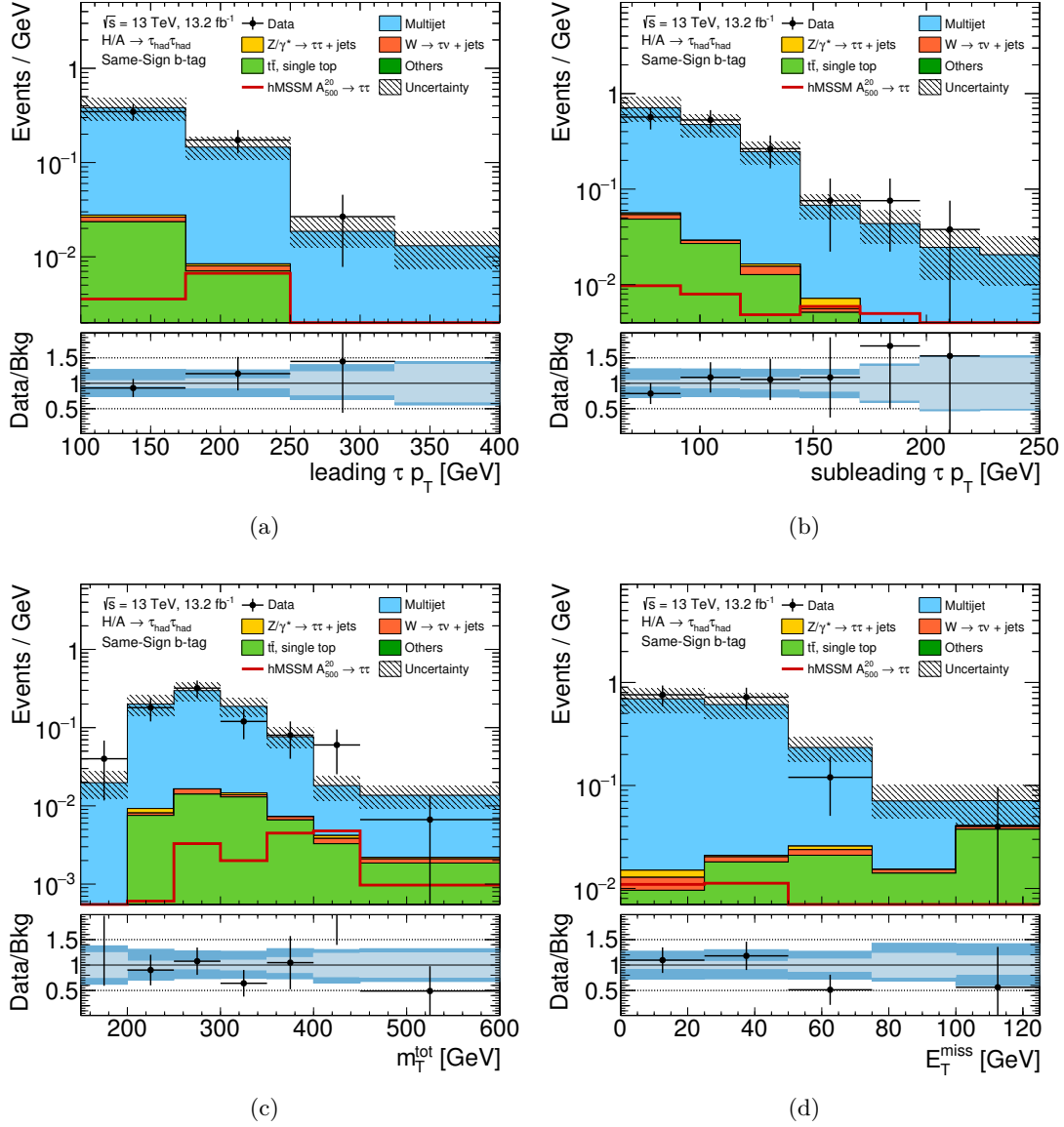


Figure 6.11: Variable distributions in the b -tag same-sign validation region: (a) Leading $\tau_{\text{had-vis}} p_T$, (b) Subleading $\tau_{\text{had-vis}} p_T$, (c) m_T^{tot} , (d) E_T^{miss} . The light blue band in the ratio plot at the bottom visualizes the statistical uncertainty of the combined background estimation, while the darker blue band also includes the systematic uncertainties (see Chap. 7).

6.3 W+jets Background

In previous publications of this analysis [208, 209] a mismodeling of the W +jets background, estimated using the SHERPA 2.1 Monte Carlo generator, was observed. To determine whether previous corrections are still necessary, the new SHERPA 2.2 modeling is checked in a dedicated control region. Due to lepton universality, the modeling can be tested for $W(\rightarrow \mu\nu)$ +jets instead of $W(\rightarrow \tau\nu)$ +jets, which has the

advantage that QCD multijet background can be suppressed much better and there is no overlap with the τ_{had} τ_{had} signal region.

The same data quality requirements as described in Sect. 5.1 are applied. Events are triggered by the HLT_mu50 muon trigger, which selects muons with $p_T > 50$ GeV. The events have to contain exactly one muon candidate, which is required to be matched to this trigger object, to pass the medium quality criterion and to satisfy $p_T > 110$ GeV. Trigger scale factors depending on η and ϕ of the triggered muon are applied as event weight to Monte Carlo simulated events. Events with additional muons with $p_T > 7$ GeV and loose quality are vetoed. Also events involving electrons with $p_T > 15$ GeV and loose likelihood-based identification are rejected. Furthermore, the events must have at least one $\tau_{\text{had-vis}}$ candidate with $p_T > 55$ GeV. The same pseudorapidity requirements as in Sect. 5.2 are imposed on muons, electrons and $\tau_{\text{had-vis}}$. No $\tau_{\text{had-vis}}$ identification criterion is applied, as the misidentification rate is corrected separately, as described in the next section, and the modeling before this correction is tested here. To reduce contributions from QCD multijet processes, the muon has to be isolated using the *gradient* criterion described in Sect. 4.3. The muon and $\tau_{\text{had-vis}}$ candidate have to be back-to-back ($\Delta\phi > 2.4$). This results in a kinematic selection similar to the main signal region.

Data and background prediction agree well and no significant mismodeling is observed, as shown in Fig. 6.12.

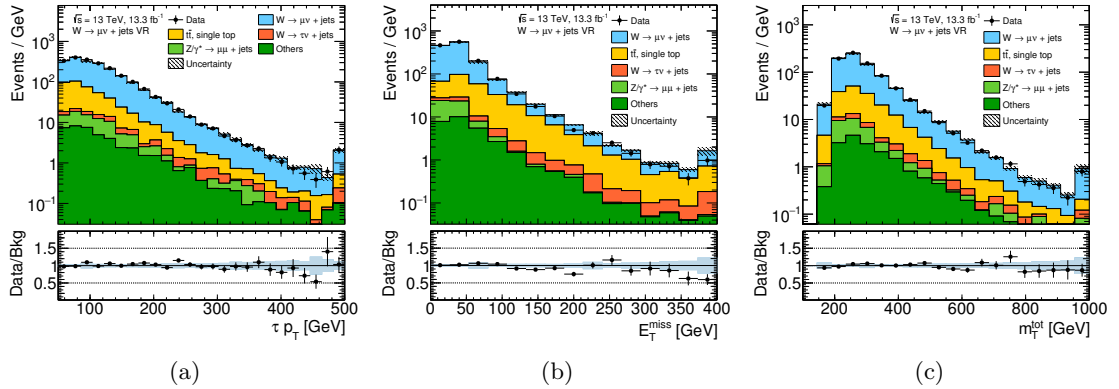


Figure 6.12: Variable distributions in the $W(\rightarrow \mu\nu)+\text{jets}$ modeling validation region: (a) $\tau_{\text{had-vis}}$ p_T , (b) E_T^{miss} , (c) m_T^{tot} . The data corresponds to an integrated luminosity of 13.3 fb^{-1} . Only statistical uncertainties are shown.

6.4 Modelling of $\tau_{\text{had-vis}}$ Misidentification Rates in Monte Carlo Backgrounds

A considerable fraction of the backgrounds estimated using Monte Carlo simulation contains at least one misidentified $\tau_{\text{had-vis}}$. It is found that in some cases the misidenti-

fication efficiency (fake rate) is not well modeled in Monte Carlo events, mostly due to the difficult simulation of the shower shape. The comparison of the fake rates as measured in data and Monte Carlo simulation is shown in Figs. 6.13 and 6.14, based on the calculations described in the following.

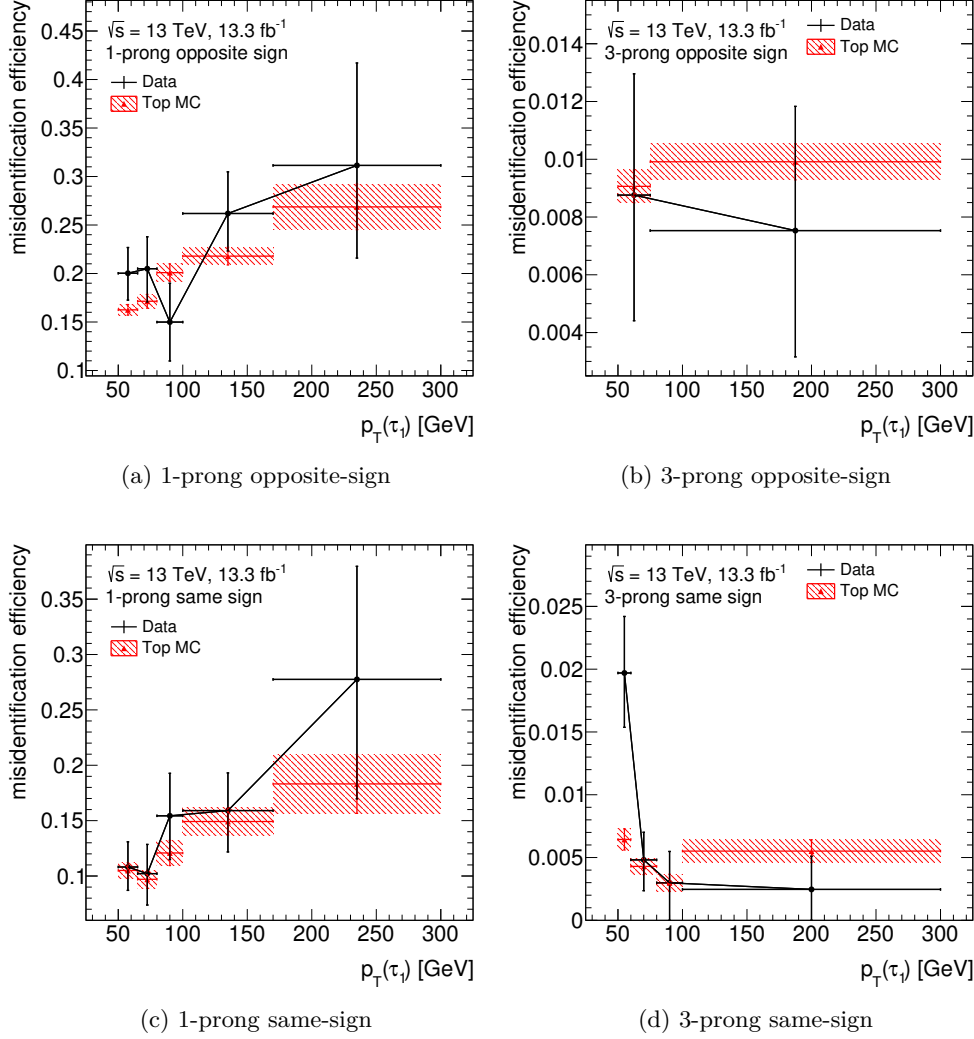


Figure 6.13: Shown is the fake rate for the loose identification working point in the top control region in data compared to the top Monte Carlo sample. It is split into opposite-sign (top) and same-sign (bottom), as well as 1-prong (left) and 3-prong (right).

As the tau misidentification is sensitive to the flavor composition of the jets, with jets initiated by quarks being more likely to be misidentified than gluon-initiated jets, the fake rates are studied separately for $t\bar{t}$ (and single-top) and W +jets. These are the most important Monte Carlo estimated backgrounds involving a significant fraction of misidentified $\tau_{\text{had-vis}}$. Other backgrounds, which have either very small fractions of misidentified $\tau_{\text{had-vis}}$ (like $Z/\gamma^* \rightarrow \tau\tau$) or a small contribution to the signal region yields

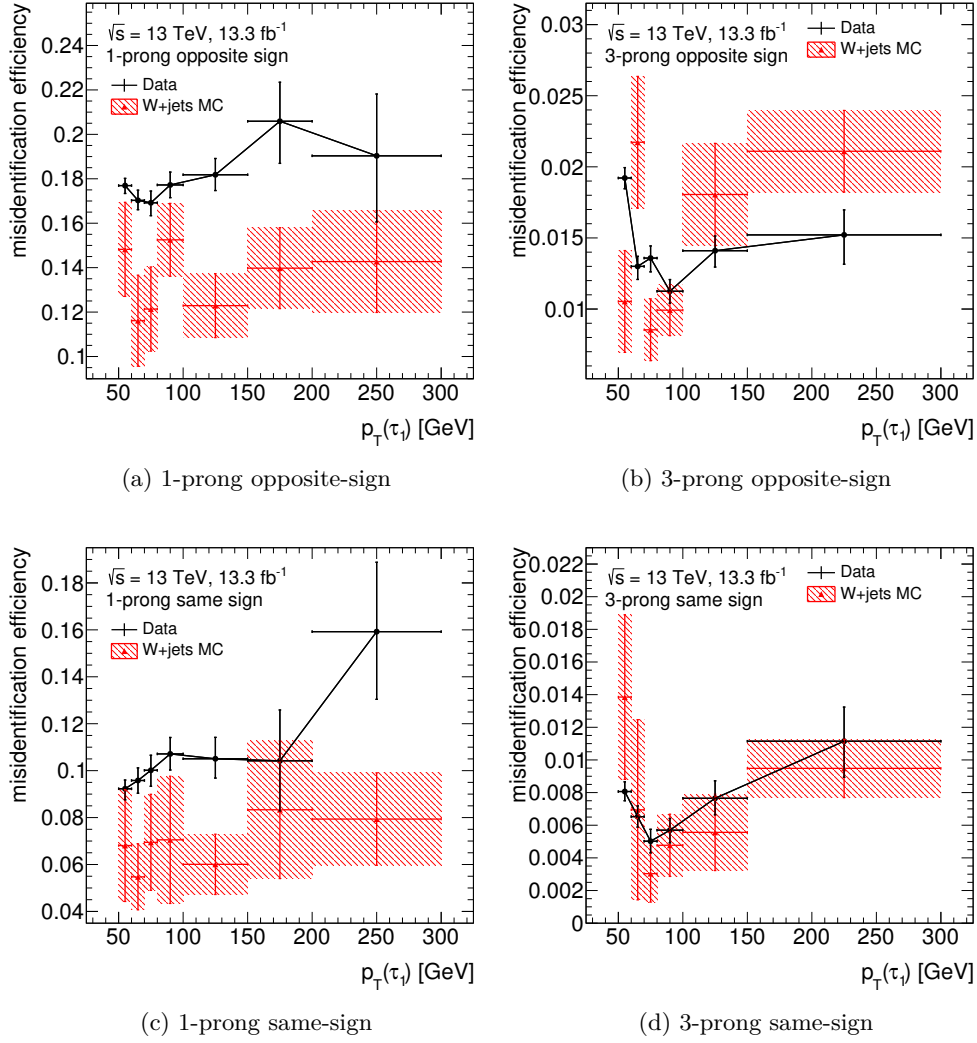


Figure 6.14: Shown is the fake rate for the loose identification working point in the $W(\rightarrow \mu\nu)$ +jets control region in data compared to the $W(\rightarrow \mu\nu)$ +jets Monte Carlo sample. It is split into opposite-sign (top) and same-sign (bottom), as well as 1-prong (left) and 3-prong (right).

(like $Z(\rightarrow \ell\ell)$ +jets or di-boson), have similar misidentification properties as W +jets and are corrected like W +jets.

Events are corrected by applying a misidentification rate per $\tau_{\text{had-vis}}$ candidate, that is not geometrically matched to a true $\tau_{\text{had-vis}}$ within $\Delta R < 0.2$, as an additional event weight. The fake rate depends on the p_T and N_{track} of the $\tau_{\text{had-vis}}$, the charge product of the two leading $\tau_{\text{had-vis}}$, as well as the identification working point. For the affected $\tau_{\text{had-vis}}$ in the signal region, the output of the identification BDT is ignored. In case the leading $\tau_{\text{had-vis}}$ is not matched to a true $\tau_{\text{had-vis}}$, also the trigger decision is not considered and instead the trigger efficiency for misidentified $\tau_{\text{had-vis}}$ is included in the *medium* working point fake rate.

The fake rates are measured in control regions with an isolated muon and a $\tau_{\text{had-vis}}$ candidate, with a similar base selection as described in Sect. 6.3, but with a lower muon p_T cut at 55 GeV. Additionally, a cut on the transverse mass of muon and $\mathbf{E}_T^{\text{miss}}$ is applied: $m_T(\mu, \mathbf{E}_T^{\text{miss}}) > 40$ GeV, which heavily suppresses the amount of QCD multijet background and removes the overlap with the $\tau_{\text{lep}} \tau_{\text{had}}$ signal region. This region is divided into two control regions, depending on whether the event contains at least one b -tagged jet ($t\bar{t}$ CR) or not ($W(\rightarrow \mu\nu)+\text{jets}$ CR).

The fake rate is determined using a tag-and-probe method. It is measured in a sample of probe $\tau_{\text{had-vis}}$ that is rich in misidentified $\tau_{\text{had-vis}}$ and is defined as

$$r_{\text{mis-ID}}(p_T, N_{\text{track}}) = \frac{N_{\text{pass-ID}}(p_T, N_{\text{track}})}{N_{\text{all}}(p_T, N_{\text{track}})},$$

where $N_{\text{pass-ID}}$ is the number of $\tau_{\text{had-vis}}$ passing the desired identification working point and N_{all} is the total number of candidates in the given p_T and N_{track} bin. To check the result of the trigger identification, the candidates in the numerator of the fake rate calculation for the *medium* identification criterion are required to match to the *resurrected* trigger decision for the 25 GeV single-tau high-level trigger. This trigger utilizes the same identification algorithm as the 80 GeV and 125 GeV triggers used in the analysis and by using this emulated low- p_T decision the result does not depend on the trigger threshold.

The $W(\rightarrow \mu\nu)+\text{jets}$ control region consists of 91.0 % $W(\rightarrow \mu\nu)+\text{jets}$ events (relative to the data), which almost exclusively contain misidentified probe $\tau_{\text{had-vis}}$. Furthermore, there is a contribution of 2.1 % from $t\bar{t}$ and single top. Of all Monte Carlo estimated backgrounds 0.7 % have genuine probe τ_{had} , mostly due to $Z/\gamma^* \rightarrow \tau\tau$. The $t\bar{t}$ control region has 71.2 % $t\bar{t}$ and single top events. There is also a large fraction of $W(\rightarrow \mu\nu)+\text{jets}$ events, 22.6 % relative to the data. A sizable 11.2 % of the Monte Carlo estimated backgrounds has genuine τ_{had} , largely from $t\bar{t}$. The composition of these control regions is visualized in Figs. 6.15 and 6.16.

Both control regions have significant fractions of events with genuine τ_{had} , which need to be subtracted from the data. As each region also contains events of the background that is targeted by the other region, the fake rates can not be measured independently. The calculation of the fake rates depends on the following measurements of event yields, where i is the $\tau_{\text{had-vis}}$ identification criterion (pass or all) and R signifies the control region (WCR or TopCR):

- d_i^R data events,
- g_i^R Monte Carlo events with genuine τ_{had} ,
- $\tilde{d}_i^R = d_i^R - g_i^R$,
- f^R $t\bar{t}$ and single top Monte Carlo events
without genuine τ_{had} , no identification requirement.

Then the fake rates F are calculated as:

$$F_W = \frac{\tilde{d}_{\text{pass}}^{\text{WCR}} f^{\text{TopCR}} - \tilde{d}_{\text{pass}}^{\text{TopCR}} f^{\text{WCR}}}{\tilde{d}_{\text{all}}^{\text{WCR}} f^{\text{TopCR}} - \tilde{d}_{\text{all}}^{\text{TopCR}} f^{\text{WCR}}},$$

$$F_{\text{Top}} = \frac{\tilde{d}_{\text{pass}}^{\text{WCR}} (f^{\text{TopCR}} - \tilde{d}_{\text{all}}^{\text{TopCR}}) + \tilde{d}_{\text{pass}}^{\text{TopCR}} (\tilde{d}_{\text{all}}^{\text{WCR}} - f^{\text{WCR}})}{\tilde{d}_{\text{all}}^{\text{WCR}} f^{\text{TopCR}} - \tilde{d}_{\text{all}}^{\text{TopCR}} f^{\text{WCR}}}.$$

Only statistical uncertainties of these quantities are considered, as the systematical uncertainties that arise from muon and $\tau_{\text{had-vis}}$ reconstruction in the Monte Carlo terms have been found to be negligible compared to the statistical uncertainty. Due to the dependencies between some of the variables and due to non-Gaussian distributions of some of the variables, the standard Gaussian uncertainty propagation can not be utilized. Therefore a stochastic simulation is performed. First, random samples of d_{all}^R are generated from Poisson distributions, where the mean is their measured value. The selection of events according to the $\tau_{\text{had-vis}}$ identification can be considered as a Binomial process, so the d_{pass}^R are sampled from a Binomial distribution $f(k|N, \epsilon) = \binom{N}{k} \epsilon^k (1 - \epsilon)^{(N-k)}$, where for each random event, N is set to the randomized d_{all}^R and the unknown ϵ is approximated as the measured $d_{\text{pass}}^R/d_{\text{all}}^R$. The g_{all}^R and f^R are sampled from a Gaussian distribution, where the mean is their measured value and the standard deviation is their statistical uncertainty. To enforce that both of them are positive and smaller than d_{all}^R , the Gaussians are truncated at 0 and at the randomized d_{all}^R . The g_{pass}^R are sampled from the normal approximation of the Binomial distributions with $N = g_{\text{all}}^R$ and ϵ as the measured $g_{\text{pass}}^R/g_{\text{all}}^R$. In rare cases the measured g_{pass}^R is 0 and therefore a good approximation of ϵ is impossible, so instead in these cases the g_{pass}^R are randomized independently from g_{all}^R , from a Gaussian around 0 with their statistical uncertainty as standard deviation. In both cases, the probability density distributions are truncated at 0 and the randomized g_{all}^R . The uncertainty interval is determined between the 15.9-th and 84.1-th percentiles of the randomized fake rate distribution. Random fake rates are generated in batches of 100 until both boundaries of the uncertainty interval change by less than 1 permille relative to the previous values.

The measured fake rates are displayed in Fig. 6.17.

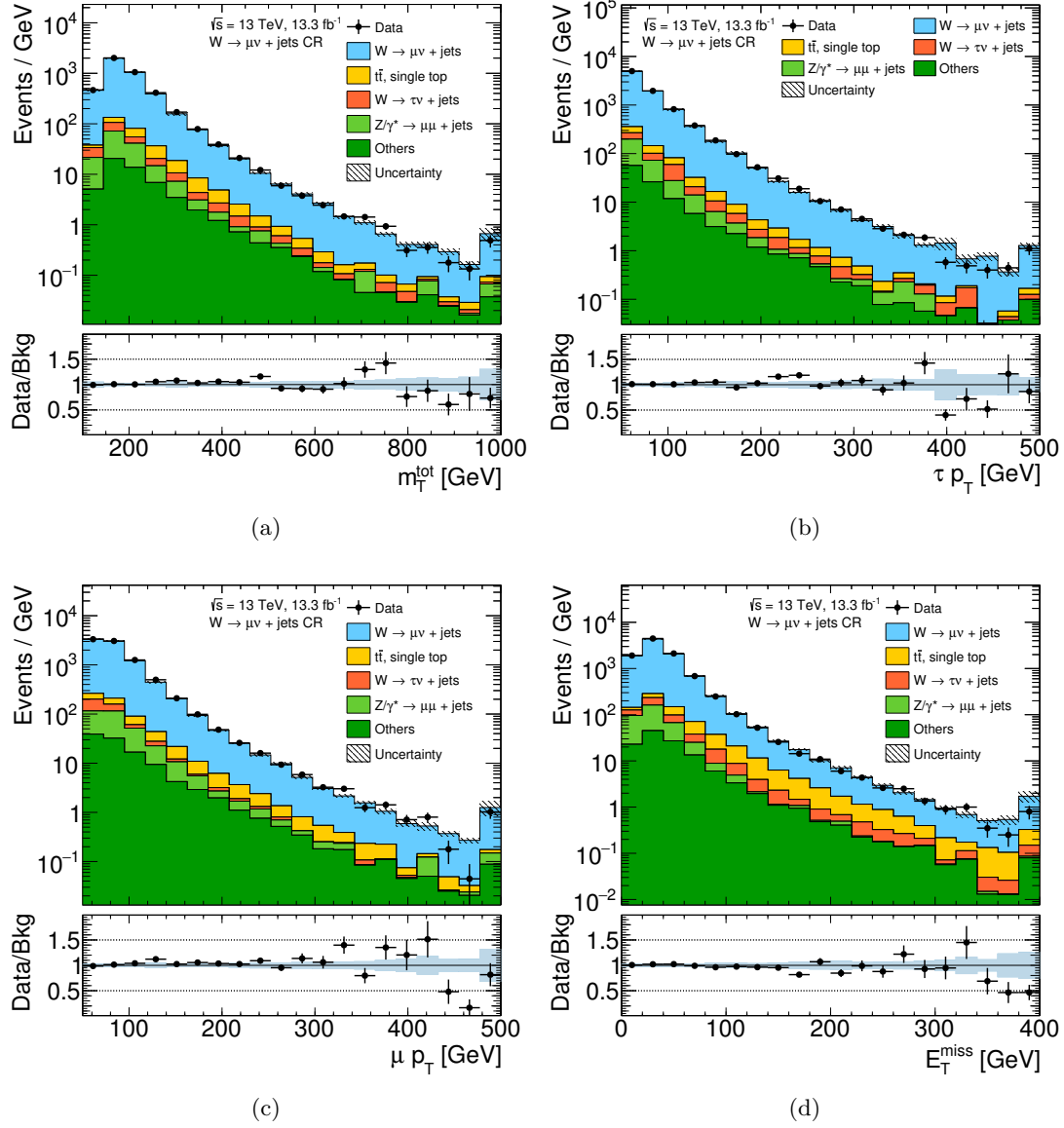


Figure 6.15: Event observables in the $W(\rightarrow \mu\nu)+\text{jets}$ $\tau_{\text{had-vis}}$ fake rate control region: (a) m_T^{tot} , (b) $\tau_{\text{had-vis}}$ p_T , (c) muon p_T , (d) E_T^{miss} . Only statistical uncertainties are shown.

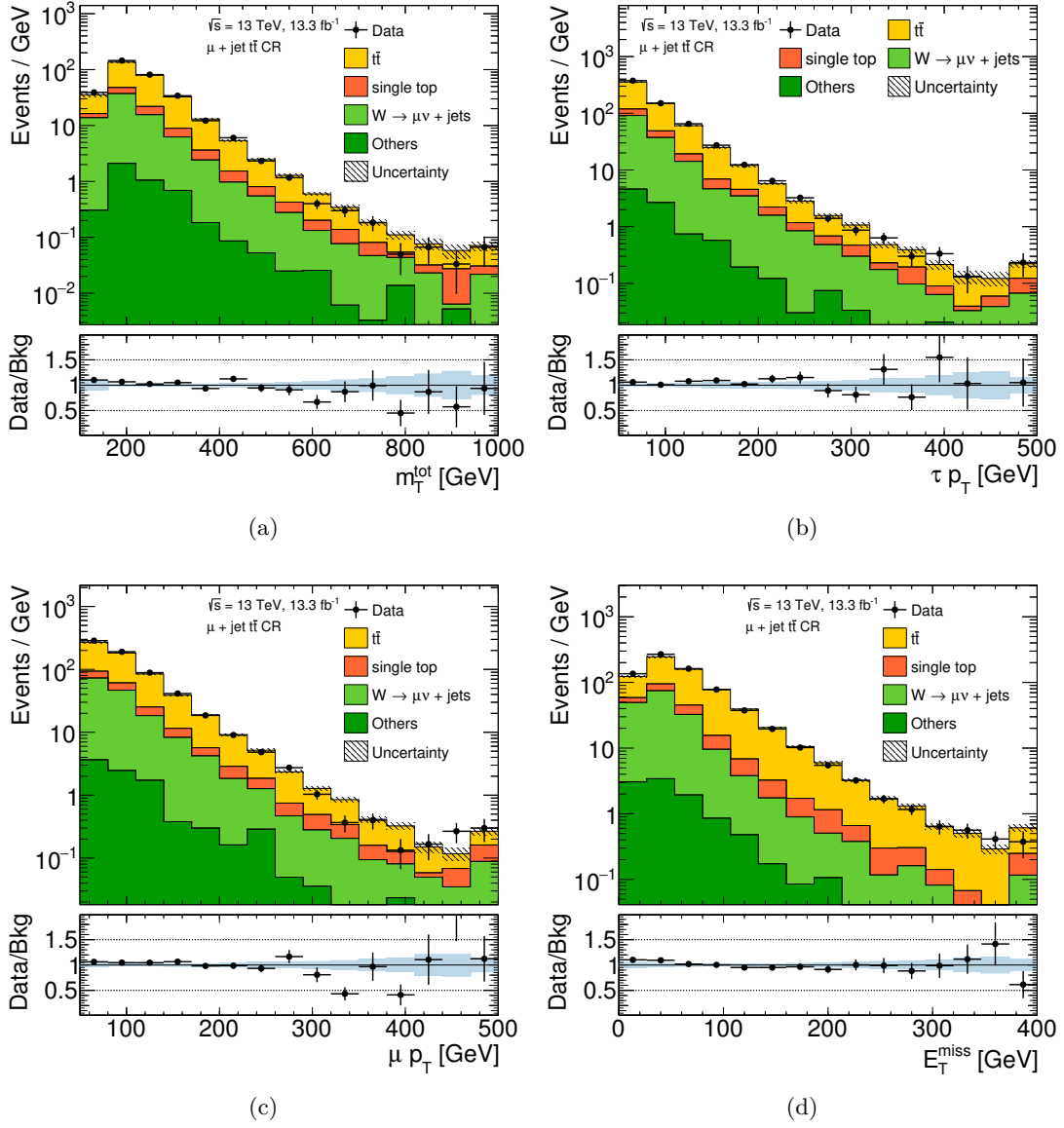


Figure 6.16: Event observables in the top $\tau_{\text{had-vis}}$ fake rate control region: (a) m_T^{tot} , (b) $\tau_{\text{had-vis}}$ p_T , (c) muon p_T , (d) E_T^{miss} . Only statistical uncertainties are shown.

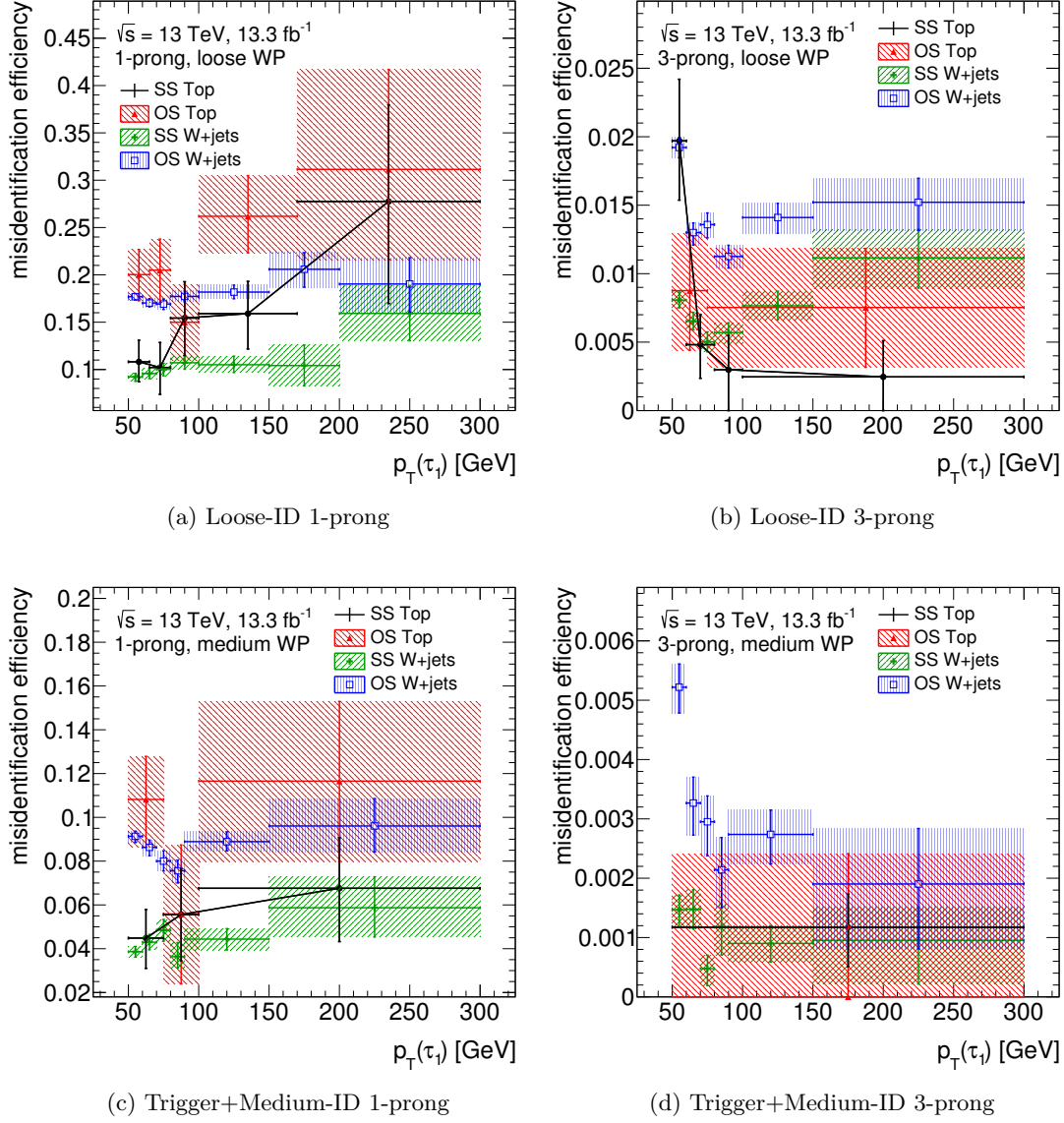


Figure 6.17: $\tau_{\text{had-vis}}$ fake rates measured in the $W(\rightarrow \mu\nu)+\text{jets}$ control region for the loose working point (top) and medium working point including the trigger (bottom). It is split in 1-prong (left) and 3-prong (right) and according to the charge product of the two leading taus.

Chapter 7

Systematic Uncertainties

7.1 Luminosity Uncertainty

The uncertainty of the luminosity measurement affects all Monte Carlo estimated backgrounds and signal. It was derived using a similar method as described in Refs. [210] and [211]. The relative uncertainty was found to be 2.1 % for the 2015 data taking and 3.7 % for 2016, as measured in luminosity calibration van der Meer scans in August 2015 and May 2016. They are treated as uncorrelated in the statistical analysis.

7.2 Background Monte Carlo Modeling

Backgrounds estimated using Monte Carlo simulated event samples have cross section uncertainties between 5 and 6 % (see Sect. 6.1).

The modeling of $t\bar{t}$ backgrounds using Monte Carlo generators suffers from significant additional uncertainties, as discussed for instance in Ref. [193]. To evaluate these modeling uncertainties, the nominal POWHEG+PYTHIA 6 sample (cf. Sect. 6.1) is compared to samples with configuration differences related to the sources of these uncertainties.

Shower generator To test the impact of a different shower model, the nominal shower generator PYTHIA 6 is replaced with Herwig++ 2.7.1 [212] using the CTEQ6L1 PDF [80] and UE-EE-5-CTEQ6L1 generator tune [213].

Hard scatter generator The effect of a different hard scatter generator is determined by comparing the POWHEG +Herwig++ sample to one generated with MADGRAPH5_aMC@NLO +Herwig++. The same Herwig++ version and configuration as above is utilized, the MADGRAPH5_aMC@NLO version is 2.2.1 [214]. The matrix element is evaluated at next-to-leading order and with the CT10 PDF [78]. Factorization and renormalization scales are set to the transverse mass $\sqrt{m_t^2 + (p_{T,t}^2 + p_{T,i}^2)}/2$.

Additional radiation and scales Samples where the factorization and renormalization scales are varied by factor 2 up and down are employed to estimate the impact of the radiation uncertainty. For these samples also the tune is varied accordingly and the sample with higher radiation also uses a doubled resummation scale parameter h_{damp} , which controls the high- p_T radiation. For the default sample the factorization and renormalization scales are chosen as $\sqrt{m_t^2 + p_T^2}$.

These uncertainties are of major importance for the b -tag category, where the top background, which consists of 89% $t\bar{t}$, constitutes a significant part of the total background. In the statistical analysis a combination of the normalization effects of these variations is used. For the hard scatter generator and shower generator variations the total relative difference is utilized as uncertainty in the positive and negative direction. The individual and combined uncertainties are listed in Table 7.1 for the b -tag and b -veto categories.

category	QCD scales	Shower generator	hard scatter generator	combined
b -tag	$+24.1$ -25.5	± 7.3	± 3.7	$+25.5$ -26.8
b -veto	$+3.9$ -14.9	± 50.8	—	$+51.0$ -52.9

Table 7.1: The effect on the final event yield of the total top background for the uncertainty arising from the choice of shower generator, hard scatter generator, as well as the variation of the additional shower radiation, given in percent.

In the b -veto category the sample with the alternative hard scatter generator is very statistically limited and therefore not considered. An artificially increased $t\bar{t}$ uncertainty did not result in any significant difference in the result of the statistical analysis, as the $t\bar{t}$ process is a very minor background in the b -veto category. Additionally, a significant systematic effect on the shape of m_T^{tot} is caused by the shower generator variation, see Fig. 7.1. A smoothing is applied to reduce statistical noise (*353QH twice smoothing* [215]).

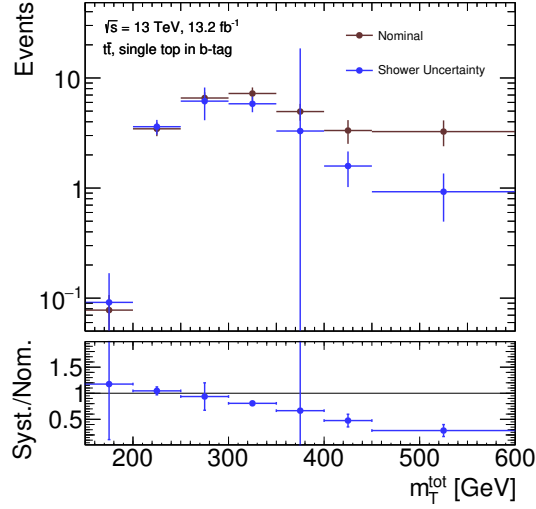


Figure 7.1: The change of m_T^{tot} shape due to changing the shower generator of the nominal sample to Herwig++. A smoothing is applied to reduce statistical noise.

7.3 Signal Acceptance

An important source of systematic uncertainty arises due to the Monte Carlo modeling of the signal. To estimate it, the nominal sample is compared to samples generated with varied generator parameters. As it is too expensive to perform the detector simulation and reconstruction for all configurations, this study is done at particle level with a selection that closely resembles the selection at reconstruction level.

The kinematic cuts (η , p_T) for the main objects ($\tau_{\text{had-vis}}$, electrons, muons and jets) are the same as for the reconstruction level analysis and the same overlap removals are performed. None of the reconstruction and identification effects are considered, as they are assumed to be uncorrelated to the modeling effects. The jet flavor is determined by geometrically matching b -hadrons, c -hadrons and τ leptons to jets ($\Delta R < 0.3$). In case one of these objects matches to more than one jet, only the closest is tagged accordingly. The b -tagging performance is emulated by weighting the events in the b -tag category by an estimated probability that one of the jets would be tagged as b -jet if the MV2c10 tagging algorithm with 70 % signal efficiency was used. Misidentifications are considered by weighting jets not matched to a b -hadron with the respective misidentification efficiency (as given in Sect. 4.2).

The following uncertainties were considered:

Parton density function For the gluon-gluon fusion signal, the uncertainty due to the parton density function is estimated using additional weights that are determined during the matrix element generation and stored in the LHE record [216]. These weights are generated for all PDFs in the PDF4LHC15_nlo_100 set [217]. As the 4-flavor scheme version of the PDF4LHC set was not yet available at the time

of this study, for the b -associated production the following PDFs are used to estimate the uncertainty: NNPDF30_nlo_as_0118_nf_4 [191], CT14nlo_NF4 [218] and MSTW2008nlo68cl_nf4 [219]. It is currently not possible to store weights for these in the LHE record for the b -associated production. To avoid generating separate samples for all these parton density functions, the LHAPDF software package [220] is employed to perform PDF reweighting. The reweighted sample is an approximation for how this sample would look like if it were generated with that different PDF. The PDF weight is the quotient of the new and the original PDF terms, depending on the Bjorken scale variables, the momentum scales and the types of the partons involved in the hard scattering. As an example, the considered PDF sets are shown for gluon and up-quark at a momentum scale of 90 GeV in Fig. 7.2. The envelope of the resulting variations was chosen as combined PDF uncertainty, as recommended in [221].

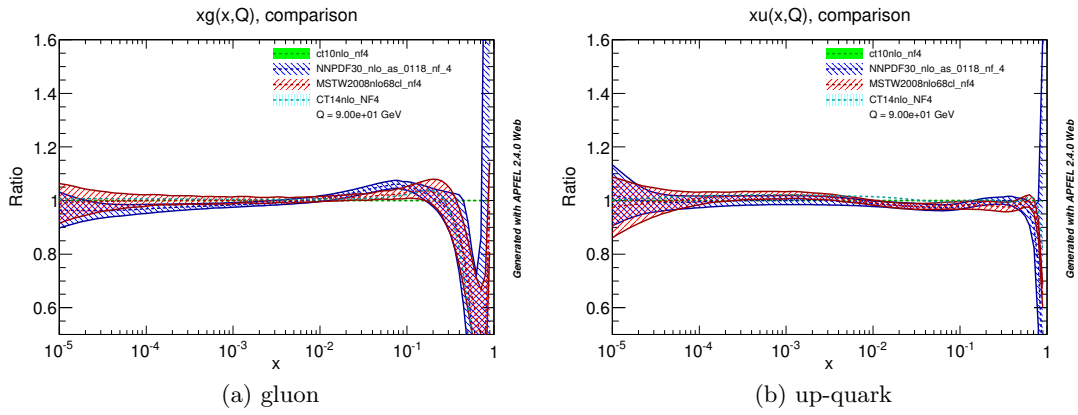


Figure 7.2: Parton density functions for gluon and up-quark multiplied by the Bjorken variable x and in dependence of x for a momentum scale $Q = 90$ GeV. The plots were generated using the APFEL PDF evolution library [222, 223].

Generator tune Parts of the Monte Carlo simulation are based on empirical models or approximations. These give rise to free parameters, which are optimized (tuned) based on measurements. The uncertainties of the generator tunes are considered by evaluating samples generated with variations of the tune parameters. These variations are related to uncertainties arising due to the modeling of ISR, FSR and MPI (cf. Sect. 2.2). The parameter variations for the PYTHIA 8 A14 tune used for the b -associated production signal samples are described in [224]. For the gluon-gluon fusion sample the AZNLO tune is utilized with systematic variations as discussed in [185], which cover only the ISR uncertainty. To estimate the uncertainties due to FSR and MPI modeling for the gluon-gluon fusion event samples, the PYTHIA 8 FSR scale parameters (renormalization and factorization scale factors for final-state showers) are varied by factor 2 simultaneously and the MPI cut-off parameter `MultipartonInteractions:pT0Ref` is varied by 10 %, as recommended in [225].

variation	400 GeV	700 GeV	1000 GeV
scales	+19.2 −19.2	+20.3 −20.1	+22.3 −21.1
PDF	+6.0 −5.5	+13.1 −15.5	+16.2 −9.5
tune	±5	±4	±3
total (pos.)	+20.7	+24.5	+27.7
total (neg.)	−20.6	−25.7	−23.3

Table 7.2: Relative signal acceptance uncertainties (in percent) for b -associated production, b -tag category

variation	400 GeV	700 GeV	1000 GeV
scales	+19.3 −18.1	+21.4 −20.3	+24.4 −21.7
PDF	+6.5 −5.2	+10.5 −9.0	+15.1 −9.2
tune	±4	±3	±3
total (pos.)	+20.8	+24.0	+28.9
total (neg.)	−19.3	−22.4	−23.8

Table 7.3: Relative signal acceptance uncertainties (in percent) for b -associated production, b -veto category

QCD Scales Renormalization and factorization scales are introduced to avoid IR and UV divergences. In principle, the outcome of the generation should not depend on the scales and they do not have an inherent uncertainty. A scale dependence arises, because the perturbative calculations are only performed up to a certain order [38]. Hence, the uncertainty that arises due to the choice of scale is strongly related to the uncertainty due to the neglected terms. These scales are varied up and down by a factor of 2 independently and fully (anti-)correlated and the largest deviation in the positive and negative direction is taken as scale uncertainty.¹

All uncertainties are evaluated for Higgs mass hypotheses of 400, 700 and 1000 GeV. They are combined quadratically for each mass and a linear regression is performed to estimate the uncertainty at other masses. The resulting uncertainties on the acceptance are listed in Tables 7.2–7.5. None of the variations were found to have a statistically significant systematic effect on the shape of the $m_{\text{T}}^{\text{tot}}$ distribution.

¹It is common practice to use factor 2, however this approach is not uncontroversial, as for instance discussed in [226]. Nevertheless, the factor of 2 is expected to generously cover the uncertainty in most cases.

variation	400 GeV	700 GeV	1000 GeV
scales	$+19$ -15	$+19$ -16	$+18$ -15
PDF	± 4.9	± 4.7	± 4.1
tune	± 21.3	± 17.4	± 16.1
total (pos.)	+29.0	+26.2	+24.5
total (neg.)	-26.5	-24.1	-22.4

Table 7.4: Relative signal acceptance uncertainties (in percent) for gluon-gluon fusion, b -tag category

variation	400 GeV	700 GeV	1000 GeV
scales	$+15$ -13	$+15$ -14	$+15$ -14
PDF	± 4.8	± 4.7	± 4.4
tune	± 3.1	± 2.6	± 1.2
total (pos.)	+16.1	+16.0	+15.7
total (neg.)	-14.2	-15.0	-14.7

Table 7.5: Relative signal acceptance uncertainties (in percent) for gluon fusion production, b -veto category

7.4 Modeling of Background with Misidentified $\tau_{\text{had-vis}}$

Uncertainties related to misidentified $\tau_{\text{had-vis}}$ belong to the most important uncertainties for this analysis. They arise from the statistical uncertainties in the di-jet control region (for the fake factor) and in the W +jets and $t\bar{t}$ control regions (for the misidentification rate) and are shown in Figs. 6.7 and 6.8, as well as Fig. 6.17. The fake factor uncertainty results in a relative uncertainty of $\pm 25.9\%$ ($\pm 12.6\%$) on the QCD multijet background yield in the b -tag (b -veto) category. The event yield uncertainties from the misidentification rate on the Monte Carlo estimated backgrounds and a selection of signal samples are listed in Table 7.6. As expected, the $W(\rightarrow \tau\nu)$ +jets and $t\bar{t}$ backgrounds are most affected by this uncertainty and the number of misidentified $\tau_{\text{had-vis}}$ in $Z/\gamma^* \rightarrow \tau\tau$ and high-mass signal is so small that the misidentification rate impact is negligible.

category	QCD Multijet	$Z/\gamma^* \rightarrow \tau\tau$	$W(\rightarrow \tau\nu)+\text{jets}$	$t\bar{t}$, single top	Others	b -assoc. A/H (500 GeV)	$gg \rightarrow A/H$ (500 GeV)
b -tag	-0.1 +0.0	+0.5 -0.6	+9.0 -9.9	+10.5 -8.6	+2.1 -2.3	+0.0 -0.0	+0.0 -0.0
b -veto	-0.0 +0.0	+0.4 -0.4	+9.4 -10.2	+11.2 -9.2	+4.5 -4.6	+0.0 -0.0	+0.0 -0.0

Table 7.6: Relative uncertainties on the background and signal event yields arising due to the misidentification rate uncertainties, in percent.

7.5 Detector-Related Uncertainties

Among the detector-related systematic uncertainties, those involving true $\tau_{\text{had-vis}}$ play a major role – $\tau_{\text{had-vis}}$ trigger, identification and reconstruction efficiencies, as well as $\tau_{\text{had-vis}}$ energy calibration (cf. Sect. 4.5). The uncertainties of the tau trigger scale factor are different between 2015 and 2016, with 2015 uncertainties divided in three components: statistics of the Monte Carlo and data event samples used for measuring the scale factor, and a systematic component. As the default uncertainties of tau reconstruction and identification are only valid up to a p_T of the order of 100 GeV, a separate uncertainty is considered for high- p_T $\tau_{\text{had-vis}}$ [227]. This uncertainty is based on a comparison of data and di-jet Monte Carlo. The $\tau_{\text{had-vis}}$ energy scale has three uncertainty components, with the most important one arising from detector effects (material modeling and calorimeter noise thresholds) [174]. The other $\tau_{\text{had-vis}}$ energy scale uncertainties come from the in-situ measurement and from model assumptions (Geant4 hadronic shower model). Additional uncertainties on $\tau_{\text{had-vis}}$ reconstruction, calibration and identification due to the use of fast simulation are considered for b -associated Higgs production event samples.

Another set of important uncertainties is related to jets: jet vertex tagging, energy scale and resolution, and flavor tagging efficiencies. There are over 70 separate sources of uncertainties of the jet energy scale. Given that this has only a small impact on this analysis, such a large set of uncertainties is disproportionate. Instead, a strongly reduced set of four uncertainties, which was determined using the method presented in [228], was utilized. However, it was checked that the full set of uncertainties yields the same result and hence no correlation information is lost due to the reduction. One of these uncertainties has negligible impact and is therefore not listed in the tables. The large number of uncertainties related to the flavor tagging is reduced by removing negligible variations from the result of an eigenvalue decomposition on the covariance matrix of statistical and systematic variations [229]. A set of 11 flavor tagging related systematic uncertainties remains, two related to b -flavored, three to c -flavored and

four to light-flavored (gluons or light quarks) jets. Furthermore, there is a b -tagging uncertainty for tau jets, which is extrapolated from charm jets and an extrapolation uncertainty for high- p_T jets.

The uncertainty of the pile-up reweighting (cf. Sect. 3.3) mainly affects samples with low statistics. The impact of uncertainties of the E_T^{miss} calculation, electron and muon calibration has been found to be negligible.

Tables 7.7 and 7.8 list the relevant relative uncertainties on the event yields of background and signal processes.

Of all uncertainties described in this section only the tau energy scale uncertainties have a statistically significant impact on the shape of the m_T^{tot} distribution. This is expected, as the tau energy scale variations lead to shifts in the $\tau_{\text{had-vis}}$ p_T spectra, since they are not distributed uniformly. The systematic shift in the m_T^{tot} distribution due to TES variations is most notable in b -veto $Z/\gamma^* \rightarrow \tau\tau$ and signal samples, as they almost exclusively contain genuine $\tau_{\text{had-vis}}$, see for instance Fig. 7.3. These distributions of the systematic shift in m_T^{tot} are smoothed similarly to the $t\bar{t}$ shower uncertainty (cf. Sect. 7.2).

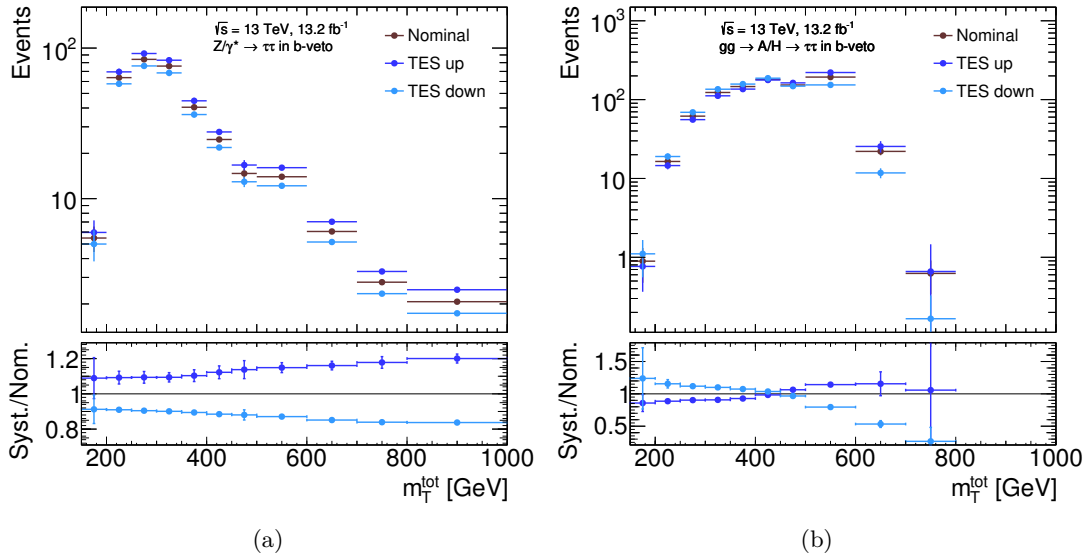


Figure 7.3: Impact of systematic variations of the detector uncertainties of the tau energy scale on the m_T^{tot} distribution of $Z/\gamma^* \rightarrow \tau\tau$ (a) and gluon-gluon fusion events for $m_H = 600$ GeV (b) in the b -veto category.

systematic	<div style="display: flex; justify-content: space-around; text-align: center;"> <div>QCD Multijet</div> <div>$Z/\gamma^* \rightarrow \tau\tau$</div> <div>$W(\rightarrow \tau\nu)+\text{jets}$</div> <div>$t\bar{t}$, single top</div> <div>Others</div> <div>b-<i>assoc.</i> A/H (500 GeV)</div> <div>$gg \rightarrow A/H$ (500 GeV)</div> </div>						
τ_{had} trigger (2015 MC stat.)	-0.0 +0.1	+3.3 -6.0	+1.9 -3.6	+2.8 -5.1	+3.1 -4.6	+3.1 -5.2	+2.8 -5.1
τ_{had} trigger (2015 data stat.)	-0.0 +0.0	+3.0 -4.4	+2.1 -2.9	+2.9 -4.1	+3.7 -4.9	+3.6 -4.9	+3.5 -4.7
τ_{had} trigger SF (2015 syst.)	-0.0 +0.0	+0.5 -0.5	+0.1 -0.1	+0.3 -0.3	-0.0 +0.0	+0.1 -0.1	+0.1 -0.1
τ_{had} trigger (2016)	-0.2 +0.2	+17.6 -16.2	+9.7 -8.9	+16.2 -15.0	+19.8 -19.2	+22.3 -21.2	+23.1 -21.7
τ_{had} identification	-0.1 +0.0	+10.3 -5.8	+5.1 -3.0	+9.1 -5.1	+9.4 -5.6	+10.7 -6.0	+10.8 -6.0
τ_{had} identification (high p_T)	-0.0 +0.0	+1.6 -1.5	+0.7 -0.7	+1.1 -1.1	+5.4 -5.3	+2.2 -2.2	+2.0 -2.0
τ_{had} reconstruction	-0.0 +0.0	+4.4 -4.3	+2.2 -2.2	+3.9 -3.8	+4.1 -4.0	+4.3 -4.3	+4.4 -4.4
τ_{had} reconstruction (high p_T)	-0.0 +0.0	+0.2 -0.2	+0.1 -0.1	+0.2 -0.2	+3.0 -3.0	+0.4 -0.4	+0.4 -0.4
TES (detector)	-0.1 +0.2	+21.7 -18.8	+5.8 -7.0	+13.5 -9.7	+0.8 -8.3	+2.9 -5.1	+5.8 -6.9
TES (in-situ)	-0.1 +0.1	+4.9 -13.9	+3.9 -6.8	+13.3 -7.9	+2.0 -8.3	+2.5 -4.3	+5.8 -5.5
TES (model)	-0.0 +0.0	+0.0 +0.8	+1.3 -1.6	+3.0 -0.8	-0.0 +0.0	+0.5 -0.6	+0.0 +0.0
pile-up reweighting	+0.1 -0.0	+4.0 +2.1	+4.2 -1.2	-1.5 -0.9	-4.8 -7.8	+1.1 -0.7	-1.3 +0.4
jet vertex tagger	-0.1 +0.0	+2.6 -2.6	+5.0 -4.8	+4.2 -4.0	+1.4 -1.3	+3.5 -3.4	+3.7 -3.6
jet energy scale (NP1)	-0.0 +0.0	+1.9 -0.7	+0.7 +0.1	-1.1 -0.2	+10.4 -8.1	+1.6 -1.9	+4.4 -3.7
jet energy scale (NP1)	+0.0 -0.0	-0.0 -0.0	+0.2 -0.1	+0.1 -0.1	-0.0 +0.0	+0.4 -0.2	+0.8 -0.0
jet energy scale (NP1)	+0.0 -0.0	+0.4 -0.3	-0.0 +0.0	+0.0 -0.0	-0.2 -0.0	+0.5 -0.5	+0.9 +0.3
jet energy resolution	+0.0 -0.0	+0.8 -0.8	+3.7 -3.7	+0.7 -0.7	+0.1 -0.1	+2.1 -2.1	+1.0 -1.0
b -tagging (b_0)	+0.0 -0.0	-1.8 +1.8	-3.1 +3.0	-3.0 +2.8	-0.8 +0.8	-5.0 +4.9	-3.2 +3.1
b -tagging (b_1)	-0.0 +0.0	+0.3 -0.3	+0.3 -0.3	+0.6 -0.6	-0.0 +0.0	+0.3 -0.3	-0.4 +0.4
b -tagging (c_0)	+0.0 -0.0	-4.3 +4.3	-1.9 +1.8	+0.0 -0.0	-0.8 +0.8	-0.2 +0.2	-2.8 +2.8
b -tagging (c_1)	-0.0 +0.0	+2.1 -2.1	+1.4 -1.4	-0.0 +0.0	+0.3 -0.3	+0.1 -0.1	+1.9 -1.9
b -tagging (c_2)	+0.0 -0.0	-0.6 +0.6	-0.7 +0.7	+0.0 -0.0	+0.2 -0.2	+0.0 -0.0	-0.7 +0.7
b -tagging (l_0)	+0.0 -0.0	-11.6 +11.7	-5.5 +5.4	-0.1 +0.1	-32.0 +32.0	-0.3 +0.3	-5.7 +5.7
b -tagging (l_1)	+0.0 -0.0	-11.6 +11.7	-5.5 +5.4	-0.1 +0.1	-32.0 +32.0	-0.3 +0.3	-5.7 +5.7
b -tagging (l_2)	+0.0 -0.0	-11.6 +11.7	-5.5 +5.4	-0.1 +0.1	-32.0 +32.0	-0.3 +0.3	-5.7 +5.7
b -tagging (l_3)	+0.0 -0.0	-11.6 +11.7	-5.5 +5.4	-0.1 +0.1	-32.0 +32.0	-0.3 +0.3	-5.7 +5.7
b -tagging (extrapol. c)	-0.0 +0.0	+1.6 -1.6	+0.0 -0.0	+0.0 -0.0	+0.0 -0.0	-0.0 -0.0	+0.0 -0.0
b -tagging (extrapol.)	-0.0 +0.0	+0.0 -0.0	+0.1 -0.1	+0.2 -0.2	+0.0 -0.0	+0.1 -0.1	+0.0 +0.0

Table 7.7: Relative uncertainty of the signal and background event yields in the b -tag category due to systematic uncertainties related to the detector, in percent. Sources of systematic uncertainty with less than 0.5 % shift in any event sample are omitted.

7.5. Detector-Related Uncertainties

systematic	<div> <div>QCD Multijet</div> <div>$Z/\gamma^* \rightarrow \tau\tau$</div> <div>$W(\rightarrow \tau\nu)+\text{jets}$</div> <div>$t\bar{t}$, single top</div> <div>Others</div> <div>b-assoc. A/H (500 GeV)</div> <div>$gg \rightarrow A/H$ (500 GeV)</div> </div>						
τ_{had} trigger (2015 MC stat.)	-0.0 +0.0	+3.4 -6.0	+1.2 -2.2	+2.6 -4.9	+2.4 -4.1	+3.2 -5.3	+3.2 -5.3
τ_{had} trigger (2015 data stat.)	-0.0 +0.0	+3.4 -4.8	+1.1 -1.6	+2.9 -4.0	+2.4 -3.4	+3.7 -4.9	+3.7 -4.9
τ_{had} trigger SF (2015 syst.)	-0.0 +0.0	+0.3 -0.3	+0.1 -0.1	+0.2 -0.2	+0.2 -0.2	+0.1 -0.1	+0.1 -0.1
τ_{had} trigger (2016)	-0.1 +0.1	+17.6 -16.4	+6.1 -5.6	+17.4 -16.1	+13.1 -12.2	+21.6 -20.5	+21.8 -20.7
τ_{had} identification	-0.0 +0.0	+10.5 -5.8	+5.0 -3.0	+8.9 -5.1	+7.5 -4.2	+10.7 -5.9	+10.7 -6.0
τ_{had} identification (high p_T)	-0.0 +0.0	+1.5 -1.5	+0.4 -0.4	+0.9 -0.9	+1.0 -1.0	+2.0 -2.0	+2.0 -2.0
τ_{had} reconstruction	-0.0 +0.0	+4.6 -4.5	+2.3 -2.3	+3.8 -3.7	+3.2 -3.2	+4.4 -4.3	+4.4 -4.3
τ_{had} reconstruction (high p_T)	-0.0 +0.0	+0.2 -0.2	+0.1 -0.1	+0.2 -0.2	+0.1 -0.1	+0.3 -0.3	+0.3 -0.3
TES (detector)	-0.0 +0.1	+12.0 -11.2	+7.0 -5.9	+8.9 -8.9	+7.6 -8.2	+3.0 -4.1	+2.7 -3.4
TES (in-situ)	-0.0 +0.0	+10.5 -10.1	+7.9 -7.5	+9.0 -7.9	+10.5 -8.0	+3.0 -3.8	+3.2 -3.0
TES (model)	-0.0 +0.0	+1.4 -1.7	+1.3 -0.3	+1.1 -0.9	+1.7 -2.0	+0.4 -0.4	+0.6 -0.4
pile-up reweighting	+0.0 -0.0	-0.7 +0.3	-0.2 +0.2	-2.1 +0.5	+7.7 -4.6	-0.5 -0.6	+0.0 +0.2
jet vertex tagger	-0.0 +0.0	+1.3 -1.3	+2.3 -2.2	+3.8 -3.7	+2.3 -2.3	+1.8 -1.8	+1.7 -1.7
jet energy scale (NP1)	+0.0 -0.0	-0.1 +0.2	-0.1 +0.2	-1.0 +0.8	-1.2 +0.8	-1.2 +1.2	-0.2 +0.3
jet energy scale (NP1)	+0.0 -0.0	-0.0 +0.0	-0.0 +0.0	-0.3 +0.4	-0.0 +0.0	-0.3 +0.1	-0.0 +0.0
jet energy scale (NP1)	+0.0 -0.0	-0.0 +0.1	-0.0 +0.1	-0.2 +0.1	-0.5 +0.1	-0.4 +0.3	-0.0 +0.1
jet energy resolution	+0.0 -0.0	+0.0 -0.0	+0.1 -0.1	+1.8 -1.8	+0.1 -0.1	+1.1 -1.1	+0.0 -0.0
b -tagging (b_0)	-0.0 +0.0	+0.0 -0.0	+0.1 -0.1	+8.4 -8.1	+0.1 -0.1	+2.2 -2.2	+0.1 -0.1
b -tagging (b_1)	+0.0 -0.0	+0.0 -0.0	-0.0 +0.0	-2.0 +2.0	-0.0 +0.0	-0.1 +0.1	+0.0 -0.0
b -tagging (c_0)	-0.0 +0.0	+0.0 -0.0	+0.1 -0.1	+0.1 -0.1	+0.2 -0.2	+0.0 -0.0	+0.0 -0.0
b -tagging (c_1)	+0.0 -0.0	-0.0 +0.0	-0.0 +0.0	-0.0 +0.0	-0.1 +0.1	-0.0 +0.0	-0.0 +0.0
b -tagging (c_2)	+0.0 +0.0	+0.0 -0.0	+0.0 -0.0	-0.0 +0.0	+0.0 -0.0	+0.0 -0.0	+0.0 -0.0
b -tagging (l_0)	-0.0 +0.0	+0.1 -0.1	+0.2 -0.2	+0.3 -0.3	+0.2 -0.2	+0.1 -0.1	+0.1 -0.1
b -tagging (l_1)	-0.0 +0.0	+0.1 -0.1	+0.2 -0.2	+0.3 -0.3	+0.2 -0.2	+0.1 -0.1	+0.1 -0.1
b -tagging (l_2)	-0.0 +0.0	+0.1 -0.1	+0.2 -0.2	+0.3 -0.3	+0.2 -0.2	+0.1 -0.1	+0.1 -0.1
b -tagging (l_3)	-0.0 +0.0	+0.1 -0.1	+0.2 -0.2	+0.3 -0.3	+0.2 -0.2	+0.1 -0.1	+0.1 -0.1
b -tagging (extrapol. c)	+0.0 -0.0	-0.0 +0.0	-0.0 +0.0	-0.0 +0.0	-0.0 +0.0	-0.0 +0.0	-0.0 +0.0
b -tagging (extrapol.)	+0.0 -0.0	-0.0 +0.0	-0.0 +0.0	-0.9 +0.9	-0.0 +0.0	-0.0 +0.0	+0.0 +0.0

Table 7.8: Relative uncertainty of the signal and background event yields in the b -veto category due to systematic uncertainties related to the detector, in percent. Sources of systematic uncertainty with less than 0.5 % shift in any event sample are omitted.

Chapter 8

Results

The $m_{\text{T}}^{\text{tot}}$ distribution shows a good separation of signal and background and is therefore chosen as final mass discriminant. More sophisticated mass reconstruction algorithms have been tested: MMC [230] and MOSAIC [231]. While they tend to have a better mass resolution, they were found to yield a worse median discovery significance $\sqrt{2((s+b)\ln(1+s/b)-s)}$ (assuming the nominal signal hypothesis, with signal yield s and background yield b) [232]. This is a result of a shift of QCD multijet background mass values to lower $m_{\text{T}}^{\text{tot}}$, resulting in a better separation especially against high-mass signal.

The data are in good agreement with the background prediction and therefore exclusion limits are calculated, as described in the next section.

8.1 Methodology of the Statistical Analysis

The statistical analysis follows the recommendations in [232, 233] and is summarized in the following. The parameter of interest for the statistical analysis is the signal strength μ , which is a scale factor of the signal normalization. The goal is to test the signal-plus-background hypothesis ($\mu = 1$, null hypothesis) and compare to the background-only hypothesis ($\mu = 0$, alternative hypothesis). In the process of frequentist hypothesis testing a p -value is calculated, which is the probability to obtain a measurement that is equally or less compatible with a given hypothesis. As is common in searches for new physics at the LHC, for the calculation of upper limits on the signal strength a confidence level of 95 % is chosen, corresponding to a p -value of 0.05. In addition to the signal strength, the statistical model has additional parameters related to the uncertainties of the signal and background modeling. They are called *nuisance parameters*, as their estimation is not of main interest.

According to the Neyman-Pearson lemma [234], the likelihood ratio test statistic for simple hypotheses is the most powerful choice. A likelihood ratio with a maximized likelihood in the denominator was proposed by Feldman and Cousins [235] to avoid

problems of the previously common Neyman construction of confidence limits [236]. To reduce the impact of the nuisance parameters on the form of the test statistic, instead this statistical analysis is based on the *profile likelihood ratio*, which is considered near-optimal. It is defined as

$$\lambda(\mu) = \frac{L(\mu, \hat{\hat{\boldsymbol{\theta}}}(\mu))}{L(\hat{\mu}, \hat{\boldsymbol{\theta}})},$$

with the likelihood function L and vector of nuisance parameters $\boldsymbol{\theta}$. In the denominator the likelihood is evaluated at its global maximum, in the numerator it is taken at a given signal strength and the corresponding conditional maximum likelihood estimator $\hat{\hat{\boldsymbol{\theta}}}$.

The likelihood function is the probability to obtain a given measurement \mathbf{x} given parameters $(\mu, \boldsymbol{\theta})$. In this case it is the Poisson probability of observing N events given an expectation of $\mu s + b$ events multiplied by the probabilities to obtain each measured event e :

$$L(\mu) = P(\mathbf{x}|\mu) = \text{Pois}(N|\mu s + b) \prod_e \frac{\mu s f_{\text{sig}}(x_e) + b f_{\text{bkg}}(x_e)}{\mu s + b},$$

with the probability density functions for signal and background $f_{\text{sig}}(x)$ and $f_{\text{bkg}}(x)$ and the Poisson distribution $\text{Pois}(n|\lambda) = \lambda^n e^{-\lambda}/n!$. As the measurement is binned and with $f_{\text{sig}}(x_e) = n_{ie}/s\Delta_i$ with the number of events observed in bin i (corresponding to event e) and the bin width Δ_i (and similar for $f_{\text{bkg}}(x)$) and ignoring a constant factor, the likelihood is equivalent to a product of the Poisson probabilities of each bin.

Considering also the nuisance parameters and that both signal and background have multiple components, the expected number of events in a given bin i is

$$\langle n_i(\mu, \boldsymbol{\theta}) \rangle = \mu \sum_j s_{ij}(\boldsymbol{\theta}) + \sum_k b_{ik}(\boldsymbol{\theta}),$$

with the predicted nominal signal yield s_{ij} for the signal component j and the estimated background yield b_{ik} of background component k . The nuisance parameters are constrained by additional likelihood terms corresponding to auxiliary measurements. For the analysis presented here, each nuisance parameter α corresponding to systematic uncertainties is constrained by a standard normal distribution (a Gaussian with standard deviation 1 and mean 0). Instead of considering statistical uncertainties for each background component, as proposed by Beeston and Barlow [237], only the statistical uncertainty of the combined background is taken into account (known as *Beeston-Barlow light* method) [238]. The nuisance parameters related to these statistical uncertainties are included as one nuisance parameter γ_i per bin and they are constrained by Poisson terms in the likelihood.

The background estimation is affected by these nuisance parameters as follows:

$$b_i(\boldsymbol{\alpha}, \gamma_i) = \gamma_i \sum_k b_{ik} \prod_m \begin{cases} 1 + \alpha_m \Delta_{mik}^+ & \text{if } \theta_m \geq 0 \\ 1 + \alpha_m \Delta_{mik}^- & \text{otherwise} \end{cases}$$

and the signal prediction analogously without γ . This allows for asymmetric uncertainties Δ_{mik}^+ and Δ_{mik}^- . Anticorrelations between processes are included in the model, as Δ^+ can increase b_i in one process, while it decreases it in another. Neglecting constant factors, this results in the likelihood

$$L(\mu, \boldsymbol{\theta} = (\boldsymbol{\alpha}, \boldsymbol{\gamma})) = \prod_i \text{Pois}(n_i | \mu s_i(\boldsymbol{\alpha}) + b_i(\boldsymbol{\alpha}, \gamma_i)) \text{Pois}'(\gamma_i^0 | \gamma_i \gamma_i^0) \prod_m \text{Gaus}(\alpha_m^0 | \alpha_m, 1)$$

where $\alpha_m^0 = 0$, $\gamma_i^0 = \frac{1}{\sigma_{i,\text{stat}}^2}$ (with the relative statistical uncertainty of the total background $\sigma_{i,\text{stat}}$ in bin i) and $\text{Gaus}(x|m, \sigma) = (2\sigma^2\pi)^{-1/2} \exp(-(x-m)^2/2\sigma^2)$. Since the Poisson terms constraining the γ nuisance parameters need to be evaluated for non-integer values, instead the Gamma function $\Gamma(x) = \int_0^\infty t^{x-1} e^{-t} dt$ is utilized as a substitute of the factorial:

$$\text{Pois}'(x|\lambda) = \begin{cases} \exp(-\lambda) & \text{if } x = 0 \\ \exp(x \ln \lambda - \lambda - \ln \Gamma(x+1)) & \text{if } x > 0. \end{cases}$$

To combine several categories, the individual likelihoods are multiplied, except the shared $\boldsymbol{\alpha}$ constraint terms, which are only included once.

It is convenient to use $-2 \ln \lambda(\mu)$ as a test statistic, as it has computational advantages to evaluate the sum of logarithms instead of a large product and under certain conditions its distribution is well approximated by a χ^2 -distribution. Additionally, the test statistic should reflect that the signal can only increase the expected event yield with respect to the Standard Model, i.e. $\mu \geq 0$. This is implemented by evaluating the likelihood in the denominator at $\mu = 0$ and $\hat{\boldsymbol{\theta}}(\mu = 0)$ if $\hat{\mu} < 0$, which corresponds to the closest allowed value. Nevertheless, $\hat{\mu}$ is allowed to take negative values and is therefore considered an effective estimator, which allows for an easier description of the test statistic distribution. When setting upper limits, best-fit values that are higher than the tested signal strength should not increase the p -value and therefore the test statistic is set to 0 if $\hat{\mu} > \mu$. This results in the following test statistic:

$$\tilde{q}_\mu = \begin{cases} -2 \ln \frac{L(\mu, \hat{\boldsymbol{\theta}}(\mu))}{L(0, \hat{\boldsymbol{\theta}}(0))} & \text{if } \hat{\mu} < 0 \\ -2 \ln \frac{L(\mu, \hat{\boldsymbol{\theta}}(\mu))}{L(\hat{\mu}, \hat{\boldsymbol{\theta}})} & \text{if } 0 \leq \hat{\mu} \leq \mu \\ 0 & \text{if } \hat{\mu} > \mu \end{cases}$$

By generating toy Monte Carlo experiments, the probability density function of

\tilde{q}_μ is determined for the signal plus background and background-only hypotheses, $f(\tilde{q}_\mu|\mu, \hat{\boldsymbol{\theta}}(\mu))$ and $f(\tilde{q}_\mu|0, \hat{\boldsymbol{\theta}}(0))$. For the toy generation the nuisance parameters are fixed to the conditional estimators obtained from observed data and their auxiliary measurements γ_i^0 and α_m^0 are randomized according to their constraint distributions. In the test statistic evaluation the nuisance parameters are left free to fit. The classical approach is to get the p -value from the signal plus background distribution:

$$p_\mu = \int_{\tilde{q}_{\mu,\text{obs}}}^{\infty} f(\tilde{q}_\mu|\mu, \hat{\boldsymbol{\theta}}(\mu)) d\tilde{q}_\mu$$

with the observed value of the test statistic $\tilde{q}_{\mu,\text{obs}}$. This approach has the problem that despite low sensitivity conditions, which appear usually in searches for new physics, a hypothesis can be rejected due to fluctuations in the observation [239]. So instead, the more conservative CL_s method [240] is utilized, in which the p -value becomes:

$$p'_\mu = \frac{p_\mu}{1 - p_b},$$

with

$$p_b = 1 - \int_{\tilde{q}_{\mu,\text{obs}}}^{\infty} f(\tilde{q}_\mu|0, \hat{\boldsymbol{\theta}}(0)) d\tilde{q}_\mu.$$

Since p'_μ does not correspond to a true frequentist probability, the interpretation is not straight-forward and usually it is considered as an approximation of confidence of the signal-only hypothesis.

To calculate the limit, one (usually iteratively) finds the μ_{limit} for which $p'_{\mu_{\text{limit}}} = 0.05$. The median sensitivity, known as expected limit, is obtained by taking the median of all μ_{limit} obtained for background-only toy experiments. Similarly, the 1σ and 2σ uncertainty bands are determined by taking the intervals in the distribution of background-only μ_{limit} corresponding to 68 % and 95 % integrated around the median.

The large number of toy experiments that need to be generated comes at a significant computational cost. Luckily, there are good approximations of the test statistic distributions in case the sample size is large enough. These are based on the finding by Wald [241]:

$$-2 \ln \lambda(\mu) = \frac{(\hat{\mu} - \mu)^2}{\sigma^2} + \mathcal{O}\left(\frac{1}{\sqrt{N}}\right),$$

where $\hat{\mu}$ is assumed to follow a Gaussian distribution with mean μ' , which is the assumed strength parameter of the data, and σ is the standard deviation of $\hat{\mu}$. It tends to the noncentral χ^2 distribution with one degree of freedom. If the strength parameter of the data is the same as the one that is being tested ($\mu' = \mu$) and for a large sample size, $-2 \ln \lambda(\mu)$ follows a χ^2 distribution with one degree of freedom, as demonstrated by Wilks [242]. The standard deviation can be estimated based on an Asimov dataset,

which is the artificial set of events which parameters are equal to their expected values:

$$\sigma = \frac{\mu - \mu'}{\sqrt{-2 \ln \lambda_{\text{Asimov}}(\mu)}}$$

(with the likelihood ratio being evaluated for the Asimov data). With this, the distribution of the test statistic is:

$$f(\tilde{q}_\mu | \mu') = \Phi\left(\frac{\mu' - \mu}{\sigma}\right) \delta(\tilde{q}_\mu) + \begin{cases} \frac{1}{2\sqrt{2\pi}\tilde{q}_\mu} \exp\left[-\frac{1}{2}\left(\sqrt{\tilde{q}_\mu} - \frac{\mu - \mu'}{\sigma}\right)^2\right] & \text{if } 0 < \tilde{q}_\mu \leq \frac{\mu^2}{\sigma^2} \\ \frac{\sigma}{2\sqrt{2\pi}\mu} \exp\left(-\frac{\sigma^2(\tilde{q}_\mu - (\mu^2 - 2\mu\mu')/\sigma^2)^2}{8\mu^2}\right) & \text{if } \tilde{q}_\mu > \frac{\mu^2}{\sigma^2} \end{cases}, \quad (8.1)$$

where Φ is the cumulative distribution of the standard Gaussian. Then the cumulative distribution of \tilde{q}_μ is found as

$$F(\tilde{q}_\mu | \mu') = \begin{cases} \Phi\left(\sqrt{\tilde{q}_\mu} - \frac{\mu - \mu'}{\sigma}\right) & \text{if } 0 < \tilde{q}_\mu \leq \frac{\mu^2}{\sigma^2} \\ \Phi\left(\frac{\tilde{q}_\mu - (\mu^2 - 2\mu\mu')/\sigma^2}{2\mu\sigma^{-1}}\right) & \text{if } \tilde{q}_\mu > \frac{\mu^2}{\sigma^2} \end{cases}.$$

Therefore the CL_s can be expressed as

$$p'_\mu = \frac{1 - F(\tilde{q}_\mu | \mu)}{F(\tilde{q}_\mu | 0)}$$

and μ_{limit} is found using an iterative process. The expected limit can be obtained by finding that limit for the Asimov dataset for $\mu' = 0$ and the error bands are found using Asimov datasets corresponding to $\pm\sigma$ and $\pm 2\sigma$.

The statistical model is constructed and fitted using the software packages **HistFactory** [243], **RooStats** [244] and **RooFit** [245], which are based on **ROOT** [246].

8.2 Results of the Statistical Analysis

To test the asymptotic approximation, toy experiments are generated following the prescription of the previous section, for signal hypotheses at $m_{A/H} = 400$ and 1200 GeV which exclusively contain gluon-gluon fusion or b -associated Higgs production events. For each of the four cases, 20 equidistant points of μ are scanned in a range that roughly covers their $2\text{-}\sigma$ -band from the asymptotic calculation. For each μ 10^5 events were generated, half of them with $\mu' = \mu$ and the other half with $\mu' = 0$ and the test statistic \tilde{q}_μ is calculated. In Fig. 8.1 the distributions of that test statistic for a μ close to the observed limit are shown together with an overlay of the asymptotic approximation (Eq. 8.1), where σ is determined by a fit. In all cases the CL_s agrees within a few percent between toy experiments and asymptotic fit. For the highest mass the test statistic of the b -associated case shows small deviations at high \tilde{q}_μ , probably caused by the small number of events in the last $m_{\text{T}}^{\text{tot}}$ bin of the b -tag category. As this high- \tilde{q}_μ range is

already two orders of magnitude below the peak of the distribution, the discrepancy has only a minor impact on CL_s and hence the much more economic asymptotic approximation is applied for the whole mass range. Table 8.1 shows a comparison of the expected and observed limits on μ between the asymptotic approximation and toy experiments. The statistical uncertainty of the limits from toy experiments is between 0.5 % and 2.0 %. An additional uncertainty arises due to the assumption of linearity when interpolating the CL_s between the considered μ points.

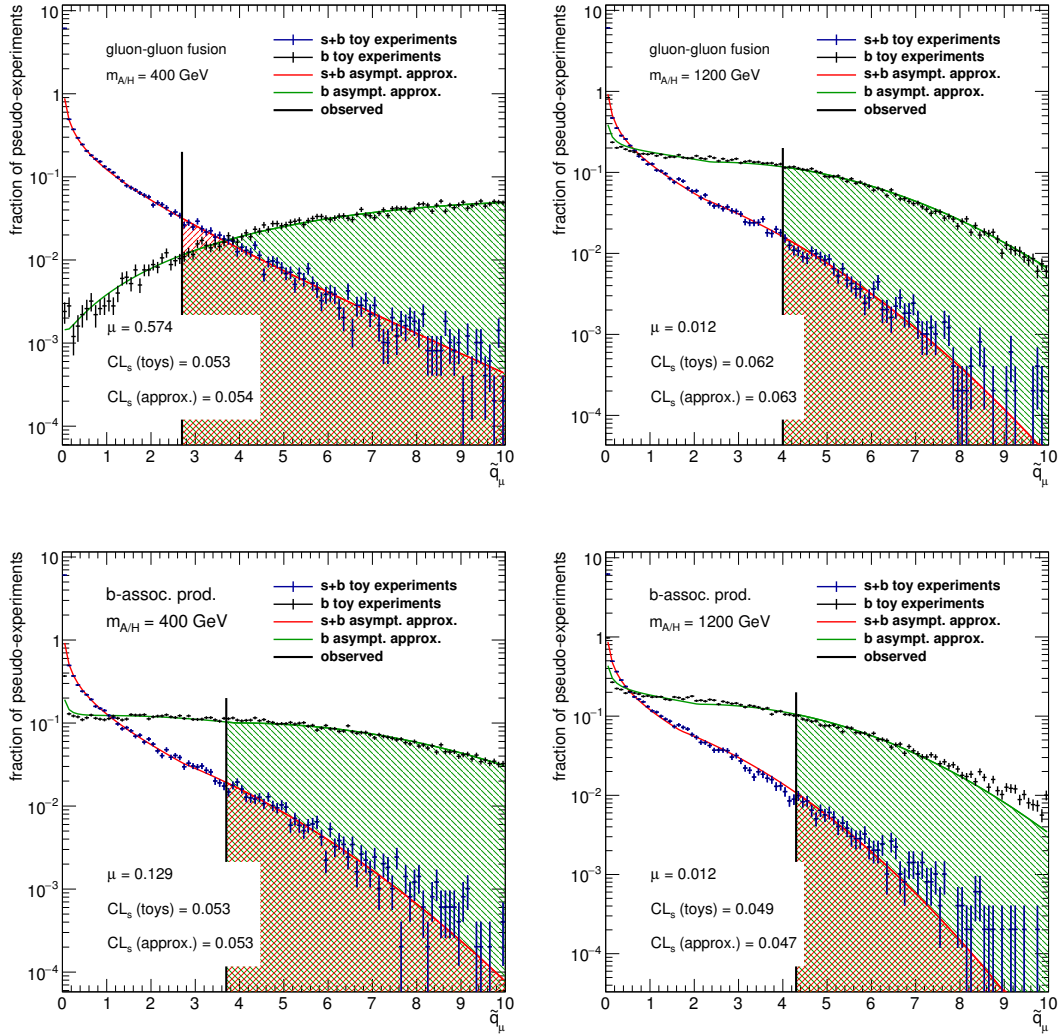


Figure 8.1: Comparison of test statistic distribution of toy experiments and asymptotic approximation for the signal hypotheses of $m_{A/H} = 400$ GeV and 1200 GeV and purely gluon-gluon fusion or b -associated production.

The m_T^{tot} distributions in the b -tag and b -veto categories are shown in Fig. 8.2 for a conditional $\mu = 0$ fit of the combined categories. The corresponding post-fit data and background yields with their uncertainties are listed in Table 8.2.

In Fig. 8.3 the fitted values of the 20 most important nuisance parameters are

signal hypothesis	Cross section limit in pb			
	toy experiments		asympt. approx.	
	obs.	exp.	obs.	exp.
gluon-gluon fusion $m_{A/H} = 400$ GeV	0.571	0.222	0.566	0.215
b -assoc. production $m_{A/H} = 400$ GeV	0.130	0.125	0.127	0.123
gluon-gluon fusion $m_{A/H} = 1200$ GeV	0.0125	0.0157	0.0124	0.0155
b -assoc. production $m_{A/H} = 1200$ GeV	0.0118	0.0168	0.0122	0.0162

Table 8.1: Comparison of expected and observed cross section limits for selected signal hypotheses between limit calculations with toy experiments and using the asymptotic approximation.

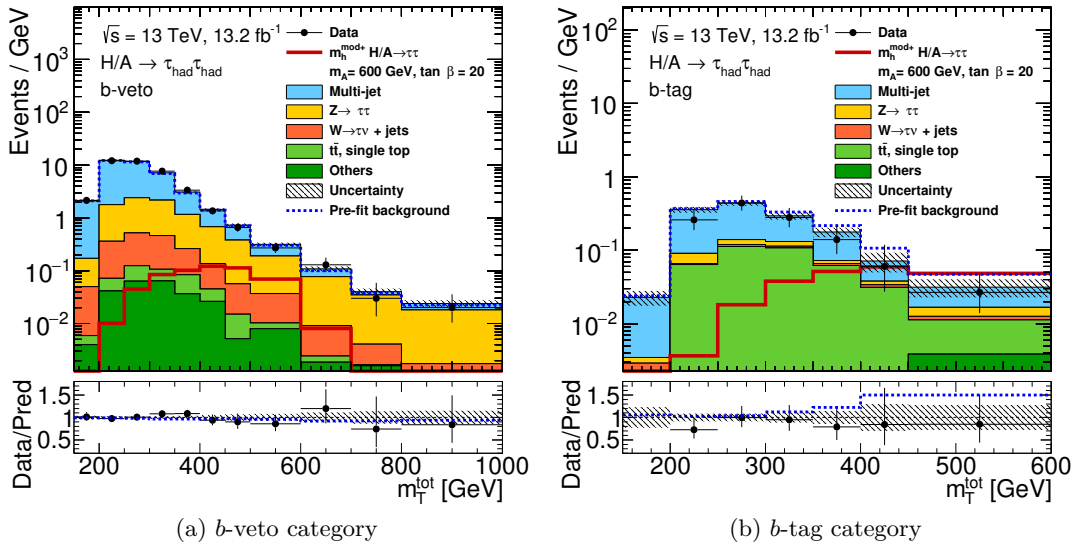


Figure 8.2: Distribution of final mass discriminant m_T^{tot} after a combined conditional $\mu = 0$ fit, with post-fit uncertainties. The signal expectation for $m_A = 600$ GeV and $\tan \beta = 20$ ($m_h^{\text{mod}+}$) is superimposed.

shown for $m_A = 300$ GeV and 1000 GeV at $\tan \beta$ values close to the limit in the $m_h^{\text{mod}+}$ scenario, ordered by their impact on $\hat{\mu}$. The impact on $\hat{\mu}$ is determined by shifting the nuisance parameter to the $1\text{-}\sigma$ boundaries of its pre-fit or post-fit uncertainty and repeating the fit of the likelihood function while keeping that nuisance parameter constant. None of the nuisance parameters has a best-fit value outside its standard deviation, which suggests that the statistical model behaves well. Plots containing all 39 nuisance parameters are found in Appendix B, including also the 600 GeV mass point. As expected, the fake factor uncertainty has the biggest impact at low mass, as it modifies the leading background. Its importance decreases for higher mass hypotheses, since its fraction of the total background prediction becomes smaller for high m_T^{tot} . The uncertainties of the shower modeling and overall normalization of the $t\bar{t}$ and single top processes plays a major role, as it affects the subleading background of the b -tag category, which has a higher sensitivity compared to b -veto. For low mass the fractional

<i>b</i> -veto			<i>b</i> -tag		
process	yield	uncertainty	process	yield	uncertainty
Multijet	1510	63	Multijet	46.6	4.3
$Z/\gamma^* \rightarrow \tau\tau$	373	49	$Z/\gamma^* \rightarrow \tau\tau$	4.39	0.96
$W \rightarrow \tau\nu$	73.9	9.3	$W \rightarrow \tau\nu$	1.31	0.21
top, $t\bar{t}$	10.9	6.8	top, $t\bar{t}$	20.0	5.6
Others	13.3	1.9	Others	0.67	0.27
Total SM	1986	43	Total SM	73.0	5.9
Data	2006		Data	63	

Table 8.2: The signal region background and data yields and uncertainties after the conditional $\mu = 0$ fit.

impact of the statistical uncertainties on $\hat{\mu}$ is of the same order as the systematical uncertainties, e.g. $^{+56}_{-43}$ % for the 300 GeV $m_h^{\text{mod}+}$ point shown in Fig. 8.3. At high mass, the fractional impact of statistical uncertainties increases, e.g. to $^{+57}_{-71}$ % for the 1000 GeV mass point ($m_h^{\text{mod}+}$, $\tan\beta = 35$).

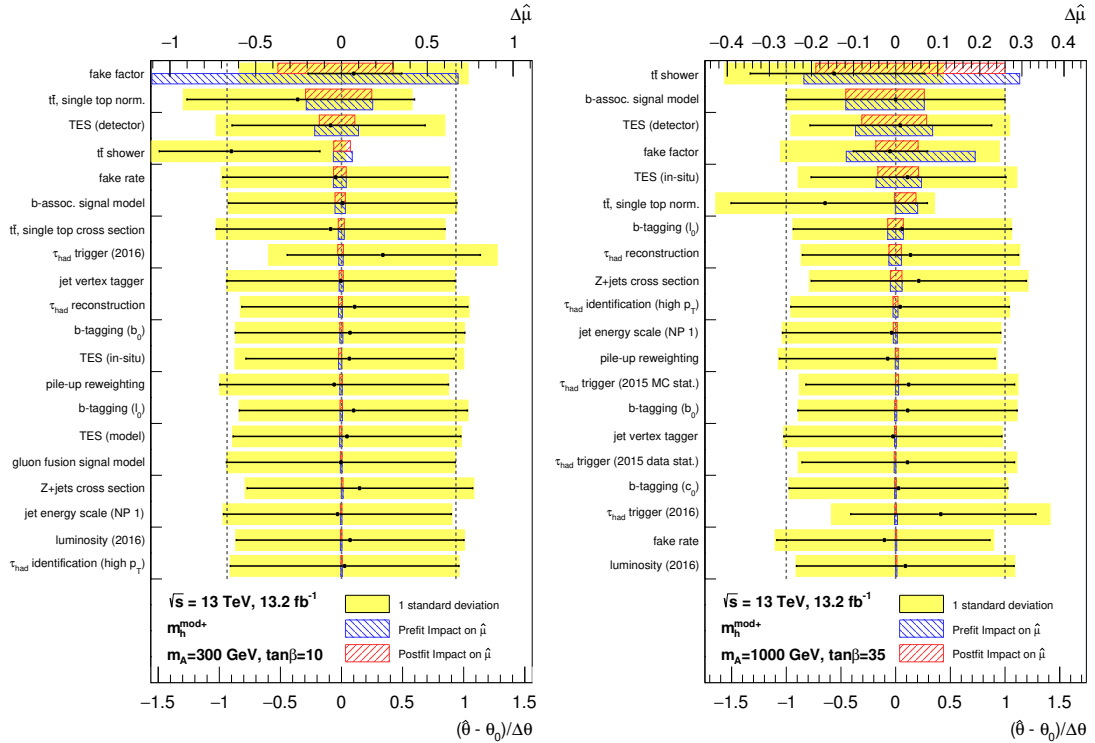


Figure 8.3: Impact of the systematic uncertainties on the fitted signal strength and variations of the nuisance parameters from their nominal values in units of their uncertainty values for $m_A = 300$ GeV and 1000 GeV in the $m_h^{\text{mod}+}$ scenario.

8.3 Limits

Besides the different magnitude of the cross sections, the only difference between the benchmark scenarios that is relevant for the limit calculations is the relative magnitude of the two production modes. Therefore asymptotic limits are calculated in the $m_{A/H} - f_{\text{bbH}}$ space, where

$$f_{\text{bbH}} = \frac{\sigma(b\text{-assoc. } A/H)}{\sigma(b\text{-assoc. } A/H) + \sigma(gg \rightarrow A/H)}$$

and from this the limits in the $m_A - \tan \beta$ parameter space of the benchmark scenarios are determined. For each considered mass hypothesis the limits are calculated for $f_{\text{bbH}} \in [0, 1]$ in steps of 1 %. Limit values for other masses and b -associated Higgs production fractions are interpolated using a Delaunay triangulation [247]. The resulting observed and expected upper limits on the total cross section are visualized in Fig. 8.4. Tables with these limits and the $\pm 1\sigma$ and $\pm 2\sigma$ uncertainty intervals for a 10 % scan of f_{bbH} are included in App. C.

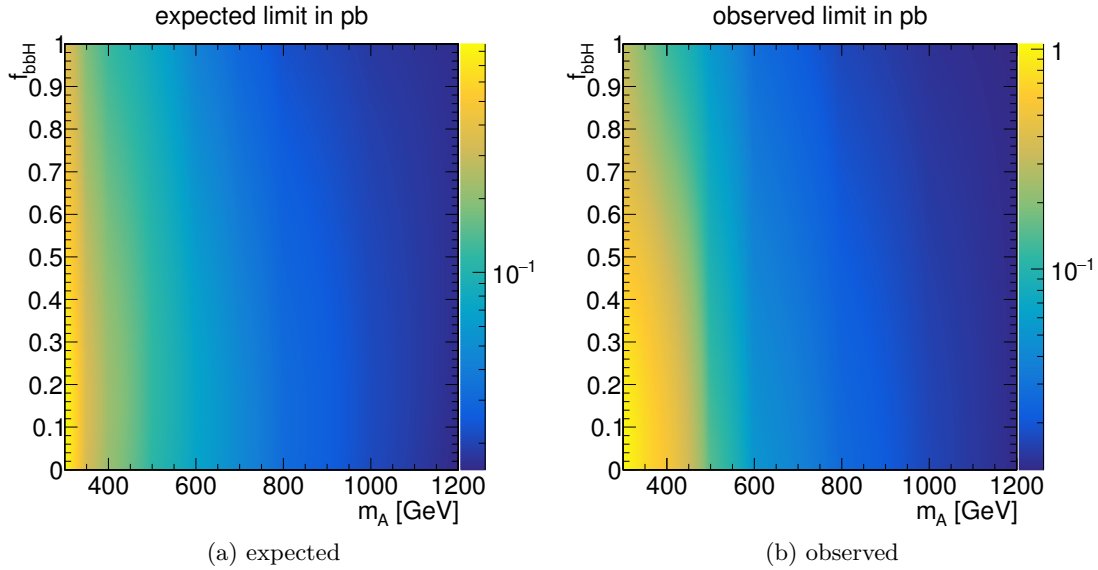


Figure 8.4: Exclusion limits on total cross section times $\tau\tau$ branching ratio in dependence of $m_{A/H}$ and the fraction of b -associated Higgs production f_{bbH} .

The individual cross section limits for gluon-gluon fusion and b -associated production, shown in Fig. 8.5, are the limits for $f_{\text{bbH}} = 0$ and $f_{\text{bbH}} = 1$ respectively.

For each point in the $m_A - \tan \beta$ parameter space of a benchmark scenario, the b -associated Higgs production fraction is calculated as:

$$f_{\text{bbH}}^{\text{benchmark}} = \frac{\sum_{\phi=A,H} \sigma(b\text{-assoc. } \phi) \text{BR}(\phi \rightarrow \tau\tau)}{\sum_{\phi=A,H} (\sigma(b\text{-assoc. } \phi) + \sigma(gg \rightarrow \phi)) \text{BR}(\phi \rightarrow \tau\tau)}.$$

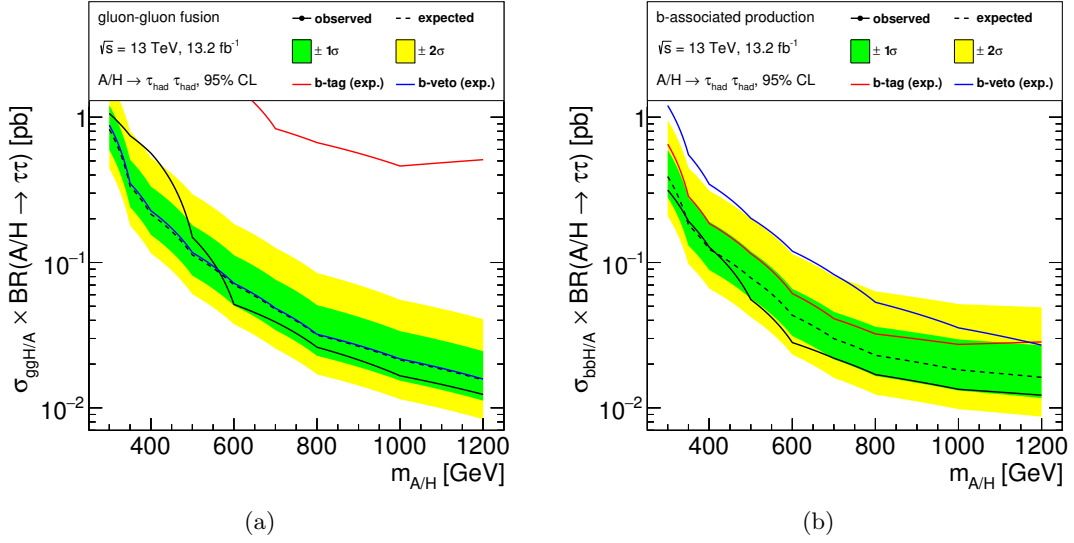


Figure 8.5: Upper limits at 95% confidence level on cross section times $\tau\tau$ branching ratio for gluon-gluon fusion (a) and b -associated Higgs production (b).

Then by comparing the limit at $m_{A/H} = m_A^{\text{benchmark}}$ and $f_{bbH} = f_{bbH}^{\text{benchmark}}$ to the benchmark cross section, it is determined whether that $(m_A, \tan\beta)$ is excluded. The limit in the $m_h^{\text{mod}+}$ scenario is shown in Fig. 8.6, overlaying the expected limits of the individually fitted b -tag and b -veto categories. Limits of the other benchmark scenarios considered in this search are displayed in Fig. 8.8. Some scenarios show increased sensitivity at low $\tan\beta$ between 300 GeV and 350 GeV, deviating from the otherwise mostly monotonic behavior. This is due to the increase of the gluon-gluon fusion cross section at low $\tan\beta$, in particular for $gg \rightarrow A$ at $m_{A/H} \sim 2m_{\text{top}}$ (cf. Sect. 2.3.3, Fig. 2.5). Not only is $\sigma(gg \rightarrow A)$ larger than $\sigma(gg \rightarrow H)$ near the $t\bar{t}$ threshold at tree level, but also it receives larger NLO QCD corrections [248].¹

In Fig. 8.7a the limit is compared to the ATLAS limit based on data corresponding to an integrated luminosity of 20 fb^{-1} recorded at $\sqrt{s} = 8 \text{ TeV}$ in 2012 [250] in the $m_h^{\text{mod}+}$ scenario.

The uncertainty of the cross section calculation in the benchmark scenarios is not included in the statistical model. A significant part of these uncertainties is already covered by the signal acceptance uncertainties determined by generator parameter variations. Instead, in Fig. 8.7b the impact of the theory uncertainties of the cross section calculation is visualized for the $m_h^{\text{mod}+}$ by overlaying the expected limits for a $\pm 1\sigma$ change in the cross section of the benchmark scenario.

¹The total angular momentum (J), charge (C) and parity (P) quantum numbers, J^{CP} , of the quark-antiquark pair in the gluon-gluon fusion loop have the allowed configurations 0^{++} , coupling to H , and 0^{+-} , coupling to A [249]. At the threshold, $t\bar{t}$ pairs can not have 0^{++} , while the 0^{+-} configuration results in a singular behavior, which is regularized by considering the decay width of the top quark.

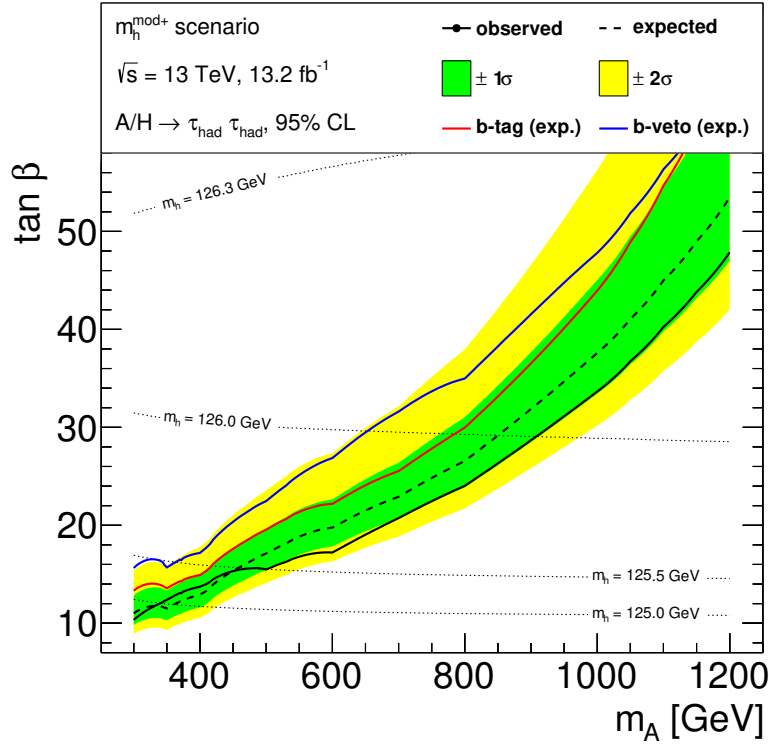


Figure 8.6: Upper limits at 95 % confidence level on $\tan \beta$ depending on m_A for the $m_h^{\text{mod}+}$ MSSM benchmark scenario.

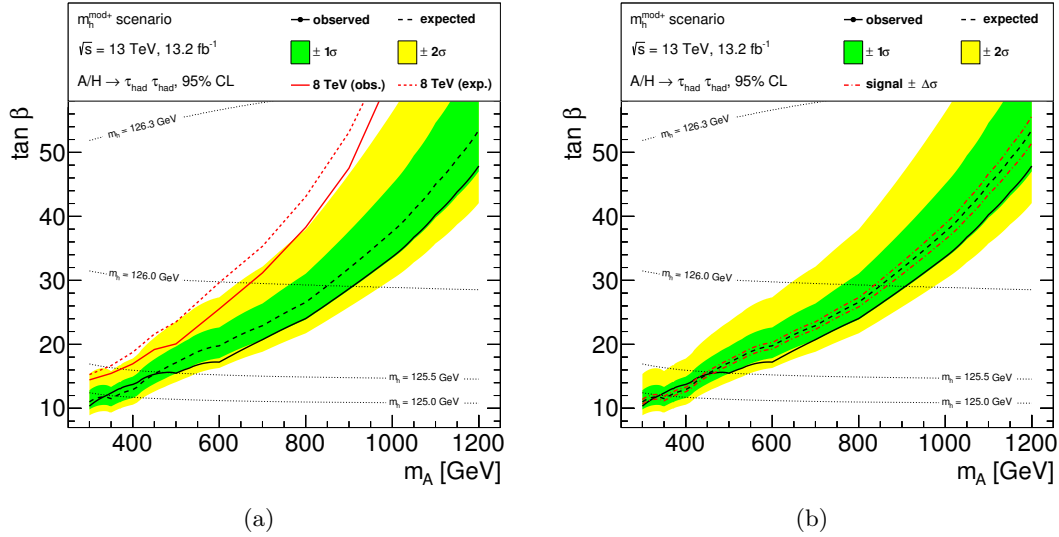


Figure 8.7: Upper limits at 95 % confidence level on $\tan \beta$ depending on m_A for the $m_h^{\text{mod}+}$ benchmark scenario, compared to the ATLAS result based on data corresponding to an integrated luminosity of 20 fb^{-1} recorded at $\sqrt{s} = 8 \text{ TeV}$ in 2012 [250] (a) and superimposed with the expected limits for a shift of the cross section by $\pm 1\sigma$ theoretical uncertainties.

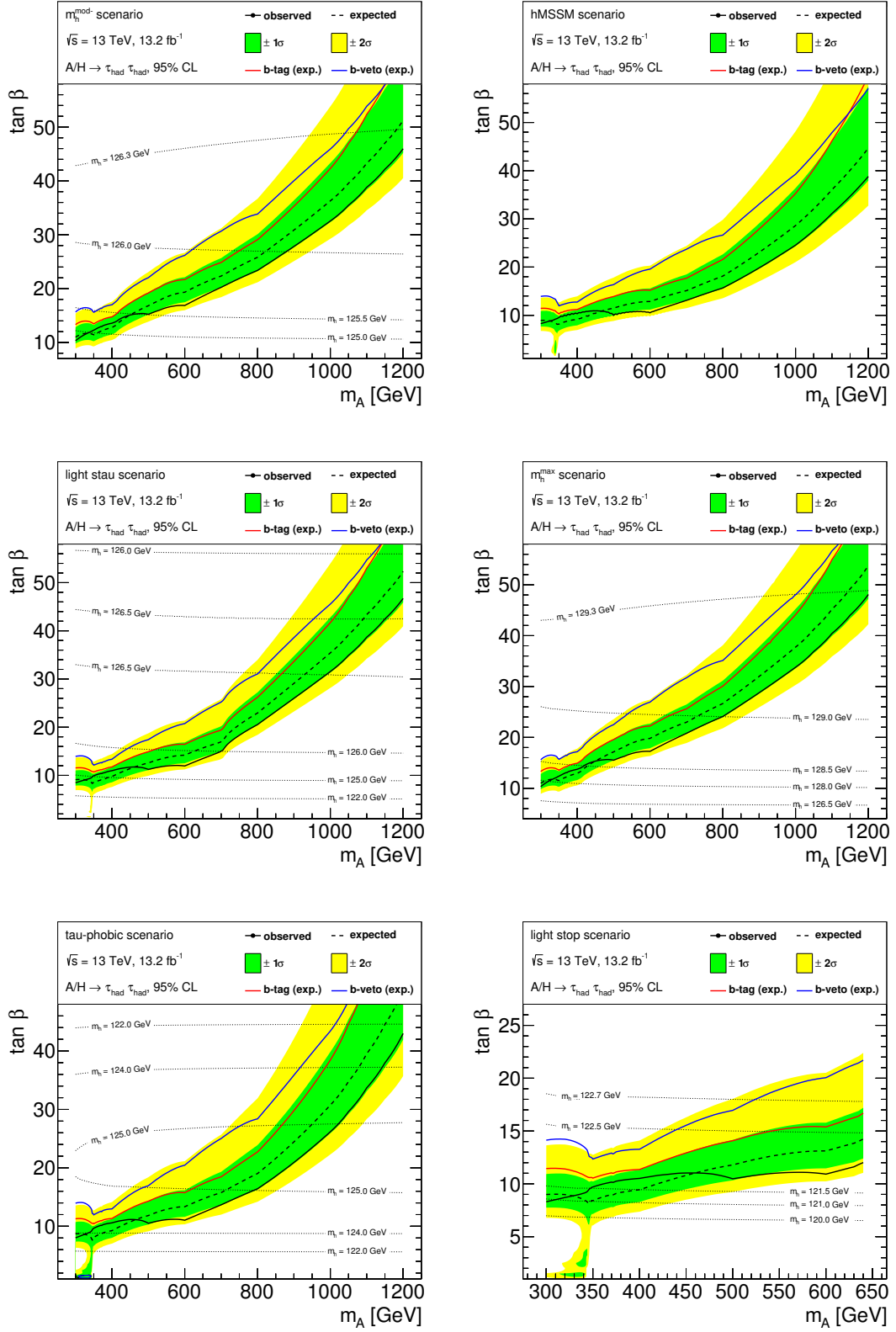


Figure 8.8: Upper limits at 95 % confidence level on $\tan \beta$ depending on m_A for various MSSM benchmark scenarios.

Chapter 9

Summary and Outlook

A search for heavy neutral MSSM Higgs bosons decaying into two hadronically decaying tau leptons is presented in this thesis. The MSSM is one of the most promising extensions of the SM, with the potential to resolve several inconsistencies of the SM and answer important open questions. In the search for this new model, the decay channel presented here is of key importance, with a sensitivity that covers large and important parts of the parameter space. No significant excess has been observed and thus CL_s exclusion limits have been set, both in specific benchmark scenarios as well as on the cross sections multiplied by the $\tau\tau$ branching ratio. In the exclusive search for Higgs produced by gluon-gluon fusion, these limits range from 1.1 pb at $m_{A/H} = 300$ GeV to 0.012 pb at 1.2 TeV. More stringent limits are set on the b -associated Higgs production, ranging from 0.31 pb to 0.012 pb.

Compared to the analysis of the LHC Run 1 data recorded by ATLAS, multiple improvements have been developed and implemented, in addition to extensive reoptimizations of selection and background estimation. The most significant enhancement is the categorization by the presence of b -tagged jets in the event, which is beneficial for the sensitivity to b -associated Higgs production. Furthermore, the measurement of $\tau_{\text{had-vis}}$ misidentification efficiencies was expanded by fake rates dedicated to $t\bar{t}$ and single top backgrounds and the calculation is more robust to control region contaminations. The limit calculation has been amended by less model dependent limits, set in the $m_{A/H} - f_{\text{bbH}}$ parameter space, which make it possible to set reliable limits in arbitrary benchmark scenarios even without access to the statistical model. Also, the mass range has been extended up to 1.2 TeV. As demonstrated in Fig. 8.7a, the new limit is significantly stronger for all considered mass hypotheses.

This search was combined with a similar search in the $\tau_{\text{lep}}\tau_{\text{had}}$ decay channel. Results of this combined analysis have been published at different stages of the development. First preliminary findings, based on data corresponding to 3.2 fb^{-1} integrated luminosity, were presented in December 2015 [208]. Despite still lacking the b -tag categorization, the limits already surpassed the earlier results at Higgs masses above 700 GeV. The

same data set was reanalyzed with several improvements, including b -tag categorization, resulting in limits that are stronger than the ATLAS results at $\sqrt{s} = 8$ TeV in the full considered mass range. It was published in August 2016 [209]. Finally, a further refined search with additional data was presented at the ICHEP conference in August 2016 [251], which, apart from an improvement of the fake rate method with minor impact, reflects the state of the analysis presented in this thesis. As shown in Fig. 9.1, the $\tau_{\text{had}}\tau_{\text{had}}$ search channel dominates the combined sensitivity in most of the mass range, especially at high m_A .

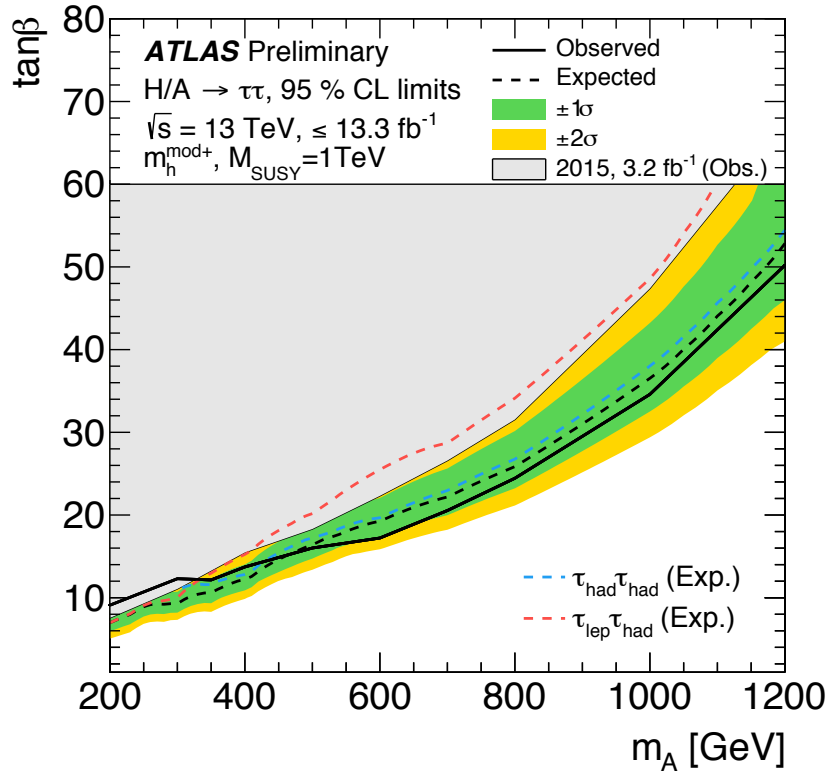


Figure 9.1: The 95 % CL limits on $\tan\beta$ in dependence of m_A for the $m_h^{\text{mod}+}$ benchmark scenario for a combination of the $\tau_{\text{lep}}\tau_{\text{had}}$ and $\tau_{\text{had}}\tau_{\text{had}}$ search channels. [251]

The CMS collaboration also presented preliminary results of a similar search in November 2016 [252]. The expected $\tau_{\text{had}}\tau_{\text{had}}$ exclusion limits obtained by CMS, shown in Fig. 9.2, are a bit less strong than the limits presented in this thesis, besides for the 300 GeV point for gluon-gluon fusion. However, the difference between the expected limits is approximately within the 1σ uncertainty band. CMS provides cross section limits up to 3.2 TeV. For the analysis presented here, no signal samples for masses above 1.2 TeV were generated, as the corresponding limits in the MSSM parameter space would be at $\tan\beta > 60$, which is disfavored [248]. Furthermore, at very high mass there is not much gain in a cross section limit, as the signal becomes concentrated in the last bin of the mass discriminant. As the CMS analysis uses signal event samples generated at leading order, their production cost is smaller than for the ATLAS analysis. By

using a different trigger strategy, the search presented by CMS manages to set limits down to $m_{A/H} = 90$ GeV.

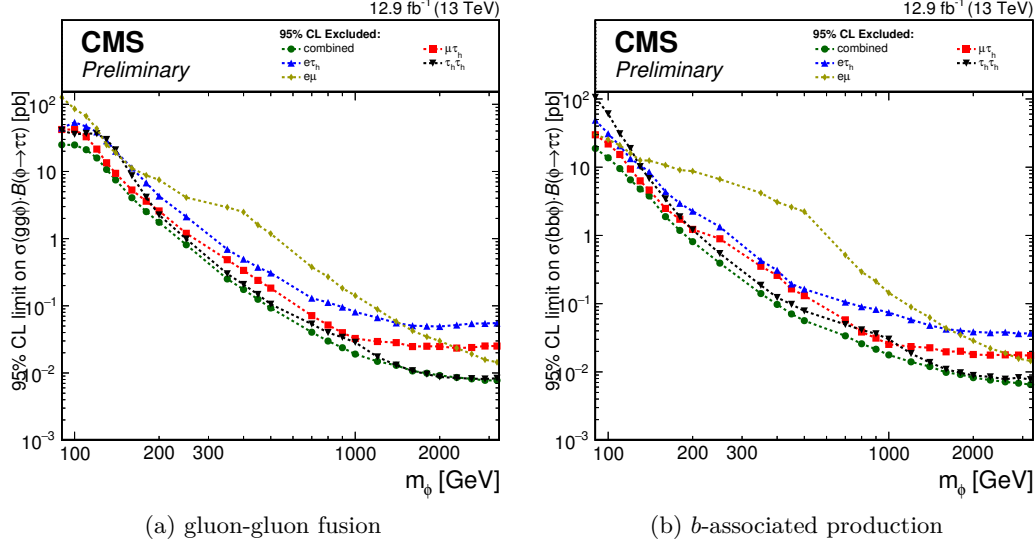


Figure 9.2: Expected exclusion limits at 95 % CL for gluon-gluon fusion and b -associated Higgs production signal processes, based on data recorded at $\sqrt{s} = 13$ TeV by the CMS detector corresponding to an integrated luminosity of 12.9 fb^{-1} . [252]

The search at ATLAS is being updated with the data recorded in the second half of 2016. More improvements, including a final discriminant based on machine learning and the estimation of backgrounds involving misidentified $\tau_{\text{had-vis}}$ based on a multivariate predictor of the jet flavor (initiated by a light quark or a gluon), are in development. The currently available data amounts to less than 1 % of the expectation of the operation of the LHC (including its planned high luminosity upgrade). An estimate of the sensitivity in the hMSSM parameter space with an integrated luminosity of 300 fb^{-1} is shown in Fig. 9.3 [89]. According to this, the $\tau\tau$ search channel will be able to probe the complete $\tan\beta \gtrsim 14$ region for $m_A < 1$ TeV and any $\tan\beta$ value below ≈ 350 GeV. The techniques developed in this thesis will be the basis for further exploration of the MSSM parameter space. The $\tau^+\tau^-$ decay channel will continue to be one of the most important options to discover additional Higgs bosons at the LHC.

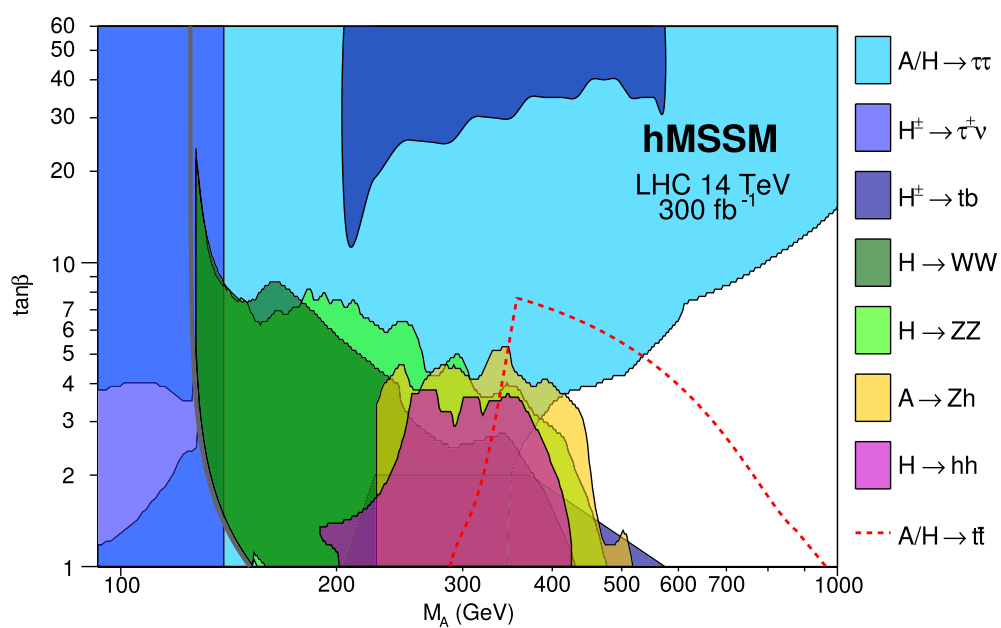


Figure 9.3: Extrapolated expected 2σ sensitivity in the hMSSM benchmark scenario for a combination of the main search channels at the LHC, for an integrated luminosity of 300 fb^{-1} recorded at $\sqrt{s} = 14 \text{ TeV}$ [89].

Appendix A

Additional Signal Region Variable Distributions

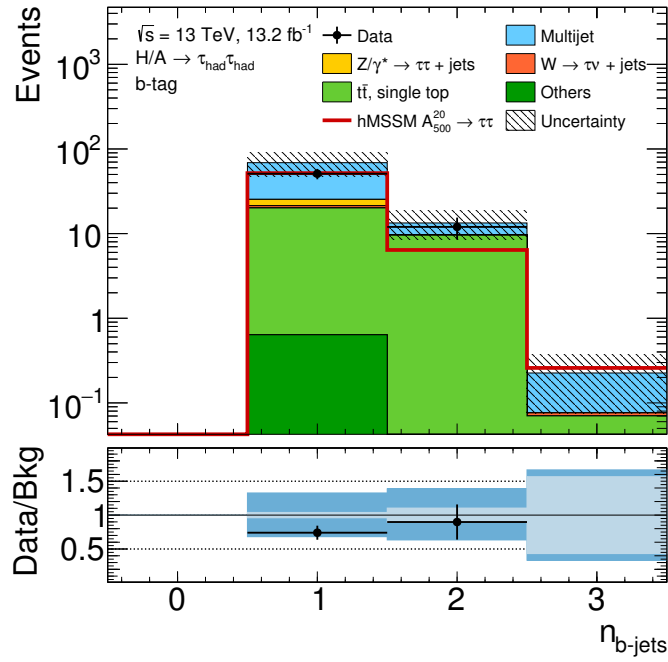


Figure A.1: Distribution of the number of b -tagged jets in the b -tag category signal region. The light blue band in the ratio plot at the bottom visualizes the statistical uncertainty of the combined background estimation, while the darker blue band also includes the systematic uncertainties described in Chapter 7.

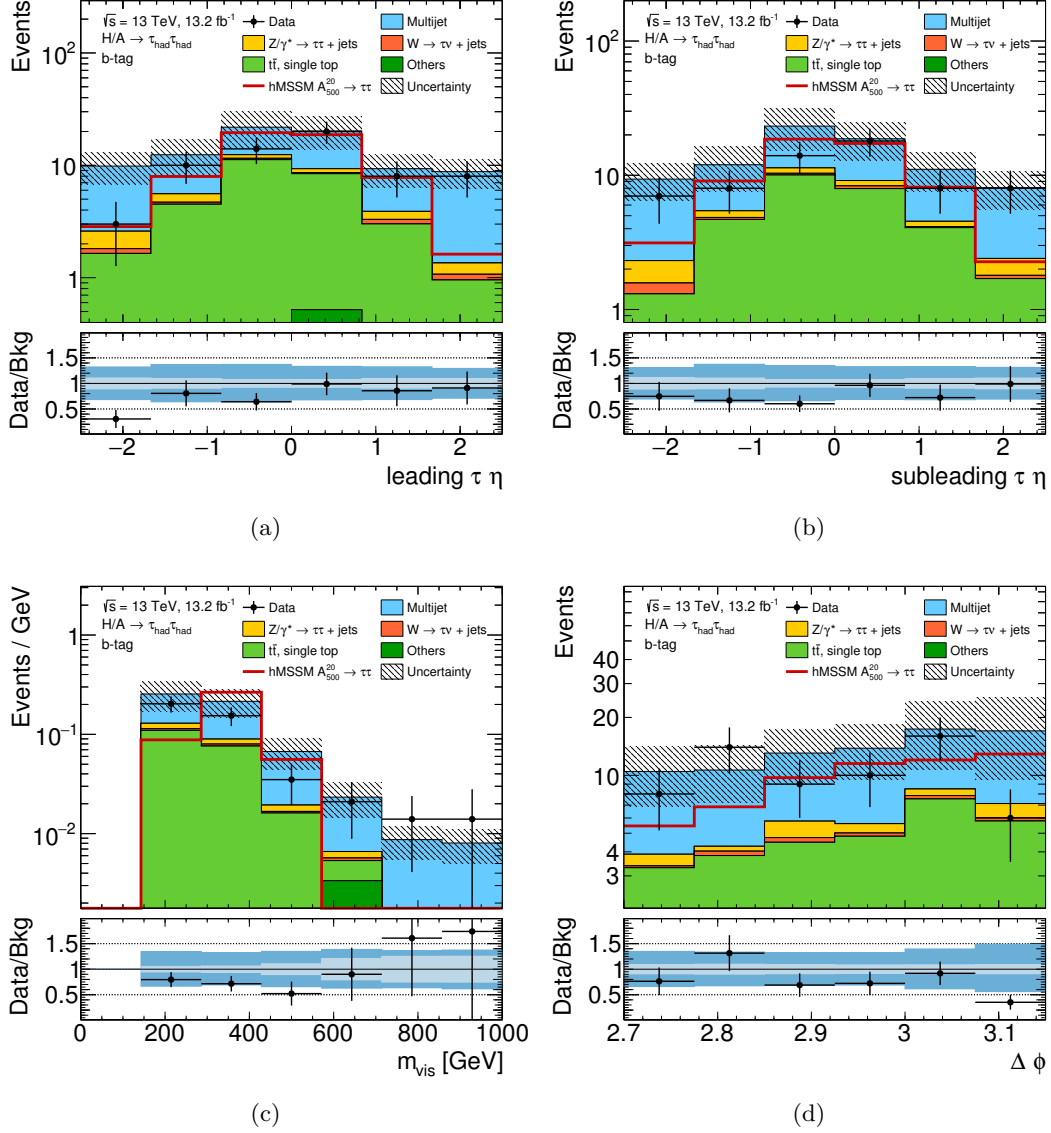


Figure A.2: Variable distributions in the b -tag category signal region: (a) Leading $\tau_{\text{had-vis}} \eta$, (b) Subleading $\tau_{\text{had-vis}} \eta$, (c) m_{vis} , (d) $\Delta\phi(\tau_1, \tau_2)$. The light blue band in the ratio plot at the bottom visualizes the statistical uncertainty of the combined background estimation, while the darker blue band also includes the systematic uncertainties described in Chapter 7.

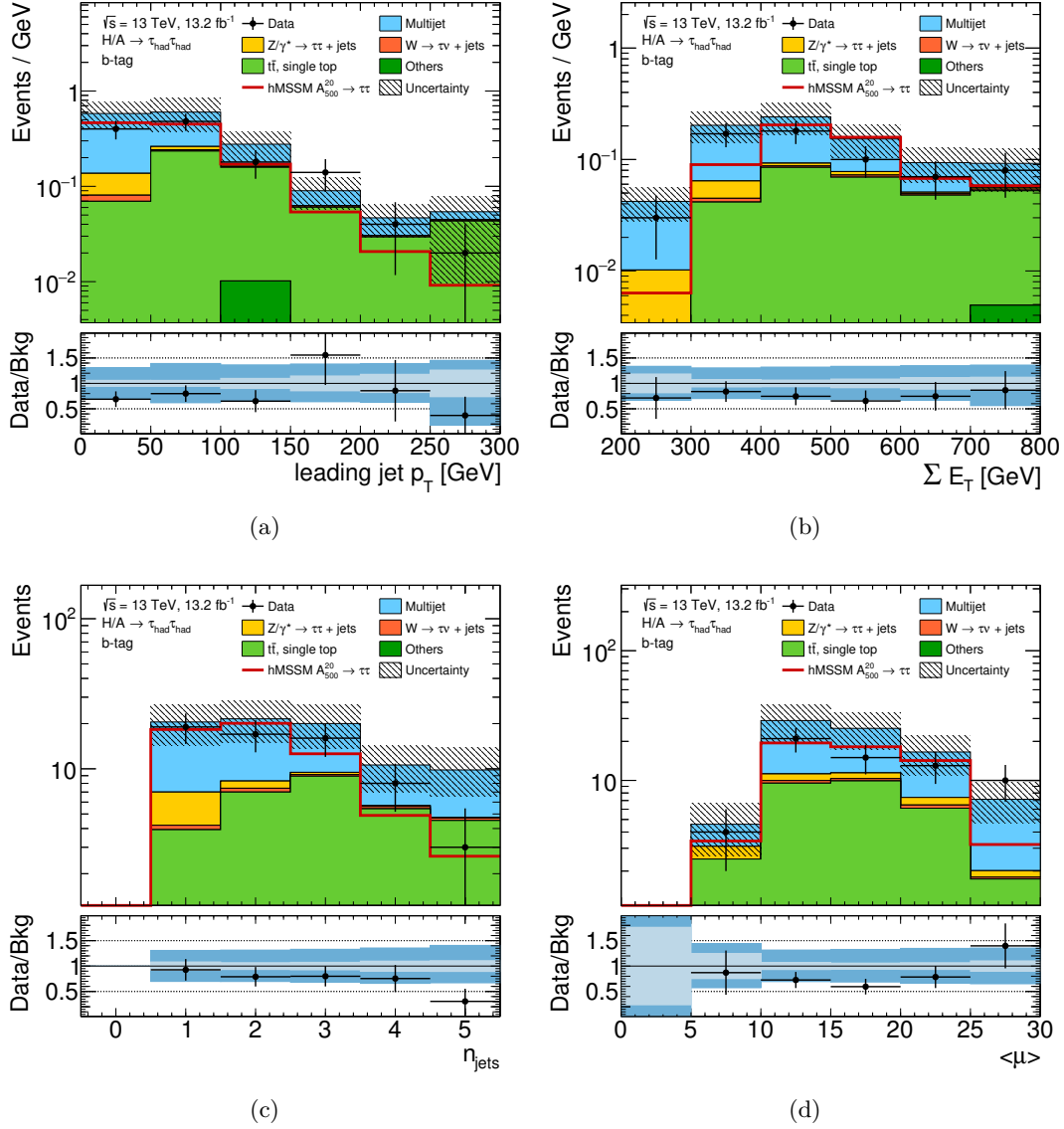


Figure A.3: Variable distributions in the b -tag category signal region: (a) Leading jet p_T , (b) scalar sum of transverse energy, (c) number of jets, (d) average number of interactions per bunch crossing. The light blue band in the ratio plot at the bottom visualizes the statistical uncertainty of the combined background estimation, while the darker blue band also includes the systematic uncertainties described in Chapter 7.

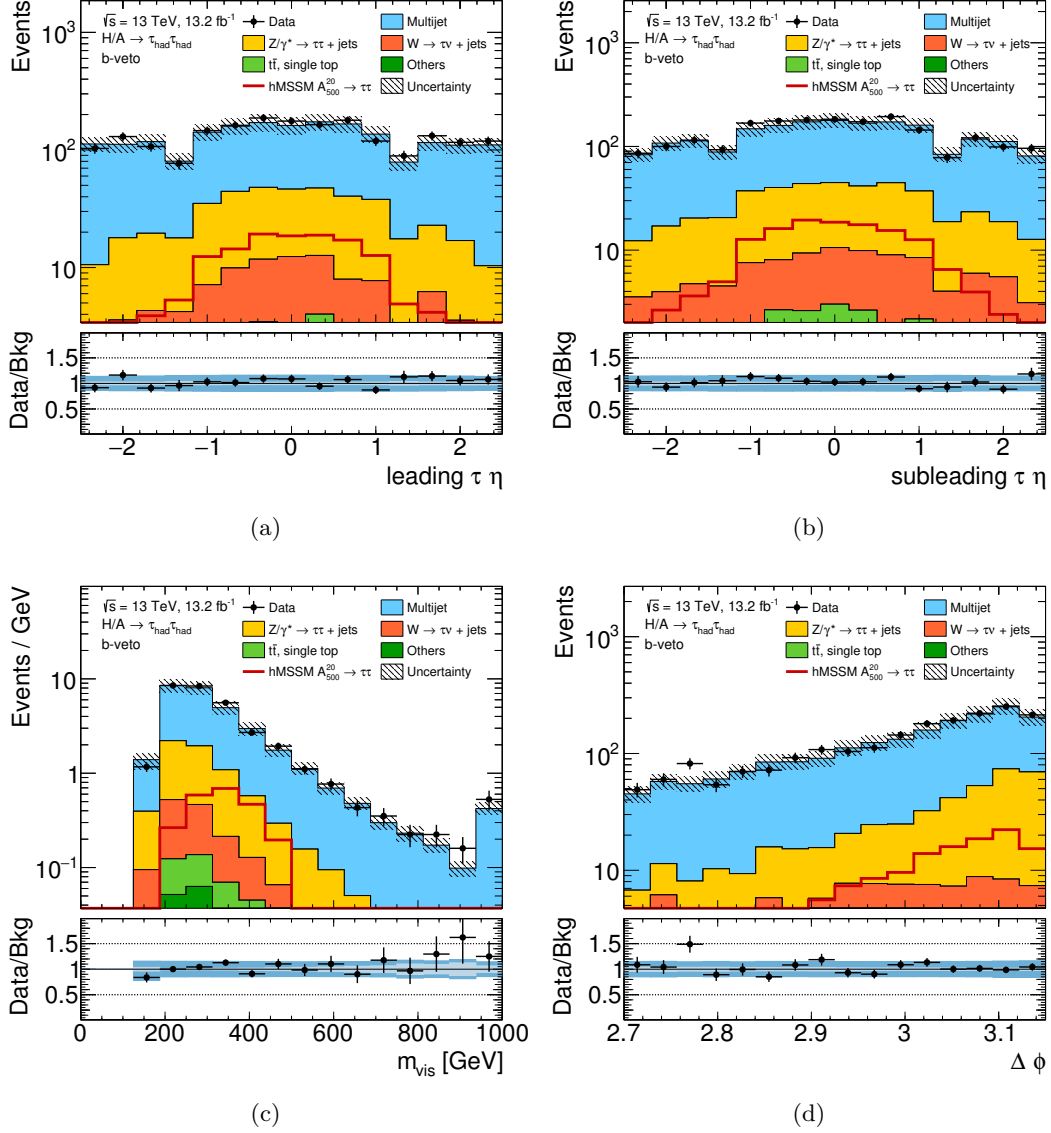


Figure A.4: Variable distributions in the b -veto category signal region: (a) Leading $\tau_{\text{had-vis}} \eta$, (b) Subleading $\tau_{\text{had-vis}} \eta$, (c) m_{vis} , (d) $\Delta\phi(\tau_1, \tau_2)$. The light blue band in the ratio plot at the bottom visualizes the statistical uncertainty of the combined background estimation, while the darker blue band also includes the systematic uncertainties described in Chapter 7.

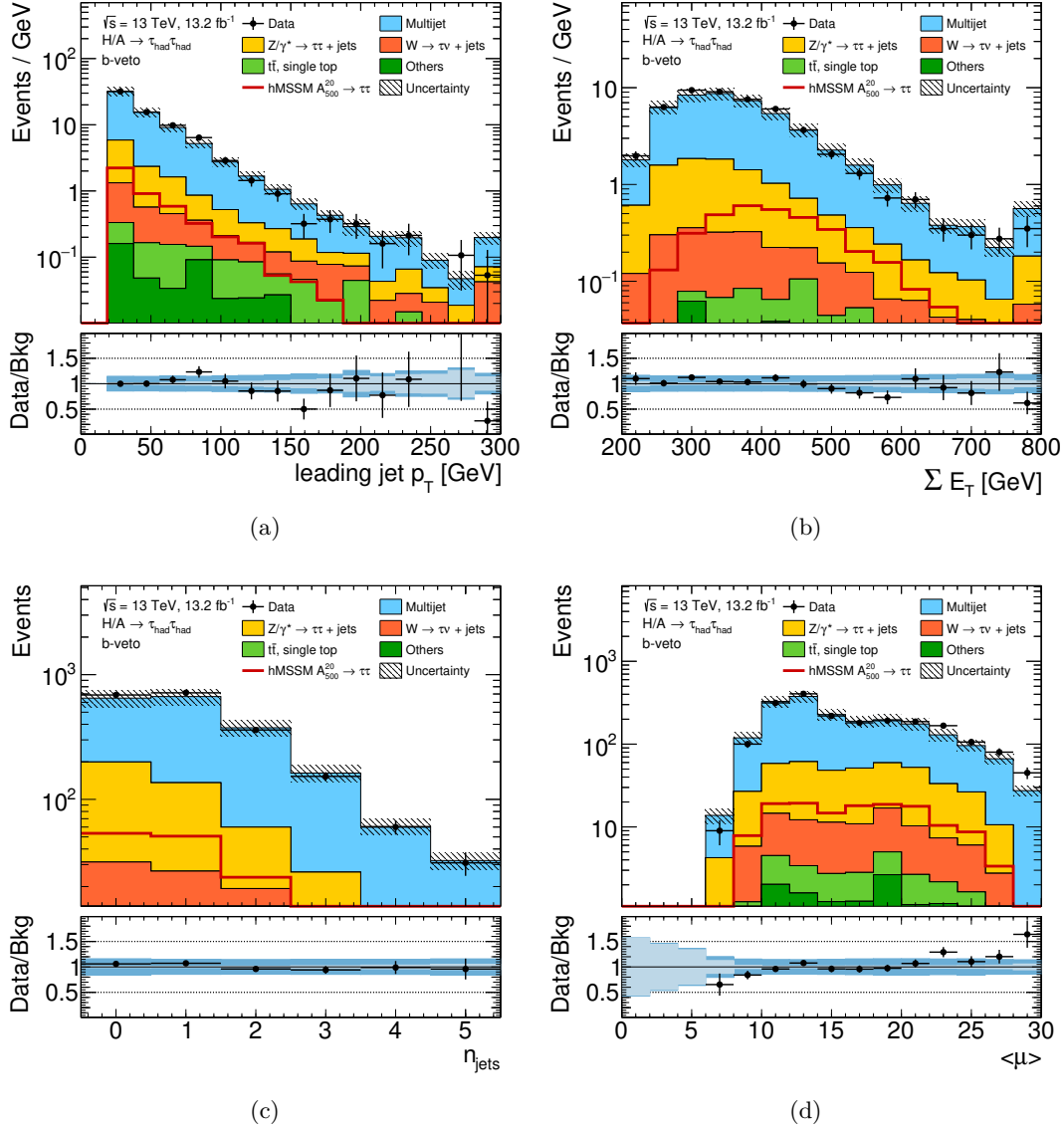


Figure A.5: Variable distributions in the b -veto category signal region: (a) Leading jet p_T , (b) scalar sum of transverse energy, (c) number of jets, (d) average number of interactions per bunch crossing. The light blue band in the ratio plot at the bottom visualizes the statistical uncertainty of the combined background estimation, while the darker blue band also includes the systematic uncertainties described in Chapter 7.

Appendix B

Nuisance Parameter Rankings

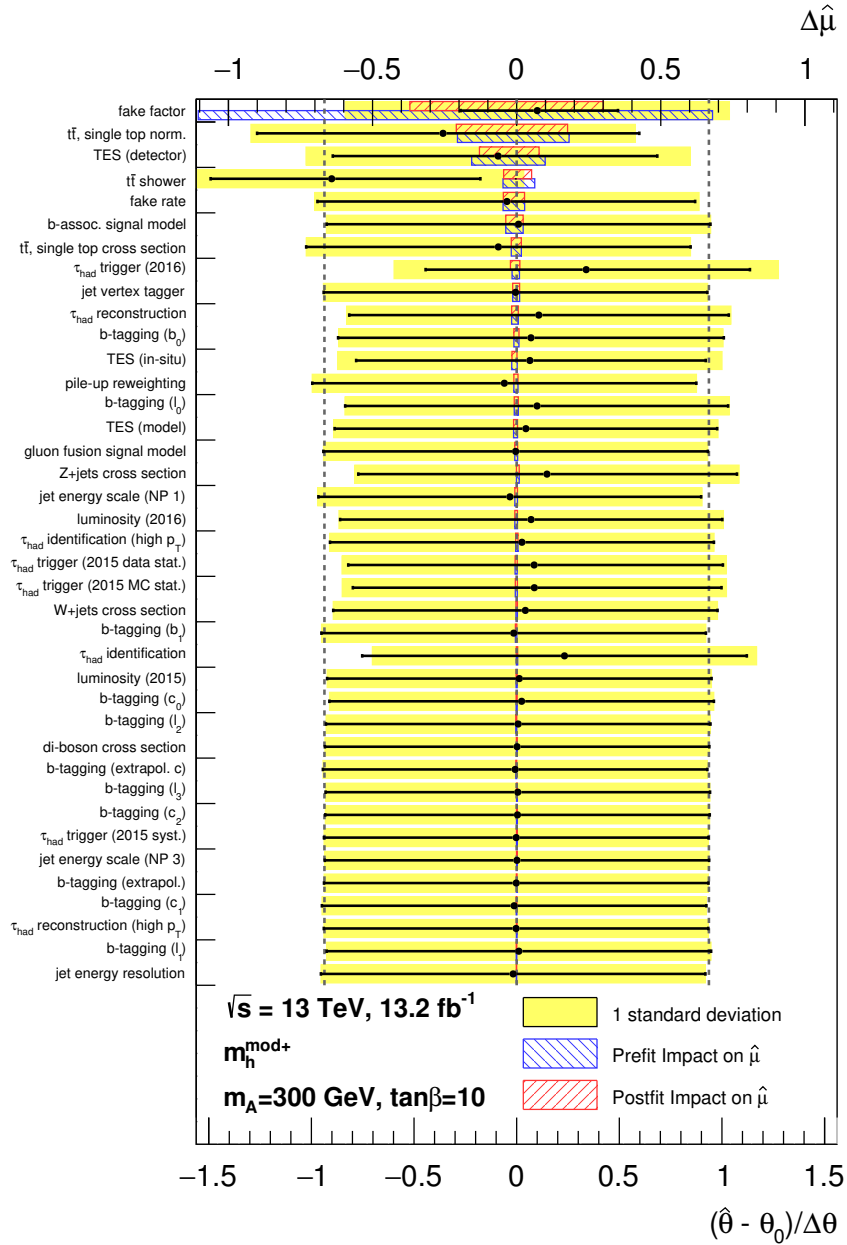


Figure B.1: Impact of the systematic uncertainties on the fitted signal strength and variations of the nuisance parameters from their nominal values in units of their uncertainty values for $m_{A/H} = 300 \text{ GeV}$ in the $m_h^{\text{mod}+}$ MSSM benchmark scenario.

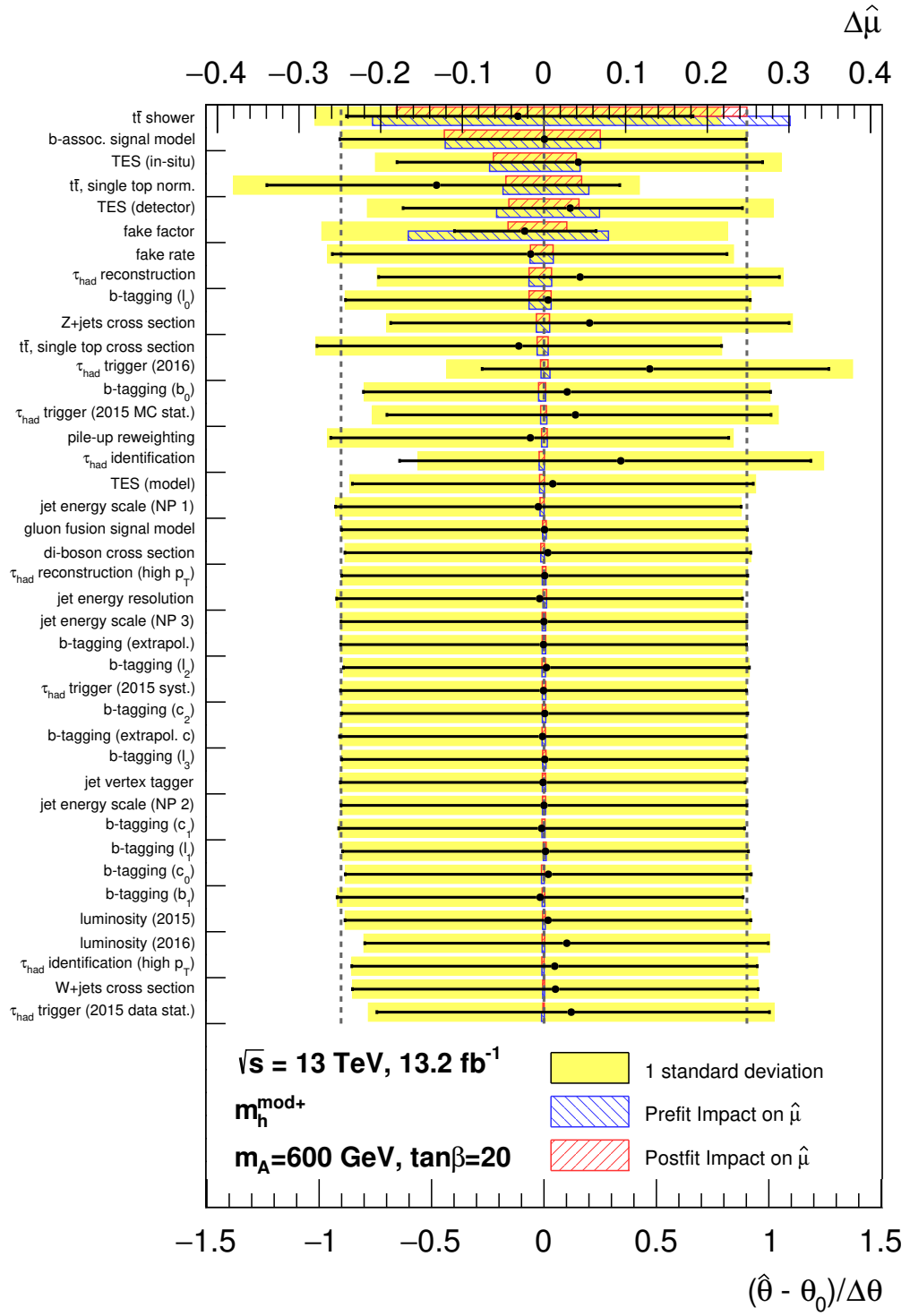


Figure B.2: Impact of the systematic uncertainties on the fitted signal strength and variations of the nuisance parameters from their nominal values in units of their uncertainty values for $m_{A/H} = 600 \text{ GeV}$ in the $m_h^{\text{mod+}}$ MSSM benchmark scenario.

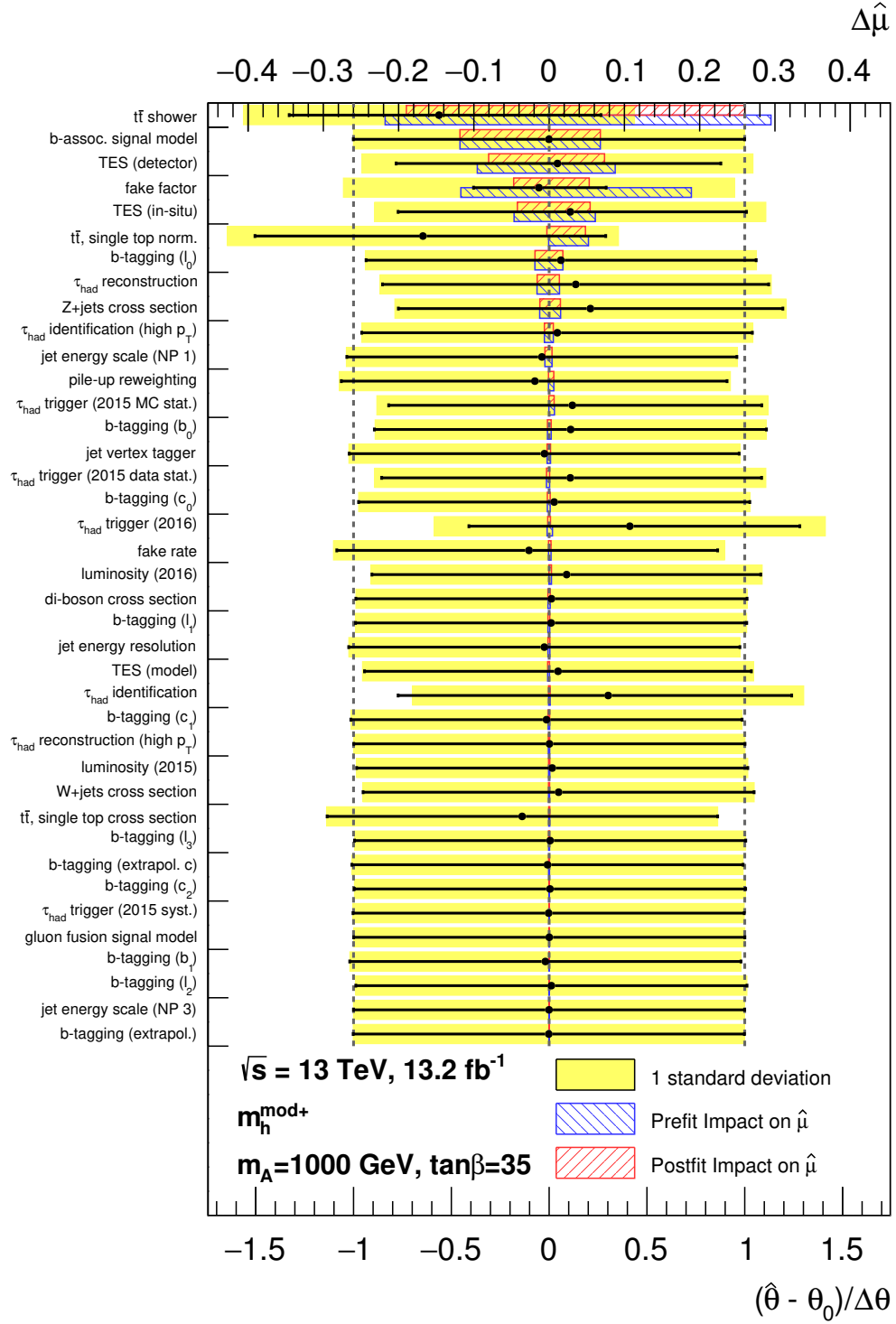


Figure B.3: Impact of the systematic uncertainties on the fitted signal strength and variations of the nuisance parameters from their nominal values in units of their uncertainty values for $m_{A/H} = 1000$ GeV in the $m_h^{\text{mod+}}$ MSSM benchmark scenario.

Appendix C

Limit Tables

$m_{A/H}$ [GeV]	f_{bbH}	obs.	exp.	+2 σ	+1 σ	-1 σ	-2 σ
300	0.0	1.1	0.83	1.8	1.2	0.59	0.44
	0.1	1.0	0.87	1.9	1.3	0.63	0.47
	0.2	0.95	0.86	1.8	1.2	0.62	0.46
	0.3	0.84	0.80	1.7	1.2	0.58	0.43
	0.4	0.72	0.73	1.6	1.1	0.53	0.39
	0.5	0.62	0.66	1.5	0.98	0.48	0.35
	0.6	0.53	0.59	1.4	0.88	0.43	0.32
	0.7	0.46	0.53	1.2	0.80	0.38	0.28
	0.8	0.40	0.48	1.1	0.72	0.34	0.26
	0.9	0.35	0.43	1.0	0.65	0.31	0.23
	1.0	0.31	0.39	0.95	0.59	0.28	0.21
350	0.0	0.75	0.33	0.80	0.51	0.24	0.18
	0.1	0.75	0.35	0.83	0.53	0.25	0.19
	0.2	0.71	0.35	0.82	0.53	0.25	0.19
	0.3	0.65	0.34	0.78	0.51	0.24	0.18
	0.4	0.57	0.31	0.73	0.47	0.23	0.17
	0.5	0.49	0.29	0.68	0.44	0.21	0.16
	0.6	0.41	0.26	0.63	0.40	0.19	0.14
	0.7	0.33	0.24	0.58	0.37	0.17	0.13
	0.8	0.27	0.22	0.53	0.33	0.16	0.12
	0.9	0.23	0.20	0.49	0.30	0.14	0.11
	1.0	0.19	0.18	0.45	0.28	0.13	0.097
400	0.0	0.57	0.22	0.53	0.33	0.16	0.12
	0.1	0.55	0.22	0.54	0.34	0.16	0.12
	0.2	0.51	0.22	0.54	0.34	0.16	0.12
	0.3	0.46	0.22	0.52	0.33	0.16	0.12
	0.4	0.41	0.20	0.49	0.31	0.15	0.11
	0.5	0.34	0.19	0.46	0.29	0.14	0.10
	0.6	0.28	0.18	0.43	0.27	0.13	0.094
	0.7	0.22	0.16	0.40	0.25	0.12	0.086
	0.8	0.18	0.15	0.37	0.23	0.11	0.079
	0.9	0.15	0.13	0.34	0.21	0.097	0.072
	1.0	0.13	0.12	0.31	0.19	0.089	0.066
500	0.0	0.15	0.11	0.29	0.18	0.081	0.060
	0.1	0.14	0.12	0.30	0.19	0.084	0.063
	0.2	0.13	0.12	0.30	0.19	0.085	0.064
	0.3	0.11	0.12	0.30	0.18	0.085	0.063
	0.4	0.10	0.11	0.28	0.18	0.083	0.062
	0.5	0.093	0.11	0.27	0.17	0.079	0.059
	0.6	0.083	0.10	0.26	0.16	0.075	0.056
	0.7	0.075	0.098	0.25	0.15	0.070	0.052
	0.8	0.068	0.091	0.23	0.14	0.066	0.049
	0.9	0.061	0.085	0.22	0.13	0.061	0.045
	1.0	0.056	0.078	0.20	0.12	0.056	0.042

Table C.1: Limit on $(\sigma(\text{bassoc.}A/H) + \sigma(gg \rightarrow A/H)) \times \text{BR}(A/H \rightarrow \tau\tau)$ in pb for Higgs masses up to 500 GeV and different fractions of b -associated production f_{bbH} .

$m_{A/H}$ [GeV]	f_{bbH}	obs.	exp.	$+2\sigma$	$+1\sigma$	-1σ	-2σ
600	0.0	0.051	0.070	0.18	0.11	0.051	0.038
	0.1	0.050	0.072	0.19	0.11	0.052	0.038
	0.2	0.047	0.071	0.18	0.11	0.051	0.038
	0.3	0.045	0.069	0.18	0.11	0.050	0.037
	0.4	0.042	0.066	0.17	0.10	0.048	0.036
	0.5	0.039	0.063	0.16	0.096	0.045	0.034
	0.6	0.037	0.059	0.15	0.090	0.042	0.032
	0.7	0.034	0.055	0.14	0.083	0.039	0.029
	0.8	0.032	0.051	0.13	0.077	0.037	0.027
	0.9	0.030	0.047	0.12	0.071	0.034	0.025
	1.0	0.028	0.043	0.11	0.066	0.031	0.023
700	0.0	0.039	0.048	0.13	0.076	0.034	0.026
	0.1	0.038	0.048	0.13	0.077	0.035	0.026
	0.2	0.036	0.047	0.12	0.075	0.034	0.025
	0.3	0.034	0.046	0.12	0.072	0.033	0.025
	0.4	0.032	0.044	0.11	0.069	0.032	0.024
	0.5	0.030	0.042	0.11	0.065	0.030	0.022
	0.6	0.029	0.039	0.10	0.061	0.028	0.021
	0.7	0.027	0.037	0.097	0.057	0.027	0.020
	0.8	0.025	0.034	0.092	0.053	0.025	0.018
	0.9	0.023	0.032	0.086	0.049	0.023	0.017
	1.0	0.022	0.030	0.081	0.046	0.022	0.016
800	0.0	0.026	0.032	0.085	0.051	0.023	0.017
	0.1	0.026	0.032	0.085	0.051	0.023	0.017
	0.2	0.025	0.032	0.083	0.051	0.023	0.017
	0.3	0.024	0.031	0.081	0.049	0.022	0.017
	0.4	0.023	0.030	0.078	0.048	0.022	0.016
	0.5	0.022	0.029	0.076	0.046	0.021	0.016
	0.6	0.021	0.028	0.073	0.044	0.020	0.015
	0.7	0.020	0.027	0.071	0.042	0.019	0.014
	0.8	0.019	0.026	0.068	0.040	0.018	0.014
	0.9	0.018	0.024	0.066	0.038	0.017	0.013
	1.0	0.017	0.023	0.063	0.036	0.017	0.012
1000	0.0	0.017	0.021	0.055	0.034	0.015	0.011
	0.1	0.017	0.022	0.056	0.034	0.016	0.012
	0.2	0.016	0.022	0.055	0.034	0.016	0.012
	0.3	0.016	0.022	0.055	0.034	0.016	0.012
	0.4	0.016	0.021	0.054	0.033	0.015	0.011
	0.5	0.015	0.021	0.054	0.033	0.015	0.011
	0.6	0.015	0.020	0.054	0.032	0.015	0.011
	0.7	0.015	0.020	0.054	0.032	0.014	0.011
	0.8	0.014	0.019	0.053	0.031	0.014	0.010
	0.9	0.014	0.019	0.053	0.031	0.014	0.010
	1.0	0.013	0.018	0.052	0.030	0.013	0.0098
1200	0.0	0.012	0.016	0.041	0.025	0.011	0.0083
	0.1	0.012	0.016	0.041	0.025	0.011	0.0085
	0.2	0.012	0.016	0.042	0.025	0.012	0.0087
	0.3	0.013	0.016	0.042	0.026	0.012	0.0087
	0.4	0.013	0.016	0.043	0.026	0.012	0.0088
	0.5	0.012	0.016	0.043	0.026	0.012	0.0088
	0.6	0.012	0.016	0.044	0.026	0.012	0.0089
	0.7	0.012	0.017	0.045	0.027	0.012	0.0089
	0.8	0.012	0.016	0.047	0.027	0.012	0.0088
	0.9	0.012	0.016	0.048	0.027	0.012	0.0088
	1.0	0.012	0.016	0.049	0.027	0.012	0.0087

Table C.2: Limit on $(\sigma(b\text{assoc.}A/H) + \sigma(gg \rightarrow A/H)) \times \text{BR}(A/H \rightarrow \tau\tau)$ in pb for Higgs masses above 500 GeV and different fractions of b -associated production f_{bbH} .

Appendix D

Implementation Details

This chapter contains details on the configuration of ATLAS internal software used for the study presented in this thesis.

Good Runs Lists

`data15_13TeV.periodAllYear_DetStatus-v79-repro20-02_DQDefects-00-02-02_PHYS_StandardGRL_All_Good_25ns`
`data16_13TeV.periodAllYear_DetStatus-v80-pro20-08_DQDefects-00-02-02_PHYS_StandardGRL_All_Good_25ns`

Luminosity Tag

`Of1Lumi-13TeV-005`

Trigger Names

`HLT_tau80_medium1_tracktwo_L1TAU60`
`HLT_tau125_medium1_tracktwo`
`HLT_tau25_medium1_tracktwo`

Analysis Software Tags

`AnalysisBase 2.4.16`
`Asg_Lhapdf-06-01-05-01`
`PMGTools-00-00-01`

ATLAS Event Samples

The following pages have tables with the ATLAS event samples used for this thesis. They are listed with their production tag, cross section, σ , filter efficiency, ϵ_{filter} , the k -factor and the number of events, n_{events} . The background event samples were further processed by the ATLAS Derivation Framework, using the production tag `p2666` and the `HIGG4D2` and `HIGG4D4` derivations.

D. Implementation Details

ATLAS event sample identifier	$Z/\gamma^*(\rightarrow e e)+\text{jets}$	production tags	$\sigma[\text{pb}]$	filter	k	N_{events}
mc15_13TeV.361106.PowhegPythia8EvtGen_AZNLOCTEQ6L1_Zee	e3601_s2576_s2132_r7725_r7676	1.90 × 10 ³	1.00 × 10 ⁰	1.00	79 045 597	
mc15_13TeV.301000.PowhegPythia8EvtGen_AZNLOCTEQ6L1_DYee_120M180	e3649_s2576_s2132_r7772_r7676	1.75 × 10 ¹	1.00 × 10 ⁰	1.00	498 000	
mc15_13TeV.301001.PowhegPythia8EvtGen_AZNLOCTEQ6L1_DYee_180M250	e3649_s2576_s2132_r7772_r7676	2.92 × 10 ⁰	1.00 × 10 ⁰	1.00	249 600	
mc15_13TeV.301002.PowhegPythia8EvtGen_AZNLOCTEQ6L1_DYee_250M400	e3649_s2576_s2132_r7772_r7676	1.08 × 10 ⁰	1.00 × 10 ⁰	1.00	149 400	
mc15_13TeV.301003.PowhegPythia8EvtGen_AZNLOCTEQ6L1_DYee_400M600	e3649_s2576_s2132_r7772_r7676	1.96 × 10 ⁻¹	1.00 × 10 ⁰	1.00	100 000	
mc15_13TeV.301004.PowhegPythia8EvtGen_AZNLOCTEQ6L1_DYee_600M800	e3649_s2576_s2132_r7772_r7676	3.74 × 10 ⁻²	1.00 × 10 ⁰	1.00	145 000	
mc15_13TeV.301005.PowhegPythia8EvtGen_AZNLOCTEQ6L1_DYee_800M1000	e3649_s2576_s2132_r7772_r7676	1.06 × 10 ⁻²	1.00 × 10 ⁰	1.00	50 000	
mc15_13TeV.301006.PowhegPythia8EvtGen_AZNLOCTEQ6L1_DYee_1000M1250	e3649_s2576_s2132_r7772_r7676	4.26 × 10 ⁻³	1.00 × 10 ⁰	1.00	50 000	
mc15_13TeV.301007.PowhegPythia8EvtGen_AZNLOCTEQ6L1_DYee_1250M1500	e3649_s2576_s2132_r7772_r7676	1.42 × 10 ⁻³	1.00 × 10 ⁰	1.00	50 000	
mc15_13TeV.301008.PowhegPythia8EvtGen_AZNLOCTEQ6L1_DYee_1500M1750	e3649_s2576_s2132_r7772_r7676	5.45 × 10 ⁻⁴	1.00 × 10 ⁰	1.00	49 800	
mc15_13TeV.301009.PowhegPythia8EvtGen_AZNLOCTEQ6L1_DYee_1750M2000	e3649_s2576_s2132_r7772_r7676	2.30 × 10 ⁻⁴	1.00 × 10 ⁰	1.00	53 400	
mc15_13TeV.301010.PowhegPythia8EvtGen_AZNLOCTEQ6L1_DYee_2000M2250	e3649_s2576_s2132_r7772_r7676	1.04 × 10 ⁻⁴	1.00 × 10 ⁰	1.00	50 000	
mc15_13TeV.301011.PowhegPythia8EvtGen_AZNLOCTEQ6L1_DYee_2250M2500	e3649_s2576_s2132_r7772_r7676	4.94 × 10 ⁻⁵	1.00 × 10 ⁰	1.00	50 000	
mc15_13TeV.301012.PowhegPythia8EvtGen_AZNLOCTEQ6L1_DYee_2500M2750	e3649_s2576_s2132_r7772_r7676	2.45 × 10 ⁻⁵	1.00 × 10 ⁰	1.00	50 000	
mc15_13TeV.301013.PowhegPythia8EvtGen_AZNLOCTEQ6L1_DYee_2750M3000	e3649_s2576_s2132_r7772_r7676	1.25 × 10 ⁻⁵	1.00 × 10 ⁰	1.00	47 800	
mc15_13TeV.301014.PowhegPythia8EvtGen_AZNLOCTEQ6L1_DYee_3000M3500	e3649_s2576_s2132_r7772_r7676	1.00 × 10 ⁻⁵	1.00 × 10 ⁰	1.00	48 600	
mc15_13TeV.301015.PowhegPythia8EvtGen_AZNLOCTEQ6L1_DYee_3500M4000	e3649_s2576_s2132_r7772_r7676	2.93 × 10 ⁻⁶	1.00 × 10 ⁰	1.00	47 600	
mc15_13TeV.301016.PowhegPythia8EvtGen_AZNLOCTEQ6L1_DYee_4000M4500	e3649_s2576_s2132_r7772_r7676	8.98 × 10 ⁻⁷	1.00 × 10 ⁰	1.00	48 000	
mc15_13TeV.301017.PowhegPythia8EvtGen_AZNLOCTEQ6L1_DYee_4500M5000	e3649_s2576_s2132_r7772_r7676	2.81 × 10 ⁻⁷	1.00 × 10 ⁰	1.00	93 000	
mc15_13TeV.301018.PowhegPythia8EvtGen_AZNLOCTEQ6L1_DYee_5000M1	e3649_s2576_s2132_r7772_r7676	1.26 × 10 ⁻⁷	1.00 × 10 ⁰	1.00	48 000	
$Z/\gamma^*(\rightarrow \mu\mu)+\text{jets}$						
mc15_13TeV.361107.PowhegPythia8EvtGen_AZNLOCTEQ6L1_Znumnu	e3601_s2576_s2132_r7725_r7676	1.90 × 10 ³	1.00 × 10 ⁰	1.00	77 497 800	
mc15_13TeV.301020.PowhegPythia8EvtGen_AZNLOCTEQ6L1_DYnumnu_120M180	e3649_s2576_s2132_r7772_r7676	1.75 × 10 ¹	1.00 × 10 ⁰	1.00	498 600	
mc15_13TeV.301021.PowhegPythia8EvtGen_AZNLOCTEQ6L1_DYnumnu_180M250	e3649_s2576_s2132_r7772_r7676	2.92 × 10 ⁰	1.00 × 10 ⁰	1.00	249 600	
mc15_13TeV.301022.PowhegPythia8EvtGen_AZNLOCTEQ6L1_DYnumnu_250M400	e3649_s2576_s2132_r7772_r7676	1.08 × 10 ⁰	1.00 × 10 ⁰	1.00	149 200	
mc15_13TeV.301023.PowhegPythia8EvtGen_AZNLOCTEQ6L1_DYnumnu_400M600	e3649_s2576_s2132_r7772_r7676	1.96 × 10 ⁻¹	1.00 × 10 ⁰	1.00	99 000	
mc15_13TeV.301024.PowhegPythia8EvtGen_AZNLOCTEQ6L1_DYnumnu_600M800	e3649_s2576_s2132_r7772_r7676	3.74 × 10 ⁻²	1.00 × 10 ⁰	1.00	60 600	
mc15_13TeV.301025.PowhegPythia8EvtGen_AZNLOCTEQ6L1_DYnumnu_800M1000	e3649_s2576_s2132_r7772_r7676	1.06 × 10 ⁻²	1.00 × 10 ⁰	1.00	50 000	
mc15_13TeV.301026.PowhegPythia8EvtGen_AZNLOCTEQ6L1_DYnumnu_1000M1250	e3649_s2576_s2132_r7772_r7676	4.26 × 10 ⁻³	1.00 × 10 ⁰	1.00	50 000	
mc15_13TeV.301027.PowhegPythia8EvtGen_AZNLOCTEQ6L1_DYnumnu_1250M1500	e3649_s2576_s2132_r7772_r7676	1.42 × 10 ⁻³	1.00 × 10 ⁰	1.00	49 800	
mc15_13TeV.301028.PowhegPythia8EvtGen_AZNLOCTEQ6L1_DYnumnu_1500M1750	e3649_s2576_s2132_r7772_r7676	5.45 × 10 ⁻⁴	1.00 × 10 ⁰	1.00	49 600	
mc15_13TeV.301029.PowhegPythia8EvtGen_AZNLOCTEQ6L1_DYnumnu_1750M2000	e3649_s2576_s2132_r7772_r7676	2.30 × 10 ⁻⁴	1.00 × 10 ⁰	1.00	50 000	
mc15_13TeV.301030.PowhegPythia8EvtGen_AZNLOCTEQ6L1_DYnumnu_2000M2250	e3649_s2576_s2132_r7772_r7676	1.04 × 10 ⁻⁴	1.00 × 10 ⁰	1.00	50 000	
mc15_13TeV.301031.PowhegPythia8EvtGen_AZNLOCTEQ6L1_DYnumnu_2250M2500	e3649_s2576_s2132_r7772_r7676	4.94 × 10 ⁻⁵	1.00 × 10 ⁰	1.00	49 800	
mc15_13TeV.301032.PowhegPythia8EvtGen_AZNLOCTEQ6L1_DYnumnu_2500M2750	e3649_s2576_s2132_r7772_r7676	2.45 × 10 ⁻⁵	1.00 × 10 ⁰	1.00	49 800	
mc15_13TeV.301033.PowhegPythia8EvtGen_AZNLOCTEQ6L1_DYnumnu_2750M3000	e3649_s2576_s2132_r7772_r7676	1.25 × 10 ⁻⁵	1.00 × 10 ⁰	1.00	50 000	
mc15_13TeV.301034.PowhegPythia8EvtGen_AZNLOCTEQ6L1_DYnumnu_3000M3500	e3649_s2576_s2132_r7772_r7676	1.00 × 10 ⁻⁵	1.00 × 10 ⁰	1.00	50 000	
mc15_13TeV.301035.PowhegPythia8EvtGen_AZNLOCTEQ6L1_DYnumnu_3500M4000	e3649_s2576_s2132_r7772_r7676	2.93 × 10 ⁻⁶	1.00 × 10 ⁰	1.00	50 000	
mc15_13TeV.301036.PowhegPythia8EvtGen_AZNLOCTEQ6L1_DYnumnu_4000M4500	e3649_s2576_s2132_r7772_r7676	8.98 × 10 ⁻⁷	1.00 × 10 ⁰	1.00	49 000	
mc15_13TeV.301037.PowhegPythia8EvtGen_AZNLOCTEQ6L1_DYnumnu_4500M5000	e3649_s2576_s2132_r7772_r7676	2.81 × 10 ⁻⁷	1.00 × 10 ⁰	1.00	50 000	
mc15_13TeV.301038.PowhegPythia8EvtGen_AZNLOCTEQ6L1_DYnumnu_5000M1	e3649_s2576_s2132_r7772_r7676	1.26 × 10 ⁻⁷	1.00 × 10 ⁰	1.00	50 000	

Table D.1: List of ATLAS event samples for $Z/\gamma^*(\rightarrow e\bar{e})+\text{jets}$ and $Z/\gamma^*(\rightarrow \mu\bar{\mu})+\text{jets}$ events with their production tag, cross section σ , filter efficiency ϵ_{filter} , the k -factor and the number of events n_{events} .

ATLAS event sample identifier	$Z/\gamma^*(\rightarrow \tau\tau)+\text{jets}$	production tags	σ [pb]	ϵ_{filter}	k	n_{events}
mc15_13TeV_361108.PowhegPythia8EvtGen_AZNLOCTEQ6L1_Ztautau	e3601_s2726_r7772_r7676	1.90×10^3	1.00×10^0	1.00	19 195 000	
mc15_13TeV_301040.PowhegPythia8EvtGen_AZNLOCTEQ6L1_DYtautau_120M180	e3649_s2576_s2132_r7772_r7676	1.75×10^1	1.00×10^0	1.00	149 800	
mc15_13TeV_301041.PowhegPythia8EvtGen_AZNLOCTEQ6L1_DYtautau_180M250	e3649_s2576_s2132_r7772_r7676	2.92×10^0	1.00×10^0	1.00	149 800	
mc15_13TeV_301042.PowhegPythia8EvtGen_AZNLOCTEQ6L1_DYtautau_250M400	e3649_s2576_s2132_r7772_r7676	1.08×10^0	1.00×10^0	1.00	149 600	
mc15_13TeV_301043.PowhegPythia8EvtGen_AZNLOCTEQ6L1_DYtautau_400M600	e3649_s2576_s2132_r7772_r7676	1.96×10^{-1}	1.00×10^0	1.00	148 200	
mc15_13TeV_301044.PowhegPythia8EvtGen_AZNLOCTEQ6L1_DYtautau_600M800	e3649_s2576_s2132_r7772_r7676	3.74×10^{-2}	1.00×10^0	1.00	150 000	
mc15_13TeV_301045.PowhegPythia8EvtGen_AZNLOCTEQ6L1_DYtautau_800M1000	e3649_s2576_s2132_r7772_r7676	1.06×10^{-2}	1.00×10^0	1.00	149 400	
mc15_13TeV_301046.PowhegPythia8EvtGen_AZNLOCTEQ6L1_DYtautau_1000M1250	e3649_s2576_s2132_r7772_r7676	4.26×10^{-3}	1.00×10^0	1.00	148 000	
mc15_13TeV_301047.PowhegPythia8EvtGen_AZNLOCTEQ6L1_DYtautau_1250M1500	e3649_s2576_s2132_r7772_r7676	1.42×10^{-3}	1.00×10^0	1.00	149 800	
mc15_13TeV_301048.PowhegPythia8EvtGen_AZNLOCTEQ6L1_DYtautau_1500M1750	e3649_s2576_s2132_r7772_r7676	5.45×10^{-4}	1.00×10^0	1.00	50 000	
mc15_13TeV_301049.PowhegPythia8EvtGen_AZNLOCTEQ6L1_DYtautau_1750M2000	e3649_s2576_s2132_r7772_r7676	2.30×10^{-4}	1.00×10^0	1.00	48 200	
mc15_13TeV_301050.PowhegPythia8EvtGen_AZNLOCTEQ6L1_DYtautau_2000M2250	e3649_s2576_s2132_r7772_r7676	1.04×10^{-4}	1.00×10^0	1.00	99 000	
mc15_13TeV_301051.PowhegPythia8EvtGen_AZNLOCTEQ6L1_DYtautau_2250M2500	e3649_s2576_s2132_r7772_r7676	4.94×10^{-5}	1.00×10^0	1.00	50 000	
mc15_13TeV_301052.PowhegPythia8EvtGen_AZNLOCTEQ6L1_DYtautau_2500M2750	e3649_s2576_s2132_r7772_r7676	2.45×10^{-5}	1.00×10^0	1.00	50 000	
mc15_13TeV_301053.PowhegPythia8EvtGen_AZNLOCTEQ6L1_DYtautau_2750M3000	e3649_s2576_s2132_r7772_r7676	1.25×10^{-5}	1.00×10^0	1.00	50 000	
mc15_13TeV_301054.PowhegPythia8EvtGen_AZNLOCTEQ6L1_DYtautau_3000M3500	e3649_s2576_s2132_r7772_r7676	1.00×10^{-5}	1.00×10^0	1.00	49 600	
mc15_13TeV_301055.PowhegPythia8EvtGen_AZNLOCTEQ6L1_DYtautau_3500M4000	e3649_s2576_s2132_r7772_r7676	2.93×10^{-6}	1.00×10^0	1.00	49 000	
mc15_13TeV_301056.PowhegPythia8EvtGen_AZNLOCTEQ6L1_DYtautau_4000M4500	e3649_s2576_s2132_r7772_r7676	8.98×10^{-7}	1.00×10^0	1.00	30 000	
mc15_13TeV_301057.PowhegPythia8EvtGen_AZNLOCTEQ6L1_DYtautau_4500M5000	e3649_s2576_s2132_r7772_r7676	2.81×10^{-7}	1.00×10^0	1.00	50 000	
mc15_13TeV_301058.PowhegPythia8EvtGen_AZNLOCTEQ6L1_DYtautau_5000M	e3649_s2576_s2132_r7772_r7676	1.26×10^{-7}	1.00×10^0	1.00	50 000	
di-boson						
mc15_13TeV_361063.Sherpa_CT10_1lll	e3836_s2608_s2183_r7725_r7676	1.28×10^1	1.00×10^0	1.00	2 964 000	
mc15_13TeV_361064.Sherpa_CT10_1llvSFMinus	e3836_s2608_s2183_r7725_r7676	1.84×10^0	1.00×10^0	1.00	448 800	
mc15_13TeV_361065.Sherpa_CT10_1llvOFMinus	e3836_s2608_s2183_r7725_r7676	3.63×10^0	1.00×10^0	1.00	898 000	
mc15_13TeV_361066.Sherpa_CT10_1llvSFPlus	e3836_s2608_s2183_r7725_r7676	2.56×10^0	1.00×10^0	1.00	596 600	
mc15_13TeV_361067.Sherpa_CT10_1llvOFPlus	e3836_s2608_s2183_r7725_r7676	5.02×10^0	1.00×10^0	1.00	1 197 000	
mc15_13TeV_361068.Sherpa_CT10_1llvv	e3836_s2608_s2183_r7725_r7676	1.40×10^1	1.00×10^0	1.00	5 929 600	
mc15_13TeV_361091.Sherpa_CT10_WplvWmqq_SHv21_improved	e4607_s2726_r7725_r7676	2.49×10^1	1.00×10^0	1.00	1 977 000	
mc15_13TeV_361092.Sherpa_CT10_WpqqWm1v_SHv21_improved	e4607_s2726_r7725_r7676	2.49×10^1	1.00×10^0	1.00	1 979 000	
mc15_13TeV_361093.Sherpa_CT10_WlvZqq_SHv21_improved	e4607_s2726_r7725_r7676	1.15×10^1	1.00×10^0	1.00	1 952 000	
mc15_13TeV_361094.Sherpa_CT10_WqqZll_SHv21_improved	e4607_s2726_r7725_r7676	3.42×10^0	1.00×10^0	1.00	490 000	
mc15_13TeV_361095.Sherpa_CT10_WqqZvv_SHv21_improved	e4607_s2726_r7772_r7676	6.78×10^0	1.00×10^0	1.00	4 962 400	
mc15_13TeV_361096.Sherpa_CT10_ZqqZll_SHv21_improved	e4607_s2726_r7725_r7676	1.64×10^1	1.43×10^{-1}	1.00	487 000	
mc15_13TeV_361097.Sherpa_CT10_ZqqZvv_SHv21_improved	e4607_s2726_r7772_r7676	1.64×10^1	2.82×10^{-1}	1.00	4 483 500	

Table D.2: List of ATLAS event samples for $Z/\gamma^*(\rightarrow \tau\tau)+\text{jets}$ and di-boson events with their production tag, cross section σ , filter efficiency ϵ_{filter} , the k -factor and the number of events n_{events} .

ATLAS event sample identifier	$W(\rightarrow \tau\nu)+\text{jets}$		production tags	$\sigma[\text{pb}]$	filter	k	n_{events}
mc15_13TeV.363331.Sherpa_NNPDF30NNLO_Wtaunu_Pt0_70_CVetoBVeto			e4709_s2726_r7725_r7676	2.00×10^4	8.14×10^{-1}	1.00	19 769 000
mc15_13TeV.363332.Sherpa_NNPDF30NNLO_Wtaunu_Pt0_70_FilterBVeto			e4709_s2726_r7725_r7676	2.00×10^4	1.38×10^{-1}	1.00	5 905 000
mc15_13TeV.363333.Sherpa_NNPDF30NNLO_Wtaunu_Pt0_70_Filter			e4709_s2726_r7725_r7676	2.00×10^4	4.68×10^{-2}	1.00	5 902 000
mc15_13TeV.363334.Sherpa_NNPDF30NNLO_Wtaunu_Pt70_140_CVetoBVeto			e4709_s2726_r7725_r7676	5.89×10^2	6.57×10^{-1}	1.00	4 455 000
mc15_13TeV.363335.Sherpa_NNPDF30NNLO_Wtaunu_Pt70_140_FilterBVeto			e4709_s2726_r7725_r7676	5.90×10^2	2.52×10^{-1}	1.00	4 430 000
mc15_13TeV.363336.Sherpa_NNPDF30NNLO_Wtaunu_Pt70_140_Filter			e4779_s2726_r7725_r7676	5.90×10^2	8.58×10^{-2}	1.00	4 450 000
mc15_13TeV.363337.Sherpa_NNPDF30NNLO_Wtaunu_Pt140_280_CVetoBVeto			e4709_s2726_r7725_r7676	8.42×10^1	6.14×10^{-1}	1.00	3 945 000
mc15_13TeV.363338.Sherpa_NNPDF30NNLO_Wtaunu_Pt140_280_FilterBVeto			e4709_s2726_r7725_r7676	8.43×10^1	2.76×10^{-1}	1.00	3 938 000
mc15_13TeV.363339.Sherpa_NNPDF30NNLO_Wtaunu_Pt140_280_Filter			e4709_s2726_r7725_r7676	8.42×10^1	1.05×10^{-1}	1.00	3 907 200
mc15_13TeV.363340.Sherpa_NNPDF30NNLO_Wtaunu_Pt280_500_CVetoBVeto			e4779_s2726_r7725_r7676	6.09×10^0	5.84×10^{-1}	1.00	989 000
mc15_13TeV.363341.Sherpa_NNPDF30NNLO_Wtaunu_Pt280_500_FilterBVeto			e4779_s2726_r7725_r7676	6.07×10^0	2.87×10^{-1}	1.00	989 000
mc15_13TeV.363342.Sherpa_NNPDF30NNLO_Wtaunu_Pt500_700_CVetoBVeto			e4779_s2726_r7725_r7676	6.08×10^0	1.21×10^{-1}	1.00	989 000
mc15_13TeV.363343.Sherpa_NNPDF30NNLO_Wtaunu_Pt500_700_FilterBVeto			e4709_s2726_r7725_r7676	3.81×10^{-1}	5.68×10^{-1}	1.00	490 000
mc15_13TeV.363344.Sherpa_NNPDF30NNLO_Wtaunu_Pt500_700_FilterBVeto			e4709_s2726_r7725_r7676	3.78×10^{-1}	2.97×10^{-1}	1.00	294 000
mc15_13TeV.363345.Sherpa_NNPDF30NNLO_Wtaunu_Pt500_700_Filter			e4779_s2726_r7725_r7676	3.76×10^{-1}	1.31×10^{-1}	1.00	295 000
mc15_13TeV.363346.Sherpa_NNPDF30NNLO_Wtaunu_Pt700_1000_CVetoBVeto			e4709_s2726_r7725_r7676	7.32×10^{-2}	5.61×10^{-1}	1.00	197 000
mc15_13TeV.363347.Sherpa_NNPDF30NNLO_Wtaunu_Pt700_1000_FilterBVeto			e4779_s2726_r7725_r7676	6.80×10^{-2}	2.92×10^{-1}	1.00	99 000
mc15_13TeV.363348.Sherpa_NNPDF30NNLO_Wtaunu_Pt700_1000_Filter			e4709_s2726_r7725_r7676	6.73×10^{-2}	1.45×10^{-1}	1.00	100 000
mc15_13TeV.363349.Sherpa_NNPDF30NNLO_Wtaunu_Pt1000_2000_CVetoBVeto			e4709_s2726_r7725_r7676	9.03×10^{-3}	5.56×10^{-1}	1.00	9 000
mc15_13TeV.363350.Sherpa_NNPDF30NNLO_Wtaunu_Pt1000_2000_FilterBVeto			e4779_s2726_r7725_r7676	8.91×10^{-3}	2.90×10^{-1}	1.00	10 000
mc15_13TeV.363351.Sherpa_NNPDF30NNLO_Wtaunu_Pt1000_2000_Filter			e4779_s2726_r7725_r7676	9.02×10^{-3}	1.41×10^{-1}	1.00	9 080
mc15_13TeV.363352.Sherpa_NNPDF30NNLO_Wtaunu_Pt2000_E_CMS_CVetoBVeto			e4709_s2726_r7725_r7676	2.62×10^{-5}	5.61×10^{-1}	1.00	10 000
mc15_13TeV.363353.Sherpa_NNPDF30NNLO_Wtaunu_Pt2000_E_CMS_FilterBVeto			e4709_s2726_r7725_r7676	3.10×10^{-5}	2.90×10^{-1}	1.00	9 000
mc15_13TeV.363354.Sherpa_NNPDF30NNLO_Wtaunu_Pt2000_E_CMS_Filter			e4709_s2726_r7725_r7676	2.94×10^{-5}	1.80×10^{-1}	1.00	10 000

Table D.3: List of ATLAS event samples for $W(\rightarrow \tau\nu)+\text{jets}$ events with their production tag, cross section σ , filter efficiency ϵ_{filter} , the k -factor and the number of events n_{events} .

ATLAS event sample identifier	$W(\rightarrow \mu\nu)+\text{jets}$										production tags	$\sigma[\text{pb}]$	ϵ_{filter}	k	n_{events}
	mc15_13TeV_363436.Sherpa	NNPDF30NNLO	Wmunu	Pt0_70	CVetoBVeto	mc15_13TeV_363437.Sherpa	NNPDF30NNLO	Wmunu	Pt0_70	CFilterBVeto					
	mc15_13TeV_363438.Sherpa	NNPDF30NNLO	Wmunu	Pt0_70	BFilter	mc15_13TeV_363439.Sherpa	NNPDF30NNLO	Wmunu	Pt70_140	CVetoBVeto	e4715_s2726_r7725_r7676	2.00×10^4	8.14×10^{-1}	1.00	19 751 000
	mc15_13TeV_363440.Sherpa	NNPDF30NNLO	Wmunu	Pt70_140	CFilterBVeto	mc15_13TeV_363441.Sherpa	NNPDF30NNLO	Wmunu	Pt70_140	BFilter <td>e4715_s2726_r7725_r7676</td> <td>2.00×10^4</td> <td>1.38×10^{-1}</td> <td>1.00</td> <td>5 913 000</td>	e4715_s2726_r7725_r7676	2.00×10^4	1.38×10^{-1}	1.00	5 913 000
	mc15_13TeV_363442.Sherpa	NNPDF30NNLO	Wmunu	Pt140_280	CVetoBVeto	mc15_13TeV_363443.Sherpa	NNPDF30NNLO	Wmunu	Pt140_280	CFilterBVeto	e4715_s2726_r7725_r7676	5.90×10^2	6.60×10^{-1}	1.00	4 445 000
	mc15_13TeV_363444.Sherpa	NNPDF30NNLO	Wmunu	Pt280_500	CVetoBVeto	mc15_13TeV_363445.Sherpa	NNPDF30NNLO	Wmunu	Pt280_500	CFilterBVeto	e4715_s2726_r7725_r7676	5.91×10^2	2.53×10^{-1}	1.00	4 431 000
	mc15_13TeV_363447.Sherpa	NNPDF30NNLO	Wmunu	Pt280_500	BFilter	mc15_13TeV_363448.Sherpa	NNPDF30NNLO	Wmunu	Pt500_700	CVetoBVeto	e4715_s2726_r7725_r7676	5.90×10^2	8.70×10^{-2}	1.00	13 306 600
	mc15_13TeV_363449.Sherpa	NNPDF30NNLO	Wmunu	Pt500_700	CFilterBVeto	mc15_13TeV_363450.Sherpa	NNPDF30NNLO	Wmunu	Pt500_700	BFilter	e4715_s2726_r7725_r7676	8.41×10^1	6.14×10^{-1}	1.00	7 886 000
	mc15_13TeV_363451.Sherpa	NNPDF30NNLO	Wmunu	Pt700_1000	CVetoBVeto	mc15_13TeV_363452.Sherpa	NNPDF30NNLO	Wmunu	Pt700_1000	CFilterBVeto	e4715_s2726_r7725_r7676	8.43×10^1	2.77×10^{-1}	1.00	7 901 000
	mc15_13TeV_363453.Sherpa	NNPDF30NNLO	Wmunu	Pt1000_2000	CVetoBVeto	mc15_13TeV_363454.Sherpa	NNPDF30NNLO	Wmunu	Pt1000_2000	CFilterBVeto	e4715_s2726_r7725_r7676	8.40×10^1	1.06×10^{-1}	1.00	11 862 000
	mc15_13TeV_363455.Sherpa	NNPDF30NNLO	Wmunu	Pt1000_2000	BFilter	mc15_13TeV_363456.Sherpa	NNPDF30NNLO	Wmunu	Pt1000_2000	BFilter	e4715_s2726_r7725_r7676	6.50×10^0	5.85×10^{-1}	1.00	1 973 000
	mc15_13TeV_363457.Sherpa	NNPDF30NNLO	Wmunu	Pt2000_E_CMS	CVetoBVeto	mc15_13TeV_363458.Sherpa	NNPDF30NNLO	Wmunu	Pt2000_E_CMS	CFilterBVeto	e4715_s2726_r7725_r7676	6.07×10^0	2.87×10^{-1}	1.00	1 974 000
	mc15_13TeV_363459.Sherpa	NNPDF30NNLO	Wmunu	Pt2000_E_CMS	BFilter	mc15_13TeV_363459.Sherpa	NNPDF30NNLO	Wmunu	Pt2000_E_CMS	BFilter	e4715_s2726_r7725_r7676	6.15×10^0	1.22×10^{-1}	1.00	1 969 600
											e4715_s2726_r7725_r7676	3.88×10^{-1}	5.67×10^{-1}	1.00	491 000
											e4715_s2726_r7725_r7676	3.80×10^{-1}	2.91×10^{-1}	1.00	295 000
											e4715_s2726_r7725_r7676	3.81×10^{-1}	1.37×10^{-1}	1.00	271 600
											e4715_s2726_r7725_r7676	6.83×10^{-2}	5.60×10^{-1}	1.00	198 000
											e4715_s2726_r7725_r7676	6.85×10^{-2}	2.74×10^{-1}	1.00	99 000
											e4715_s2726_r7725_r7676	6.82×10^{-2}	1.42×10^{-1}	1.00	98 000
											e4715_s2726_r7725_r7676	8.95×10^{-3}	5.52×10^{-1}	1.00	10 000
											e4715_s2726_r7725_r7676	8.90×10^{-3}	2.89×10^{-1}	1.00	10 000
											e4715_s2726_r7725_r7676	8.90×10^{-3}	1.49×10^{-1}	1.00	10 000
											e4715_s2726_r7725_r7676	2.63×10^{-5}	4.83×10^{-1}	1.00	10 000
											e4715_s2726_r7725_r7676	3.29×10^{-5}	3.07×10^{-1}	1.00	9000
											e4715_s2726_r7725_r7676	2.78×10^{-5}	1.97×10^{-1}	1.00	10 000

Table D.4: List of ATLAS event samples for $W(\rightarrow \mu\nu)+\text{jets}$ events with their production tag, cross section σ , filter efficiency ϵ_{filter} , the k -factor and the number of events n_{events} .

ATLAS event sample identifier	$W(\rightarrow e\nu)+\text{jets}$	production tags	$\sigma[\text{pb}]$	filter	k	n_{events}
mc15_13TeV.363460.Sherpa_NNPDF30NNLO_Wenu_Pt0_70_CVetoBVeto		e4715_s2726_r7725_r7676	2.00×10^4	8.14×10^{-1}	1.00	19 771 000
mc15_13TeV.363461.Sherpa_NNPDF30NNLO_Wenu_Pt0_70_CFilterBVeto		e4715_s2726_r7725_r7676	2.00×10^4	1.38×10^{-1}	1.00	5 919 000
mc15_13TeV.363462.Sherpa_NNPDF30NNLO_Wenu_Pt0_70_BFilter		e4715_s2726_r7725_r7676	2.00×10^4	4.70×10^{-2}	1.00	5 932 000
mc15_13TeV.363463.Sherpa_NNPDF30NNLO_Wenu_Pt70_140_CVetoBVeto		e4715_s2726_r7725_r7676	5.88×10^2	6.60×10^{-1}	1.00	4 440 000
mc15_13TeV.363464.Sherpa_NNPDF30NNLO_Wenu_Pt70_140_CFilterBVeto		e4715_s2726_r7725_r7676	5.89×10^2	2.56×10^{-1}	1.00	4 439 000
mc15_13TeV.363465.Sherpa_NNPDF30NNLO_Wenu_Pt70_140_BFilter		e4715_s2726_r7725_r7676	5.89×10^2	8.67×10^{-2}	1.00	13 320 000
mc15_13TeV.363466.Sherpa_NNPDF30NNLO_Wenu_Pt140_280_CVetoBVeto		e4715_s2726_r7725_r7676	8.41×10^1	6.15×10^{-1}	1.00	7 911 000
mc15_13TeV.363467.Sherpa_NNPDF30NNLO_Wenu_Pt140_280_CFilterBVeto		e4715_s2726_r7725_r7676	8.42×10^1	2.77×10^{-1}	1.00	7 875 000
mc15_13TeV.363468.Sherpa_NNPDF30NNLO_Wenu_Pt140_280_BFilter		e4715_s2726_r7725_r7676	8.41×10^1	1.06×10^{-1}	1.00	11 860 000
mc15_13TeV.363469.Sherpa_NNPDF30NNLO_Wenu_Pt280_500_CVetoBVeto		e4715_s2726_r7725_r7676	6.09×10^0	5.82×10^{-1}	1.00	1 972 000
mc15_13TeV.363470.Sherpa_NNPDF30NNLO_Wenu_Pt280_500_CFilterBVeto		e4715_s2726_r7725_r7676	6.08×10^0	2.87×10^{-1}	1.00	1 976 000
mc15_13TeV.363471.Sherpa_NNPDF30NNLO_Wenu_Pt280_500_BFilter		e4715_s2726_r7725_r7676	6.08×10^0	1.24×10^{-1}	1.00	1 972 000
mc15_13TeV.363472.Sherpa_NNPDF30NNLO_Wenu_Pt500_700_CVetoBVeto		e4715_s2726_r7725_r7676	3.82×10^{-1}	5.71×10^{-1}	1.00	469 000
mc15_13TeV.363473.Sherpa_NNPDF30NNLO_Wenu_Pt500_700_CFilterBVeto		e4715_s2726_r7725_r7676	3.81×10^{-1}	2.90×10^{-1}	1.00	297 000
mc15_13TeV.363474.Sherpa_NNPDF30NNLO_Wenu_Pt500_700_BFilter		e4715_s2726_r7725_r7676	3.85×10^{-1}	1.37×10^{-1}	1.00	290 000
mc15_13TeV.363475.Sherpa_NNPDF30NNLO_Wenu_Pt700_1000_CVetoBVeto		e4715_s2726_r7725_r7676	6.84×10^{-2}	5.57×10^{-1}	1.00	199 000
mc15_13TeV.363476.Sherpa_NNPDF30NNLO_Wenu_Pt700_1000_CFilterBVeto		e4715_s2726_r7725_r7676	6.77×10^{-2}	2.90×10^{-1}	1.00	98 000
mc15_13TeV.363477.Sherpa_NNPDF30NNLO_Wenu_Pt700_1000_BFilter		e4715_s2726_r7725_r7676	7.21×10^{-2}	1.36×10^{-1}	1.00	100 000
mc15_13TeV.363478.Sherpa_NNPDF30NNLO_Wenu_Pt1000_2000_CVetoBVeto		e4715_s2726_r7725_r7676	8.74×10^{-3}	5.48×10^{-1}	1.00	9000
mc15_13TeV.363479.Sherpa_NNPDF30NNLO_Wenu_Pt1000_2000_CFilterBVeto		e4715_s2726_r7725_r7676	8.87×10^{-3}	2.84×10^{-1}	1.00	10 000
mc15_13TeV.363480.Sherpa_NNPDF30NNLO_Wenu_Pt1000_2000_BFilter		e4715_s2726_r7725_r7676	8.89×10^{-3}	1.52×10^{-1}	1.00	10 000
mc15_13TeV.363481.Sherpa_NNPDF30NNLO_Wenu_Pt2000_E_CMS_CVetoBVeto		e4715_s2726_r7725_r7676	3.13×10^{-5}	4.27×10^{-1}	1.00	9000
mc15_13TeV.363482.Sherpa_NNPDF30NNLO_Wenu_Pt2000_E_CMS_CFilterBVeto		e4715_s2726_r7725_r7676	2.59×10^{-5}	9.41×10^{-2}	1.00	10 000
mc15_13TeV.363483.Sherpa_NNPDF30NNLO_Wenu_Pt2000_E_CMS_BFilter		e4715_s2726_r7725_r7676	2.91×10^{-5}	1.31×10^{-1}	1.00	10 000

Table D.5: List of ATLAS event samples for $W(\rightarrow e\nu)+\text{jets}$ events with their production tag, cross section σ , filter efficiency ϵ_{filter} , the k -factor and the number of events n_{events} .

ATLAS event sample identifier	$t\bar{t}$, single top	production tags	$\sigma[\text{pb}]$	ϵ_{filter}	k	n_{events}
mc15_13TeV_410000.PowhegPythiaEvtGen_P2012_ttbar_hdamp172p5_nonallhad		e3698_s2608_s2183_r7725_r7676	6.96×10^2	5.43×10^{-1}	1.19	49 386 600
mc15_13TeV_410007.PowhegPythiaEvtGen_P2012_ttbar_hdamp172p5_allhad		e4135_s2608_s2183_r7725_r7676	6.96×10^2	4.57×10^{-1}	1.20	9 989 200
mc15_13TeV_410011.PowhegPythiaEvtGen_P2012_singletop_tchan_lept_top		e3824_s2608_s2183_r7725_r7676	4.37×10^1	1.00×10^0	1.01	4 986 200
mc15_13TeV_410012.PowhegPythiaEvtGen_P2012_singletop_tchan_lept_antitop		e3824_s2608_s2183_r7725_r7676	2.58×10^1	1.00×10^0	1.02	4 989 800
mc15_13TeV_410013.PowhegPythiaEvtGen_P2012_Wt_inclusive_top		e3753_s2608_s2183_r7725_r7676	3.40×10^1	1.00×10^0	1.05	4 985 800
mc15_13TeV_410014.PowhegPythiaEvtGen_P2012_Wt_inclusive_antitop		e3753_s2608_s2183_r7725_r7676	3.40×10^1	1.00×10^0	1.05	4 985 600
mc15_13TeV_410025.PowhegPythiaEvtGen_P2012_SingleTopSchan_noAllHad_top		e3998_s2608_s2183_r7725_r7676	2.05×10^0	1.00×10^0	1.68	997 800
mc15_13TeV_410026.PowhegPythiaEvtGen_P2012_SingleTopSchan_noAllHad_antitop		e3998_s2608_s2183_r7725_r7676	1.26×10^0	1.00×10^0	1.71	995 400
$t\bar{t}$ systematics samples						
mc15_13TeV_410001.PowhegPythiaEvtGen_P2012radHi_ttbar_hdamp345_down_nonallhad		e3783_s2608_r7725_r7676	7.84×10^2	5.44×10^{-1}	1.06	19 953 000
mc15_13TeV_410002.PowhegPythiaEvtGen_P2012radLo_ttbar_hdamp172_up_nonallhad		e3783_s2608_r7725_r7676	6.11×10^2	5.44×10^{-1}	1.36	19 816 000
mc15_13TeV_410003.aMcAtNloHerwigppEvtGen_ttbar_nonallhad		e3964_a766_a822_r7676	6.95×10^2	5.44×10^{-1}	1.20	4 884 000
mc15_13TeV_410004.PowhegHerwigppEvtGen_UEEE5_ttbar_hdamp172p5_nonallhad		e3836_a766_a822_r7676	6.96×10^2	5.44×10^{-1}	1.19	9 655 000
mc15_13TeV_410008.aMcAtNloHerwigppEvtGen_ttbar_allhad		e3964_a766_a818_r7676	6.94×10^2	4.56×10^{-1}	1.20	4 889 000

Table D.6: List of ATLAS event samples for $t\bar{t}$ and single top events with their production tag, cross section σ , filter efficiency ϵ_{filter} , the k -factor and the number of events n_{events} .

Table D.7: List of ATLAS event samples for b -associated Higgs production and their production tags. The number of events are given in Table 2.2.

ATLAS event sample identifier	b -associated Higgs production	production tags
mc15_13TeV.341858.aMcAtNloPythia8EvtGen_A14NNPDF23LO_bbH200_yb2_tautauhh		e4482_a766_a821_r7676
mc15_13TeV.341860.aMcAtNloPythia8EvtGen_A14NNPDF23LO_bbH300_yb2_tautauhh		e4482_a766_a821_r7676
mc15_13TeV.341861.aMcAtNloPythia8EvtGen_A14NNPDF23LO_bbH350_yb2_tautauhh		e4482_a766_a821_r7676
mc15_13TeV.341862.aMcAtNloPythia8EvtGen_A14NNPDF23LO_bbH400_yb2_tautauhh		e4298_a766_a821_r7676
mc15_13TeV.341863.aMcAtNloPythia8EvtGen_A14NNPDF23LO_bbH500_yb2_tautauhh		e4482_a766_a821_r7676
mc15_13TeV.341864.aMcAtNloPythia8EvtGen_A14NNPDF23LO_bbH600_yb2_tautauhh		e4482_a766_a821_r7676
mc15_13TeV.341865.aMcAtNloPythia8EvtGen_A14NNPDF23LO_bbH700_yb2_tautauhh		e4482_a766_a821_r7676
mc15_13TeV.341866.aMcAtNloPythia8EvtGen_A14NNPDF23LO_bbH800_yb2_tautauhh		e4482_a766_a821_r7676
mc15_13TeV.341868.aMcAtNloPythia8EvtGen_A14NNPDF23LO_bbH1000_yb2_tautauhh		e4298_a766_a821_r7676
mc15_13TeV.341870.aMcAtNloPythia8EvtGen_A14NNPDF23LO_bbH1200_yb2_tautauhh		e4482_a766_a821_r7676
mc15_13TeV.341875.aMcAtNloPythia8EvtGen_A14NNPDF23LO_bbH200_yb2_tautauhh		e4482_a766_a821_r7676
mc15_13TeV.341877.aMcAtNloPythia8EvtGen_A14NNPDF23LO_bbH300_yb2_tautauhh		e4482_a766_a821_r7676
mc15_13TeV.341878.aMcAtNloPythia8EvtGen_A14NNPDF23LO_bbH350_yb2_tautauhh		e4482_a766_a821_r7676
mc15_13TeV.341879.aMcAtNloPythia8EvtGen_A14NNPDF23LO_bbH400_yb2_tautauhh		e4298_a766_a821_r7676
mc15_13TeV.341880.aMcAtNloPythia8EvtGen_A14NNPDF23LO_bbH500_yb2_tautauhh		e4482_a766_a821_r7676
mc15_13TeV.341881.aMcAtNloPythia8EvtGen_A14NNPDF23LO_bbH600_yb2_tautauhh		e4482_a766_a821_r7676
mc15_13TeV.341882.aMcAtNloPythia8EvtGen_A14NNPDF23LO_bbH700_yb2_tautauhh		e4482_a766_a821_r7676
mc15_13TeV.341883.aMcAtNloPythia8EvtGen_A14NNPDF23LO_bbH800_yb2_tautauhh		e4482_a766_a821_r7676
mc15_13TeV.341885.aMcAtNloPythia8EvtGen_A14NNPDF23LO_bbH1000_yb2_tautauhh		e4298_a766_a821_r7676
mc15_13TeV.341917.aMcAtNloPythia8EvtGen_A14NNPDF23LO_bbH1200_yb2_tautauhh		e4482_a766_a821_r7676

ATLAS event sample identifier	production tags
gluon-gluon fusion	
mc15_13TeV.342305.PowhegPythia8EvtGen_CT10_AZNLOCTEQ6L1_ggH200W1_tautauhh	e4284_s2608_s2183_r7772_r7676
mc15_13TeV.342306.PowhegPythia8EvtGen_CT10_AZNLOCTEQ6L1_ggH200W1_tautauhh	e4284_s2608_s2183_r7772_r7676
mc15_13TeV.342310.PowhegPythia8EvtGen_CT10_AZNLOCTEQ6L1_ggH300W2_tautauhh	e4284_s2608_s2183_r7772_r7676
mc15_13TeV.342311.PowhegPythia8EvtGen_CT10_AZNLOCTEQ6L1_ggH300W2_tautauhh	e4284_s2608_s2183_r7772_r7676
mc15_13TeV.342312.PowhegPythia8EvtGen_CT10_AZNLOCTEQ6L1_ggH350W3_tautauhh	e4284_s2608_s2183_r7772_r7676
mc15_13TeV.342313.PowhegPythia8EvtGen_CT10_AZNLOCTEQ6L1_ggH350W3_tautauhh	e4284_s2608_s2183_r7772_r7676
mc15_13TeV.342314.PowhegPythia8EvtGen_CT10_AZNLOCTEQ6L1_ggH400W5_tautauhh	e4284_s2608_s2183_r7772_r7676
mc15_13TeV.342315.PowhegPythia8EvtGen_CT10_AZNLOCTEQ6L1_ggH400W5_tautauhh	e4284_s2608_s2183_r7772_r7676
mc15_13TeV.342316.PowhegPythia8EvtGen_CT10_AZNLOCTEQ6L1_ggH500W5_tautauhh	e4284_s2608_s2183_r7772_r7676
mc15_13TeV.342317.PowhegPythia8EvtGen_CT10_AZNLOCTEQ6L1_ggH500W5_tautauhh	e4284_s2608_s2183_r7772_r7676
mc15_13TeV.342318.PowhegPythia8EvtGen_CT10_AZNLOCTEQ6L1_ggH600W10_tautauhh	e4284_s2608_s2183_r7772_r7676
mc15_13TeV.342319.PowhegPythia8EvtGen_CT10_AZNLOCTEQ6L1_ggH600W10_tautauhh	e4284_s2608_s2183_r7772_r7676
mc15_13TeV.342320.PowhegPythia8EvtGen_CT10_AZNLOCTEQ6L1_ggH700W20_tautauhh	e4284_s2608_s2183_r7772_r7676
mc15_13TeV.342321.PowhegPythia8EvtGen_CT10_AZNLOCTEQ6L1_ggH700W20_tautauhh	e4284_s2608_s2183_r7772_r7676
mc15_13TeV.342322.PowhegPythia8EvtGen_CT10_AZNLOCTEQ6L1_ggH800W20_tautauhh	e4284_s2608_s2183_r7772_r7676
mc15_13TeV.342323.PowhegPythia8EvtGen_CT10_AZNLOCTEQ6L1_ggH800W20_tautauhh	e4284_s2608_s2183_r7772_r7676
mc15_13TeV.342326.PowhegPythia8EvtGen_CT10_AZNLOCTEQ6L1_ggH1000W30_tautauhh	e4284_s2608_s2183_r7772_r7676
mc15_13TeV.342327.PowhegPythia8EvtGen_CT10_AZNLOCTEQ6L1_ggH1000W30_tautauhh	e4284_s2608_s2183_r7772_r7676
mc15_13TeV.342330.PowhegPythia8EvtGen_CT10_AZNLOCTEQ6L1_ggH1200W40_tautauhh	e4284_s2608_s2183_r7772_r7676
mc15_13TeV.342331.PowhegPythia8EvtGen_CT10_AZNLOCTEQ6L1_ggH1200W40_tautauhh	e4284_s2608_s2183_r7772_r7676

Table D.8: List of ATLAS event samples for gluon-gluon fusion Higgs production and their production tags. The number of events are given in Table 2.2.

ATLAS data run number	production tags
276073 – 284484	r7562_p2521_p2667
297730	f694_m1583_p2667
298595 – 298773	f698_m1594_p2667
298862 – 298967	f696_m1588_p2667
299055 – 299243	f698_m1594_p2667
299584	f703_m1600_p2667
300279 – 300571	f705_m1606_p2667
300600 – 300908	f708_m1606_p2667
301912 – 302269	f709_m1620_p2689
302300 – 302831	f711_m1620_p2689
302919 – 303266	f715_m1620_p2689
302872, 303291 – 303560	f716_m1620_p2689

Table D.9: List of ATLAS data run numbers and the production tags used for this thesis.

List of Figures

2.1	Visualization of the Higgs potential.	7
2.2	Visualization of the stages of event generation	11
2.3	Evolution of inverse gauge couplings in the MSSM and SM	14
2.4	MSSM Higgs production tree-level Feynman diagrams	18
2.5	$m_h^{\text{mod+}}$ Higgs production cross sections and $\tau\tau$ branching ratios . . .	23
2.6	hMSSM sum of Higgs production cross sections multiplied by $\tau\tau$ branching ratios	24
2.7	Fraction of gluon-gluon fusion in the hMSSM scenario	24
2.8	MSSM exclusion limits from LEP and Tevatron	25
2.9	MSSM exclusion limits from ATLAS and CMS at $\sqrt{s} = 7$ TeV	25
2.10	MSSM exclusion limits from ATLAS and CMS with LHC Run 1 data	26
3.1	Schematic overview of the current CERN accelerator complex	29
3.2	A schematic view of the ATLAS detector and its subsystems	30
3.3	The ATLAS coordinate system.	31
3.4	Visualization of pseudorapidity η and polar angle θ	31
3.5	Schematic view of the Inner Detector	33
3.6	Schematic view of the ATLAS calorimeters	34
3.7	Schematic view of the ATLAS muon systems	35
3.8	Integrated luminosity and peak luminosity during data taking	38
3.9	Average number of interactions per bunch crossing	38
4.1	Jet energy scale uncertainty	41
4.2	Jet energy resolution uncertainty	42
4.3	JVT selection efficiency and pile-up dependence	42
4.4	MV2c10 b -tagging score distributions	43
4.5	Muon reconstruction efficiency	45
4.6	Muon isolation efficiency	46
4.7	Electron reconstruction efficiency	47
4.8	Electron identification efficiency	48
4.9	$\tau_{\text{had-vis}}$ reconstruction efficiency	49
4.10	$\tau_{\text{had-vis}}$ identification efficiency	50

4.11	$\tau_{\text{had-vis}}$ energy resolution	50
4.12	$E_{\text{T}}^{\text{miss}}$ resolution	52
5.1	Distribution of $\Delta\phi$ and mean signal $\Delta\phi$ in dependence of Higgs mass	56
5.2	Variable distributions in the b -tag category	59
5.3	Variable distributions in the b -veto category	60
6.1	Fake factor dependence on $p_{\text{T}}(\tau_1)/p_{\text{T}}(\tau_0)$	64
6.2	Fake factor dependence on the number of <i>tag</i> tracks	65
6.3	Fake factor dependence on the number of <i>probe</i> tracks	66
6.4	Fake factor dependence on the presence of b -jets	66
6.5	Fake factor dependence on $\Delta\phi$	67
6.6	Fake factor dependence on the <i>tag</i> and <i>probe</i> charge product	68
6.7	Fake factors for the b -veto category	69
6.8	Fake factors for the b -tag category	70
6.9	Uncorrected 1-prong $\tau_{\text{had-vis}}$ p_{T} in the b -tag same-sign validation region	71
6.10	Variable distributions in the b -veto same-sign validation region . . .	72
6.11	Variable distributions in the b -tag same-sign validation region	73
6.12	Variable distributions in the $W(\rightarrow \mu\nu)$ +jets modeling validation region	74
6.13	Fake rate comparison between data and Monte Carlo for $t\bar{t}$	75
6.14	Fake rate comparison between data and Monte Carlo for $W(\rightarrow \mu\nu)$ +jets	76
6.15	Event observables in the $W(\rightarrow \mu\nu)$ +jets $\tau_{\text{had-vis}}$ fake rate control region	79
6.16	Event observables in the $t\bar{t}$ $\tau_{\text{had-vis}}$ fake rate control region	80
6.17	Fake rates	81
7.1	Systematic uncertainty on the choice of $t\bar{t}$ shower generator	85
7.2	Uncertainty of parton density functions	86
7.3	Impact of tau energy scale uncertainties on $m_{\text{T}}^{\text{tot}}$	90
8.1	Test statistic for toy experiment and asymptotic approximation . . .	98
8.2	Post-fit $m_{\text{T}}^{\text{tot}}$ distributions	99
8.3	Nuisance parameter rankings and pulls	100
8.4	Observed and expected limits in $m_A - f_{\text{bbH}}$	101
8.5	Cross section limits	102
8.6	MSSM limits in the $m_h^{\text{mod+}}$ benchmark scenario	103
8.7	Limit comparison to the Run 1 results and impact of signal cross section uncertainty	103
8.8	MSSM limits in various benchmark scenarios	104
9.1	Limit combination with the $\tau_{\text{lep}}\tau_{\text{had}}$ channel	106
9.2	Expected cross section limits by CMS	107
9.3	Extrapolated expected 2σ sensitivity in the hMSSM benchmark scenario	108

A.1	Number of b -jets in the b -tag category	109
A.2	Additional variable distributions in the b -tag category	110
A.3	Additional variable distributions in the b -tag category	111
A.4	Additional variable distributions in the b -veto category	112
A.5	Additional variable distributions in the b -veto category	113
B.1	Nuisance parameter impact and pulls for $m_A = 300$ GeV, $\tan \beta = 10$ ($m_h^{\text{mod}+}$)	115
B.2	Nuisance parameter impact and pulls for $m_A = 600$ GeV, $\tan \beta = 20$ ($m_h^{\text{mod}+}$)	116
B.3	Nuisance parameter impact and pulls for $m_A = 1000$ GeV, $\tan \beta = 35$ ($m_h^{\text{mod}+}$)	117

List of Tables

2.1	Elementary particles of the Standard Model	5
2.2	Signal Monte Carlo event sample sizes	20
4.1	Physic object overlap removal ΔR	51
5.1	Signal selection efficiencies	56
5.2	Expected event yields for SM backgrounds and observed events during the event selection	57
5.3	Expected event yields for selected signal hypotheses during the event selection	58
7.1	Effect of Monte Carlo modeling uncertainties on top background event yields	84
7.2	Signal acceptance uncertainties, b -associated production, b -tag category	87
7.3	Signal acceptance uncertainties, b -associated production, b -veto cate- gory	87
7.4	Signal acceptance uncertainties, gluon-gluon fusion, b -tag category .	88
7.5	Signal acceptance uncertainties, gluon-gluon fusion, b -veto category .	88
7.6	Uncertainties on background and signal event yields due to mid- identification rate uncertainties	89
7.7	Impact of detector-related uncertainties, b -tag category	91
7.8	Impact of detector-related uncertainties, b -veto category	92
8.1	Limit comparison between toy experiments and asymptotic approxi- mation	99
8.2	Post-fit background and data event yields	100
C.1	Limits for Higgs masses up to 500 GeV for different values of f_{bbH} . .	119
C.2	Limits for Higgs masses above 500 GeV for different values of f_{bbH} .	120
D.1	ATLAS event samples for $Z/\gamma^*(\rightarrow ee)+\text{jets}$ and $Z/\gamma^*(\rightarrow \mu\mu)+\text{jets}$.	122
D.2	ATLAS event samples for $Z/\gamma^*(\rightarrow \tau\tau)+\text{jets}$ and di-boson	123
D.3	ATLAS event samples for $W(\rightarrow \tau\nu)+\text{jets}$	124

D.4	ATLAS event samples for $W(\rightarrow \mu\nu)+\text{jets}$	125
D.5	ATLAS event samples for $W(\rightarrow e\nu)+\text{jets}$	126
D.6	ATLAS event samples for $t\bar{t}$ and single top	127
D.7	ATLAS event samples for b -associated Higgs production	128
D.8	ATLAS event samples for gluon-gluon fusion	129
D.9	ATLAS production tags for data event samples	130

List of Abbreviations

ATLAS	A Toroidal LHC ApparatuS
BDT	boosted decision tree
CERN	European Organization for Nuclear Research
CL	confidence level
CMS	Compact Muon Solenoid
CP	charge parity
CR	control region
CSC	Cathode Strip Chamber
ECAL	Electromagnetic Calorimeter
EM	electromagnetic
EMB	Electromagnetic Barrel Calorimeter
EMEC	Electromagnetic End-cap Calorimeter
DESY	Deutsches Elektronen-Synchrotron
FCal	Forward Calorimeter
FPGA	field-programmable gate array
FSR	final state radiation
HCAL	Hadronic Calorimeter
HEC	Hadronic End-cap Calorimeter
HL-LHC	High Luminosity Large Hadron Collider
HLT	High Level Trigger
IBL	Insertable B-Layer
ISR	initial state radiation
JVT	jet vertex tagger
LCW	local hadronic cell weighting
LHC	Large Hadron Collider
LHE	Les Houches Event
LEP	Large Electron-Positron Collider
LO	leading order
LSP	lightest supersymmetric particle
MDT	Monitored Drift Tube
MPI	multiple parton interactions

MSSM	Minimal Supersymmetric Standard Model
NLO	next-to-leading order
NNLO	next-to-next-to-leading order
NP	nuisance parameter
PDF	parton distribution function
QCD	quantum chromodynamics
QED	quantum electrodynamics
QFT	quantum field theory
RPC	Resistive Plate Chambers
SCT	Semiconductor Tracker
SM	Standard Model
SUSY	Supersymmetry
TES	$\tau_{\text{had-vis}}$ energy scale
TGC	Thin Gap Chambers
TRT	Transition Radiation Tracker
VEV	vacuum expectation value
WIMP	weakly interacting massive particle

Bibliography

- [1] Murray Gell-Mann, *A Schematic Model of Baryons and Mesons*, Phys. Lett. 8 (1964), pp. 214–215. DOI: 10.1016/S0031-9163(64)92001-3.
- [2] G. Zweig, “An SU(3) model for strong interaction symmetry and its breaking. Version 2”. In: *DEVELOPMENTS IN THE QUARK THEORY OF HADRONS. VOL. 1. 1964 - 1978*. Ed. by D.B. Lichtenberg and Simon Peter Rosen. 1964, pp. 22–101. URL: <https://cds.cern.ch/record/570209>.
- [3] H. Fritzsch, Murray Gell-Mann, and H. Leutwyler, *Advantages of the Color Octet Gluon Picture*, Phys. Lett. B47 (1973), pp. 365–368. DOI: 10.1016/0370-2693(73)90625-4.
- [4] David J. Gross and Frank Wilczek, *Ultraviolet Behavior of Non-Abelian Gauge Theories*, Phys. Rev. Lett. 30 (26 June 1973), pp. 1343–1346. DOI: 10.1103/PhysRevLett.30.1343.
- [5] H. David Politzer, *Reliable Perturbative Results for Strong Interactions?*, Phys. Rev. Lett. 30 (26 June 1973), pp. 1346–1349. DOI: 10.1103/PhysRevLett.30.1346.
- [6] Sheldon L. Glashow, *Partial-symmetries of weak interactions*, Nuclear Physics 22.4 (Feb. 1961), pp. 579–588. DOI: 10.1016/0029-5582(61)90469-2.
- [7] Steven Weinberg, *A Model of Leptons*, Physical Review Letters 19.21 (Nov. 1967), pp. 1264–1266. DOI: 10.1103/PhysRevLett.19.1264.
- [8] Abdus Salam, “Weak and electromagnetic interactions”. In: *Elementary particle theory: Relativistic groups and analyticity. Proceedings of the Eighth Nobel Symposium held May 19-25, 1968 at Aspenäs garden, Lerum, in the county of Älvsborg, Sweden*. Nobel symposium. Almqvist & Wiksell, 1968.
- [9] Nicola Cabibbo, *Unitary Symmetry and Leptonic Decays*, Phys. Rev. Lett. 10 (12 June 1963), pp. 531–533. DOI: 10.1103/PhysRevLett.10.531.
- [10] Makoto Kobayashi and Toshihide Maskawa, *CP Violation in the Renormalizable Theory of Weak Interaction*, Prog. Theor. Phys. 49 (1973), pp. 652–657. DOI: 10.1143/PTP.49.652.

- [11] G. S. Guralnik, C. R. Hagen, and T. W. B. Kibble, *Global Conservation Laws and Massless Particles*, Phys. Rev. Lett. 13 (20 Nov. 1964), pp. 585–587. DOI: 10.1103/PhysRevLett.13.585.
- [12] F. Englert and R. Brout, *Broken Symmetry and the Mass of Gauge Vector Mesons*, Physical Review Letters 13.9 (Aug. 1964), pp. 321–323. DOI: 10.1103/PhysRevLett.13.321.
- [13] Peter Higgs, *Broken Symmetries and the Masses of Gauge Bosons*, Physical Review Letters 13.16 (Oct. 1964), pp. 508–509. DOI: 10.1103/PhysRevLett.13.508.
- [14] ATLAS Collaboration, *Observation of a new particle in the search for the Standard Model Higgs boson with the ATLAS detector at the LHC*, Phys. Lett. B716 (2012), pp. 1–29. DOI: 10.1016/j.physletb.2012.08.020. arXiv: 1207.7214 [hep-ex].
- [15] CMS Collaboration, *Observation of a new boson at a mass of 125 GeV with the CMS experiment at the LHC*, Phys. Lett. B716 (2012), pp. 30–61. DOI: 10.1016/j.physletb.2012.08.021. arXiv: 1207.7235 [hep-ex].
- [16] Planck Collaboration, *Planck 2015 results. XIII. Cosmological parameters*, Astron. Astrophys. 594 (2016), A13. DOI: 10.1051/0004-6361/201525830. arXiv: 1502.01589 [astro-ph.CO].
- [17] Stephen P. Martin, “A Supersymmetry Primer”. In: *Perspectives on Supersymmetry II*. World Scientific, 2011, pp. 1–153. DOI: 10.1142/9789814307505_0001. arXiv: hep-ph/9709356.
- [18] Lyndon Evans and Philip Bryant, *LHC Machine*, JINST 3 (2008), S08001. DOI: 10.1088/1748-0221/3/08/S08001.
- [19] ATLAS Collaboration, *The ATLAS Experiment at the CERN Large Hadron Collider*, JINST 3 (2008), S08003. DOI: 10.1088/1748-0221/3/08/S08003.
- [20] ALEPH, DELPHI, L3, OPAL Collaborations and LEP Working Group for Higgs Boson Searches, *Search for neutral MSSM Higgs bosons at LEP*, Eur. Phys. J. C47 (2006), pp. 547–587. DOI: 10.1140/epjc/s2006-02569-7. arXiv: hep-ex/0602042.
- [21] CDF Collaboration, *Search for Higgs Bosons Produced in Association with b-quarks*, Phys. Rev. D85 (2012), p. 032005. DOI: 10.1103/PhysRevD.85.032005. arXiv: 1106.4782 [hep-ex].
- [22] D0 Collaboration, *Search for neutral Higgs bosons in the multi-b-jet topology in 5.2 fb⁻¹ of pp collisions at $\sqrt{s} = 1.96$ TeV*, Phys. Lett. B698 (2011), pp. 97–104. DOI: 10.1016/j.physletb.2011.02.062. arXiv: 1011.1931 [hep-ex].

-
- [23] CDF and D0 Collaborations, Tevatron New Phenomena & Higgs Working Group, *Search for Neutral Higgs Bosons in Events with Multiple Bottom Quarks at the Tevatron*, Phys. Rev. D86 (2012), p. 091101. DOI: 10.1103/PhysRevD.86.091101. arXiv: 1207.2757 [hep-ex].
- [24] ATLAS Collaboration, *Search for neutral MSSM Higgs bosons decaying to $\tau^+\tau^-$ pairs in proton-proton collisions at $\sqrt{s} = 7$ TeV with the ATLAS detector*, Phys. Lett. B705 (2011), pp. 174–192. DOI: 10.1016/j.physletb.2011.10.001. arXiv: 1107.5003 [hep-ex].
- [25] CMS Collaboration, *Search for Neutral MSSM Higgs Bosons Decaying to Tau Pairs in pp Collisions at $\sqrt{s} = 7$ TeV*, Phys. Rev. Lett. 106 (2011), p. 231801. DOI: 10.1103/PhysRevLett.106.231801. arXiv: 1104.1619 [hep-ex].
- [26] ATLAS Collaboration, *Constraints on new phenomena via Higgs boson couplings and invisible decays with the ATLAS detector*, JHEP 11 (2015), p. 206. DOI: 10.1007/JHEP11(2015)206. arXiv: 1509.00672 [hep-ex].
- [27] CMS Collaboration, *Summary results of high mass BSM Higgs searches using CMS run-I data*. Tech. rep. CMS-PAS-HIG-16-007. Geneva: CERN, 2016. URL: <http://cds.cern.ch/record/2142432>.
- [28] C. Patrignani et al. (Particle Data Group), *Review of Particle Physics*, Chin. Phys. C40.10 (2016), p. 100001. DOI: 10.1088/1674-1137/40/10/100001.
- [29] Abdelhak Djouadi, *The Anatomy of electro-weak symmetry breaking. I: The Higgs boson in the standard model*, Phys. Rept. 457 (2008), pp. 1–216. DOI: 10.1016/j.physrep.2007.10.004. arXiv: hep-ph/0503172.
- [30] S. F. Novaes, “Standard model: An Introduction”. In: *Particles and fields. Proceedings, 10th Jorge Andre Swieca Summer School, Sao Paulo, Brazil, February 6-12, 1999*. 1999, pp. 5–102. arXiv: hep-ph/0001283.
- [31] Ettore Majorana, *Teoria simmetrica dell’elettrone e del positrone*, Il Nuovo Cimento (1924-1942) 14.4 (1937), p. 171. DOI: 10.1007/BF02961314.
- [32] F. Wilczek, *Majorana returns*, Nature Physics 5 (Sept. 2009), pp. 614–618. DOI: 10.1038/nphys1380.
- [33] B. Pontecorvo, *Inverse beta processes and nonconservation of lepton charge*, Sov. Phys. JETP 7 (1958). [Zh. Eksp. Teor. Fiz.34,247(1957)], pp. 172–173.
- [34] Ziro Maki, Masami Nakagawa, and Shoichi Sakata, *Remarks on the Unified Model of Elementary Particles*, Progress of Theoretical Physics 28.5 (1962), p. 870. DOI: 10.1143/PTP.28.870.
- [35] Tadao Nakano and Kazuhiko Nishijima, *Charge Independence for V-particles**, Progress of Theoretical Physics 10.5 (1953), p. 581. DOI: 10.1143/PTP.10.581.
-

- [36] M. Gell-Mann, *The interpretation of the new particles as displaced charge multiplets*, Il Nuovo Cimento (1955-1965) 4.2 (1956), pp. 848–866. DOI: 10.1007/BF02748000.
- [37] Marco Drewes, *The Phenomenology of Right Handed Neutrinos*, Int. J. Mod. Phys. E22 (2013), p. 1330019. DOI: 10.1142/S0218301313300191. arXiv: 1303.6912 [hep-ph].
- [38] K. A. Olive et al. (Particle Data Group), *Review of Particle Physics*, Chin. Phys. C38 (2014), p. 090001. DOI: 10.1088/1674-1137/38/9/090001.
- [39] G. Arnison et al. (UA1 Collaboration), *Experimental observation of isolated large transverse energy electrons with associated missing energy at $\sqrt{s}=540$ GeV*, Physics Letters B 122.1 (1983), pp. 103–116. DOI: 10.1016/0370-2693(83)91177-2.
- [40] M. Banner et al. (UA2 Collaboration), *Observation of single isolated electrons of high transverse momentum in events with missing transverse energy at the CERN $\bar{p}p$ collider*, Physics Letters B 122.5–6 (1983), pp. 476–485. DOI: 10.1016/0370-2693(83)91605-2.
- [41] G. Arnison et al. (UA1 Collaboration), *Experimental observation of lepton pairs of invariant mass around $95 \text{ GeV}/c^2$ at the CERN SPS collider*, Physics Letters B 126.5 (1983), pp. 398–410. DOI: 10.1016/0370-2693(83)90188-0.
- [42] P. Bagnaia et al. (UA2 Collaboration), *Evidence for $Z^0 \rightarrow e^+e^-$ at the CERN $\bar{p}p$ collider*, Physics Letters B 129.1 (1983), pp. 130–140. DOI: 10.1016/0370-2693(83)90744-X.
- [43] R. Brandelik et al. (TASSO Collaboration), *Evidence for Planar Events in e^+e^- Annihilation at High Energies*, Phys. Lett. B86 (1979), pp. 243–249. DOI: 10.1016/0370-2693(79)90830-X.
- [44] D. P. Barber et al. (MARK-J Collaboration), *Discovery of Three-Jet Events and a Test of Quantum Chromodynamics at PETRA*, Phys. Rev. Lett. 43 (1979), p. 830. DOI: 10.1103/PhysRevLett.43.830.
- [45] Christoph Berger et al. (PLUTO Collaboration), *Evidence for Gluon Bremsstrahlung in e^+e^- Annihilations at High Energies*, Phys. Lett. B86 (1979), pp. 418–425. DOI: 10.1016/0370-2693(79)90869-4.
- [46] W. Bartel et al. (JADE Collaboration), *Observation of Planar Three-Jet Events in e^+e^- Annihilation and Evidence for Gluon Bremsstrahlung*, Phys. Lett. B91 (1980), pp. 142–147. DOI: 10.1016/0370-2693(80)90680-2.
- [47] Tatsumi Aoyama, Masashi Hayakawa, Toichiro Kinoshita, and Makiko Nio, *Tenth-Order QED Contribution to the Electron $g-2$ and an Improved Value of the Fine Structure Constant*, Phys. Rev. Lett. 109 (2012), p. 111807. DOI: 10.1103/PhysRevLett.109.111807. arXiv: 1205.5368 [hep-ph].

-
- [48] Sebastian de Haro, Dennis Dieks, Gerard 't Hooft, and Erik Verlinde, *Forty Years of String Theory Reflecting on the Foundations*, Foundations of Physics 43.1 (2013), pp. 1–7. DOI: 10.1007/s10701-012-9691-3.
- [49] V. C. Rubin, W. K. Ford Jr., and N. Thonnard, *Rotational properties of 21 SC galaxies with a large range of luminosities and radii, from NGC 4605 / $R = 4\text{kpc}$ / to UGC 2885 / $R = 122\text{kpc}$ /*, The Astrophysical Journal 238 (June 1980), pp. 471–487. DOI: 10.1086/158003.
- [50] Massimo Persic, Paolo Salucci, and Fulvio Stel, *The Universal rotation curve of spiral galaxies: 1. The Dark matter connection*, Mon. Not. Roy. Astron. Soc. 281 (1996), p. 27. DOI: 10.1093/mnras/278.1.27. arXiv: astro-ph/9506004.
- [51] Bernard Carr, Florian Kuhnel, and Marit Sandstad, *Primordial Black Holes as Dark Matter*, Phys. Rev. D 94.8 (2016), p. 083504. DOI: 10.1103/PhysRevD.94.083504. arXiv: 1607.06077 [astro-ph.CO].
- [52] Matthew J. Strassler and Kathryn M. Zurek, *Echoes of a hidden valley at hadron colliders*, Phys. Lett. B 651 (2007), pp. 374–379. DOI: 10.1016/j.physletb.2007.06.055. arXiv: hep-ph/0604261.
- [53] Svend Erik Rugh and Henrik Zinkernagel, *The Quantum Vacuum and the Cosmological Constant Problem*, Stud. Hist. Phil. Sci. B33 (2002), pp. 663–705. DOI: 10.1016/S1355-2198(02)00033-3. arXiv: hep-th/0012253.
- [54] G. W. Bennett et al. (Muon g-2 Collaboration), *Final report of the E821 muon anomalous magnetic moment measurement at BNL*, Phys. Rev. D 73 (7 Apr. 2006), p. 072003. DOI: 10.1103/PhysRevD.73.072003.
- [55] T. Gleisberg, S. Höche, F. Krauss, M. Schönherr, S. Schumann, F. Siegert, and J. Winter, *Event generation with SHERPA 1.1*, Journal of High Energy Physics 2009.02 (Feb. 2009), pp. 007–007. DOI: 10.1088/1126-6708/2009/02/007. arXiv: 0811.4622 [hep-ph].
- [56] Andy Buckley et al., *General-purpose event generators for LHC physics*. Jan. 2011. arXiv: 1101.2599 [hep-ph].
- [57] V.N. Gribov and L.N. Lipatov, *Deep inelastic $e p$ scattering in perturbation theory*, Sov. J. Nucl. Phys. 15 (1972), pp. 438–450.
- [58] Yuri L. Dokshitzer, *Calculation of the Structure Functions for Deep Inelastic Scattering and e^+e^- Annihilation by Perturbation Theory in Quantum Chromodynamics*, Sov. Phys. JETP 46 (1977), pp. 641–653.
- [59] G. Altarelli and G. Parisi, *Asymptotic freedom in parton language*, Nuclear Physics B 126.2 (Aug. 1977), pp. 298–318. DOI: 10.1016/0550-3213(77)90384-4.
-

- [60] Stefano Catani, Frank Krauss, Bryan R. Webber, and Ralf Kuhn, *QCD Matrix Elements + Parton Showers*, Journal of High Energy Physics 2001.11 (Nov. 2001), pp. 063–063. DOI: 10.1088/1126-6708/2001/11/063. arXiv: hep-ph/0109231.
- [61] Stefan Höche, Frank Krauss, Steffen Schumann, and Frank Siegert, *QCD matrix elements and truncated showers*, Journal of High Energy Physics 2009.05 (May 2009), pp. 053–053. DOI: 10.1088/1126-6708/2009/05/053. arXiv: 0903.1219 [hep-ph].
- [62] Michelangelo L. Mangano, Mauro Moretti, Fulvio Piccinini, and Michele Trecani, *Matching matrix elements and shower evolution for top-pair production in hadronic collisions*, Journal of High Energy Physics 2007.01 (Jan. 2007), pp. 013–013. DOI: 10.1088/1126-6708/2007/01/013. arXiv: hep-ph/0611129.
- [63] ATLAS Collaboration, *The ATLAS Simulation Infrastructure*, Eur. Phys. J. C70 (2010), pp. 823–874. DOI: 10.1140/epjc/s10052-010-1429-9. arXiv: 1005.4568 [physics.ins-det].
- [64] S. Agostinelli et al., *Geant4—a simulation toolkit*, Nuclear Instruments and Methods in Physics Research Section A: Accelerators, Spectrometers, Detectors and Associated Equipment 506.3 (2003), pp. 250–303. DOI: 10.1016/S0168-9002(03)01368-8.
- [65] M. Beckingham et al. (ATLAS Collaboration), *The simulation principle and performance of the ATLAS fast calorimeter simulation FastCaloSim*. Tech. rep. ATL-PHYS-PUB-2010-013. Geneva: CERN, Oct. 2010. URL: <http://cds.cern.ch/record/1300517>.
- [66] Ian J. R. Aitchison, *Supersymmetry and the MSSM: An Elementary introduction*. 2005. arXiv: hep-ph/0505105.
- [67] Rudolf Haag, Jan T. Łopuszański, and Martin Sohnius, *All possible generators of supersymmetries of the S-matrix*, Nuclear Physics B 88.2 (1975), pp. 257–274. DOI: 10.1016/0550-3213(75)90279-5.
- [68] Sidney Coleman and Jeffrey Mandula, *All Possible Symmetries of the S Matrix*, Phys. Rev. 159 (5 July 1967), pp. 1251–1256. DOI: 10.1103/PhysRev.159.1251.
- [69] Savas Dimopoulos, David Eichler, Rahim Esmailzadeh, and Glenn D. Starkman, *Getting a Charge Out of Dark Matter*, Phys. Rev. D41 (1990), p. 2388. DOI: 10.1103/PhysRevD.41.2388.
- [70] A. H. Chamseddine, R. Arnowitt, and Pran Nath, *Locally Supersymmetric Grand Unification*, Phys. Rev. Lett. 49 (14 Oct. 1982), pp. 970–974. DOI: 10.1103/PhysRevLett.49.970.
- [71] E. Bagnaschi, G. Degrandi, P. Slavich, and A. Vicini, *Higgs production via gluon fusion in the POWHEG approach in the SM and in the MSSM*, JHEP 02 (2012), p. 088. DOI: 10.1007/JHEP02(2012)088. arXiv: 1111.2854 [hep-ph].

-
- [72] Fabio Maltoni, Giovanni Ridolfi, and Maria Ubiali, *b-initiated processes at the LHC: a reappraisal*, JHEP 07 (2012). [Erratum: JHEP04,095(2013)], p. 022. DOI: 10.1007/JHEP07(2012)022. arXiv: 1203.6393 [hep-ph].
- [73] M. Wiesemann, R. Frederix, S. Frixione, V. Hirschi, F. Maltoni, and P. Torrielli, *Higgs production in association with bottom quarks*, JHEP 02 (2015), p. 132. DOI: 10.1007/JHEP02(2015)132. arXiv: 1409.5301 [hep-ph].
- [74] J. Alwall et al., *The automated computation of tree-level and next-to-leading order differential cross sections, and their matching to parton shower simulations*, JHEP 07 (2014), p. 079. DOI: 10.1007/JHEP07(2014)079. arXiv: 1405.0301 [hep-ph].
- [75] Torbjörn Sjöstrand et al., *An Introduction to PYTHIA 8.2*, Comput. Phys. Commun. 191 (2015), pp. 159–177. DOI: 10.1016/j.cpc.2015.01.024. arXiv: 1410.3012 [hep-ph].
- [76] Stefano Frixione and Bryan R. Webber, *Matching NLO QCD computations and parton shower simulations*, JHEP 06 (2002), p. 029. DOI: 10.1088/1126-6708/2002/06/029. arXiv: hep-ph/0204244.
- [77] Robert Harlander, Michael Kramer, and Markus Schumacher, *Bottom-quark associated Higgs-boson production: reconciling the four- and five-flavour scheme approach*. 2011. arXiv: 1112.3478 [hep-ph].
- [78] Hung-Liang Lai, Marco Guzzi, Joey Huston, Zhao Li, Pavel M. Nadolsky, Jon Pumplin, and C. -P. Yuan, *New parton distributions for collider physics*, Phys. Rev. D82 (2010), p. 074024. DOI: 10.1103/PhysRevD.82.074024. arXiv: 1007.2241 [hep-ph].
- [79] Richard D. Ball et al., *Parton distributions with LHC data*, Nucl. Phys. B867 (2013), pp. 244–289. DOI: 10.1016/j.nuclphysb.2012.10.003. arXiv: 1207.1303 [hep-ph].
- [80] J. Pumplin, D. R. Stump, J. Huston, H. L. Lai, Pavel M. Nadolsky, and W. K. Tung, *New generation of parton distributions with uncertainties from global QCD analysis*, JHEP 07 (2002), p. 012. DOI: 10.1088/1126-6708/2002/07/012. arXiv: hep-ph/0201195.
- [81] S. Heinemeyer, W. Hollik, and G. Weiglein, *FeynHiggs: A Program for the calculation of the masses of the neutral CP even Higgs bosons in the MSSM*, Comput. Phys. Commun. 124 (2000), pp. 76–89. DOI: 10.1016/S0010-4655(99)00364-1. arXiv: hep-ph/9812320.
- [82] S. Heinemeyer, W. Hollik, and G. Weiglein, *The Masses of the neutral CP - even Higgs bosons in the MSSM: Accurate analysis at the two loop level*, Eur. Phys. J. C9 (1999), pp. 343–366. DOI: 10.1007/s100529900006. arXiv: hep-ph/9812472.
-

- [83] G. Degrandi, S. Heinemeyer, W. Hollik, P. Slavich, and G. Weiglein, *Towards high precision predictions for the MSSM Higgs sector*, Eur. Phys. J. C28 (2003), pp. 133–143. DOI: 10.1140/epjc/s2003-01152-2. arXiv: hep-ph/0212020.
- [84] M. Frank, T. Hahn, S. Heinemeyer, W. Hollik, H. Rzehak, and G. Weiglein, *The Higgs Boson Masses and Mixings of the Complex MSSM in the Feynman-Diagrammatic Approach*, JHEP 02 (2007), p. 047. DOI: 10.1088/1126-6708/2007/02/047. arXiv: hep-ph/0611326.
- [85] T. Hahn, S. Heinemeyer, W. Hollik, H. Rzehak, and G. Weiglein, *High-Precision Predictions for the Light CP -Even Higgs Boson Mass of the Minimal Supersymmetric Standard Model*, Phys. Rev. Lett. 112.14 (2014), p. 141801. DOI: 10.1103/PhysRevLett.112.141801. arXiv: 1312.4937 [hep-ph].
- [86] Henning Bahl and Wolfgang Hollik, *Precise prediction for the light MSSM Higgs boson mass combining effective field theory and fixed-order calculations*, Eur. Phys. J. C76.9 (2016), p. 499. DOI: 10.1140/epjc/s10052-016-4354-8. arXiv: 1608.01880 [hep-ph].
- [87] D. de Florian et al. (LHC Higgs Cross Section Working Group), *Handbook of LHC Higgs Cross Sections: 4. Deciphering the Nature of the Higgs Sector*. 2016. arXiv: 1610.07922 [hep-ph].
- [88] A. Djouadi, L. Maiani, G. Moreau, A. Polosa, J. Quevillon, and V. Riquer, *The post-Higgs MSSM scenario: Habemus MSSM?*, Eur. Phys. J. C73 (2013), p. 2650. DOI: 10.1140/epjc/s10052-013-2650-0. arXiv: 1307.5205 [hep-ph].
- [89] A. Djouadi, L. Maiani, A. Polosa, J. Quevillon, and V. Riquer, *Fully covering the MSSM Higgs sector at the LHC*, JHEP 06 (2015), p. 168. DOI: 10.1007/JHEP06(2015)168. arXiv: 1502.05653 [hep-ph].
- [90] Robert V. Harlander, Stefan Liebler, and Hendrik Mantler, *SusHi: A program for the calculation of Higgs production in gluon fusion and bottom-quark annihilation in the Standard Model and the MSSM*, Comput. Phys. Commun. 184 (2013), pp. 1605–1617. DOI: 10.1016/j.cpc.2013.02.006. arXiv: 1212.3249 [hep-ph].
- [91] M. Spira, A. Djouadi, D. Graudenz, and P. M. Zerwas, *Higgs boson production at the LHC*, Nucl. Phys. B453 (1995), pp. 17–82. DOI: 10.1016/0550-3213(95)00379-7. arXiv: hep-ph/9504378.
- [92] Robert Harlander and Philipp Kant, *Higgs production and decay: Analytic results at next-to-leading order QCD*, JHEP 12 (2005), p. 015. DOI: 10.1088/1126-6708/2005/12/015. arXiv: hep-ph/0509189.
- [93] Robert V. Harlander and William B. Kilgore, *Next-to-next-to-leading order Higgs production at hadron colliders*, Phys. Rev. Lett. 88 (2002), p. 201801. DOI: 10.1103/PhysRevLett.88.201801. arXiv: hep-ph/0201206.

-
- [94] Robert V. Harlander and William B. Kilgore, *Production of a pseudoscalar Higgs boson at hadron colliders at next-to-next-to leading order*, JHEP 10 (2002), p. 017. DOI: 10.1088/1126-6708/2002/10/017. arXiv: hep-ph/0208096.
- [95] U. Aglietti, R. Bonciani, G. Degrassi, and A. Vicini, *Two loop light fermion contribution to Higgs production and decays*, Phys. Lett. B595 (2004), pp. 432–441. DOI: 10.1016/j.physletb.2004.06.063. arXiv: hep-ph/0404071.
- [96] R. Bonciani, G. Degrassi, and A. Vicini, *On the Generalized Harmonic Polylogarithms of One Complex Variable*, Comput. Phys. Commun. 182 (2011), pp. 1253–1264. DOI: 10.1016/j.cpc.2011.02.011. arXiv: 1007.1891 [hep-ph].
- [97] Robert V. Harlander and William B. Kilgore, *Higgs boson production in bottom quark fusion at next-to-next-to leading order*, Phys. Rev. D68 (2003), p. 013001. DOI: 10.1103/PhysRevD.68.013001. arXiv: hep-ph/0304035.
- [98] Stefan Dittmaier, Michael Krämer, and Michael Spira, *Higgs radiation off bottom quarks at the Tevatron and the CERN LHC*, Phys. Rev. D70 (2004), p. 074010. DOI: 10.1103/PhysRevD.70.074010. arXiv: hep-ph/0309204.
- [99] S. Dawson, C. B. Jackson, L. Reina, and D. Wackeroth, *Exclusive Higgs boson production with bottom quarks at hadron colliders*, Phys. Rev. D69 (2004), p. 074027. DOI: 10.1103/PhysRevD.69.074027. arXiv: hep-ph/0311067.
- [100] S. Heinemeyer, W. Hollik, and G. Weiglein, *Constraints on $\tan \beta$ in the MSSM from the upper bound on the mass of the lightest Higgs boson*, JHEP 06 (2000), p. 009. DOI: 10.1088/1126-6708/2000/06/009. arXiv: hep-ph/9909540.
- [101] M. Carena, S. Heinemeyer, O. Stål, C. E. M. Wagner, and G. Weiglein, *MSSM Higgs Boson Searches at the LHC: Benchmark Scenarios after the Discovery of a Higgs-like Particle*, Eur. Phys. J. C73.9 (2013), p. 2552. DOI: 10.1140/epjc/s10052-013-2552-1. arXiv: 1302.7033 [hep-ph].
- [102] ATLAS Collaboration, *Search for the Supersymmetric Partner of the Top Quark in the $Jets+E_T^{miss}$ Final State at $\sqrt{s} = 13$ TeV*. Tech. rep. ATLAS-CONF-2016-077. Geneva: CERN, Aug. 2016. URL: <http://cds.cern.ch/record/2206250>.
- [103] ATLAS Collaboration, *Search for top squarks in final states with one isolated lepton, jets, and missing transverse momentum in $\sqrt{s} = 13$ TeV pp collisions with the ATLAS detector*. Tech. rep. ATLAS-CONF-2016-050. Geneva: CERN, Aug. 2016. URL: <http://cds.cern.ch/record/2206132>.
- [104] ATLAS Collaboration, *Search for direct top squark pair production and dark matter production in final states with two leptons in $\sqrt{s} = 13$ TeV pp collisions using 13.3 fb^{-1} of ATLAS data*. Tech. rep. ATLAS-CONF-2016-076. Geneva: CERN, Aug. 2016. URL: <http://cds.cern.ch/record/2206249>.
-

- [105] ATLAS Collaboration, *Search for direct top squark pair production in events with a Z boson, b-jets and missing transverse momentum in $\sqrt{s}=13$ TeV pp collisions with the ATLAS detector*. Tech. rep. ATLAS-CONF-2016-038. Geneva: CERN, Aug. 2016. URL: <http://cds.cern.ch/record/2205747>.
- [106] ATLAS Collaboration, *Measurement of fiducial, differential and production cross sections in the $H \rightarrow \gamma\gamma$ decay channel with 13.3 fb^{-1} of 13 TeV proton-proton collision data with the ATLAS detector*. Tech. rep. ATLAS-CONF-2016-067. Geneva: CERN, Aug. 2016. URL: <http://cds.cern.ch/record/2206210>.
- [107] CMS Collaboration, *Updated measurements of Higgs boson production in the diphoton decay channel at $\sqrt{s} = 13$ TeV in pp collisions at CMS*. Tech. rep. CMS-PAS-HIG-16-020. Geneva: CERN, 2016. URL: <https://cds.cern.ch/record/2205275>.
- [108] A. Djouadi, J. Kalinowski, and M. Spira, *HDECAY: A Program for Higgs boson decays in the standard model and its supersymmetric extension*, Comput. Phys. Commun. 108 (1998), pp. 56–74. DOI: 10.1016/S0010-4655(97)00123-9. arXiv: [hep-ph/9704448](https://arxiv.org/abs/hep-ph/9704448).
- [109] Philip Bechtle, Howard E. Haber, Sven Heinemeyer, Oscar Stål, Tim Stefaniak, Georg Weiglein, and Lisa Zeune, *The Light and Heavy Higgs Interpretation of the MSSM*. 2016. arXiv: 1608.00638 [hep-ph].
- [110] S. van der Meer, *Stochastic damping of betatron oscillations in the ISR*. Tech. rep. ISR-PO-72-31. Geneva: CERN, Aug. 1972. URL: <http://cds.cern.ch/record/312939>.
- [111] Oliver Sim Brüning, Paul Collier, P. Lebrun, Stephen Myers, Ranko Ostojic, John Poole, and Paul Proudlock, *LHC Design Report, Volume 1: The LHC Main Ring*. Geneva: CERN, 2004. URL: <http://cds.cern.ch/record/782076>.
- [112] Mike Lamont, “The First Years of LHC Operation for Luminosity Production”. In: *Proceedings, 4th International Particle Accelerator Conference (IPAC 2013): Shanghai, China, May 12-17, 2013*. 2013. URL: <https://cds.cern.ch/record/2010134>.
- [113] CMS Collaboration, *The CMS experiment at the CERN LHC*, Journal of Instrumentation 3.08 (2008), S08004. DOI: 10.1088/1748-0221/3/08/S08004.
- [114] A. Siemko, *Magnet Quench Process*. 2001. URL: <https://cds.cern.ch/record/567209>.
- [115] CERN, *Restarting the LHC: Why 13 TeV?* June 2014. URL: <https://cds.cern.ch/record/1998739>.
- [116] CERN, *Accelerator Performance and Statistics*. 2016. URL: <https://acc-stats.web.cern.ch/> (visited on 09/07/2016).

- [117] Michael Benedikt, Paul Collier, V Mertens, John Poole, and Karlheinz Schindl, *LHC Design Report, Volume 3: The LHC Injector Chain*. Geneva: CERN, 2004. URL: <https://cds.cern.ch/record/823808>.
- [118] E. Boltezar et al., *Performance of the New CERN 50 MeV Linac*, IEEE Trans. Nucl. Sci. 26 (1979), pp. 3674–3676. DOI: 10.1109/TNS.1979.4330576.
- [119] L. Arnaudon et al., *Linac4 Technical Design Report*. Tech. rep. CERN-AB-2006-084. Geneva: CERN, Dec. 2006. URL: <https://cds.cern.ch/record/1004186>.
- [120] I. Bejar Alonso and L. Rossi, *HiLumi LHC Technical Design Report*. Tech. rep. CERN-ACC-2015-0140. CERN, Nov. 2015. URL: <https://cds.cern.ch/record/2069130>.
- [121] K. H. Reich, *The CERN Proton Synchrotron Booster*, IEEE Trans. Nucl. Sci. 16 (1969), pp. 959–961. DOI: 10.1109/TNS.1969.4325414.
- [122] Michael Barnes et al., *The PS complex as proton pre-injector for the LHC: design and implementation report*. Geneva: CERN, 2000. URL: <https://cds.cern.ch/record/449242>.
- [123] Jean-Paul Burnet et al., *Fifty years of the CERN Proton Synchrotron: Volume 1*. Geneva: CERN, 2011. URL: <https://cds.cern.ch/record/1359959>.
- [124] K. Hanke et al., *Status of the LIU project at CERN*. CERN-ACC-2014-0125. June 2014. URL: <https://cds.cern.ch/record/1742199>.
- [125] Cinzia De Melis, *The CERN accelerator complex. Complexe des accélérateurs du CERN*. OPEN-PHO-ACCEL-2016-009. July 2016. URL: <https://cds.cern.ch/record/2197559>.
- [126] ATLAS Collaboration, *Studies related to gender and geographic diversity in the ATLAS Collaboration*. Tech. rep. ATL-GEN-PUB-2016-001. Geneva: CERN, July 2016. URL: <https://cds.cern.ch/record/2202392>.
- [127] CERN, *ATLAS: Letter of intent for a general purpose p p experiment at the large hadron collider at CERN*. CERN-LHCC-92-04, CERN-LHCC-I-2. 1992. URL: <https://cds.cern.ch/record/291061>.
- [128] ATLAS Collaboration, *ATLAS: technical proposal for a general-purpose pp experiment at the Large Hadron Collider at CERN*. LHC Tech. Proposal. Geneva: CERN, 1994. URL: <https://cds.cern.ch/record/290968>.
- [129] Joao Pequeno, *Computer generated image of the whole ATLAS detector*. CERN-GE-0803012. Mar. 2008. URL: <https://cds.cern.ch/record/1095924>.
- [130] Lorenz Hauswald, *Systematic and Experimental Uncertainties in the Search for Neutral MSSM Higgs Bosons Decaying to Two Tau Leptons*, diploma thesis. TU Dresden, 2013.

- [131] M. Capeans et al., *ATLAS Insertable B-Layer Technical Design Report*. Tech. rep. CERN-LHCC-2010-013. ATLAS-TDR-19. CERN, Sept. 2010. URL: <https://cds.cern.ch/record/1291633>.
- [132] S. McMahon, P. Allport, H. Hayward, and B. Di Girolamo, *Initial Design Report of the ITk*. Tech. rep. ATL-COM-UPGRADE-2014-029. Geneva: CERN, Oct. 2014. URL: <https://cds.cern.ch/record/1952548>.
- [133] Bartosz Mindur (ATLAS Collaboration), *ATLAS Transition Radiation Tracker (TRT): Straw Tubes for Tracking and Particle Identification at the Large Hadron Collider*. Tech. rep. ATL-INDET-PROC-2016-001. Geneva: CERN, Mar. 2016. URL: <https://cds.cern.ch/record/2139567>.
- [134] Joao Pequeno, *Computer generated image of the ATLAS inner detector*. CERN-GE-0803014. Mar. 2008. URL: <https://cds.cern.ch/record/1095926>.
- [135] Joao Pequeno, *Computer Generated image of the ATLAS calorimeter*. CERN-GE-0803015. Mar. 2008. URL: <https://cds.cern.ch/record/1095927>.
- [136] ATLAS Collaboration, *ATLAS Phase-II Upgrade Scoping Document*. Tech. rep. CERN-LHCC-2015-020. LHCC-G-166. Geneva: CERN, Sept. 2015. URL: <https://cds.cern.ch/record/2055248>.
- [137] Joao Pequeno, *Computer generated image of the ATLAS Muons subsystem*. CERN-GE-0803017. Mar. 2008. URL: <https://cds.cern.ch/record/1095929>.
- [138] Aranzazu Ruiz-Martinez (ATLAS Collaboration), *The Run-2 ATLAS Trigger System*. Tech. rep. ATL-DAQ-PROC-2016-003. Geneva: CERN, Feb. 2016. URL: <https://cds.cern.ch/record/2133909>.
- [139] Yu Nakahama (ATLAS Collaboration), *The ATLAS Trigger System: Ready for Run-2*, Journal of Physics: Conference Series 664.8 (2015), p. 082037. DOI: 10.1088/1742-6596/664/8/082037.
- [140] M. Shochet, L. Tompkins, V. Cavaliere, P. Giannetti, A. Annovi, and G. Volpi, *Fast TracKer (FTK) Technical Design Report*. Tech. rep. CERN-LHCC-2013-007. ATLAS-TDR-021. CERN, June 2013. URL: <https://cds.cern.ch/record/1552953>.
- [141] ATLAS Collaboration, *Technical Design Report for the Phase-I Upgrade of the ATLAS TDAQ System*. Tech. rep. CERN-LHCC-2013-018. ATLAS-TDR-023. CERN, Sept. 2013. URL: <https://cds.cern.ch/record/1602235>.
- [142] Oleksandr Viazlo (ATLAS LUCID Collaboration), “ATLAS LUCID detector upgrade for LHC Run 2”. In: *Proceedings, 2015 European Physical Society Conference on High Energy Physics (EPS-HEP 2015): Vienna, Austria, July 22-29, 2015*. Vol. EPS-HEP2015. 2015, p. 275. URL: <https://cds.cern.ch/record/2062038>.

-
- [143] V. Cindro et al., *The ATLAS beam conditions monitor*, JINST 3 (2008), P02004. DOI: 10.1088/1748-0221/3/02/P02004.
- [144] S. Abdel Khalek et al., *The ALFA Roman Pot Detectors of ATLAS*, JINST 11.11 (2016), P11013. DOI: 10.1088/1748-0221/11/11/P11013. arXiv: 1609.00249 [physics.ins-det].
- [145] T. Cornelissen, M. Elsing, S. Fleischmann, W. Liebig, E. Moyse, and A. Salzburger, *Concepts, Design and Implementation of the ATLAS New Tracking (NEWT)*. Tech. rep. ATL-SOFT-PUB-2007-007. ATL-COM-SOFT-2007-002. Geneva: CERN, Mar. 2007. URL: <http://cds.cern.ch/record/1020106>.
- [146] T. Cornelissen, M. Elsing, I. Gavrilenko, W. Liebig, E. Moyse, and A. Salzburger, *The new ATLAS track reconstruction (NEWT)*, Journal of Physics: Conference Series 119.3 (2008), p. 032014. DOI: 10.1088/1742-6596/119/3/032014.
- [147] ATLAS Collaboration, *Early Inner Detector Tracking Performance in the 2015 data at $\sqrt{s} = 13$ TeV*. Tech. rep. ATL-PHYS-PUB-2015-051. Geneva: CERN, Dec. 2015. URL: <https://cds.cern.ch/record/2110140>.
- [148] G. Piacquadio, K. Prokofiev, and A. Wildauer, *Primary vertex reconstruction in the ATLAS experiment at LHC*, Journal of Physics: Conference Series 119.3 (2008), p. 032033. DOI: 10.1088/1742-6596/119/3/032033.
- [149] ATLAS Collaboration, *Vertex Reconstruction Performance of the ATLAS Detector at $\sqrt{s} = 13$ TeV*. Tech. rep. ATL-PHYS-PUB-2015-026. Geneva: CERN, July 2015. URL: <https://cds.cern.ch/record/2037717>.
- [150] ATLAS Collaboration, *Topological cell clustering in the ATLAS calorimeters and its performance in LHC Run 1*. 2016. arXiv: 1603.02934 [hep-ex].
- [151] Matteo Cacciari, Gavin P. Salam, and Gregory Soyez, *FastJet User Manual*, Eur. Phys. J. C72 (2012), p. 1896. DOI: 10.1140/epjc/s10052-012-1896-2. arXiv: 1111.6097 [hep-ph].
- [152] Matteo Cacciari, Gavin P. Salam, and Gregory Soyez, *The anti- k_t jet clustering algorithm*, JHEP 04 (2008), p. 063. DOI: 10.1088/1126-6708/2008/04/063. arXiv: 0802.1189 [hep-ph].
- [153] ATLAS (ATLAS Collaboration), *Jet Calibration and Systematic Uncertainties for Jets Reconstructed in the ATLAS Detector at $\sqrt{s} = 13$ TeV*. Tech. rep. ATL-PHYS-PUB-2015-015. Geneva: CERN, July 2015. URL: <https://cds.cern.ch/record/2037613>.
- [154] Craig Sawyer, Christopher John Young, Cigdem Issever, and David Lopez Mateos (ATLAS Collaboration), *Monte Carlo Calibration and Combination of In-situ Measurements of Jets in ATLAS*. Tech. rep. ATL-COM-PHYS-2015-071. [ATLAS internal document]. Geneva: CERN, Jan. 2015. URL: <https://cds.cern.ch/record/1987296>.
-

- [155] ATLAS Collaboration, *Jet energy measurement with the ATLAS detector in proton-proton collisions at $\sqrt{s} = 7$ TeV*, Eur. Phys. J. C73.3 (2013), p. 2304. DOI: 10.1140/epjc/s10052-013-2304-2. arXiv: 1112.6426 [hep-ex].
- [156] ATLAS Collaboration, *Performance of pile-up mitigation techniques for jets in pp collisions at $\sqrt{s} = 8$ TeV using the ATLAS detector*, Eur. Phys. J. C76.11 (2016), p. 581. DOI: 10.1140/epjc/s10052-016-4395-z. arXiv: 1510.03823 [hep-ex].
- [157] Jeffrey Rogers Dandoy et al. (ATLAS Collaboration), *Jet energy scale and resolution measurements and their systematic uncertainties in proton-proton collisions at $\sqrt{s} = 13$ TeV with the ATLAS detector*. Tech. rep. ATL-COM-PHYS-2016-213. [ATLAS internal document]. Geneva: CERN, Mar. 2016. URL: <https://cds.cern.ch/record/2136864>.
- [158] ATLAS Collaboration, *Public plots: Jet energy scale uncertainties updated for ICHEP 2016 using full 13 TeV 2015 dataset*. 2016. URL: <https://atlas.web.cern.ch/Atlas/GROUPS/PHYSICS/PLOTS/JETM-2016-010/> (visited on 08/11/2016).
- [159] ATLAS Collaboration, *Data-driven determination of the energy scale and resolution of jets reconstructed in the ATLAS calorimeters using dijet and multijet events at $\sqrt{s} = 8$ TeV*. Tech. rep. ATLAS-CONF-2015-017. Geneva: CERN, Apr. 2015. URL: <https://cds.cern.ch/record/2008678>.
- [160] ATLAS Collaboration, *Tagging and suppression of pileup jets with the ATLAS detector*. Tech. rep. ATLAS-CONF-2014-018. Geneva: CERN, May 2014. URL: <https://cds.cern.ch/record/1700870>.
- [161] ATLAS Collaboration, *JVT Public Plots for ICHEP 2016*. 2016. URL: <https://atlas.web.cern.ch/Atlas/GROUPS/PHYSICS/PLOTS/JETM-2016-011/> (visited on 08/01/2016).
- [162] ATLAS Collaboration, *Characterisation and mitigation of beam-induced backgrounds observed in the ATLAS detector during the 2011 proton-proton run*, JINST 8 (2013), P07004. DOI: 10.1088/1748-0221/8/07/P07004. arXiv: 1303.0223 [hep-ex].
- [163] ATLAS Collaboration, *Selection of jets produced in 13 TeV proton-proton collisions with the ATLAS detector*. Tech. rep. ATLAS-CONF-2015-029. Geneva: CERN, July 2015. URL: <http://cds.cern.ch/record/2037702>.
- [164] ATLAS Collaboration, *Expected performance of the ATLAS b-tagging algorithms in Run-2*. Tech. rep. ATL-PHYS-PUB-2015-022. Geneva: CERN, July 2015. URL: <https://cds.cern.ch/record/2037697>.

-
- [165] ATLAS Collaboration, *Optimisation of the ATLAS b-tagging performance for the 2016 LHC Run*. Tech. rep. ATL-PHYS-PUB-2016-012. Geneva: CERN, June 2016. URL: <https://cds.cern.ch/record/2160731>.
- [166] Andrew Stuart Bell et al. (ATLAS Collaboration), *Calibration of b-tagging using di-leptonic $t\bar{t}$ events produced in pp collisions at $\sqrt{s} = 13$ TeV and a combinatorial likelihood approach*. Tech. rep. ATL-COM-PHYS-2016-135. [ATLAS internal document]. Geneva: CERN, Feb. 2016. URL: <https://cds.cern.ch/record/2132351>.
- [167] M. Bosman, L. Fiorini, C. Helsens, A. Juste, L. Mir, J. Nadal, and V. Vorwerk (ATLAS Collaboration), *Weighting method to propagate heavy-flavor tagging calibrations and related uncertainties*. Tech. rep. ATL-COM-PHYS-2010-331. [ATLAS internal document]. Geneva: CERN, June 2010. URL: <https://cds.cern.ch/record/1269912>.
- [168] ATLAS Collaboration, *Muon reconstruction performance of the ATLAS detector in proton-proton collision data at $\sqrt{s} = 13$ TeV*, Eur. Phys. J. C76.5 (2016), p. 292. DOI: 10.1140/epjc/s10052-016-4120-y. arXiv: 1603.05598 [hep-ex].
- [169] ATLAS Collaboration, *Muon reconstruction performance of the ATLAS detector in proton-proton collision data at $\sqrt{s} = 13$ TeV*. 2016. URL: <https://atlas.web.cern.ch/Atlas/GROUPS/PHYSICS/PAPERS/PERF-2015-10/> (visited on 08/11/2016).
- [170] ATLAS Collaboration, *Electron efficiency measurements with the ATLAS detector using the 2015 LHC proton-proton collision data*. Tech. rep. ATLAS-CONF-2016-024. Geneva: CERN, June 2016. URL: <https://cds.cern.ch/record/2157687>.
- [171] ATLAS Collaboration, *Electron and photon energy calibration with the ATLAS detector using data collected in 2015 at $\sqrt{s} = 13$ TeV*. Tech. rep. ATL-PHYS-PUB-2016-015. Geneva: CERN, Aug. 2016. URL: <https://cds.cern.ch/record/2203514>.
- [172] ATLAS Collaboration, *Electron and photon energy calibration with the ATLAS detector using LHC Run 1 data*, Eur. Phys. J. C74.10 (2014), p. 3071. DOI: 10.1140/epjc/s10052-014-3071-4. arXiv: 1407.5063 [hep-ex].
- [173] ATLAS Collaboration, *Electron identification efficiency measured with $Z \rightarrow ee$ events using 2016 data*. 2016. URL: <https://atlas.web.cern.ch/Atlas/GROUPS/PHYSICS/PLOTS/EGAM-2016-002/> (visited on 08/11/2016).
- [174] ATLAS Collaboration, *Reconstruction, Energy Calibration, and Identification of Hadronically Decaying Tau Leptons in the ATLAS Experiment for Run-2 of the LHC*. Tech. rep. ATL-PHYS-PUB-2015-045. Geneva: CERN, Nov. 2015. URL: <https://cds.cern.ch/record/2064383>.
-

- [175] ATLAS Collaboration, *Identification and energy calibration of hadronically decaying tau leptons with the ATLAS experiment in pp collisions at $\sqrt{s}=8$ TeV*, Eur. Phys. J. C75.7 (2015), p. 303. DOI: 10.1140/epjc/s10052-015-3500-z. arXiv: 1412.7086 [hep-ex].
- [176] Andrzej Mikolaj Karamaoun (ATLAS Collaboration), “The Upgrade and Performance of the ATLAS Tau Triggers towards Run 2”. In: *Proceedings, 2015 European Physical Society Conference on High Energy Physics (EPS-HEP 2015): Vienna, Austria, July 22-29, 2015*. Vol. EPS-HEP2015. 2015, p. 268. URL: <https://cds.cern.ch/record/2058617>.
- [177] Benjamin Brunt et al. (ATLAS Collaboration), *Performance of missing transverse momentum reconstruction with the ATLAS detector using proton-proton collisions at $\sqrt{s} = 13$ TeV*. Tech. rep. ATL-COM-PHYS-2016-407. [ATLAS internal document]. Geneva: CERN, Apr. 2016. URL: <https://cds.cern.ch/record/2149445>.
- [178] ATLAS Collaboration, *Public plots: Missing transverse energy (E_T^{miss}) performance and systematic uncertainties using the full 2015 dataset*. 2016. URL: <https://atlas.web.cern.ch/Atlas/GROUPS/PHYSICS/PLOTS/JETM-2016-003/> (visited on 02/29/2016).
- [179] ATLAS Collaboration, *Public Plots: Missing Transverse Momentum Distribution and Performance in 2016 data*. 2016. URL: <https://atlas.web.cern.ch/Atlas/GROUPS/PHYSICS/PLOTS/JETM-2016-008/> (visited on 07/29/2016).
- [180] ATLAS Collaboration, *Monte Carlo Generators for the Production of a W or Z/γ^* Boson in Association with Jets at ATLAS in Run 2*. Tech. rep. ATL-PHYS-PUB-2016-003. Geneva: CERN, Jan. 2016. URL: <https://cds.cern.ch/record/2120133>.
- [181] Simone Alioli, Paolo Nason, Carlo Oleari, and Emanuele Re, *A general framework for implementing NLO calculations in shower Monte Carlo programs: the POWHEG BOX*, JHEP 06 (2010), p. 043. DOI: 10.1007/JHEP06(2010)043. arXiv: 1002.2581 [hep-ph].
- [182] Stefano Frixione, Paolo Nason, and Carlo Oleari, *Matching NLO QCD computations with Parton Shower simulations: the POWHEG method*, JHEP 11 (2007), p. 070. DOI: 10.1088/1126-6708/2007/11/070. arXiv: 0709.2092 [hep-ph].
- [183] Paolo Nason, *A New method for combining NLO QCD with shower Monte Carlo algorithms*, JHEP 11 (2004), p. 040. DOI: 10.1088/1126-6708/2004/11/040. arXiv: hep-ph/0409146.
- [184] Torbjorn Sjöstrand, Stephen Mrenna, and Peter Z. Skands, *A Brief Introduction to PYTHIA 8.1*, Comput. Phys. Commun. 178 (2008), p. 852. DOI: 10.1016/j.cpc.2008.01.036. arXiv: 0710.3820 [hep-ph].

-
- [185] ATLAS Collaboration, *Measurement of the Z/γ^* boson transverse momentum distribution in pp collisions at $\sqrt{s} = 7$ TeV with the ATLAS detector*, JHEP 09 (2014), p. 145. DOI: 10.1007/JHEP09(2014)145. arXiv: 1406.3660 [hep-ex].
- [186] N. Davidson, T. Przedzinski, and Z. Was, *PHOTOS Interface in C++: Technical and Physics Documentation*. 2010. arXiv: 1011.0937 [hep-ph].
- [187] Tanju Gleisberg and Stefan Höche, *Comix, a new matrix element generator*, JHEP 0812 (2008), p. 039. DOI: 10.1088/1126-6708/2008/12/039. arXiv: 0808.3674 [hep-ph].
- [188] Fabio Cascioli, Philipp Maierhofer, and Stefano Pozzorini, *Scattering Amplitudes with Open Loops*, Phys. Rev. Lett. 108 (2012), p. 111601. DOI: 10.1103/PhysRevLett.108.111601. arXiv: 1111.5206 [hep-ph].
- [189] Stefan Höche, Frank Krauss, Marek Schönherr, and Frank Siegert, *QCD matrix elements + parton showers: The NLO case*, JHEP 04 (2013), p. 027. DOI: 10.1007/JHEP04(2013)027. arXiv: 1207.5030 [hep-ph].
- [190] Steffen Schumann and Frank Krauss, *A Parton shower algorithm based on Catani-Seymour dipole factorisation*, JHEP 0803 (2008), p. 038. DOI: 10.1088/1126-6708/2008/03/038. arXiv: 0709.1027 [hep-ph].
- [191] Richard D. Ball et al. (NNPDF Collaboration), *Parton distributions for the LHC Run II*, JHEP 04 (2015), p. 040. DOI: 10.1007/JHEP04(2015)040. arXiv: 1410.8849 [hep-ph].
- [192] ATLAS Collaboration, *Multi-Boson Simulation for 13 TeV ATLAS Analyses*. Tech. rep. ATL-PHYS-PUB-2016-002. Geneva: CERN, Jan. 2016. URL: <https://cds.cern.ch/record/2119986>.
- [193] ATLAS Collaboration, *Simulation of top quark production for the ATLAS experiment at $\sqrt{s} = 13$ TeV*. Tech. rep. ATL-PHYS-PUB-2016-004. Geneva: CERN, Jan. 2016. URL: <https://cds.cern.ch/record/2120417>.
- [194] Stefano Frixione, Paolo Nason, and Giovanni Ridolfi, *A Positive-weight next-to-leading-order Monte Carlo for heavy flavour hadroproduction*, JHEP 09 (2007), p. 126. DOI: 10.1088/1126-6708/2007/09/126. arXiv: 0707.3088 [hep-ph].
- [195] Emanuele Re, *Single-top Wt -channel production matched with parton showers using the POWHEG method*, Eur. Phys. J. C71 (2011), p. 1547. DOI: 10.1140/epjc/s10052-011-1547-z. arXiv: 1009.2450 [hep-ph].
- [196] Simone Alioli, Paolo Nason, Carlo Oleari, and Emanuele Re, *NLO single-top production matched with shower in POWHEG: s - and t -channel contributions*, JHEP 09 (2009). [Erratum: JHEP02,011(2010)], p. 111. DOI: 10.1088/1126-6708/2009/09/111. arXiv: 0907.4076 [hep-ph].
-

- [197] Rikkert Frederix, Emanuele Re, and Paolo Torrielli, *Single-top t -channel hadroproduction in the four-flavour scheme with POWHEG and aMC@NLO*, JHEP 09 (2012), p. 130. DOI: 10.1007/JHEP09(2012)130. arXiv: 1207.5391 [hep-ph].
- [198] Pierre Artoisenet, Rikkert Frederix, Olivier Mattelaer, and Robbert Rietkerk, *Automatic spin-entangled decays of heavy resonances in Monte Carlo simulations*, JHEP 1303 (2013), p. 015. DOI: 10.1007/JHEP03(2013)015. arXiv: 1212.3460 [hep-ph].
- [199] Torbjorn Sjöstrand, Stephen Mrenna, and Peter Z. Skands, *PYTHIA 6.4 Physics and Manual*, JHEP 05 (2006), p. 026. DOI: 10.1088/1126-6708/2006/05/026. arXiv: hep-ph/0603175.
- [200] Peter Zeiler Skands, *Tuning Monte Carlo Generators: The Perugia Tunes*, Phys. Rev. D82 (2010), p. 074018. DOI: 10.1103/PhysRevD.82.074018. arXiv: 1005.3457 [hep-ph].
- [201] LHC Top Physics Working Group, *ATLAS-CMS recommended predictions for top-quark-pair cross sections using the Top++v2.0 program*. 2015. URL: <https://twiki.cern.ch/twiki/bin/view/LHCPhysics/TtbarNNLO> (visited on 11/30/2016).
- [202] Michal Czakon and Alexander Mitov, *Top++: A Program for the Calculation of the Top-Pair Cross-Section at Hadron Colliders*, Comput. Phys. Commun. 185 (2014), p. 2930. DOI: 10.1016/j.cpc.2014.06.021. arXiv: 1112.5675 [hep-ph].
- [203] P. Kant, O. M. Kind, T. Kintscher, T. Lohse, T. Martini, S. Mölbitz, P. Rieck, and P. Uwer, *HatHor for single top-quark production: Updated predictions and uncertainty estimates for single top-quark production in hadronic collisions*, Comput. Phys. Commun. 191 (2015), pp. 74–89. DOI: 10.1016/j.cpc.2015.02.001. arXiv: 1406.4403 [hep-ph].
- [204] M. Aliev, H. Lacker, U. Langenfeld, S. Moch, P. Uwer, and M. Wiedermann, *HATHOR: HAdronic Top and Heavy quarks crOss section calculatoR*, Comput. Phys. Commun. 182 (2011), pp. 1034–1046. DOI: 10.1016/j.cpc.2010.12.040. arXiv: 1007.1327 [hep-ph].
- [205] LHC Top Physics Working Group, *ATLAS-CMS recommended predictions for single-top cross sections using the Hathor v2.1 program*. 2016. URL: <https://twiki.cern.ch/twiki/bin/view/LHCPhysics/SingleTopRefXsec> (visited on 11/30/2016).
- [206] Nikolaos Kidonakis, *Two-loop soft anomalous dimensions for single top quark associated production with a W^- or H^-* , Phys. Rev. D82 (2010), p. 054018. DOI: 10.1103/PhysRevD.82.054018. arXiv: 1005.4451 [hep-ph].

-
- [207] D. J. Lange, *The EvtGen particle decay simulation package*, Nucl. Instrum. Meth. A462 (2001), p. 152. DOI: 10.1016/S0168-9002(01)00089-4.
- [208] ATLAS Collaboration, *Search for Neutral Minimal Supersymmetric Standard Model Higgs Bosons $H/A \rightarrow \tau\tau$ produced in pp collisions at $\sqrt{s} = 13$ TeV with the ATLAS Detector*. Tech. rep. ATLAS-CONF-2015-061. Geneva: CERN, Dec. 2015. URL: <https://cds.cern.ch/record/2114827>.
- [209] ATLAS Collaboration, *Search for Minimal Supersymmetric Standard Model Higgs bosons H/A and for a Z' boson in the $\tau\tau$ final state produced in pp collisions at $\sqrt{s} = 13$ TeV with the ATLAS Detector*, Eur. Phys. J. C76.11 (2016), p. 585. DOI: 10.1140/epjc/s10052-016-4400-6. arXiv: 1608.00890 [hep-ex].
- [210] ATLAS Collaboration, *Improved luminosity determination in pp collisions at $\sqrt{s} = 7$ TeV using the ATLAS detector at the LHC*, Eur. Phys. J. C73.8 (2013), p. 2518. DOI: 10.1140/epjc/s10052-013-2518-3. arXiv: 1302.4393 [hep-ex].
- [211] ATLAS Collaboration, *Luminosity determination in pp collisions at $\sqrt{s} = 8$ TeV using the ATLAS detector at the LHC*, Eur. Phys. J. C76.12 (2016), p. 653. DOI: 10.1140/epjc/s10052-016-4466-1. arXiv: 1608.03953 [hep-ex].
- [212] M. Bahr et al., *Herwig++ Physics and Manual*, Eur. Phys. J. C58 (2008), pp. 639–707. DOI: 10.1140/epjc/s10052-008-0798-9. arXiv: 0803.0883 [hep-ph].
- [213] Michael H. Seymour and Andrzej Siodmok, *Constraining MPI models using σ_{eff} and recent Tevatron and LHC Underlying Event data*, JHEP 10 (2013), p. 113. DOI: 10.1007/JHEP10(2013)113. arXiv: 1307.5015 [hep-ph].
- [214] J. Alwall et al., *The automated computation of tree-level and next-to-leading order differential cross sections, and their matching to parton shower simulations*, JHEP 07 (2014), p. 079. DOI: 10.1007/JHEP07(2014)079. arXiv: 1405.0301 [hep-ph].
- [215] J. H. Friedman, *Data analysis techniques for high energy particle physics*. SLAC-176. Oct. 1974, 96 p. DOI: 10.5170/CERN-1974-023.271.
- [216] J. M. Butterworth et al., “THE TOOLS AND MONTE CARLO WORKING GROUP Summary Report from the Les Houches 2009 Workshop on TeV Colliders”. In: *Physics at TeV colliders. Proceedings, 6th Workshop, dedicated to Thomas Binoth, Les Houches, France, June 8-26, 2009*. 2010. arXiv: 1003.1643 [hep-ph].
- [217] Jon Butterworth et al., *PDF4LHC recommendations for LHC Run II*, J. Phys. G43 (2016), p. 023001. DOI: 10.1088/0954-3899/43/2/023001. arXiv: 1510.03865 [hep-ph].
-

- [218] Sayipjamal Dulat et al., *New parton distribution functions from a global analysis of quantum chromodynamics*, Phys. Rev. D93.3 (2016), p. 033006. DOI: 10.1103/PhysRevD.93.033006. arXiv: 1506.07443 [hep-ph].
- [219] A. D. Martin, W. J. Stirling, R. S. Thorne, and G. Watt, *Heavy-quark mass dependence in global PDF analyses and 3- and 4-flavour parton distributions*, Eur. Phys. J. C70 (2010), pp. 51–72. DOI: 10.1140/epjc/s10052-010-1462-8. arXiv: 1007.2624 [hep-ph].
- [220] Andy Buckley, James Ferrando, Stephen Lloyd, Karl Nordström, Ben Page, Martin Rüfenacht, Marek Schönherr, and Graeme Watt, *LHAPDF6: parton density access in the LHC precision era*, Eur. Phys. J. C75 (2015), p. 132. DOI: 10.1140/epjc/s10052-015-3318-8. arXiv: 1412.7420 [hep-ph].
- [221] Michiel Botje et al., *The PDF4LHC Working Group Interim Recommendations*. 2011. arXiv: 1101.0538 [hep-ph].
- [222] Valerio Bertone, Stefano Carrazza, and Juan Rojo, *APFEL: A PDF Evolution Library with QED corrections*, Comput. Phys. Commun. 185 (2014), pp. 1647–1668. DOI: 10.1016/j.cpc.2014.03.007. arXiv: 1310.1394 [hep-ph].
- [223] Stefano Carrazza, Alfio Ferrara, Daniele Palazzo, and Juan Rojo, *APFEL Web*, J. Phys. G42.5 (2015), p. 057001. DOI: 10.1088/0954-3899/42/5/057001. arXiv: 1410.5456 [hep-ph].
- [224] ATLAS Collaboration, *ATLAS Run 1 Pythia8 tunes*. Tech. rep. ATL-PHYS-PUB-2014-021. Geneva: CERN, Nov. 2014. URL: <https://cds.cern.ch/record/1966419>.
- [225] ATLAS Collaboration, *Recommendations for MC tunes: systematic uncertainties and non-pQCD corrections*. [ATLAS internal document]. 2015. URL: <https://twiki.cern.ch/twiki/bin/view/AtlasProtected/MCTuningRecommendations?rev=10> (visited on 09/29/2015).
- [226] Xing-Gang Wu, Stanley J. Brodsky, and Matin Mojaza, *The Renormalization Scale-Setting Problem in QCD*, Prog. Part. Nucl. Phys. 72 (2013), pp. 44–98. DOI: 10.1016/j.pnpnp.2013.06.001. arXiv: 1302.0599 [hep-ph].
- [227] Takashi Mitani et al. (ATLAS Collaboration), *Measurement of the tau lepton reconstruction and identification performance in the ATLAS experiment using pp collisions at $\sqrt{s} = 13$ TeV*. Tech. rep. ATL-COM-PHYS-2016-929. [ATLAS internal document]. Geneva: CERN, July 2016. URL: <https://cds.cern.ch/record/2199788>.
- [228] ATLAS Collaboration, *A method for the construction of strongly reduced representations of ATLAS experimental uncertainties and the application thereof to the jet energy scale*. Tech. rep. ATL-PHYS-PUB-2015-014. Geneva: CERN, July 2015. URL: <http://cds.cern.ch/record/2037436>.

-
- [229] Peter Berta et al. (ATLAS Collaboration), *Flavour tagging pre-recommendations for Run-II*. Tech. rep. ATL-COM-PHYS-2016-092. [ATLAS internal document]. Geneva: CERN, Feb. 2016. URL: <https://cds.cern.ch/record/2128507>.
- [230] A. Elagin, P. Murat, A. Pranko, and A. Safonov, *A New Mass Reconstruction Technique for Resonances Decaying to di-tau*, Nucl. Instrum. Meth. A654 (2011), pp. 481–489. DOI: 10.1016/j.nima.2011.07.009. arXiv: 1012.4686 [hep-ex].
- [231] Masahiro Morinaga et al. (ATLAS Collaboration), *Search for neutral MSSM Higgs bosons $H/A \rightarrow \tau_{lep}\tau_{had}$ produced in 13 TeV collisions with the ATLAS detector*. Tech. rep. ATL-COM-PHYS-2016-425. [ATLAS internal document]. Geneva: CERN, May 2016. URL: <https://cds.cern.ch/record/2150207>.
- [232] Glen Cowan, Kyle Cranmer, Eilam Gross, and Ofer Vitells, *Asymptotic formulae for likelihood-based tests of new physics*, Eur. Phys. J. C71 (2011). [Erratum: Eur. Phys. J.C73,2501(2013)], p. 1554. DOI: 10.1140/epjc/s10052-011-1554-0. arXiv: 1007.1727 [physics.data-an].
- [233] ATLAS Statistics Forum, *Frequentist Limit Recommendation*. Tech. rep. Draft 1.1. CERN, Feb. 2011.
- [234] J. Neyman and E. S. Pearson, *On the Problem of the Most Efficient Tests of Statistical Hypotheses*, Philosophical Transactions of the Royal Society of London A: Mathematical, Physical and Engineering Sciences 231.694-706 (1933), pp. 289–337. DOI: 10.1098/rsta.1933.0009.
- [235] Gary J. Feldman and Robert D. Cousins, *Unified approach to the classical statistical analysis of small signals*, Phys. Rev. D 57 (7 Apr. 1998), pp. 3873–3889. DOI: 10.1103/PhysRevD.57.3873.
- [236] J. Neyman, *Outline of a Theory of Statistical Estimation Based on the Classical Theory of Probability*, Philosophical Transactions of the Royal Society of London A: Mathematical, Physical and Engineering Sciences 236.767 (1937), pp. 333–380. DOI: 10.1098/rsta.1937.0005.
- [237] Roger J. Barlow and Christine Beeston, *Fitting using finite Monte Carlo samples*, Comput. Phys. Commun. 77 (1993), pp. 219–228. DOI: 10.1016/0010-4655(93)90005-W.
- [238] J. S. Conway, “Incorporating Nuisance Parameters in Likelihoods for Multisource Spectra”. In: *Proceedings, PHYSTAT 2011 Workshop on Statistical Issues Related to Discovery Claims in Search Experiments and Unfolding, CERN, Geneva, Switzerland 17-20 January 2011*. 2011, pp. 115–120. DOI: 10.5170/CERN-2011-006.115. arXiv: 1103.0354 [physics.data-an].
- [239] Aart Heijboer and Ivo van Vulpen, “Analysis Walk-Throughs”. In: *Data Analysis in High Energy Physics*. Wiley-VCH Verlag GmbH & Co. KGaA, 2013, pp. 357–379. DOI: 10.1002/9783527653416.ch11.
-

- [240] A. L. Read, *Presentation of search results: the CL_s technique*, Journal of Physics G: Nuclear and Particle Physics 28.10 (2002), p. 2693. DOI: 10.1088/0954-3899/28/10/313.
- [241] Abraham Wald, *Tests of Statistical Hypotheses Concerning Several Parameters When the Number of Observations is Large*, Transactions of the American Mathematical Society 54.3 (1943), pp. 426–482. DOI: 10.2307/1990256.
- [242] S. S. Wilks, *The Large-Sample Distribution of the Likelihood Ratio for Testing Composite Hypotheses*, Ann. Math. Statist. 9.1 (Mar. 1938), pp. 60–62. DOI: 10.1214/aoms/1177732360.
- [243] Kyle Cranmer, George Lewis, Lorenzo Moneta, Akira Shibata, and Wouter Verkerke (ROOT Collaboration), *HistFactory: A tool for creating statistical models for use with RooFit and RooStats*. Tech. rep. CERN-OPEN-2012-016. New York: New York U., Jan. 2012. URL: <https://cds.cern.ch/record/1456844>.
- [244] L. Moneta, K. Cranmer, G. Schott, and W. Verkerke, “The RooStats project”. In: *Proceedings of the 13th International Workshop on Advanced Computing and Analysis Techniques in Physics Research. February 22-27, 2010, Jaipur, India*. 2010, p. 57. arXiv: 1009.1003 [physics.data-an].
- [245] W. Verkerke and D. Kirkby, *RooFit Users Manual v2.07*. 2006. URL: http://roofit.sourceforge.net/docs/RooFit_Users_Manual_2.07-29.pdf (visited on 08/29/2016).
- [246] Rene Brun and Fons Rademakers, *New Computing Techniques in Physics Research V ROOT — An object oriented data analysis framework*, Nuclear Instruments and Methods in Physics Research Section A: Accelerators, Spectrometers, Detectors and Associated Equipment 389.1 (1997), pp. 81–86. DOI: 10.1016/S0168-9002(97)00048-X.
- [247] Boris Delaunay, *Sur la sphère vide. A la mémoire de Georges Voronoï*, Bulletin de l’Académie des Sciences de l’URSS 6 (1934), pp. 793–800.
- [248] Abdelhak Djouadi, *The Anatomy of electro-weak symmetry breaking. II. The Higgs bosons in the minimal supersymmetric model*, Phys. Rept. 459 (2008), pp. 1–241. DOI: 10.1016/j.physrep.2007.10.005. arXiv: hep-ph/0503173.
- [249] John F Gunion, Sally Dawson, Howard E Haber, and Gordon L Kane, *The Higgs hunter’s guide*. Vol. 80. Upton, NY: Brookhaven Nat. Lab., 1989.
- [250] ATLAS Collaboration, *Search for neutral Higgs bosons of the minimal supersymmetric standard model in pp collisions at $\sqrt{s} = 8$ TeV with the ATLAS detector*, JHEP 11 (2014), p. 056. DOI: 10.1007/JHEP11(2014)056. arXiv: 1409.6064 [hep-ex].

- [251] ATLAS Collaboration, *Search for Minimal Supersymmetric Standard Model Higgs Bosons H/A in the $\tau\tau$ final state in up to 13.3 fb^{-1} of pp collisions at $\sqrt{s}=13\text{ TeV}$ with the ATLAS Detector*. Tech. rep. ATLAS-CONF-2016-085. Geneva: CERN, Aug. 2016. URL: <https://cds.cern.ch/record/2206278>.
- [252] CMS Collaboration, *Search for a neutral MSSM Higgs boson decaying into $\tau\tau$ with 12.9 fb^{-1} of data at $\sqrt{s}=13\text{ TeV}$* . Tech. rep. CMS-PAS-HIG-16-037. Geneva: CERN, 2016. URL: <https://cds.cern.ch/record/2231507>.

Acknowledgments

First and foremost, I would like to express my sincere gratitude to my supervisor Arno Straessner for his support throughout my thesis, with advice and by providing good opportunities for my academic career. I also very much appreciate to have had the freedom to follow my own ideas.

Furthermore, I would like to thank my collaborators in the MSSM analysis, especially Nikolaos Rompotis, from whom I learnt a lot and enjoyed to coordinate the analysis together. Many thanks also to the other analysis contact colleagues, Lei Zhang, Matthew Beckingham and Dirk Duschinger. It was great having such reliable and knowledgeable collaborators. A special thanks to the rest of the analysis team, Mark Pickering, Damián Álvarez Piqueras, Guillermo Hamity, Pedro de Bruin, Masahiro Morinaga, Allison McCarn, Hao Liu, Samina Jabbar, Rachel Hyneman and especially to Luca Fiorini. This analysis and our publications would not have been possible without the great support by the HBSM conveners, Allison McCarn, Carl Gwilliam, Arnaud Ferrari and Erez Etzion – thanks for the input and helping us to succeed. The same goes for our editorial boards, of which I would like to especially thank Jean-Baptiste de Vivie and German Montoya. I also enjoyed being a part of the ATLAS Tau Working Group; thank you Will Davey, Pier-Olivier DeViveiros and Attilio Andreazza for making it the most fun group in ATLAS.

A big thanks to the Research Training Group 1504 for their support, especially Martin zur Nedden for the great organization and advice on my project.

A huge thanks to my colleagues of the Dresden Tau Group, who it was very enjoyable to work with. I especially thank Sebastian Wahrmond for the interesting discussions and for providing useful code. I also learned a lot from the previous generation of doctoral students, especially Marcus Morgenstern, Felix Friedrich and Christian Gumpert – thank you guys so much.

Also my other colleagues at the institute contributed significantly to a nice work atmosphere. Thanks Felix Socher, it was nice developing ELCORE together. Stefanie Todt and Carsten Bittrich deserve my gratitude for being great office mates at CERN. I would like to thank our institute director Michael Kobel and our administrative team – thank you a lot for your effort in making the institute the great place it is. This work would not have been possible without stable computing resources, which were masterfully maintained by Wolfgang Mader and Robert Mantey at the institute. Furthermore, I thank the DESY NAF and WLCG administrators.

A big thanks to Arno Straessner and Fabian Multrus for their help to improve this thesis.

Last but not the least, I would like to thank my parents, sister, brother and my friends for their kind support.

Versicherung

Hiermit versichere ich, dass ich die vorliegende Arbeit ohne unzulässige Hilfe Dritter und ohne Benutzung anderer als der angegebenen Hilfsmittel angefertigt habe; die aus fremden Quellen direkt oder indirekt übernommenen Gedanken sind als solche kenntlich gemacht. Die Arbeit wurde bisher weder im Inland noch im Ausland in gleicher oder ähnlicher Form einer anderen Prüfungsbehörde vorgelegt.

Die vorliegende Dissertation wurde am Institut für Kern- und Teilchenphysik der Technischen Universität Dresden unter der wissenschaftlichen Betreuung von Prof. Dr. Arno Straessner angefertigt.

Es haben keine früheren erfolglosen Promotionsverfahren stattgefunden.

Ich erkenne die Promotionsordnung der Fakultät Mathematik und Naturwissenschaften an der Technischen Universität Dresden vom 23.02.2011 in der Fassung vom 18.06.2014 an.

Dresden, den 06.02.2017

Dipl. Phys. Lorenz Hauswald